IECO

Volume 8 No 1 Year 2025

■ Volume 8

■ No 1

■ Year 2025

University of Sistan and Baluchestan

Iranian Association of Electrical and Electronics Engineers

International Journal Of

Industrial Electronics Control and Optimization

In This Issue:

Research Articles:

IECO

International Journal of Industrial Electronics Control and Optimization

About Journal

The University of Sistan and Baluchestan entered into strategic partnership with Iranian Association of Electrical and Electronic Engineers (IAEEE) to publish the **International Journal of Industrial Electronics Control and Optimization (IECO)**. The IECO is a refereed international journal which presents to the international scientific community important results of work in these fields, whether in the form of modeling simulation, analysis, fundamental research, development, application, design or real-time implementation. The scope of IECO is broad, encompassing all aspects of Industrial Electronics, Control and Optimization.

Note: International Journal of Industrial Electronics, Control and Optimization (IECO) has qualified to **ACADEMIC RESEARCH JOURNAL (ELMI-PAJOHESHI)** status certified by the ministry of Science, Research and Technology of Iran (No. 231566/3/18 dated 1396/10/09), and is published by the University of Sistan and Baluchestan through a formal partnership (No. 952/2/1500 dated 1395/11/04) with Iranian Association of Electrical and electronic Engineers (IAEEE) in order to develop scientific and research cooperation.

Aims and Scope

International Journal of Industrial Electronics, Control and Optimization (IECO) is a Peer reviewed journal of advanced and state-of-the-art in the science and engineering of Industrial Electronics, Control and Optimization. Its Scope encompasses the applications of Industrial Electronics, power systems, control, optimization and computational intelligence for the enhancement of industrial and manufacturing system and processes. The scope of the journal include the following:

I. Industrial Electronics

- Low and high-power converters
- Renewable energy
- Drive control techniques
- Techniques for advanced power semiconductor devices
- Power quality and utility applications
- Communications
- Flexible AC Transmission Systems (FACTS)
- Control in power electronics
- Electromagnetic and thermal performance of electronic power converters
- Motion control, robotics, sensors and actuators
- Fault detection and diagnosis
- Power systems
- Factory automation, communication, and computer networks

II. Control

- Adaptive control
- Control of process systems
- Control theory
- Data processing
- Design of control systems
- Hybrid systems
- Identification and observation
- Intelligent systems
- Model-predictive control
- Optimal control
- Robust control
- Fractional order systems

III. Optimization

- Ant Colony
- Chaos Theory
- Evolutionary Computing
- Fuzzy Computing
- Hybrid Methods
- Immunological Computing
- Neuro Computing
- Particle Swarm
- Probabilistic Computing
- Rough Sets
- Wavelet

International Journal Of
Industrial Electronics Control and Optimization
Print ISSN: 3517-2645
Online ISSN: 3568-2645
Homepage: https://ieco.usb.ac.ir/

Adaptive Fractional-Order Consensus Control of Cyber-Physical Power Systems in the Presence of Unbounded Perturbations

Mahmood Nazifi | Mahdi Pourgholi

Faculty of Electrical Engineering, Shahid Beheshti University, Tehran, Iran.
Corresponding author's email: m_pourgholi@sbu.ac.ir

Article Info

Article type:
Research Article

Article history:
Received: 22-May-2024
Received in revised form: 31-August-2024
Accepted: 28-September-2024
Published online:22-June-2025

Keywords:
Cyber-Physical Power Systems,
Fractional-order,
multi agent systems,
Sliding-mode control,
Adaptive control.

ABSTRACT

The consensus of Cyber-Physical Power Systems (CPPSs), where generators agree on common desired rotor angles and speeds, is vital for maintaining system stability and efficiency. This study explores this consensus using fractional-order multi-agent systems, offering advantages over traditional methods. CPPSs often encounter issues like faults, uncertainties, disturbances, and cyber-attacks. To address these, a new Adaptive Fractional-Order Sliding Mode Controller (AFOSMC) is proposed, designed to achieve consensus despite unknown nonlinear functional upper bounds characterizing system perturbations. The AFOSMC uses stable adaptive laws to determine these unknown coefficients, ensuring robust performance even under adverse conditions. It outperforms conventional Integer-Order counterparts by reducing chattering and enabling faster convergence during the initial phase of CPPS operations. The AFOSMC also ensures finite-time convergence to the sliding surface, enhancing system responsiveness and stability. The controller's stability is rigorously proven using Lyapunov's theorem. Finally, extensive simulations demonstrate the practical benefits of the AFOSMC, and comparisons with recent research highlight its superior performance in robustness and efficiency.

I. INTRODUCTION

a) Introduction and Literature review

CPPSs, introduced as a convergence of cyber-physical systems and power systems, integrate various computing devices, data acquisition instruments, and physical components through communication and transmission networks [1]. These systems leverage computing capabilities, data acquisition technologies, and physical devices to enhance the efficiency, reliability, and overall performance of power systems. The integration of sophisticated technologies in CPPSs introduces technical and security challenges [2,3]. These challenges arise from the intricate interplay between the cyber and physical components, requiring robust solutions to ensure the resilience and integrity of the power systems. Research in CPPSs spans various domains, including traffic networks and aviation electric power systems [4-7]. The emphasis on stability stems from its critical role in preventing problems such as voltage collapse and system failure. The overall goal is to leverage the benefits of CPPSs while effectively managing the associated complexities and challenges. Stability is a primary concern for CPPSs and is often addressed through the lenses of supply and demand balance and rotor angle stability [8,9]. In [10] a robust control scheme based on H_∞ performance index is presented for CPPSs which is based on attack estimation. However, the upper bound of disturbance is considered known in this paper. The supply-demand balance ensures a harmonious match between electricity production and consumption across diverse networks. On the other hand, rotor angle stability is crucial for the smooth and efficient operation of CPPSs, allowing each generator to attain a time-varying common rotor angle and speed. These stability aspects are viewed through the framework of consensus theory [11-12]. Consensus theory plays a pivotal role in addressing stability challenges in CPPSs [11-12]. By employing consensus theory, researchers aim to achieve agreement and coordination among different components within the system. This approach facilitates the attainment of a common understanding or state, ensuring the

stable and synchronized functioning of the diverse elements within CPPS. In summary, CPPSs represent an innovative paradigm in power systems, integrating advanced technologies to enhance performance [1]. The challenges and research focus on stability underscore the importance of developing robust solutions to ensure the reliable and secure operation of these complex systems.

Sliding Mode Control (SMC) stands out as a nonlinear variable structure control method known for its swift response and robustness against system uncertainties and disturbances [13]. Fractional order equations can also be used for achieving robust control. For example in [14] a variable structure of fractional-order equations is presented which is using floated pole controller in order to achieve robust approach. Using fractional order equations in SMC, in recent years, numerous studies have delved into the stabilization of nonlinear fractional-order systems, with a predominant reliance on robust SMC [13-22]. In a study by [15], a sliding mode control law was developed based on a back-stepping technique for nonlinear fractional-order systems. This innovative approach achieved external disturbances rejection through the application of a new fractional-order back-stepping technique. Another noteworthy contribution is found in [16], where a fractional-order sliding mode control, utilizing the Particle Swarm Optimization (PSO) algorithm, was designed for a specific class of nonlinear fractional-order systems. Consideration of uncertainty in the linear parts of a nonlinear fractional-order system was addressed in [17]. Stability in the face of uncertainty was guaranteed by defining an integer-order sliding surface. In [18] a robust and adaptive terminal SMC is designed for Cyber-Physical systems which are exposed to external disturbances. By considering attacks as false data injections, an even triggered adaptive SMC in also presented in [19] for controlling Cyber-Physical systems. SMC in also combined with adaptive fuzzy fractional order concept in [20] to achieve stability in an uncertain nonlinear system. The weakness of all these references is to know about disturbance or its upper bound and considering this upper bound as a simple scalar value. Output feedback sliding mode control for nonlinear fractional-order systems was the focal point in [21]. The study provided a necessary and sufficient condition for the existence of the sliding surface in the form of a Linear Matrix Inequality (LMI).

These studies collectively showcase the versatility and effectiveness of Sliding Mode Control, particularly in stabilizing nonlinear fractional-order systems amidst uncertainties and disturbances. The integration of innovative techniques, such as back-stepping, PSO algorithms, and LMI, further enriches the applicability and robustness of SMC in addressing the complexities inherent in these systems. In the study presented in [22], the focus is on a second-order system where the upper band of disturbance and its derivatives are assumed to be known. The sliding surface is carefully defined, and the stability of the sliding mode control law is subsequently demonstrated.

A distinctive approach is taken in [23] for a specific class of nonlinear fractional-order systems with nonlinear dynamics. Here, a sliding mode observer is employed to estimate the states, and a novel sliding mode control law is utilized to converge the system states to zero. A recent contribution in [24] introduces a sliding mode active disturbance rejection control for fractional-order nonlinear systems characterized by unknown states and disturbances. This innovative method combines a sliding mode extended state observer with sliding mode control, providing a comprehensive solution. In [25], an attempt is made to design SMC based Linear Quadratic Regulator (LQR) for nonlinear fractional-order systems (FOSs). This paper presents a fractional-order switching surface and some unique conditions are derived by using Lyapunov theory and linear matrix inequalities (LMIs) to guarantee the stability of FOS. An observer based distributed sliding mode secondary control is also presented in [26] to achieve consensus in DC microgrids that are under cyber-attacks. In this method, the detected false signals have been compensated using the control variables in the secondary stage control of the micro grid. The work presented in [27] introduces a fractional integral sliding surface, leveraging the Composite Learning Sliding Mode Control method to manage fractional-order nonlinear systems afflicted with actuator faults. This method integrates the benefits of fractional calculus and sliding mode control techniques to achieve effective control in the presence of actuator faults. However, dealing with modeling uncertainties and external disturbances with unknown upper bounds, especially when the upper bounds are a function of system states, is still an open problem.

b) Contribution and novelty of paper

It is crucial to highlight that, despite extensive research in the control of nonlinear fractional-order systems in the presence of uncertainties and disturbances, two key challenges persist in most studies. Firstly, many studies fail to address the stabilization problem for the general form of nonlinear affine fractional-order systems. Secondly, in most cases, the upper bounds of uncertainties are assumed to be known. However, in practical applications, the limits of model uncertainties and external disturbances are typically unknown, adding a layer of complexity to real-world systems.

In this context, the sliding mode control of the general form of fractional-order nonlinear systems, where the upper bounds of

uncertainties and external disturbances are unknown (a more realistic and practical assumption), remains a challenging problem. This specific issue is the focal point of discussion and investigation in the current paper. To illustrate the practical implications of the proposed method, the nonlinear fractional-order model of multi agent Cyber-Physical Power System (CPPS) is considered as an application. This application serves as a tangible example to showcase the effectiveness and relevance of the method in real-world scenarios, emphasizing the need for robust control strategies in the face of uncertainties and disturbances.

Therefore, the novelty and the main contribution of this paper can be summarized as achieving consensus in Cyber-Physical Power Systems in a more realistic and more applicable situation that have not been considered in previous studies:

1) Considering the fractional order model of agents in a Cyber-Physical Power System (CPPS) which is a more accurate description of the system.
2) Introducing a novel concept, postulating that the upper bound of external disturbances and model uncertainties transcends mere a known scalar value like other references, but an unknown nonlinear function of CPPS state variables.
3) Designing a new Adaptive Fractional-Order Sliding Mode Controller (AFOSMC) to achieve consensus in CPPS, in which a specific adaptive procedure is created to predict the external disturbances' functional upper bound coefficients.
4) The presented method can be easily extended for the stabilization problem of the general form of nonlinear affine fractional-order systems.

This paper is organized as follows. Section II describes the CPPS model considering cyber-attacks, uncertainties and external disturbances. The main results of the paper are presented in Section III. In this section, a new adaptive sliding mode controller is designed to guarantee asymptotic stability for the CPPS system. A chattering avoidance technique is also given in this section. Numerical examples are provided in Section IV to confirm the effectiveness of the designed controller. Finally, conclusions close the paper in Section V.

II. PROBLEM STATEMENT

a) CPPS Network Mathematical Model

In this section, we delve into the stability analysis of the rotor angle within the Cyber-Physical Power System (CPPS). The CPPS can be effectively modeled using the following formulas [28]:

$$\dot{\delta}_i = \omega_i \tag{1}$$

$$\begin{cases} \dot{\omega}_i = -\dfrac{D_i}{M_i}\omega_i + \dfrac{1}{M_i}(P_{mi} - P_{ei}) \\ \dot{E}_i' = F_i\dot{E}_i' + L_i(\delta_i)V_i + H_iE_{fi} \\ P_{ei} = V_i^T[R_i(\delta_i)V_i + T_i(\delta_i)E_i'] \\ P_{mi} = \dfrac{B_{mi}P}{A_{mi}P}u_{mi} \\ E_{fi} = \dfrac{B_{fi}P}{A_{fi}P}u_{fi} \\ V = [Y - R(\delta)]^{-1}T(\delta)E' \end{cases} \tag{2}$$

where δ_i is the rotor angle, ω_i is the rotor speed, D_i is the damping coefficient, M_i is the inertia constant, P_{mi} is the mechanical power, P_{ei} is the electrical power, E_i' is the internal bus voltage vector, V is the generator terminal voltage vector. Also, $B_{mi}P$ and $A_{mi}P$ are respectively the polynomials of the numerator and denominator of the mechanical power transfer function and $B_{fi}P$ and $A_{fi}P$ are the same case for bus voltage transfer function. Also u_{mi} and u_{fi} are respectively turbine–governor subsystem input and bus voltage input. Additionally, Y is a constant matrix and $R(\delta)$ and $T(\delta)$ are matrices constructed from elements $R_i(\delta_i)$ and $T_i(\delta_i)$ respectively. The detailed descriptions of $R_i(\delta_i)$, $T_i(\delta_i)F_i$ and $H_i$can be found in [28]. These matrices and parameters play crucial roles in characterizing the dynamics of the CPPS. A classical coherency criterion asserts that a generator pair (i, j) is deemed coherent if

$$\begin{cases} \lim\limits_{t\to\infty}\|\delta_i - \delta_j\| = 0 \\ \lim\limits_{t\to\infty}\|\omega_i - \omega_j\| = 0 \end{cases} \tag{3}$$

We can treat the rotor angle stability of the Cyber-Physical Power System (CPPS) as a consensus problem for a second-order multi-agent system. By utilizing a multi-agent system, we can delve into the study of rotor angle stability.

Considering equations (1) and (2), if the controller input is selected as follows:

$$\bar{P}_{mi} = M_iu_i' + D_i\omega_i + P_{ei} \tag{4}$$

Introducing u_i' as the new input to be determined, the differential equations governing the rotor angle and rotor speed in the Cyber-Physical Power System (CPPS) are expressed as follows:

$$\begin{cases} \dot{\delta}_i = \omega_i \\ \dot{\omega}_i = u_i' \end{cases} \tag{5}$$

Hence, the design of u_i' holds significance in this context. Subsequently, we explore the rotor angle stability of the Cyber-Physical Power System (CPPS) using a multi-agent system model.

In such multi-agent system, communication among the agents is described by a weighted directed graph G with N nodes. In

this graph, each vertex corresponds to an agent and $w_{ij} \geq 0$ denotes the weight of the edge between *i*th and *jth* agents. This weight is a value that determines the connection strength between *i*th and *j*th agents in the swarm system. Graph G is described by its adjacency matrix given as follows [29].

$$W = \begin{bmatrix} w_{11} & \cdots & w_{1N} \\ \vdots & \ddots & \vdots \\ w_{N1} & \cdots & w_{NN} \end{bmatrix} \quad (6)$$

Fractional-order calculus is adopted for its generality, as an extension of the integer-order calculus. The fractional-order format of rotor equations in the Cyber-Physical Power System (CPPS) in (5) is considered as follows [30]

$$\begin{cases} D^{\alpha}\delta_i = \omega_i \\ D^{\alpha}\omega_i = u_i \quad i = 1,2,\dots,N \end{cases} \quad (7)$$

where $.\alpha \in (0,1], \delta_i, \omega_i \in R^n$. In this equation, ${}_0D_t^a$ is the fractional-order differentiator, which signifies a generalized extension of the conventional differential and integral operators, as defined in reference [31]:

$${}_0D_t^a = \begin{cases} \frac{d^{\alpha}}{dt^{\alpha}} & , \alpha > 0 \\ 1 & , \alpha = 0 \\ \int_0^t (d\tau)^{-\alpha} & , \alpha < 0 \end{cases} \quad (8)$$

In this context, α denotes the fractional-order, which can assume the form of a complex number. There are several definitions for general fractional and integration differentiation. Because of the congruence of initial conditions between fractional-order differential equations using Caputo derivatives and their integer-order counterparts, the Caputo fractional derivative is commonly used in fractional-order system models. As documented in references [31-32], the Caputo fractional derivative operator is expressed as follows:

$${}_0D_t^{\alpha}x(t) = \frac{1}{\Gamma(\lceil\alpha\rceil-\alpha)}\int_0^t \frac{x^{(\lceil\alpha\rceil)}(\tau)}{(t-\tau)^{\alpha-\lceil\alpha\rceil+1}}d\tau,\ 0 < \alpha \notin Z_+ \quad (9)$$

in which $\Gamma(.)$ represents the Gamma function, and $\lceil\alpha\rceil$ signifies the mapping of α to the smallest integer greater than or equal to α, as expounded in [31-33].

Now, with definitions $x_{i1} = \delta_i$ and $x_{i2} = \omega_i$, equation (6) can be expressed as follows:

$$\begin{cases} D^{\alpha}x_{i1} = x_{i2} \\ D^{\alpha}x_{i2} = u_i \end{cases} \quad (10)$$

And, considering the vector $x_i = [x_{i1}, x_{i2}] \in R^2$,we have:

$$D^{\alpha}x_i = Ax_i + Bu_i \quad (11)$$

In this expression, we have:

$$A = \begin{bmatrix} 0 & 1 \\ 0 & 0 \end{bmatrix}, \quad B = \begin{bmatrix} 0 \\ 1 \end{bmatrix} \quad (12)$$

Now, let's introduce disturbances, encompassing uncertainties, disturbance modeling, cyberattacks, and input bias faults into the multi-agent system. Hence, the model of factors exposed to disturbances can be expressed as:

$$D^{\alpha}x_i = Ax_i + B_i[u_i(t) + f_{ia}(t) + f_i(t)] + \Delta f_i(x) + d_i(t) \quad (13)$$

In the provided expression, $d_i(t)$ characterizes external disturbances and is constrained by $\|d_i(t)\| < \alpha$, where α denotes the upper bound of disturbances. $f_{ia}(t)$ represents the input bias error of each factor in the system, with $\|f_{ia}(t)\| < \beta$ and $\Delta f_i(x)$ accounts for modeling uncertainties and unmodeled dynamics, assumed to be limited as $\|\Delta f_i(x)\| < \delta$. Additionally, it is posited that cyberattacks $f_i(t)$ are bounded by $\|f_i(t)\| < \xi$, where ξ signifies the maximum intensity value of cyberattacks applicable to an energy source in the CPPS.

Model (13) can be reformulated as follows:

$$D^{\alpha}x_i = Ax_i + B_iu_i(t) + h_i(x,t) \quad (14)$$

In this context, the components are defined as follows:

$$h_i(x,t) = B_if_{ia}(t) + B_if_i(t) + \Delta f_i(x) + d_i(t) \quad (15)$$

The term $h_i(x,t)$ serves as a representation of bias, collective error, cyberattacks, modeling uncertainties, and disturbances within each factor. In essence, $h_i(x,t)$ encapsulates the summation of these elements, colloquially referred to as "disturbance." The distinctive characteristic of the various components constituting this disturbance is their unknown nature and their confinement within limited upper bounds. The system represented by equation (15) is denoted as a model of distributed energy resources with disturbances in a CPPS.

The objective of controller design is to formulate a distributed control law such that, accounting for the disturbances outlined in the model of agents in the CPPS within equation (15), the following goal is achieved in terms of consensus:

$$\lim_{t\to\infty}\|x_i - x_{ref}\| = 0, \quad \forall i \neq j \quad (16)$$

b) Consensus error model in CPPS Network

After formulating the agent model, representing the distributed energy resources in a CPPS under disturbances as given in equation (15), the proposed generalized secondary control law is presented to attain consensus and drive the agents toward x_{ref}. Drawing inspiration from [26] with slight modifications, we propose the following expression, highlighting the incorporation of information from neighboring agents in the graph:

$$u_i = -\sum_{j=1}^{N} w_{ij}(x_i - x_j) - g_i(x_i - x_{ref}) + u_{a_i} \quad i\epsilon\{1,2,\dots N\} \tag{17}$$

The scalar value g_i serves as an indicator distinguishing whether the i-th node functions as a leader or a follower within the CPPS, with $g_i > 0$ for $i = 1,2,\dots,l$ denoting leader nodes and $g_i = 0$ for $i = l+1,\dots,N$ indicating follower nodes. Consequently, leader nodes are orchestrated to adhere to the reference value, while follower nodes are steered towards achieving consensus.

Upon applying the control input from equation (17) to the agent model in the CPPS outlined in equation (15), the resulting expression is as follows:

$$D^{\alpha}x_i = Ax_i - B\sum_{j=1}^{N} w_{ij}(x_i - x_j) - Bg_i(x_i - x_{ref}) + Bu_{a_i} + h_i(x,t) \tag{18}$$

By defining the difference between the state variable of each distributed energy source x_i and the reference value x_{ref}, we introduce the state variable error as $e_i = x_i - x_{ref}$. Consequently, the equation governing the error is expressed as follows:

$$\begin{aligned} D^{\alpha}e_i &= D^{\alpha}x_i - D^{\alpha}x_{ref} \\ &= Ax_i - B\sum_{j=1}^{N} w_{ij}(x_i - x_j) - Bg_i(x_i - x_{ref}) + Bu_{a_i} + h_i(x,t) - D^{\alpha}x_{ref} \end{aligned} \tag{19}$$

By incorporating both addition and subtraction of Ax_{ref} into equation (19) and taking into account the generalized error state vector in the distributed resource system as $e = [e_1,\dots,e_N]^T$, the disturbances vector as $H = [h_1(x,t),\dots,h_N(x,t)]^T$, and the secondary input vector as $U = [u_{a1},\dots,u_{aN}]^T$, the dynamics of the system and the dynamics of errors in the state variables can be expressed as follows:

$$D^{\alpha}e = (\tilde{A} - \tilde{B}(L+G))e + \tilde{B}U + H + \Phi \tag{20}$$

where L is the Laplacian graph matrix, $\Phi = Ax_{ref} - D^{\alpha}x_{ref}[1,\dots,1]^T$ and we have:

$$\tilde{B} = \begin{bmatrix} B & 0 & 0 & \cdots & 0 \\ 0 & B & 0 & \cdots & 0 \\ \vdots & \ddots & \ddots & \ddots & \vdots \\ 0 & 0 & \ddots & \ddots & 0 \\ 0 & 0 & \cdots & 0 & B \end{bmatrix} \in R^{2N\times N} \tag{21}$$

$$G = \begin{bmatrix} g_1 & 0 & 0 & \cdots & 0 \\ 0 & g_2 & 0 & \cdots & 0 \\ \vdots & \ddots & \ddots & \ddots & \vdots \\ 0 & 0 & \ddots & \ddots & 0 \\ 0 & 0 & \cdots & 0 & g_N \end{bmatrix} \in R^{N\times N}$$

$$\tilde{A} = \begin{bmatrix} A & 0 & 0 & \cdots & 0 \\ 0 & A & 0 & \cdots & 0 \\ \vdots & \ddots & \ddots & \ddots & \vdots \\ 0 & 0 & \ddots & \ddots & 0 \\ 0 & 0 & \cdots & 0 & A \end{bmatrix} \in R^{2N\times 2N}$$

By defining $\hat{A} = \tilde{A} - \tilde{B}(L+G)$, the model described in equation (16) can be expressed as follows:

$$D^{\alpha}e = \hat{A}e + \tilde{B}U + \Phi + H \tag{22}$$

This equation provides a concise representation of the error dynamics in the distributed resource system, incorporating the Laplacian graph matrix, disturbance vector, and secondary input vector.

Note 1: It should be noted that in order to obtain (22), we have used and extended the procedure that is presented in [34] for linear fractional order multiagent systems. We extended it from a linear model to a nonlinear model of agents as shown in equation (13).

c) Objective of the study

Reflect upon the forthcoming statement concerning CPPS system model uncertainty and external disturbances:

Remark 1. The model uncertainties $\Delta f_i(x)s$ are contingent on the CPPS system states. Furthermore, the situation and states of a CPPS is influenced by external disturbances and more importantly, the magnitude and how the cyber attack $f_i(t)$ is applied to the system, depend on the current state of the CPPS system. Hence, this study introduces a novel concept, postulating that the upper limit encompassing external disturbances and model uncertainties in equation (15) transcends mere scalar value but the form of a nonlinear function contingent upon CPPS state variables. Concurrent with this, stable adaptive laws will be established to estimate the coefficients governing this upper boundary function, assuming their initial unknown status. This causes the CPPS reference tracking issue to have more appropriate and practical assumptions. Therefore, consider the following assumption:

Assumption 1. Let us assume that the upper limit for the vector encompassing model uncertainties and external disturbances within the CPPS model is bounded, as illustrated in equation (22):

$$\|H(x(t),t)\| \le \alpha h(x(t),t) + \beta \tag{23}$$

in which α and β refer to the unknown values and $h(x(t),t)$ represents an arbitrary nonlinear function contingent upon the CPPS system's state variables.

It is worth mentioning that in [34], the upper bounds of modelling uncertainties and external disturbances were

considered as a linear function of system states norm as $\alpha\|x(t)\| + \beta$. However, the upper bound of the perturbations that is considered here in Assumption 1 is a more general form of what is considered in [34]. Using the assumption in (23), it can even be claimed that the perturbations may be unbounded. The nonlinear CPPS system faces external disturbances and model uncertainties, and this study seeks to build Adaptive Fractional-Order Sliding Mode Controller (AFOSMC) for it. The indicated convergences in (11) would be attained by developing the controllers as mentioned above while taking Assumption 1 into account. Additionally, specific adaptive procedures are created to predict external disturbances' functional upper limit coefficients and model uncertainties in (23). This paper's novelty lies in its approach to addressing the CPPS challenge under realistic conditions, assuming the validity of Assumption 1. In the next section, we introduce AFOSMC to address CPPS reference tracking while upholding this foundational assumption.

Before dealing with the stabilizing controller, consider the following Lemma:

Lemma 1 [33-34]: The Fractional Order system $D_t^{\alpha}x(t) = Ax(t)$, where $x(t) \in R^n$ for $t \geq 0$, $A \in R^{n\times n}$, and D_t^{α} denotes the Caputo fractional derivative operator is asymptotically stable if and only if $|arg(\lambda)| > \alpha\frac{\pi}{2}$ for each eigenvalue λ of matrix A (In this case the matrix A is called an α-Hurwitz matrix).

III. PROPOSED METHODOLOGY

Fractional-order equations enable controllers with more adjustability than traditional integer-order ones. They effectively reduce chattering in sliding mode control, as shown ahead.

In this section, we create a Fractional Order Sliding Mode surface and then introduce a new Robust-Adaptive Fractional Order Sliding Mode Controller (AFOSMC) to handle CPPS system perturbations, considering model uncertainties, cyber-attacks and external disturbances. We account for the assumption that the upper bound of model uncertainties is an unknown nonlinear function of CPPS system states.

This section also examines the convergence of CPPS system states to the switching surface and presents an innovative approach to mitigate chattering.

a) Sliding manifold and reaching law

Considering the CPPS system in (22), we define an $(N-1)d$-dimensional sliding manifold in the form

$$s(t) = C\int_0^t D_{\tau}^{\alpha}e(\tau)\,d\tau - C\int_0^t (\hat{A} + BK)\,e(\tau)d\tau \qquad (24)$$

where $s(t) = [s_1, s_2, \dots, s_{2N}] \in R^{2N}$ is the sliding manifold vector, $C \in R^{2N\times 2N}$ is an arbitrary matrix in such a way that CB is invertible and $K \in R^{2N\times 2N}$ is designed parameter matrix that will be obtained in the next subsection. According to the sliding mode approach, the switching manifold and its derivative should be equal to zero. To this end, consider the following reaching law [33-34]

$$\dot{s}(t) = -\mu s - \rho\, sgn(s) \qquad (25)$$

where $\mu, \rho \in R^+$ and $sgn(S) = [sgn(s_1), sgn(s_2), \dots, sgn(s_{2N})]^T \in R^{2N}$.

The reaching law is a stable vector first-order equation that is chosen in such a way that the sliding surface $s(t)$, which is the independent variable of this equation, converges to zero. Then, after selecting this reaching law, it is time to design the control law. The control law is chosen in such a way that the equation governing the sliding surface $s(t)$ becomes this reaching law.

As you can see from (25) left side of reaching law is $\dot{s}(t)$. Now, it is easy to take a derivative from the sliding surface in (24) to appear $\dot{s}(t)$. Then, we easily set the result of the derivative of the sliding surface equal to the right side of the reaching law and using this idea, the control law will be easily obtained as in next subsection, although with a few changes.

b) Proposed Adaptive Fractional-Order Sliding Mode Controller (AFOSMC)

The AFOSMC for stabilizing the CPPS system described in equation (15) is introduced using the fractional-order sliding surface outlined in equation (18) as follows:

$$u = (CB)^{-1}(CBKe - C\Phi - \mu s - sgn(s) \times \left(\rho + \hat{\beta}\|C\| + \hat{\alpha}\|C\|h(x(t),t)\right)) \qquad (26)$$

where $\hat{\alpha}$ and $\hat{\beta}$ come from the following adaptive rules and represent estimates of the unknown parameters in (23):

$$\dot{\hat{\alpha}} = \eta_1\|C\|s^T\, sgn(s)\, h(x,t)$$
$$\dot{\hat{\beta}} = \eta_2\|C\|s^T\, sgn(s) \qquad (27)$$

where η_1 and η_2 stand for two arbitrary, positive constant values representing adaptive gains. The following theorem expresses the primary outcome of the current study, which is the design of AFOSMC.

Theorem 1. Consider the CPPS system in (22), which is affected by external disturbances, Cyber-attacks and model uncertainty. Assuming the validity of Assumption 1, where the upper bound on model uncertainty and external disturbances depends on CPPS states with unknown coefficients, the reference tracking errors within the CPPS system (22) now asymptotically converges to zero. This is achieved using AFOSMC as defined in (26)-(27), with positive constant values $\eta_1, \eta_2 > 0$, $\mu, \rho > 0$ and constant matrix K that

satisfies $\left|\arg\left(eig(\hat{A}+BK)\right)\right| \geq \alpha\frac{\pi}{2}$.

Proof: Consider the following proposition for the Lyapunov function.

$$V = \frac{1}{2}s^T s + \frac{1}{2\eta_1}\tilde{\alpha}^2 + \frac{1}{2\eta_2}\tilde{\beta}^2 \tag{28}$$

where $\tilde{\alpha} = \hat{\alpha} - \alpha$ and $\tilde{\beta} = \hat{\beta} - \beta$ represent adaptive parameter errors. Now, differentiating (28) and substituting $\dot{s}$ from (24) yields:

$$\dot{V} = s^T\dot{s} + \frac{1}{\eta_1}\tilde{\alpha}\dot{\tilde{\alpha}} + \frac{1}{\eta_2}\tilde{\beta}\dot{\tilde{\beta}} = s^T\left(CD_\tau^\alpha e - C\left(\hat{A}+BK\right)e\right) + \frac{1}{\eta_1}\tilde{\alpha}\dot{\tilde{\alpha}} + \frac{1}{\eta_2}\tilde{\beta}\dot{\tilde{\beta}} \tag{29}$$

Substituting $D_\tau^\alpha e$ from the CPPS system in (22) into (29) and given that $\dot{\tilde{\alpha}} = \dot{\hat{\alpha}}$and $\dot{\tilde{\beta}} = \dot{\hat{\beta}}$, results in

$$\dot{V} = s^T\left(C\hat{A}e + CBU + C\Phi + CH - C\left(\hat{A}+BK\right)e\right) + \frac{1}{\eta_1}\tilde{\alpha}\dot{\hat{\alpha}} + \frac{1}{\eta_2}\tilde{\beta}\dot{\hat{\beta}} \tag{30}$$

Using the suggested AFOSMC from (26) in combination with the adaptive laws from (27) will results in:

$$\dot{V} = s^T\left(-\mu s - sgn(s)\left(\rho + \hat{\beta}\|C\| + \hat{\alpha}\|C\|h(x(t),t)\right) + CH\right) + \frac{1}{\eta_1}(\hat{\alpha}-\alpha)\dot{\hat{\alpha}} + \frac{1}{\eta_2}(\hat{\beta}-\beta)\dot{\hat{\beta}} \tag{31}$$

which results

$$\begin{aligned}\dot{V} = {} & -\mu\|s\|^2 - \rho s^T sgn(s) - \hat{\beta}\|C\|s^T sgn(s) \\ & -s^T\|C\|\hat{\alpha}h(x(t),t)\,sgn(s) + s^T CH(x,t) \\ & +(\hat{\alpha}-\alpha)\|C\|s^T sgn(s)\,h(x,t) \\ & +(\hat{\beta}-\beta)\|C\|s^T sgn(s)\end{aligned} \tag{32}$$

By eliminating similar terms and considering $s^T sgn(s) = \|s\|$ we obtain:

$$\begin{aligned}\dot{V} = {} & -\mu\|s\|^2 - \rho\|s\| + s^T CH(x,t) \\ & -\alpha\|C\|\|s\|h(x,t) - \beta\|C\|\|s\|\end{aligned} \tag{33}$$

In addition, using $s^T CH(x,t) \leq \|s^T CH(x,t)\| \leq \|s\|\|C\|\|H(x,t)\|$ and, then, the inequality in (23) will yields:

$$\begin{aligned}\dot{V} & \leq -\mu\|s\|^2 - \rho\|s\| + \|s\|\|C\|\|H(x,t)\| \\ & \quad -\alpha\|C\|\|s\|h(x,t) - \beta\|C\|\|s\| \\ & \leq -\mu\|s\|^2 - \rho\|s\| + \|s\|\|C\|(\alpha h(x,t)+\beta) \\ & -\alpha\|C\|\|s\|h(x,t) - \beta\|C\|\|s\| = -\mu\|s\|^2 - \rho\|s\|\end{aligned} \tag{34}$$

Consequently, with the positivity of μ and ρ as well as in accordance with Barbalat's lemma $s(t)$ converges to zero as $t \to \infty$ This, in turn, leads to the convergence of the reference error in the CPPS system to zero, as specified by the sliding surface equation in (24) and utilizing Lemma 1.

Remark 2. In the AFOSMC presented in equations (26)-(27), a sign function, which is a discontinuous function centered around $s = 0$, has been utilized. This function can lead to highly precarious situations for the CPPS system, characterized by high-frequency oscillations, commonly referred to as chattering, within the controller signal. In a sliding mode controller, chattering may be minimized in a number of methods, including by applying saturation or a hyperbolic tangent function. Although using these continuous functions to approximate the sign function may lessen chattering, the closed-loop system's controller performance may suffer. To mitigate chattering, we introduce a novel successive approximation function similar to what was outlined in [35]. Consequently, the term $\rho sgn(s)$, $\rho > 0$ is computed as follows:

$$\rho sgn(S) \cong \frac{\rho^2 S}{\rho\|S\| + \sigma(t)} \tag{35}$$

in which $\sigma(t) > 0$ represents a positively bounded function with the property $\int_0^\infty \sigma(t)dt < \infty$. An example of such a function $\sigma(t) > 0$ is as follows

$$\sigma(t) = \frac{1}{1+t^n}, n \geq 2 \tag{36}$$

The approximation in equation (35) is continuous and will continue to be continuous throughout time. Therefore, the chattering will lessen. The function $\sigma(t)$ converges to zero rapidly, rendering the approximation closer to the sign function with greater precision compared to alternative approximations such as the hyperbolic tangent function.

Lemma 2. Utilizing the reaching law as $\dot{s} = -\mu s - \rho sign(s)$ defined in equation (25), which is employed in AFOSMC, the CPPS system states reach the sliding surface in finite time t^* as follows:

$$t^* = \frac{1}{\mu}ln\left(\frac{\rho + \mu|s(0)|}{\rho}\right), \tag{37}$$

Proof: For the initial states of the sliding surface with$s(0) > 0$ or $s(0) < 0$, the differential equation governing the reaching law is derived as follows:

$$\begin{cases}\dot{s} = -\mu s - \rho, & s(0) > 0 \\ \dot{s} = -\mu s + \rho, & s(0) < 0\end{cases} \tag{38}$$

The solution to the above equations is as follows:

$$\begin{cases}s(t) = \left(s(0) + \frac{\rho}{\mu}\right)e^{-\mu t} - \frac{\rho}{\mu}, & s(0) > 0 \\ s(t) = \left(s(0) - \frac{\rho}{\mu}\right)e^{-\mu t} + \frac{\rho}{\mu}, & s(0) < 0\end{cases} \tag{39}$$

Now, given that sliding surface has $i = 1,\ldots,2N$ components, by setting $s_i(t_i) = 0$, it is found that

$$t_i = \frac{1}{\mu} ln(\frac{\rho + \mu|s_i(0)|}{\rho}), \quad (40)$$

Now, the final finite time is:

$$t^* = max_{i=1..2N}(t_i), i = 1, \ldots, 2N \quad (41)$$

This demonstrates that the system states reach the sliding surface within a finite time denoted by t^*, depending on the initial value of the sliding surface.

Remark 3. We had claimed that the method presented in this paper can be easily extended to solve the stabilization problem of a more general form meaning nonlinear affined fractional order systems i.e. $D^\alpha x = f(x) + g(x)u + H$. We first add and subtract the desired linear value Ax to above affine system and then we have:

$$D^\alpha x = f(x) + g(x)u + H + Ax - Ax \quad (42)$$

It should be said that the controller presented in Theorem 1 is designed for achieving asymptotic stability in system in (22). The point is that the fractional order nonlinear affine system in (42) can be easily transformed to system in (22), by considering the following change of variables:

$$x \to e, \; A \to \hat{A}, \; g(x) \to \tilde{B}, \quad (43)$$
$$(f(x) - Ax) \to \Phi(x)$$

IV. SIMULATION RESULTS

In this section, the effectiveness of the proposed controller is verified through numerical examples. The numerical simulations in this section use the Adams-type predictor-corrector method suggested in [36] for obtaining the solution of fractional-order differential equations.

This segment illustrates the efficacy of the main findings through a specific numerical scenario. Consider a 5-generator cyber-physical power system with 14 buses, as depicted in Figure 1. The data pertinent to this setup is sourced from the IEEE standard test system for such configurations. Each generator is linked to an agent enabling the exchange of information among them, as illustrated in Figure 2. The interconnected cyber and physical networks are connected via distinct arrow types.

With a distributed multi-agent approach, these networks are seamlessly integrated. If each agent (generator) contains two tiers of information, denoted as $N = 5, n = 2$, the rotor angle and rotor speed profiles for the cyber-physical power systems can be examined in Figures 3(a) and 3(b) respectively. Observing the plots indicates the convergence of rotor angles and speeds toward a shared dynamic value.

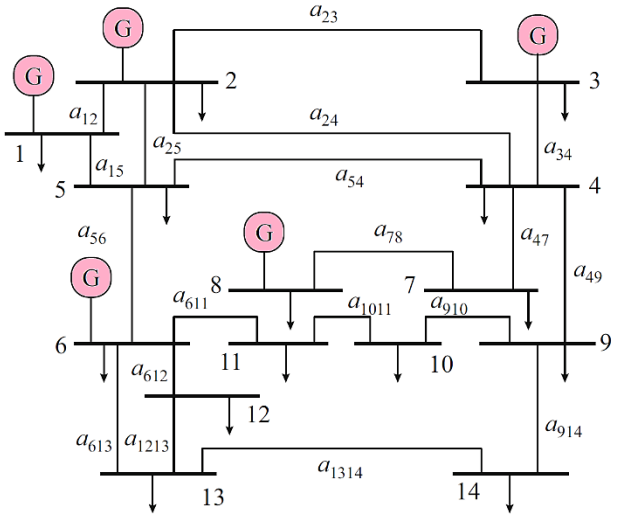

Fig. 1: A 5-generator 14-bus CPPS for simulation [30]

-

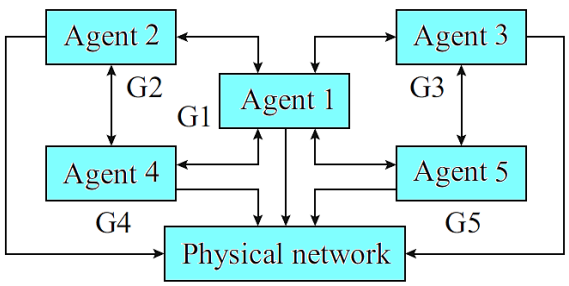

Fig. 2: Graph representation of 5-generator 14-bus CPPS in Figure 1 [30]

To simulate such a multi-agent cyber-physical power system, the system parameters are considered the same as those presented in [30]. The control parameters of AFOSMC control law, which should be set according to Theorem 1, are considered as follows:

$$\mu = 10, \quad \rho = 3,$$
$$\eta_1 = 2, \quad \eta_2 = 3 \quad (44)$$
$$h(x(t), t) = 5\|x\|$$

The values of sliding plates are shown in Figure 4. This figure also clearly shows that by applying the designed AFOSMC control law, the sliding surfaces converge to zero in a finite time according to Lemma 2. From that moment, the system enters the so-called sliding mode, in which the consensus error converges to zero. Adaptive parameters for employing the AFOSMC control law are presented in Fig. 5. This figure makes it evident that both adaptive parameters tend to specific bounded scalar values, demonstrating the stability of adaptive laws designed in (27).

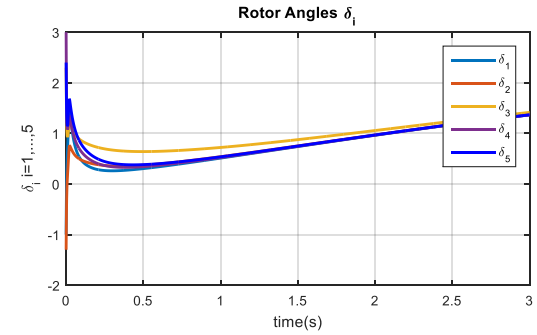

(a)

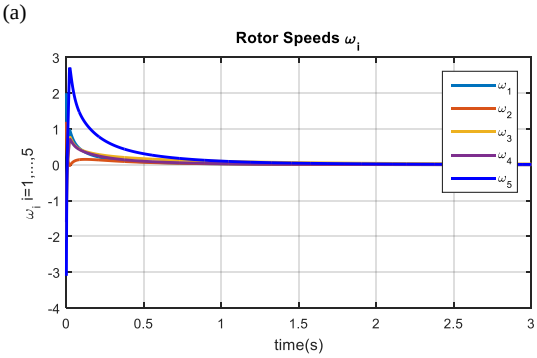

(b)

Fig. 3: Rotor angles (a) and Rotor speeds (b) of CPPS in simulation part and achieving consensus among them

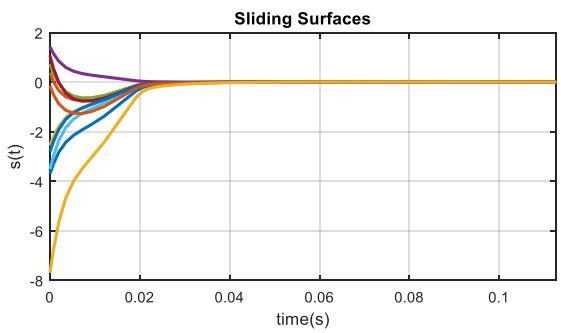

Fig. 4: Sliding surfaces of closed loop CPPs system

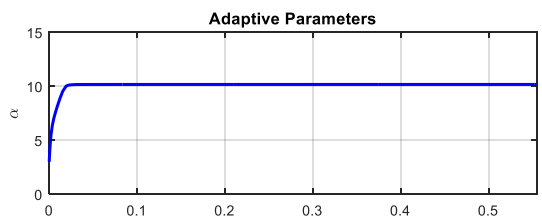

(a)

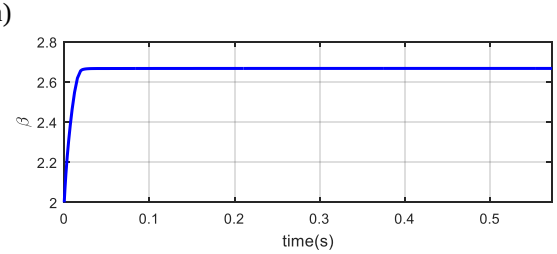

(b)

Fig. 5: Adaptive parameters of control law in (24)

Finally, the control input signals for all agents, i.e. rotors, are shown in Figure 6. The bounded amplitude values of these signals and the convergence to zero as expected, show that this controller has performed well in achieving consensus among the angles and speeds of the rotors in the CPPS system.

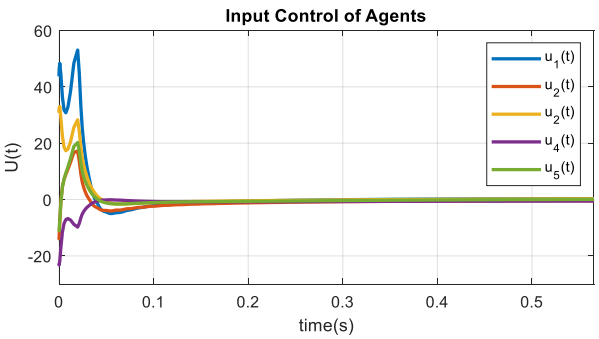

Fig. 6: Control input of rotors in closed loop CPPS system

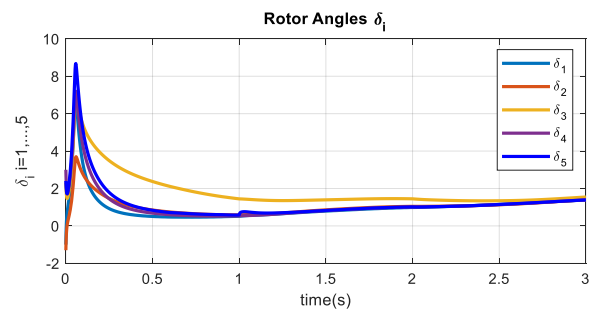

(a)

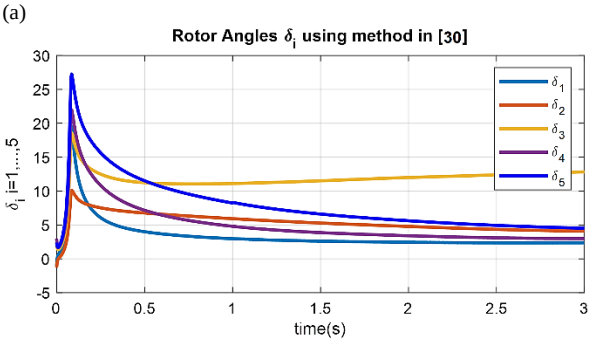

(b)

Fig. 7. Consensus in rotor angles of CPPS system by applying: (a) AFOSMC control law designed in this paper and (b) the event triggered method presented in [30]

- *A Comparison with other reference*

In this subsection a comparison with one of the recent related references that is about using event-trigger method to achieve consensus of cyber-physical power systems based on multi-agent systems with communication constraints, is presented [30].

Figures 7 and 8 show the results of comparing the AFOSMC controller proposed in this paper with a recent controller proposed in reference [30] for achieving consensus in fractional-order cyber-physical power systems based on the event-trigger method. To do this, the disturbances, consisting of two cyber-attack signals applied to agent 1 and agent 3, are defined as follows:

$$f_1(t) = \begin{bmatrix} f_{11} \\ f_{12} \end{bmatrix}, \quad f_{11} = \begin{cases} 5, & 0.5 \le t \le 0.7 \\ 0 & otherwise \end{cases},$$
$$f_{12} = \begin{cases} 6, & 1 \le t \le 2 \\ 0 & otherwise \end{cases}, \qquad (45)$$
$$f_2(t) = \begin{bmatrix} f_{21} \\ f_{22} \end{bmatrix}, \quad f_{21} = \begin{cases} 4, & 1 \le t \le 3 \\ 0 & otherwise \end{cases},$$
$$f_{22} = \begin{cases} 7, & 0.6 \le t \le 0.9 \\ 0 & otherwise \end{cases}$$

Additionally, the modeling uncertainties in the CPPS system are as follows:

$$\Delta f_i(x) = \begin{bmatrix} 6\sin(4t) + 0.01\sin(2x_{i1}) + 0.01\cos(4x_{i2}) \\ 6\sin(4t) + 0.01\cos(4x_{i1}) + 0.01\sin(2x_{i1}) \end{bmatrix}, \qquad (46)$$

Both the method presented in reference [30] and our method consider uncertainties and disturbances as cyber-attacks in the CPPS system. However, Figures 7 and 8 clearly show the superiority of the method described in this paper by comparing the convergence of rotor angles and rotor speeds in achieving consensus. It is clear that the AFOSMC controller proposed in this paper has a better performance with a small overshoot and low rise time. However, in the presence of uncertainties and disturbances with unknown functional upper bounds, the event-trigger control law in [30] is unable to achieve consensus and cannot handle these uncertainties and disturbances.

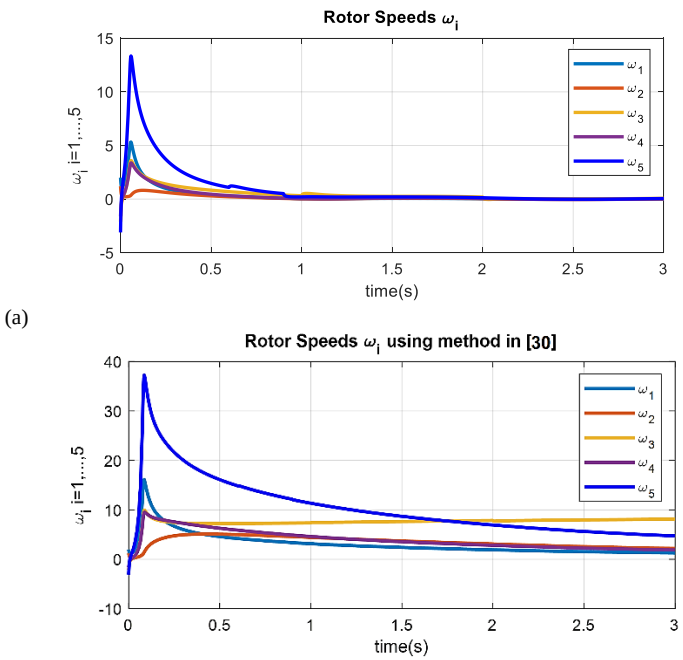

Fig. 8. Consensus in rotor speeds of CPPS system by applying: (a) AFOSMC control law designed in this paper and (b) the event triggered method presented in [30]

The comparison of transient response characteristics in the time domain between reference [30] and the proposed AFOSMC controller is also presented in Table 1. As we can see, in the convergence of both the rotor angles and the rotor speeds, by applying the control law designed in this paper (AFOSMC), both the overshoot and the settling time are less compared to the event-trigger method resented in [30]. This is, of course, next to this important feature that in our method, firstly, unlike reference [30] the upper band of disturbances is assumed to be unknown. And besides, this upper band, is not just a scalar but a nonlinear function of the system states.

TABLE 1 COMPARING THE SIMULATION RESULTS OF APPLYING CONTROL LAW IN [30] WITH OUR CONTROL LAW AFOSMC

Specifications	Controller in [30]	AFOSMC in this paper
Overshoot in Rotor Angles	28	8.7
Overshoot in Rotor Speeds	37	13
Settling Time of Rotor angle consensus	7	2.5
Settling Time of Rotor Speed consensus	10.5	0.9

V. CONCLUSION

Consensus of fractional-order linear time invariant cyber-physical power systems, in the presence of model uncertainties, disturbances and cyber-attacks in both of inherent and interactive dynamics and graph topology, was studied in this paper. In this study, an adaptive-robust fractional order sliding mode controller has been designed to achieve consensus in the presence of mentioned uncertainties and disturbances with the important constraint that the upper bound of system perturbations is a nonlinear unbounded function with unknown coefficients. To deal with these perturbations, a chattering-free fractional order AFOSMC method is presented in which the coefficients of the upper bound function are estimated by stable adaptive laws. Numerical simulation results confirm the effectiveness of the proposed controller compared to other recent references. The consensus of Cyber-Physical Power Systems in the presence of *communication time delay* among fractional order model of agents, achieving *finite time consensus* in the fractional order model of CPPS using terminal sliding mode control and designing fractional order sliding control *considering input constrains*, can be considered as three future research plans to continue this work.

REFERENCES

[1] P. A. Oyewole and D. Jayaweera, "Power System Security with Cyber-Physical Power System Operation," in IEEE Access, vol. 8, pp. 179970-179982, 2020.

[2] M. Abdelmalak, V. Venkataramanan and R. Macwan, "A Survey of Cyber-Physical Power System Modeling Methods for Future Energy Systems," in IEEE Access, vol. 10, pp. 99875-99896, 2022.

[3] Z. Dong, M. Tian and L. Ding, "A Framework for Modeling and Structural Vulnerability Analysis of Spatial Cyber-Physical Power Systems from an Attack–Defense Perspective," in IEEE Systems Journal, vol. 15, no. 1, pp. 1369-1380, March 2021.

[4] Y. He, Q. Feng, Z. Chen, X. Yang and C. Wu, "Research and simulation of freight vehicle cooperative adaptive cruise formation control model," 6th International Conference on Transportation Information and Safety (ICTIS), Wuhan, China, pp. 1327-1331, 2021.

[5] J. B. Hu, F. Li, J. Wu et al, “Research on aviation electric power cyber physical systems,” Adv Mater Res, pp. 846–847:126–133, 2013.
[6] S. Mokred, Y. Wang, T. Chen, “Modern voltage stability index for prediction of voltage collapse and estimation of maximum load-ability for weak buses and critical lines identification,” International Journal of Electrical Power & Energy Systems, Vol. 145, pp. 108596, 2023.
[7] T. Kim, T. K. Oh, K. S. Kook, Y. H. Moon, “Bifurcation Control Application to-Voltage Collapse in a Model Power System,” IFAC Proceedings Volumes, vol. 36, no. 20, pp. 815-819, 2003.
[8] K. Khan, F. Hassan, J. Koo, M. A. Mohammed, Y. Hasan, Shamsheela, D. Muhammad, B. S. Chowdhry, N. M. Faseeh Qureshi, “Blockchain-based applications and energy effective electric vehicle charging – A systematic literature review, challenges, comparative analysis and opportunities,” Computers and Electrical Engineering, vol. 112, pp. 108959, 2023,
[9] P. Wu, H. Sun, W. Zhong, H. Chang, D. Huang and Y. Jiang, "Rotor Angle Stability with Different Penetration Levels of Wind Generation in the Sending Grid," 2020 IEEE Sustainable Power and Energy Conference (iSPEC), Chengdu, China, pp. 948-954, 2020,
[10] [10] Pan K, Yang F, Feng Z, Pan Q. Attack estimation–based resilient control for cyber-physical power systems. Transactions of the Institute of Measurement and Control, 45(5), pp. 886-898, 2023.
[11] Y. Li, T. Yong, J. Cao J et al, “A consensus control strategy for dynamic power system look-ahead scheduling,” Neurocomputing, vol. 168, pp.1085–1093, 2015.
[12] M. J. Morshed and A. Fekih, "A Coordinated Controller Design for DFIG-Based Multi-Machine Power Systems," in IEEE Systems Journal, vol. 13, no. 3, pp. 3211-3222, Sept. 2019.
[13] A. Pisano and E. Usai, “Sliding mode control: A survey with applications in math,” Mathematics and Computers in Simulation, vol. 81(5), pp. 954-979, 2011.
[14] [14] M. H. Zarif and E. Abbaszadeh, Fractional-Order Variable Structure Equations In Robust Control, International Journal of Industrial Electronics, Control and Optimization (IECO), 6(2), pp. 101-111, 2023.
[15] Q. H. Zhang, J. G. Lu, “Robust stability of fractional-order systems with mixed uncertainties: The $0<\alpha<1$ case,” Communications in Nonlinear Science and Numerical Simulation, vol. 126, pp. 107511, 2023.
[16] A. Djari, T. Bouden, A. Boulkroune, “Design of Fractional-order Sliding Mode Controller (FSMC) for a class of Fractional-order Non-linear Commensurate Systems using a Particle Swarm Optimization (PSO) Algorithm,” CEAI, Vol.16, No.3 pp. 46-55, 2014.
[17] L. Chen, R. Wu, Y. He, Y. Chai, “Adaptive sliding-mode control for fractional-order uncertain linear systems with nonlinear disturbances,” Nonlinear Dyn, 2014.
[18] [18] A. Nemati, M. Peimani, S. Mobayen and S. J. Sayyedfattahi, Adaptive terminal sliding mode controller design for cyber-physical systems under external disturbance and actuator cyber-attack, Int J Adapt Control Signal Process, 37(6), pp. 1369-1388, 2023.
[19] [19] Yanmei Xue, Wen Ren, Bo-Chao Zheng, Jinke Han, Event-triggered adaptive sliding mode control of cyber-physical systems under false data injection attack, Applied Mathematics and Computation, 433, 127403, 2022.
[20] [20] A. Razzaghian, R. K. Moghaddam and N. Pariz, Adaptive fuzzy fractional-order fast terminal sliding mode control for a class of uncertain nonlinear systems, International Journal of Industrial Electronics, Control and Optimization (IECO), 5(1), pp. 77-87, 2022.
[21] T. Zhan, X. Liu, S. Ma, “A new singular system approach to output feedback sliding mode control for fractional order nonlinear systems,” Journal of the Franklin Institute, 2018.
[22] J. l. Zhou, S. Q. Zhang, Y. B. He, “Existence and stability of solution for a nonlinear fractional differential equation,” Journal of Mathematical Analysis and Applications, vol. 498, no. 1, pp. 124921, 2021,
[23] M. A. Zahedi Tajrishi, A. Akbarzadeh Kalat, “Fast finite time fractional-order robust-adaptive sliding mode control of nonlinear systems with unknown dynamics,” Journal of Computational and Applied Mathematics, Vol. 438, pp. 115554, 2024.
[24] N. Djeghali, M. Bettayeb, S. Djennoune, “Sliding mode active disturbance rejection control for uncertain nonlinear fractional-order systems,” European Journal of Control, vol. 57, pp. 54-67, 2021.
[25] K. Mathiyalagan and G. Sangeetha, Second-order sliding mode control for nonlinear fractional-order systems, Applied Mathematics and Computation, 383, 125264, 2020.
[26] Yajie Jiang, Yun Yang, Siew-Chong Tan, and Shu Yuen Hui, Distributed Sliding Mode Observer-Based Secondary Control for DC Microgrids Under Cyber-Attacks, ieee journal on emerging and selected topics in circuits and systems, vol. 11, no. 1, march 2021.
[27] H. Liu, H. Wang, J. Cao, A. Alsaedi and T. Hayat, Composite learning adaptive sliding mode control of fractional-order nonlinear systems with actuator faults, Journal of the Franklin Institute, 356(16), pp. 9580-9599, 2019.
[28] Tuglie E, Iannone S, Torelli F, A coherency-based method to increase dynamic security in power systems. Electronic Power System Res 78(8):1425–1436, 2008.
[29] Godsil, C. and G. Royle (2000). Algebraic graph theory. Springer.
[30] Huang, Ch., Ch. Feng and J. Cao. Consensus of cyber-physical power systems based on multi-agent systems with communication constraints, , 2019.
[31] Soorki, M., & Tavazoei, M. Fractional-order linear time invariant swarm systems: asymptotic swarm stability and time response analysis. Open Physics, 11(6), 845-854, 2013.
[32] Caponetto, R., G. Dongola, L. Fortuna and I. Petras. Fractional-order Systems: Modeling and Control Applications. World Scientific, 2010.
[33] Naderi Soorki, M., & Saleh Tavazoei, M. Adaptive consensus tracking for fractional-order linear time invariant swarm systems. Journal of Computational and Nonlinear Dynamics, 9(3), 031012, 2014.
[34] Soorki, M. N., & Tavazoei, M. S. Adaptive robust control of fractional-order swarm systems in the presence of model uncertainties and external disturbances. IET control theory & applications, 12(7), 961-969, 2018.
[35] Wang, Zh., X. Huang and H. Shen. Control of an uncertain fractional order economic system via adaptive sliding mode. Neurocomputing, 83, pp. 83–88, 2012.
[36] Diethelm, K., N. J. Ford and A. D. Freed. A predictor-corrector approach for the numerical solution of fractional differential equations. Nonlinear Dynamics, 29(1-4), pp. 3-22, 2002.

Mahmood Nazifi received the B.S. degree in Control Engineering from Qom University of Technology, Iran, in 2014, the M.S. degree at control engineering from the K. N. Toosi University of Technology, Iran, in 2017. He is currently working toward the Ph.D. degree in Control engineering with Shahid Beheshti University, Iran. His research interests include control and optimization of Fractional multi-agent systems.

Mahdi Pourgholi, He, was born in Tehran in the year of 1977, he got his BSc. and MSc. degree in 2000 and 2003 respectively. He has taken his PhD in the department of Control Engineering, Tarbiat Modares University (TMU) in 2010, Tehran, Iran. He currently is an assistant professor in Shahid Beheshti University (SBU) in Tehran, Iran. His research interests include Nonlinear control, Fuzzy systems, Connectivity maintenance and Consensus in the multi agent systems.

International Journal Of
Industrial Electronics Control and Optimization
Print ISSN: 3517-2645
Online ISSN: 3568-2645
Homepage: https://ieco.usb.ac.ir/

Adaptive Fuzzy Control of Blood Glucose Level in Patients with Type 1 Diabetes in Presence of Input Saturation

Fatemeh Soleimannouri[1] | Saeed Khorashadizadeh[2] | Mohsen Farshad[3] | Nasser Mehrshad[4]

Faculty of Electrical and Computer Engineering, University of Birjand, Birjand, Iran.[1,2,3,4]
Corresponding author's email: s.khorashadizadeh@birjand.ac.ir

Article Info

Article type:
Research Article

Article history:
Received: 22-June-2024
Received in revised form: 02-September-2024
Accepted: 08-September-2024
Published online: 22-June-2025

Keywords:
Adaptive fuzzy control,
Blood glucose level,
Type 1 diabetes,
Input saturation.

ABSTRACT

In this research, an adaptive fuzzy controller is presented to regulate the blood glucose level of type 1 diabetic patients in the presence of input saturation. This controller along with an adaptive anti-windup compensator is considered to deal with the uncertainty of the Bergmann minimal nonlinear model parameters as well as the input saturation. Anti windup compensator is designed to prevent to saturation problems as hyperglycemia or hypoglycemia in regulating the blood glucose level of type 1 diabetes patients. The Bergman minimal model is used to mathematically model type 1 diabetes, depicting the dynamic behavior of the human body's blood glucose-insulin system. In the first step, the stability of the closed-loop system has been theoretically investigated and proved from the point of view of Lyapunov's theory. Next, to evaluate the effectiveness of the proposed method in regulating blood glucose levels, the proposed control system has been implemented in the presence of meal disturbances using the Simulink environment of MATLAB software. The implementation results show a lower control effort and less convergence time of the proposed method compared to the existing methods.

I. Introduction

Blood glucose level is one of the most important parameters that determines the health of the metabolic system. The normal function of this system is to maintain the blood glucose level in the range 70 to 110 mg/dl [1]. The amount of insulin secretion on the one hand and the amount of glucose received by the cells in response to insulin on the other hand are decisive in regulation of the blood glucose level.

Type 1 diabetes is originated by an autoimmune response in which the beta cells of the pancreas that are responsible for insulin production are attacked by the immune system. Consequently, insulin production will decrease [2, 3, 4, 5, 6] and blood glucose will increase.

Due to the complications caused by abnormal blood glucose levels, regulation of blood glucose concentration is very important and vital for patients. Therefore, many researches have been planned in recent years. Robust controllers [7, 8] and sliding mode control (SMC) [9, 10] are very popular. They can handle disturbances and uncertainties. However, a common drawback of SMC is the chattering phenomenon. To cope with this problem, higher order sliding mode controllers have been proposed. PID controllers [11, 12, 13, 14] need to be tuned for optimal performance. In addition, PID controllers are not able to cope with saturated insulin conditions. As a result, these controllers can lead to decrease blood glucose levels and hypoglycemia. Model predictive controllers [15, 16, 17] require a robust optimization scheme, which may be computationally expensive. In biomedicine, the accuracy of estimated models limits the performance of model-based predictive control methods. Moreover, providing a generally accurate model is difficult when the controlled subject is a human due to day-to-day and subject-to-subject variations.

In [18], an observer-based adaptive controller is designed to deal with the patient parameter variations and lack of access to all state variables for measurement. In [19], an adaptive fuzzy integral sliding mode controller was proposed for regulating blood glucose levels. System dynamics were identified online using fuzzy logic systems. In [20], an adaptive backstepping control strategy is designed for a non-linear minimal Bergman model considering all the unknown parameters. In the aforementioned article, the control effort does not have a smooth behavior and also the problem of input saturation is not considered. In [21], the output-feedback continuous-twisting algorithm is applied to regulate the blood glucose concentration. The Robust output controller has been provided a practical criterion to tune the controller gains that may be used to individualize the insulin therapy. In [22], a positive input observer-based controller is designed for an Extended Bergman's Minimal Model. The backstepping approach is employed to design the feedback controller. The controller used the first state as feedback. The second state and the third states are estimated using the proposed observers. The controller is robust upon external disturbance and uncertainties in system parameters. In [23], a robust adaptive fractional sliding mode controller is studied for a nonlinear fractional order model of glucose insulin Systems. In [23], the unknown upper bound of model uncertainties and disturbances is obtained via a stable adaptive law and proposed controller was designed to stabilize a nonlinear affine fractional order system. In [24], robust fuzzy adaptive approach is considered to control the blood glucose level of type 1 diabetic patients in the presence of uncertainties. The proposed controller is based on the feedback linearization control approach and robust adaptive compensator confront with nonlinear dynamics, in which frequently involve uncertainties in system parameters and disturbance.

Due to physical constraints, most of control systems have limitations on the input signal (control signal) that may lead to input saturation. In this situation, if input saturation occurs, undesirable effects such as performance degradation or instability, known as windup phenomenon, will happen. Anti-windup is a method of preventing windup or recovering the unconstrained response after saturation has occurred by modifying the controller in a feedback loop. Anti-windup controllers have been studied in the literature extensively. In [25], adaptive fuzzy control is developed for a class of non-strict feedback systems with input saturation and output constraint. Combining fuzzy logic and adaptive back-stepping can solve input saturation and output limitation. In [26], a virtual saturation function and adaptive anti-windup compensator has been designed to deal with input saturation. In [27], the stability problem in systems with uncertainty and input saturation is investigated and an adaptive PID control method is proposed that uses both state-feedback and output-feedback methodologies. In [27], an adaptive anti-windup controller for chaos synchronization has been presented. The gain in the anti-windup compensator in [27] can be constant or variable and both of these strategies have been studied. The main controller is a PID controller with time-varying coefficients.

In order to highlight the superiority of the proposed controller in this paper, it must be mentioned that the problem of input saturation has not been considered in most of the previous related works [1-24]. Therefore, in the current research, the focus is on designing the controller to cope with input saturation as hyperglycemia or hypoglycemia in regulating the blood glucose level of type 1 diabetes patients and also determine the dose injected insulin to remain in appropriate range. For this purpose, an adaptive controller for regulation of blood glucose has been designed considering limitations on insulin injection. All uncertainties including parametric and non-parametric uncertainties are estimated and compensated using adaptive fuzzy systems. Similar to [27], two strategies have been adopted for the feedback gain in the anti-windup compensator. Based on the Lyapunov theorem, the adaptation rules for the fuzzy system and the gain of the anti-windup compensator are obtained. However, in comparison with [27], the number of virtual differential equations used in the controller design and stability analysis has been reduced which results in less computational complexity of the controller. In comparison with [20], the proposed controller is superior due to considering input saturation and more flexibility against uncertainties. In fact, in [20], parametric uncertainty has been considered which needs nominal model of the system. However, the proposed controller, compensates the lumped uncertainty. In other words, the proposed controller is model-free and can be used in the situations where the nominal model is not available. The novelties of the current work can be summarized as:

i. Designing adaptive fuzzy controller with adaptive anti-windup compensator for to regulate the blood glucose level of type 1 diabetic patients in the presence of input saturation has been studied in this paper, while the problem of input saturation has not been considered in most of the previous related works [1-24].

ii. In comparison with [27], the number of virtual control laws has been reduced which results in fewer adaptation laws.

iii. In comparison with [27], it must be mentioned that instead of PID controller, adaptive fuzzy controller has been designed in this paper. Adaptive fuzzy control is a more powerful strategy in uncertainty estimation and compensation.

iv. The need for Lipshitz property of the uncertainty function has been relaxed in the proposed method, while in [27], it is a necessary assumption.

The rest of the paper is organized as follows: Mathematical model is discussed in section 2. The controller design and stability analysis are presented in section 3. The simulation

results of the control method are presented in Section 4 and finally, concluding remarks are given in Section 5.

II. Mathematical representation of glucose-insulin system

Bergman's minimal model is a mathematical model that illustrates the insulin-glucose system with some parameters [28, 29]. One of the main advantages of Bergman's minimal model is that it contains a minimal number of parameters. This model describes the interactions without biological complexity between the main components such as insulin and glucose concentration [30]. This model has a relative degree of three and consists of three differential equations that describe the insulin-glucose regulatory system with sufficient accuracy as follows [31]:

$$\dot{G}(t) = -p_1(G(t) - G_b) - G(t)X(t) + d(t) \quad (1)$$

$$\dot{X}(t) = -p_2X(t) + p_3(I(t) - I_b) \quad (2)$$

$$\dot{I}(t) = -p_4(I(t) - I_b) + \gamma(G(t) - h)^+ t + u(t) \quad (3)$$

The signals $G(t)$, $X(t)$, and $I(t)$ are the blood glucose concentration (mg/dl), the effect of insulin on glucose concentration reduction (min^{-1}), and the insulin concentration in plasma $(\mu U/ml)$, respectively. The parameter $G_b$represents the basal plasma glucose (mg/dl), I_b is the basal plasma insulin concentration $(\mu U/ml)$. The parameter p_1 denotes the insulin-independent glucose-utilization rate (min^{-1}), p_2 is the rate of decrease of the tissue glucose uptake ability (min^{-1}), p_3 denotes the insulin-dependent increase of glucose uptake ability $(\mu U/ml)^{-1}min^{-1}$, n is the first order decay rate for insulin blood (min^{-1}), γ is the rate of pancreatic release of insulin after bolus and h is the glucose threshold level for insulin secretion by the pancreas. The "+" sign in (3) indicates the positive reflection of glucose intake [20, 32] and "u" is the system input and actually the insulin injection rate. Also, d(t) represents a meal that is an external disturbance and is defined as follows

$$d(t) = \begin{cases} 0 & t < t_0 \\ A_1 exp\big(-B(t - t_0)\big) & t \geq t_0 \end{cases} \quad (4)$$

To describe what food intake will do to the concentration of glucose term. The coefficients A_1, and B have positive values

III. The proposed controller design

An adaptive fuzzy control structure and an adaptive anti-windup compensator are proposed to handle input saturation and compensate the lumped uncertainty. It is shown in the appendix that equations 1 to 3 can be converted to equation 5. Consider the following nonlinear model

$$\begin{aligned} \dot{x}_1 &= x_2 \\ \dot{x}_2 &= x_3 \\ &\vdots \\ \dot{x}_{n-1} &= x_n \\ \dot{x}_n = x^{(n)} &= f(x) + b(x)u \\ y &= Cx \end{aligned} \quad (5)$$

Where u is the control input, y is the desired output, $x = \left[x, \dot{x}, \dots, x^{(n-1)}\right]^T$ is the state vector, $f(x)$ and $b(x)$ are non-linear functions of are the state. The representation of state space (5) can be rewritten as:

$$\frac{d}{dt}\begin{bmatrix} x_1 \\ \dots \\ x_{n-1} \\ x_n \end{bmatrix} = \begin{bmatrix} x_2 \\ \dots \\ x_n \\ f(x) + b(x)u \end{bmatrix} \quad (6)$$

In the input-output linearization method, a controller is determined after establishing a linear input-output relationship. To explicitly relate output y and input u, the system output is differentiated n times if necessary (n denotes relative degree). The relative degree of the system is needed for controller design. The number of successive differentiations until the control appears in the equation will define the relative degree. The relative degree of this system is three.

For systems that can be represented in a conventional form of controllability using the following control input (assuming that b is opposite to zero).

$$bu + f = v \ , \qquad u = \frac{1}{b}(v - f) \quad (7)$$

Non-linearities can be removed and the following input-output relationship can be obtained.

$$y^{(n)} = v \quad (8)$$

Therefore, the control law

$$v = -k_0y - k_1\dot{y} - \dots - k_{n-1}y^{(n-1)} \quad (9)$$

Choose k_i so that the roots of polynomial $p^n + k_{n-1}p^{n-1} + \dots + k_0$ have negative real parts, resulting in exponential stable dynamics.

$$y^{(n)} + k_{n-1}y^{(n-1)} + \dots + k_0y = 0 \quad (10)$$

Which implies that $y(t) \to 0$. For tracking the desired output $y_d(t)$, the following control law

$$v = y_d^{(n)} - k_0e - k_2\dot{e} - \dots - k_{n-1}e^{(n-1)} \quad (11)$$

Where $e(t) = y(t) - y_d(t)$ is the tracking error, it results in exponential convergence of tracking.

To design the controller, rewrite the system model with input saturation.

$$\begin{aligned} \dot{x} &= Ax + b(x)f(x) + b(x)sat(u) + b(x)d(t) \\ y &= cx \end{aligned} \quad (12)$$

$$A=\begin{bmatrix}0 & 1 & 0\\ 0 & 0 & 1\\ 0 & 0 & 0\end{bmatrix},\quad b=\begin{bmatrix}0\\0\\1\end{bmatrix},\quad c=\begin{bmatrix}1 & 0 & 0\end{bmatrix} \tag{13}$$

where $x \in R^n$, $u \in R$ and $y \in R$ are the state vector, input and output of the system respectively. Let f be a uniform vector field on R^n. $A \in R^{n\times n}$ and $b, c \in R^n$ are constant matrices of the system, (A, b) is controllable and $f(x)$ is the nonlinear vector function and $d(t)$ is an external disturbance in diabetic patients.

Remark 1 Transformation of the Bergman's minimal model to (12) and (13) paves the way for designing adaptive anti-windup controller.

A. *Input saturation*

In equation (12), sat(u) is the saturation function [27]

$$sat\big(u(t)\big)=\begin{cases}u_{uppper} & u(t)\geq u_{uppper}\\ u(t) & u_{lower}<u(t)<u_{uppper}\\ u_{lower} & u(t)\leq u_{lower}\end{cases} \tag{14}$$

where $u_{uppper} > 0$ and $u_{lower} = 0$ are known constants and are defined as the upper and lower input saturation values of the system, respectively.

In order to design adaptive fuzzy control and anti-windup compensator to deal with input saturation and parameter uncertainty, the following assumptions are proposed:

Assumption 1: A_m is a satisfactory Horwitz matrix. $A_m^T P + P A_m = -Q$, P and Q are symmetric and positive definite matrices.

Assumption 2: Suppose there are constant vectors $K_1^{*T} \in R^n$ and $K_b \in R$ to satisfy the following equation

$$A_m = A + (1 - K_b) b K_1^{*T} u_{uppper} \tag{15}$$

B. *Anti-windup compensation model*

In the case that saturation occurs, a corrective feedback action $u_{aw}(t)$ is needed as follows [27, 35].

$$u_{aw}(t) = K_b\big(sat(u) - u_c(t)\big) \tag{16}$$

Where K_b is the weighting factor for anti-windup.

Remark 2 There are two strategies for K_b. In the first strategy, the value of K_b remains unchanged and in the second strategy, K_b is variable and can be estimated online. Both of these strategies are studied in this paper.

C. *The proposed controller design with constant K_b*

The tracking error is defined as $\tilde{x} = G - G_{bref}$ and $G_{bref}=120exp(-\alpha t)+80 \quad 0<\alpha<1$ is the reference value of glucose. Consider the following definitions:

$$\begin{aligned}&\tilde{x}_1 = G - G_{bref}\\ &\dot{\tilde{x}}_1 = \dot{G} - \dot{G}_{bref}\\ &\ddot{\tilde{x}}_1 = \ddot{G} - \ddot{G}_{bref}\end{aligned}\quad \tilde{x}=\begin{bmatrix}\tilde{x}_1\\ \dot{\tilde{x}}_1\\ \ddot{\tilde{x}}_1\end{bmatrix} \tag{17}$$

$$\Delta u = sat(u) - u(t) \tag{18}$$

The equations of the closed-loop system (12) can be rewritten as follows

$$\dot{\tilde{x}} = A\tilde{x} + bf(x) + bu + b\Delta u + bd - bv \quad , \quad v = \dddot{G}_{bref} \tag{19}$$

$$\begin{aligned}&y = c\tilde{x}\\ &\dot{\tilde{x}} = A\tilde{x} + b\big(f(x) + u + \Delta u + d - \dddot{G}_{bref}\big)\\ &y = c\tilde{x}\end{aligned} \tag{20}$$

Now consider the control input u as below

$$u = u_c(t) + u_{aw}(t) + \ddot{G}_{bref} \tag{21}$$

Where u_c is the control input and u_{aw} is the anti-windup compensator. To remove the effect of the Δu term in equation (19), Δx is defined as the following differential equation

$$\dot{\Delta x} = A_m \Delta x + \hat{K}_\Delta \Delta u \text{ ، } \Delta x(0) = 0 \tag{22}$$

Consider the following definitions.

$$\tilde{K}_\Delta = b - \hat{K}_\Delta \tag{23}$$

$$e = \tilde{x} - \Delta x \tag{24}$$

By replacing equations (20) in $\dot{\tilde{x}}$, (22) in $\dot{\Delta x}$ and also using the assumption two instead of A and the definition $\tilde{K}_\Delta = b - \hat{K}_\Delta$, The derivative of the Augmented error e is obtained as follows

$$\dot{e} = \dot{\tilde{x}} - \dot{\Delta x} = A_m e + bf(x) + bu + \tilde{K}_\Delta \Delta u + bd - b\dddot{G}_{bref} - (1 - K_b) b K_1^{*T} \tilde{x} \tag{25}$$

According to equation (16), $sat(u)$ is bounded and has an upper bound as follows [27]

$$|sat(u)| \leq L_1^* \tag{26}$$

Where L_1^* is a constant. The control input u_c is as follows

$$u_c = -\big(u_{fuzzy}/(1 - K_b)\big) + u_{classical} \tag{27}$$

Remark 3 The need for Lipshitz property of the uncertainty function has been relaxed in the proposed method, while in [27], it is a necessary assumption.

Remark 4 In comparison with [27], it must be mentioned that instead of PID controller, adaptive fuzzy controller has been designed in this paper. Adaptive fuzzy control is a more powerful strategy in uncertainty estimation and compensation.

The fuzzy IF-THEN rules that describe human control actions [33]

$$If\ x_1\ is\ P_1^r\ and\ ...\ and\ x_n\ is\ P_n^r, then\ u\ is\ Q^r \tag{28}$$

where P_n^r and Q^r are fuzzy sets in R and $r = 1,2,\dots,L_u$. The fuzzy controller should be designed in such a way that the rules (28) can be naturally incorporated [33]. To incorporate the rules (28), the fuzzy controller is as follows

$$u = u_{fuzzy}(X|\theta) \tag{29}$$

where u_{fuzzy} is a fuzzy system and θ is a set of adjustable parameters. Specifically, the fuzzy system $u_{fuzzy}(X|\theta)$ is constructed from the following two steps.

First step: for each variable x_i $(i = 1,2,\dots,n)$, m_i the fuzzy set $A_i^{l_i}$ $(l_i = 1,2,\dots,m_i)$ is defined, where P_n^r $(r = 1,2,\dots,L_u)$ in (28) as a special case.

The second step: construct the fuzzy system $u_{fuzzy}(X|\theta)$ from following $\prod_{i=1}^{n} m_i$ rules.

$$\begin{aligned} &If\ x_1\ is\ A_1^{L_1}\ and \dots and\ x_n\ is A_n^{L_n}, then \\ &u_{fuzzy} is\ S^{L_1 \dots L_n} \end{aligned} \tag{30}$$

where $l_i = 1,2,\dots,m_i$, $i = 1,2,\dots,n$, and $S^{L_1 \dots L_n}$ will be equivalent to Q^r in equation (28), so that the part if the equation (30) with the part If equation (28) agrees; Otherwise, it is equivalent to an arbitrary fuzzy set. Specifically, by using the product fuzzy inference engine the singleton fuzzifier and the center average de-fuzzifier, the following relationship will be obtained [33].

$$u_{fuzzy}(X|\theta) = \frac{\sum_{l_1=1}^{m_1} \dots \sum_{l_n=1}^{m_n} \bar{y}_u^{l_1 \dots l_n} \left[\prod_{i=1}^{n} \mu_{A_i}^{l_i(x_i)}\right]}{\sum_{l_1=1}^{m_1} \dots \sum_{l_n=1}^{m_n} \left[\prod_{i=1}^{n} \mu_{A_i}^{l_i(x_i)}\right]} \tag{31}$$

where $\bar{y}_u^{l_1 \dots l_n}$ are selected as adjustable parameters and these parameters are collected in the vector $\theta \epsilon R^{\prod_{i=1}^{n} m_i}$. The fuzzy controller u_{fuzzy} is defined as below [33]

$$u_{fuzzy} = \hat{\theta}^T \zeta(x) \tag{32}$$

where $\zeta(x)$ is the vector of the fuzzy basis function and θ is the adjustable parameter.

Also, $u_{classical}$, which is used for system stability as follows

$$u_{classical} = \hat{K}_1^T \tilde{x} - \frac{K_b}{1 - K_b} \hat{L}_1 sgn(e^T P b) \tag{33}$$

where $\hat{K}_1$ is the estimate of classical control gain K_1. By substituting equations (32) and (33) into equation (27) and also by substituting equations (27) and (15) into equation (21) and by using equation (21) into equation (25), the derivative of the augmented error e as follows

$$\begin{aligned} \dot{e} = A_m e + bf(x) + (1 - K_b) b \Big[& \hat{K}_1^T \tilde{x} \\ & - \frac{K_b}{1 - K_b} \hat{L}_1 sgn(e^T P b) \\ & - \left(\hat{\theta}^T \zeta(x)/(1 - K_b)\right) \Big] \\ & + K_b b sat(u) + \tilde{K}_\Delta \Delta u \\ & + bd - (1 - K_b) b K_1^{*T} \tilde{x} \end{aligned} \tag{34}$$

By definition

$$\acute{f}(x) = f(x) + d = \theta^T \zeta(x) \tag{35}$$

$$\tilde{K}_1 = \hat{K}_1 - K_1^*, \qquad \tilde{\theta} = \hat{\theta} - \theta \tag{36}$$

By Substituting equations (35) and (36) into equation (34), the derivative of the augmented error e is defined as follows

$$\begin{aligned} \dot{e} = A_m e + K_b b sat(u) + \tilde{K}_\Delta \Delta u \\ + (1 - K_b) b \tilde{K}_1^T \tilde{x} - b \tilde{\theta}^T \zeta(x) \\ - b K_b \hat{L}_1 sgn(e^T P b) \end{aligned} \tag{37}$$

To remove the effect of the term K_b in equation (37), Δe is defined as the following differential equation

$$\dot{\Delta e} = A_m \Delta e + u_e, \qquad \Delta e(0) = 0 \tag{38}$$

The u_e is defined as follows

$$u_e = \hat{K}_{be} b sat(u) \tag{39}$$

By defining $\tilde{K}_{be} = K_b - \hat{K}_{be}$ and using equation (37) instead of $\dot{e}$ and replacing equation (39) in equation (38) and also using equation (38) instead of $\dot{\Delta e}$, the derivative of the augmented error $e_1 = e - \Delta e$, will be as follows

$$\begin{aligned} \dot{e_1} = \dot{e} - \dot{\Delta e} = A_m e_1 - \tilde{K}_{be} b\big(sat(u)\big) + \tilde{K}_\Delta \Delta u \\ + (1 - K_b) b \tilde{K}_1^T \tilde{x} - b \tilde{\theta}^T \zeta(x) \\ - b K_b \hat{L}_1 sgn(e^T P b) \end{aligned} \tag{40}$$

According to equation (40) and to substitute equations (32) and (33) into equation (27) and also to substitute equations (27) and (15) into equation (21), the adaptive laws are derived as

$$\dot{\tilde{K}}_1 = -\gamma_1 {e_1}^T P b \tilde{x} \tag{41}$$

$$\dot{\tilde{K}}_\Delta^T = -\gamma_2 {e_1}^T P b \Delta u \tag{42}$$

$$\dot{\tilde{K}}_{be} = \gamma_3 {e_1}^T P b sat(u) \tag{43}$$

$$\dot{\tilde{\theta}} = \gamma_4 {e_1}^T P \zeta \tag{44}$$

$$\dot{\tilde{L}}_1 = \gamma_5 |{e_1}^T P b| \tag{45}$$

where $\tilde{L}_i = \hat{L}_i - L_i^*$, γ_j $j = 1,2,3,\dots$ are positive constant coefficients.

Proof: With $0 < K_b < 1$, the positive definite Lyapunov function can be considered as follows

$$\begin{aligned} V = {e_1}^T P e_1 + (1 - K_b) \gamma_1^{-1} \tilde{K}_1^T \tilde{K}_1 + \gamma_2^{-1} \tilde{K}_\Delta^T \tilde{K}_\Delta \\ + \gamma_3^{-1} \tilde{K}_{be}^2 + \gamma_4^{-1} \tilde{\theta}^T \tilde{\theta} \\ + K_b \gamma_5^{-1} \tilde{L}_1^2 \end{aligned} \tag{46}$$

The derivative of the Lyapunov function is

$$\dot{V} = \dot{e_1}^T P e_1 + e_1^T P \dot{e_1} + 2(1-K_b)\gamma_1^{-1}\tilde{K}_1^T\dot{\tilde{K}}_1 + 2\gamma_2^{-1}\tilde{K}_\Delta^T\dot{\tilde{K}}_\Delta + 2\gamma_3^{-1}\tilde{K}_{be}\dot{\tilde{K}}_{be} + 2\gamma_4^{-1}\tilde{\theta}^T\dot{\tilde{\theta}} + 2\gamma_5^{-1}K_b\tilde{L}_1\dot{\tilde{L}}_1 \quad (47)$$

By substituting equations (40) - (45) respectively instead of $\dot{e_1}$, $\dot{\tilde{K}}_1$, $\dot{\tilde{K}}_\Delta$, $\dot{\tilde{K}}_{be}$, $\dot{\tilde{\theta}}$, and $\dot{\tilde{L}}_1$ in equation (47), by using the assumption of one and two in equation (47) and also $e_1^T P b sgn(e_1^T P b) = |e_1^T P b|$ [34]. Finally, we have

$$\dot{V} \le -\tilde{x}^T Q \tilde{x} \quad (48)$$

D. The proposed controller design with variable K_b

Considering K_b as the controlling variable coefficient, the second assumption should be modified as follows [27].

Third assumption: Suppose there is a constant vector K_1^* so that the following equation is satisfied [27].

$$A_m = A + bK_1^{*T} \quad (49)$$

Assuming that K_b is variable, equation (15) can be written as follows [27]

$$u_{aw}(t) = \hat{K}_b\big(sat(u) - u_c(t)\big) \quad (50)$$

The u_c control input is as follows

$$u_c = -u_{fuzzy} + u_{classical} \quad (51)$$

The fuzzy controller $u_{fuzzy}$is defined as follows

$$u_{fuzzy} = \hat{\theta}^T\zeta(x) \quad (52)$$

$\zeta(x)$ is a fuzzy basis function vector and θ is an adjustable parameter. Also, $u_{classical}$ is used for system stability, as follows

$$u_{classical} = \hat{K}_1^T\tilde{x} - \hat{L}_1 sgn(e^T P b) \quad (53)$$

By substituting equations (52) and (53) in equation (51) and also by substituting (50), (51) in equation (21), also by substituting equation (21) in equation (19) and by considering the third assumption, $\dot{\tilde{x}}$ is obtained

$$\begin{aligned}\dot{\tilde{x}} &= A\tilde{x} + bf(x) + bu + b\Delta u + bd - b\ddot{G}_{bref}\\ &= (A_m - bK_1^{*T})\tilde{x} + bf(x)\\ &\quad + b\big(\hat{K}_b\big(sat(u) - u_c(t)\big)\\ &\quad - \hat{\theta}^T\zeta(x) + \hat{K}_1^T\tilde{x}\\ &\quad - \hat{L}_1\|x\|sgn(e^T P b)\\ &\quad - \hat{d}sgn(e^T P b) + \ddot{G}_{bref}\big)\\ &\quad + b\Delta u + bd - b\ddot{G}_{bref}\end{aligned} \quad (54)$$

By definition

$$\acute{f}(x) = f(x) + d = \theta^T\zeta(x) \quad (55)$$

By placing equations (55) in equation (54) and using the definitions $\tilde{K}_1^T = \hat{K}_1^T - K_1^{*T}$ and $\tilde{\theta} = \hat{\theta} - \theta$, equation (54) can be written as follows

$$\begin{aligned}\dot{\tilde{x}} &= A_m\tilde{x} + b\tilde{K}_1^T x - b\tilde{\theta}^T\zeta(x) + b\Delta u\\ &\quad + b\hat{K}_b\big(sat(u) - u_c(t)\big)\\ &\quad - b\hat{L}_1 sgn(e^T P b)\end{aligned} \quad (56)$$

To remove the effect of some terms, Δx is defined as the following differential equation [27]

$$\dot{\Delta x} = A_m\Delta x + u_x \text{ ، } \Delta x(0) = 0 \quad (57)$$

The virtual control u_x is defined as follows

$$u_x = K_b b\big(sat(u) - u_c(t)\big) + \hat{K}_\Delta\Delta u, \quad \Delta x(0) = 0 \quad (58)$$

Remark 5 The number of virtual systems such as (57) has been reduced in the proposed method in comparison with [27].

By substituting equation (56) in $\dot{\tilde{x}}$, substituting equation (58) in equation (57), substituting equation (57) in $\dot{\Delta x}$ and also using the third assumption $A_m + bK_1^{*T}$ instead of A and using the definitions $\tilde{K}_\Delta = b - \hat{K}_\Delta$ and $\tilde{K}_b = \hat{K}_b - K_b$, the augmented error derivative of the equation $e = \tilde{x} - \Delta x$ is obtained as follows

$$\begin{aligned}\dot{e} = \dot{\tilde{x}} - \dot{\Delta x} &= A_m e + b\tilde{K}_1^T\tilde{x} - b\tilde{\theta}^T\zeta(x)\\ &\quad + \tilde{K}_\Delta\Delta u\\ &\quad + b\tilde{K}_b\big(sat(u) - u_c(t)\big)\\ &\quad - b\hat{L}_1 sgn(e^T P b)\end{aligned} \quad (59)$$

According to equation (59) and to substitute equations (52) and (53) in equation (51) and also to substitute equations (50) and (51) in equation (21), the adaptive laws are derived as

$$\dot{\tilde{K}}_1 = -\gamma_1 e^T P b\tilde{x} \quad (60)$$

$$\dot{\tilde{K}}_\Delta^T = -\gamma_2 e^T P\Delta u \quad (61)$$

$$\dot{\tilde{K}}_b = -\gamma_3 e^T P b\big(sat(u) - u_c(t)\big) \quad (62)$$

$$\dot{\tilde{\theta}} = -\gamma_4 e^T P b\zeta \quad (63)$$

$$\dot{\tilde{L}}_1 = \gamma_5|e_1^T P b| \quad (64)$$

Where γ_j $j = 1,2,3,\ldots$ are positive constant coefficients

Proof: The following Lyapunov function candidate is chosen

$$V = e^T P e + \gamma_1^{-1}\tilde{K}_1^T\tilde{K}_1 + \gamma_2^{-1}\tilde{K}_\Delta^T\tilde{K}_\Delta + \gamma_3^{-1}\tilde{K}_b^2 + \gamma_4^{-1}\tilde{\theta}^T\tilde{\theta} + \gamma_5^{-1}\tilde{L}_1^2 \quad (65)$$

The derivative of the Lyapunov function is

$$\dot{V} = \dot{e}^T P e + e^T P\dot{e} + 2\gamma_1^{-1}\tilde{K}_1^T\dot{\tilde{K}}_1 + 2\gamma_2^{-1}\tilde{K}_\Delta^T\dot{\tilde{K}}_\Delta + 2\gamma_3^{-1}\tilde{K}_b\dot{\tilde{K}}_b + 2\gamma_4^{-1}\tilde{\theta}^T\dot{\tilde{\theta}} + 2\gamma_5^{-1}\tilde{L}_1\dot{\tilde{L}}_1 \quad (66)$$

By substituting equations (59) - (64) instead of $\dot{e}$, $\dot{\tilde{K}}_1$, $\dot{\tilde{K}}_\Delta$, $\dot{\tilde{K}}_b$, $\dot{\tilde{\theta}}$, $\dot{\tilde{L}}_1$ and also by replacing the assumption of $A_m^T P + PA_m = -Q$ in equation (66), the derivative of the Lyapunov function is obtained as follows

$$\dot{V} = -e^T Qe - 2e^T Pb\hat{L}_1\|x\|sgn(e^T Pb) + 2\tilde{L}_1|e_1{}^T Pb|\|x\| \quad (67)$$

Finally, using $e^T Pbsgn(e^T Pb) = |e^T Pb|$, the derivative of the Lyapunov function will be as follows

$$\dot{V} \leq -\tilde{x}^T Q\tilde{x} \quad (68)$$

IV. Simulation results

In this section, the simulation results of the fuzzy adaptive controller with input saturation in the Simulink environment of MATLAB software are presented. In this simulation, the initial values of the Bergman model state variables $\boldsymbol{G(t)}$, $\boldsymbol{X(t)}$, and $\boldsymbol{I(t)}$ are considered to be 200, 0, and 50, respectively and $\boldsymbol{0 \leq u(t) \leq 60}$ $\boldsymbol{\mu U/ml/min}$ [32]. Bergman model simulation parameters for two patients and a normal person are used according to Table 1.

TABLE 1 PARAMETERS OF BERGMAN MODEL [20]

Parameters	Normal	Patient 1	Patient 2	Units
$\boldsymbol{p_1}$	0.0317	0	0	$\min^{-1}$
$\boldsymbol{p_2}$	0.0123	0.0142	0.02	$\min^{-1}$
$\boldsymbol{p_3}$	$4.92e-06$	$1.54e-05$	$5.3e-06$	$(\mu U/ml)^{-1}\min^{-1}$
$\boldsymbol{\gamma}$	0.0039	0	0	$(\mu U/ml)(mg/dl)^{-1}\min^{-2}$
$\boldsymbol{n}$	0.2659	0.2814	0.3	$\min^{-1}$
$\boldsymbol{h}$	79.035	_	_	mg/dl
$\boldsymbol{G_b}$	80	80	80	mg/dl
$\boldsymbol{I_b}$	7	7	7	μU/ml
$\boldsymbol{A_1}$	1	1	1	_
$\boldsymbol{B}$	0.05	0.05	0.05	_
$\boldsymbol{t_0}$	450	450	450	min
$\boldsymbol{p_1}$	0.0317	0	0	$\min^{-1}$

The open-loop simulation of Bergman's minimal model has been presented. In the open-loop simulation, the behavior of a diabetic patient and a healthy person have been compared. In Fig. 1, the blood glucose for a healthy person and two patients without insulin injection have been shown. It is easy to see that the blood glucose level of a healthy person will eventually be at the base level, but the patient's blood glucose level cannot reach the desired value and remains out of range.

In order to compare the performances of the different controllers, consider Fig. 3. As shown in this figure, the proposed controller with variable K_b approach can reduce the patient's blood glucose level to the desired value faster than other approaches. Also, it can be seen that using anti-windup compensator in the constant K_b structure will lead to superior results in comparison with the case where no anti-windup compensation is used.

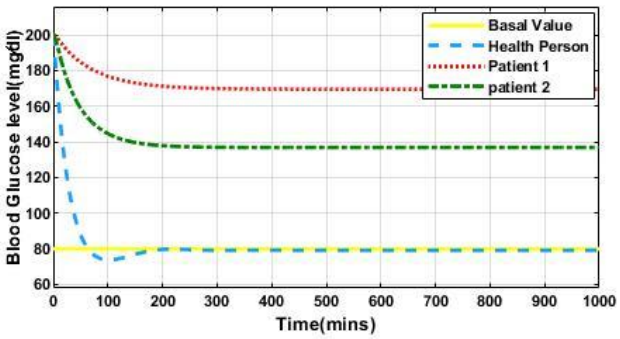

Fig. 1. Blood glucose concentration of patients and a healthy person in open loop simulation

In Fig. 2, the performance of the proposed controller in a diabetic patient and a healthy person have been investigated. In this simulation, the proposed controller can reduce the blood glucose level of type 1 diabetic patients to the desired basal level.

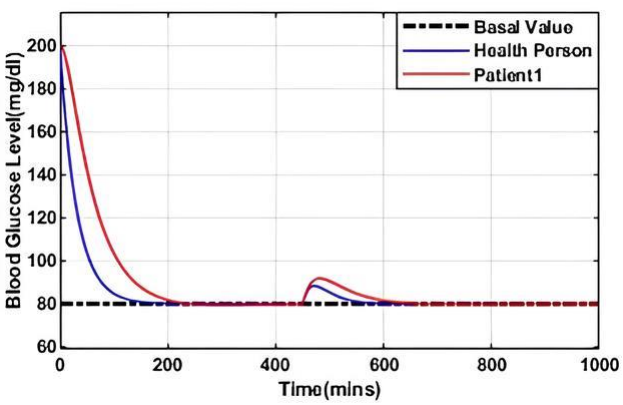

Fig. 2. Blood glucose concentration of patient and a healthy person using the proposed controller

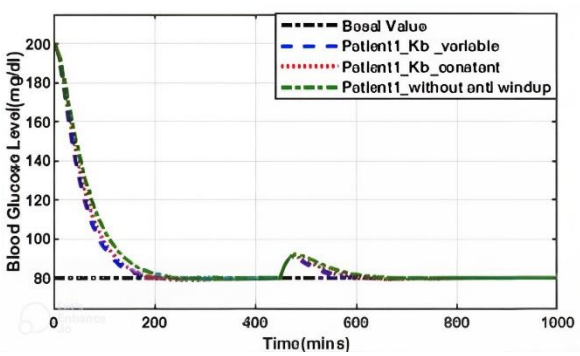

Fig. 3. Comparison of blood glucose level using different controllers

The ideal plasma insulin concentration level is around $7\,(\mu U/ml)$. Fig. 4 shows a comparison between different controllers for plasma insulin concentration. The simulation shows that the insulin concentration converges to the desired

level of plasma insulin but variable K_b approach is faster.

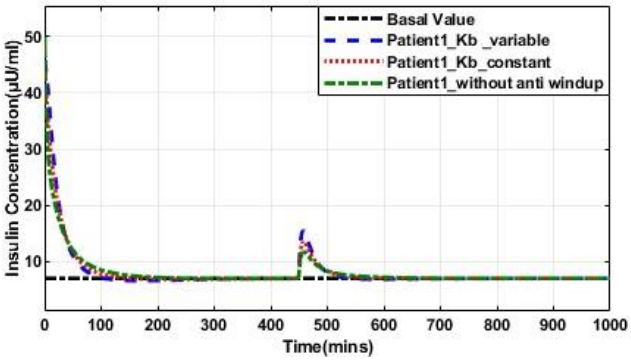

Fig. 4. Comparison of plasma insulin concentration for different controllers

Fig. 5. shows insulin injected by an insulin pump using different controllers. According to this figure, the proposed controller with variable K_b approach has a faster performance than other controllers.

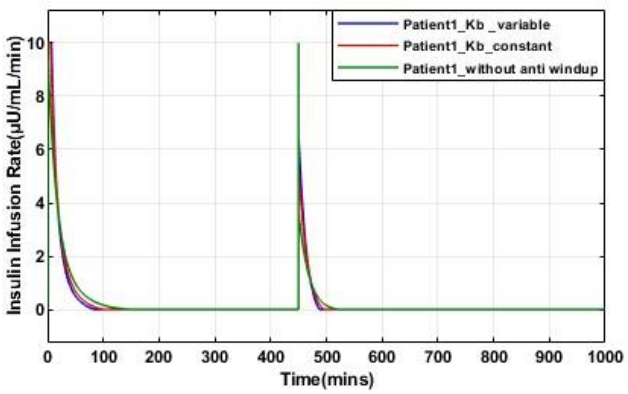

Fig. 5. Comparison of control input (insulin injection rate) using

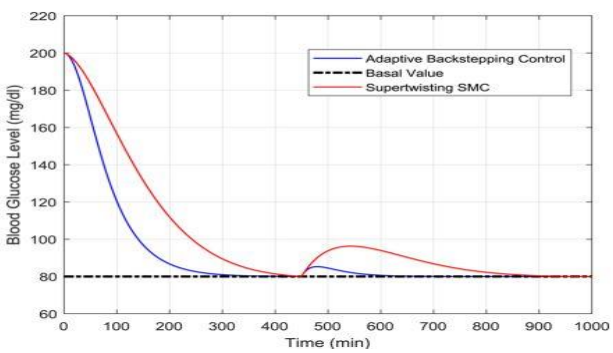

different controllers

In Fig. 6. the convergence of blood glucose level of two different patients are shown. As shown in this figure, for both patients, variable K_b controller is faster.

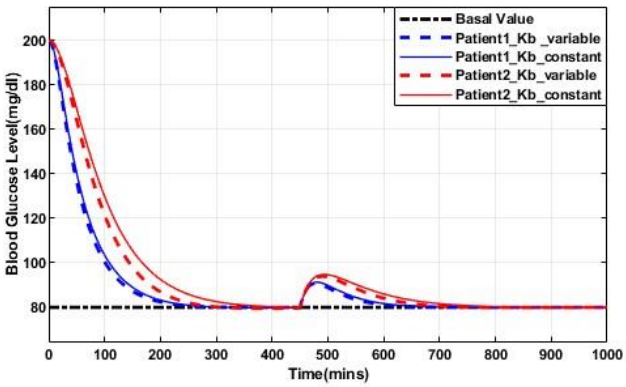

Fig. 6. Comparison of blood glucose levels for two different patients

Comparison of the anti-windup compensator with constant and variable K_b approaches for insulin requirements of two patients is presented in Fig. 7. According to this figure, in both patients, variable K_b controller is faster.

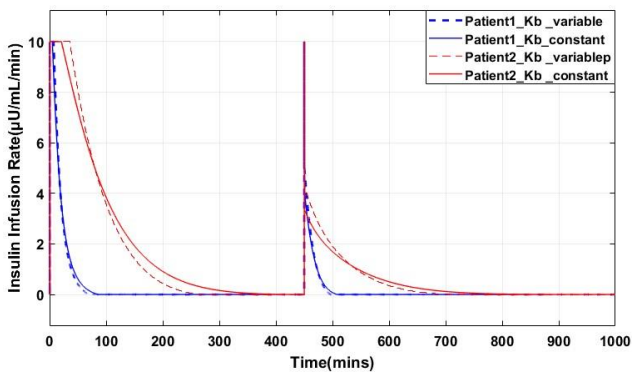

Fig. 7. Comparison of control input for two patients with constant and variable K_b approaches

In Fig. 8, a comparison of blood glucose level and control effort of the adaptive back-stepping and the super twisting SMC has been depicted [20]. It should be mentioned that in these controllers, the limitation on the control effort has not been considered and therefore, the saturation phenomenon in practical implementation may happen. It is obvious that the system operates in an open loop in the presence of saturation for a while. As a result, satisfactory performance of the sliding mode controller and the adaptive back-stepping controller in achieving the desired blood glucose level and dealing with saturation are not guaranteed. According to Fig. 3, Fig. 5 and Fig. 8, it is evident that the proposed controller outperforms the sliding mode controller and the adaptive back-stepping controller in terms of faster output tracking. Moreover, the proposed controllers require less control effort and exhibit faster convergence time.

(a) Blood glucose level

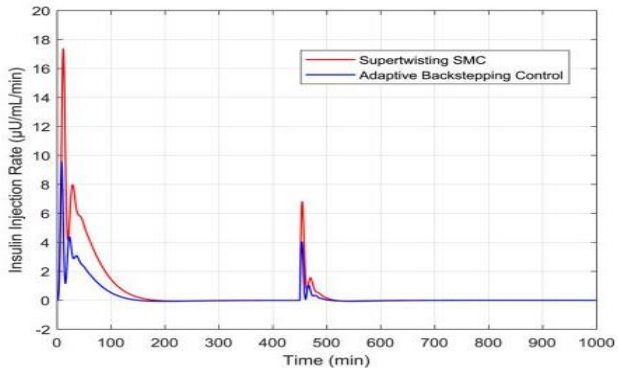

(b) Control effort

Fig. 8. Blood glucose level and control effort using adaptive back-stepping controller and super twisting SMC [20]

In order to have a quantitative comparison, the integral of squared error between the desired glucose and the patient glucose level has been selected as a cost function. The results are presented in Table 2. According to this table, for both patients, the variable K_b approach outperforms the constant K_b approach. Moreover, the controller with constant K_b is superior to the controller with no anti-windup compensation.

TABLE 2 COMPARISON OF COST FUNCTION

Controller	The integral of squared error for patient 1	The integral of squared error for patient 2
variable K_b approach	8.217×10^4	2.846×10^5
Constant K_b approach	1.022×10^5	3.721×10^5
Without anti-windup	1.552×10^5	5.213×10^5

V. Conclusions

In this paper, an adaptive fuzzy controller with anti-windup compensator has been designed to prevent saturation problems in regulating the blood glucose level of type 1 diabetes patients. Bergman's minimal model is considered in this paper for simulations. Stability analysis has been presented based on Lyapunov theorem. Adaptive fuzzy systems have been used to estimate uncertainties. In comparison with previous related works on adaptive anti-windup controllers, the proposed method is simpler with less adaptation laws and less virtual differential equations. Simulation results show the superiority of the proposed method in regulating the blood glucose level of type 1 diabetes patients. According to simulation results, using anti-windup compensator with constant gain results in better performance in comparison with the controller without anti-windup compensator. Also, the controller with variable anti-windup compensator gain outperforms the controller with constant anti-windup compensator gain. For future work, the dynamic anti-windup compensator can be considered as a topic to deal with input saturation in regulating the blood glucose level of type 1 diabetes patients.

APPENDIX

In this article, equation 5 is used to design the parameter $v = \ddot{G}_{bref}$ based on feedback linearization to simplify the structure of the proposed nonlinear control law.

The output is considered as follows

$$y = cx = G \tag{69}$$

By taking time derivative of eq (69), we have

$$\dot{y} = \dot{G} = -p_1(G(t) - G_b) - G(t)X(t) + d(t) \tag{70}$$

The second derivative is given by

$$\begin{aligned}\ddot{y} = \ddot{G} = {} & p_1^2(G(t) - G_b) + p_1X(t)(G(t) - G_b) \\ & + \big(p_1 + X(t)\big)X(t)G(t) \\ & - \big(p_1 + X(t)\big)d(t) \\ & + p_2G(t)X(t) \\ & - p_3G(t)\big((I(t) - I_b)\big)\end{aligned} \tag{71}$$

The control input did not appear in the second derivative. So, the third derivative must be computed:

$$\begin{aligned}\dddot{y} = \dddot{G} = {} & G(t)[-p_1(p_1^2 + 3p_3I_b) \\ & - p_3I_b(p_2 + p_4) \\ & - p_3\gamma(G(t) - h)^+t] \\ & + X(t)[-p_1^2(1 + G_b) \\ & + p_1p_2(2G_b - 1) \\ & + 2d(t)(p_1 + p_2)] \\ & + I(t)\big[-2p_3\big(p_1 + d(t)\big)\big] \\ & + G(t)X(t)[-(p_1 + p_2)^2 \\ & - 3p_3I_b] \\ & + G(t)I(t)[p_3(3p_1 + p_2 \\ & + p_4)] \\ & + G(t)X(t)^2[-3(p_1 + p_2)] \\ & + X(t)^2\big(p_1G_b + d(t)\big) \\ & + 3p_3G(t)X(t)I(t) \\ & - G(t)X(t)^3 + \ddot{d(t)} \\ & + \big(p_1G_b + d(t)\big)(p_1^2 \\ & + 2p_3I_b) - p_3G(t)u(t) \\ & = f(x) + b(x)u\end{aligned} \tag{72}$$

The control input u appears for the first time at the third derivative. So, the relative degree of the system is 3. The state variables are considered as follows

$$\begin{aligned} x_1 &= G - G_{bref} \\ x_2 &= \dot{G} - \dot{G}_{bref} \\ x_3 &= \ddot{G} - \ddot{G}_{breff} \end{aligned} \qquad x = \begin{bmatrix} x_1 \\ x_2 \\ x_3 \end{bmatrix} \tag{73}$$

Then, the stste space equations are given by:

$$\begin{aligned} \dot{x}_1 &= \dot{G} - \dot{G}_{bref} \\ \dot{x}_2 &= \dot{G} - \dot{G}_{bref} \\ \dot{x}_3 &= \ddot{G} - \ddot{G}_{bref} = f(x) + b(x)u \end{aligned} \tag{74}$$

REFERENCES

[1] A. Makroglou , J. Li and . Y. Kuang, "Mathematical models and software tools for the glucose-insulin regulatory system and diabetes: an overview," *Applied Numerical Mathematics*, vol. 56, no. 3–4, pp. 559-573, March–April 2006.

[2] A. Haidar, "The Artificial Pancreas: How Closed-Loop Control Is Revolutionizing Diabetes," IEEE Control Systems Magazine, vol. 36, no. 5, pp. 28 - 47, Oct. 2016.

[3] I. Ahmad, F. Munir and M. F. Munir, "An adaptive backstepping based non-linear controller for artificial pancreas in type 1 diabetes patients," *Biomedical Signal Processing and Control*, vol. 47, p. 49–56, 2019.

[4] D. C. Klonoff and M. FACP, "The Artificial Pancreas: How Sweet Engineering Will Solve Bitter Problems," *Journal of Diabetes Science and Technology*, vol. 1, no. 1, pp. 72-81, January 2007.

[5] K. Turksoy and A. Cinar, "Adaptive control of artificial pancreas systems-a review," Journal of healthcare engineering, vol. 5, no. 1, pp. 1-22, 2014.

[6] M. Eren-Oruklu, A. Cinar, L. Quinn and D. Smith, "Adaptive control strategy for regulation of blood glucose levels in patients with type 1 diabetes," *Journal of Process Control*, vol. 19, no. 8, pp. 1333-1346, September 2009.

[7] E. Ruiz-Velazquez, R. Femat and D. Campos-Delgado, "Blood glucose control for type I diabetes mellitus: A robust tracking H∞ problem," Control Engineering Practice, vol. 12, no. 9, p. 1179–1195, 2004.

[8] L. Kovács, "Linear parameter varying (LPV) based robust control of type-I diabetes driven for real patient data," *Knowledge-Based Systems*, vol. 122, pp. 199-213, 15 April 2017.

[9] H. Delavari, H. Heydarinejad and D. Baleanu, "Adaptive fractional-order blood glucose regulator based on high-order sliding mode observer," *IET Systems Biology*, vol. 13, no. 2, pp. 43-54, March 2019.

[10] S. Ahmad, N. Ullah , N. Ahmed, M. Ilyas and W. Khan, "Super twisting sliding mode control algorithm for developing artificial pancreas in type 1 diabetes patients," vol. 38, pp. 200-211, September 2017.

[11] G. M. Steil, K. Rebrin, C. Darwin, F. Hariri and M. F. Saad, "Feasibility of Automating Insulin Delivery for the," *Diabetes*, vol. 55, pp. 3344-3350, 2006.

[12] G. Marchetti, M. Barolo, L. Jovanovic, . H. Zisser and D. E. Seborg, "An Improved PID Switching Control Strategy for Type 1 Diabetes," *IEEE TRANSACTIONS ON BIOMEDICAL ENGINEERING*, vol. 55, no. 3, MARCH 2008..

[13] T. MohammadRidha, M. Aït-Ahmed, L. Chaillous, M. Krempf, I. Guilhem, J.-Y. Poirier and C. H. Moog, "Model Free iPID Control for Glycemia Regulation of Type-1 Diabetes," *IEEE Transactions on Biomedical Engineering*, vol. 65, no. 1, pp. 199 - 206, 2017.

[14] A. K. Patra, A. Nanda, S. Panigrahi and A. K. Mishra, "The Fractional Order PID Controller Design for BG Control in Type-I Diabetes Patient," in Advances in Intelligent Computing and Communication, vol. 109), Singapore, Springer, 2020, pp. 321-329.

[15] R. Hovorka, . V. Canonico, L. J. Chassin, U. Haueter, M. Massi-Benedetti, M. Orsini Federici, T. R Pieber, H. C Schaller, L. Schaupp, T. Vering and M. E Wilinska, "Nonlinear model predictive control of glucose concentration in subjects with type 1 diabetes," *Physiological Measurement*, vol. 25, no. 4, pp. 905-920, July 2004.

[16] S. Lynch and B. Bequette, "Estimation-based model predictive control of blood glucose in type I diabetics: a simulation study," in Proceedings of the IEEE 27th Annual Northeast Bioengineering Conference, Storrs, CT, USA, April 2001.

[17] A. Mohammadzadeh and T. Kumbasar , "A new fractional-order general type-2 fuzzy predictive control system and its application for glucose level regulation," Applied Soft Computing Journal, vol. 91, 2020.

[18] A. Nath, D. Deb and R. Dey, "Robust observer-based adaptive control of blood glucose in diabetic patients," *International Journal of Control*, vol. 94, no. 11, 2021.

[19] S. Asadi and V. Nekoukar, "Adaptive fuzzy integral sliding mode control of blood glucose level in patients with type 1 diabetes: In silico studies," *Mathematical Biosciences*, vol. 305, pp. 122-132, November 2018.

[20] S. Sepasi, A. AkbarzadehKalat and M. Seyedabadi, "An adaptive back-stepping control for blood glucose regulation in type 1 diabetes," *Biomedical Signal Processing and Control*, vol. 66, April 2021

[21] R. Franco, A. Ferreira de Loza, H. Ríos, L. Cassany, D. Gucik-Derigny, J. Cieslak, L. Olçomendy and D. Henry, "Output-Feedback Sliding-Mode Controller for Blood Glucose Regulation in Critically Ill Patients affected by Type 1 Diabetes," *IEEE Transactions on Control Systems Technology* , vol. 29, no. 6, pp. 2704-2711, 2021.

[22] M. Homayounzade, "Positive input observer-based controller design for blood glucose regulation for type 1 diabetic patients: A backstepping approach," IET Systems Biology, vol. 16, no. 5, pp. 157-172, 2022

[23] F. Roshanravan and A. Heydari, "Sliding Mode Control Design for a Class of Nonlinear Fractional Systems with Application to Glucose-Insulin Systems," International Journal of Industrial Electronics Control and Optimization, vol. 5, no. 4, pp. 337-347, 2022.

[24] Z. Kouchaki1, M. R. Yousefi and K. Shojaei, "Blood Glucose Control for Type 1 Diabetic Patients: Robust Fuzzy Adaptive Approach," *Intelligent Procedures in Electrical Technology*, vol. 14, no. 53, pp. 172-188, 2023.

[25] Q. Zhou, L. Wang, C. Wu, H. Li and H. Du, "Adaptive Fuzzy Control for Nonstrict-Feedback Systems With Input Saturation and Output Constraint," *IEEE Transactions on Systems, Man, and Cybernetics: Systems*, vol. 47, no. 1, pp. 1 - 12, Jan. 2017..

[26] W. GAI, Y. ZHOU, M. ZHONG, C. SHENG and J. ZHANG, "Simple Adaptive Control With an Adaptive Anti-Windup Compensator for the Unmanned Aerial Vehicle Attitude Control," *IEEE Access*, vol. 8, pp. 52323 - 52332, 10 March 2020.

[27] A. Tahoun, "Anti-windup adaptive PID control design for a class of uncertain chaotic systems with input saturation," *ISA Transactions*, vol. 66, pp. 176-184, 2017.

[28] A. De Gaetano and O. Arino, "Mathematical modelling of the intravenous glucose," *Journal of mathematical biology*, vol. 40, no. 2, pp. 136-168, 2000.

[29] A. Boutayeb and . A. Chetouani, "A critical review of mathematical models and data used in diabetology," *BioMedical Engineering OnLine*, vol. 5, no. 43, 2006.

[30] C. Cobelli, C. Dalla Man, . G. Sparacino, L. Magni, . G. De Nicolao and B. P. Kovatchev, "Diabetes: Models, Signals, and Control," *IEEE Reviews in Biomedical Engineering*, vol. 2, pp. 54 - 96, 2009.

[31] A. Gabriela Gallardo Herna´ndez , L. Fridman , A. Levant, Y.

Shtessel, R. Leder, C. Revilla Monsalve and S. Islas Andrade, "High-order sliding-mode control for blood glucose: Practical relative degree approach," *Control Engineering Practice,* vol. 21, no. 5, pp. 747-758, May 2013.

[32] A. Nath and R. Dey, "Robust observer based control for plasma glucose regulation in type 1 diabetes patient using attractive ellipsoid method," *IET Systems Biology,* 2019.

[33] M. M. Fateh and S. Khorashadizadeh, S. "Robust control of electrically driven robots by adaptive fuzzy estimation of uncertainty." *Nonlinear Dynamics*, vol. *69*, pp. 1465-1477, 2012.

[34] S. Khorashadizadeh, and M. M. Fateh, "Adaptive fourier series-based control of electrically driven robot manipulators." In *The 3rd international conference on control, instrumentation, and automation* (pp. 213-218), 2013.

[35] F. Wu and B. Lu, "Anti-windup control design for exponentially unstable LTI systems with actuator saturation," *Systems & Control Letters*, vol. 52, no. 3–4, p. 305– 322, 2004.

Fatemeh Soleimannouri received the B.Sc. degree in Control Engineering from Islamic Azad University, Gonabad Branch, Gonabad, Iran and the M.Sc. degree in Control Engineering from Shahrood University of Technology, Shahrood, Iran, respectively. She is currently Ph.D candidate at Birjand University, Birjand, Iran. Her research interests include adaptive control, fuzzy control, nonlinear control and intelligent systems.

Saeed Khorashadizadeh was born in Mashhad, Iran. He studied at Ferdowsi University of Mashhad and received his B.S. degree in electrical engineering in 2009. Then he moved to Shahrood and received his M.S. and Ph.D degrees in control engineering from Shahrood University of Technology, in 2011 and 2015, respectively. Now, he is an assistant professor in University of Birjand, Iran. His research interests include Control, dynamical system, robotics and artificial intelligence.

Mohsen Farshad was born in Birjand, Iran, in 1967. He received the B.Sc. degree in electrical engineering from Sharif University of Technology, Tehran, Iran, in 1990 and the M.Sc. degree in electrical engineering from the University of Tehran, Tehran, Iran, in 1994. He received the Ph.D. degree from the Department of Electrical and Computer Engineering, University of Tehran in 2006. His teaching and research interests are switched reluctance and VR motors design, design and modeling of electrical machines and drives, intelligent modeling, and control. He is an associate professor at Department of power Engineering, Birjand University, South Khorasan, Iran.

Nasser Mehrshad Associate Professor of Electrical Engineering at the University of Birjand, Iran. Research interests: Signal Processing, Image Processing, Modeling the human visual system, Biomedical Instrumentation.

IECO

This page intentionally left blank.

International Journal Of
Industrial Electronics Control and Optimization
Print ISSN: 3517-2645
Online ISSN: 3568-2645
Homepage: https://ieco.usb.ac.ir/

Radiation Improvement of Low-Profile Microstrip Antenna by Utilizing AMC Surface for MIMO and Wireless Systems

Hossein Malekpoor[1] | Mehdi Hamidkhani[2]

Department of Electrical Engineering, Faculty of Engineering, Arak University, Arak, 38156-8-8349, Iran[1]
Department of Electrical Engineering, Isfahan (khorasgan) Branch, Islamic Azad University, Isfahan, Iran[2]
Corresponding author's email: h-malekpoor@araku.ac.ir

Article Info

Article type:
Research Article

Article history:
Received: 06-May-2024
Received in revised form: 17-August-2024
Accepted: 04-October-2024
Published online: 22-June-2025

Keywords:
Artificial Magnetic Conductor,
Printed Antenna,
Multi-Input Multi-Output,
Wideband,
Wireless.

ABSTRACT

A compact microstrip antenna by applying a parasitic artificial magnetic conductor (AMC), is proposed for facilitating 4G and 5G wireless communications. The antenna design includes microstrip dipoles fed by a T-shaped feedline. Notably, the antenna achieves a measured bandwidth of 5.32-6.73 GHz (with $S_{11} \leq$ -10 dB). To enhance performance, a proposed parasitic AMC reflector is integrated into the antenna structure. Incorporating an 8×8 AMC array, the antenna extends its -10 dB measured bandwidth from 4.51 to 6.83 GHz, catering to both 4G and 5G communication standards. Comparative analysis with an antenna lacking AMC reveals a reduced size of 35%, alongside a notable gain of 8 dBi and uni-directional radiation patterns. The efficiency and gain of all elements are approximately 90% and 8 dBi, respectively. Moreover, the introduction of an AMC unit cell, well-founded on a parasitic patch, resonates at 6.15 GHz with a bandwidth extending from 5.21 to 7.10 GHz. Furthermore, the offered equivalent transmission line model of the antenna with the AMC is demonstrated, yielding desirable results. This model accurately predicts the input impedance of the antenna with AMC across a broad frequency band ranging from 4.64 to 6.74 GHz. This comprehensive study demonstrates the effectiveness and versatility of the offered model in characterizing the operating band's behavior of the antenna across a wide frequency band to facilitate its design and optimization for various applications.

I. Introduction

structures have found application across various wireless networks and high-frequency devices [1-4]. Artificial Magnetic Conductor (AMC) structures, which utilize periodic boundary conditions across their operating band, have been increasingly adopted for applications such as cost-effective patch antennas, low-profile antennas, and mode suppression. These structures are particularly valued for their ability to mimic a perfect magnetic conductor over a specific frequency range, leading to enhanced antenna performance. AMCs are advantageous in reducing antenna size and improving radiation efficiency while maintaining a low profile, making them ideal for integration into modern wireless communication systems. By suppressing unwanted modes and enhancing the desired ones, AMCs contribute to the overall efficiency and effectiveness of antenna designs, especially in compact and complex wireless systems. [5-10]. In a recent work [9], a broadband patch array featuring EBG-AMCs was introduced to enhance the wireless transmission rate for 5G communication. The investigation of periodic AMC surfaces without vias has been explored in [11-18]. In [16], an EBG mushroom reflector with a two-layer configuration was utilized, resulting in a 60% size reduction. However, achieving a broad AMC bandwidth remains a significant challenge [19], prompting numerous efforts [20-22]. In [22], an AMC unit cell at a resonance of 6.2 GHz with a bandwidth of 4.4% was reported, exhibiting acceptable angular stability.

The Multi-Input Multi-Output (MIMO) method has become a pivotal technology in recent wireless communication systems, primarily due to its capability to transmit high data rates while minimizing latency [23-24]. This method leverages multiple antennas at both the transmitter and receiver ends to enhance communication reliability and increase channel capacity. A critical aspect of MIMO system design is achieving high port isolation, which

helps reduce interference between antenna elements and improves overall system performance. Various techniques have been explored to achieve this, including the use of orthogonal modes, mirrored elements, and different propagation modes [25-28]. These approaches are aimed at enhancing the isolation between the antenna ports, thereby ensuring better performance of MIMO antennas in terms of signal clarity and transmission efficiency.

Numerous techniques have been proposed to integrate broad AMC surfaces with microstrip antennas [29-30]. For instance, a low-profile circular polarized microstrip antenna incorporating AMC was presented in [30] to boost gain and bandwidth. Additionally, the development of two-layer boards has been prevalent in achieving improved radiation properties in most literature. The electromagnetic properties and applications of AMCs have led to a diverse range of studies aimed at enhancing antenna performance and miniaturization [31-38]. A low-profile and wide-axial-ratio-beamwidth (ARBW) circularly polarized antenna loaded with a honeycomb-shaped artificial magnetic conductor (AMC) is presented [36].

This study specifically concentrates on a proposed antenna utilizing AMC for MIMO applications. Initially, a low-profile wideband microstrip antenna configured with two printed dipoles fed by a T-shaped feedline is designed to enlarge the impedance bandwidth. Subsequently, a parasitic AMC is demonstrated to intensify at 6.15 GHz (5.21-7.10 GHz). The printed antenna with an 8×8 parasitic AMC reflector exhibits a measured -10 dB bandwidth of 4.55-6.83 GHz, suitable for 5G and MIMO applications. Furthermore, the proposed equivalent transmission line model is designed to offer a simplified yet accurate representation of the antenna integrated with the AMC structure. This model enables efficient analysis and optimization of the antenna's input impedance, which is crucial for achieving the desired performance characteristics.

II. Printed Microstrip Antenna with Planar AMC

Figure 1 illustrates the overall schematic of the printed antenna, which consists of two elements featuring folded dipoles mounted on Taconic TLT substrate (98.4 mm×98.4 mm, with a thickness of h_1=0.8 mm, dielectric constant ε_r=2.55, and a loss tangent of 0.0006). Positioned beneath the antenna is a periodic parasitic AMC surface, separated by an air gap (Styrofoam layer) from the antenna to facilitate broadband operation. The optimal air gap distance, denoted

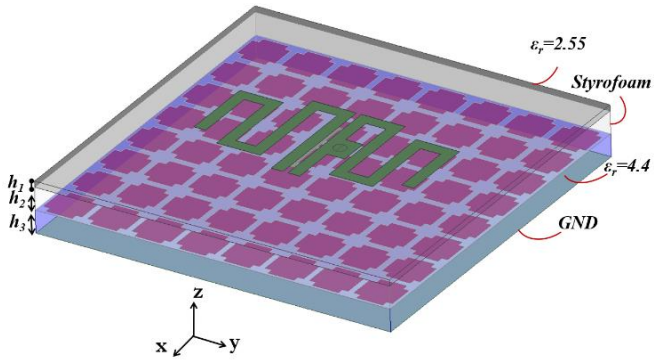

(a)

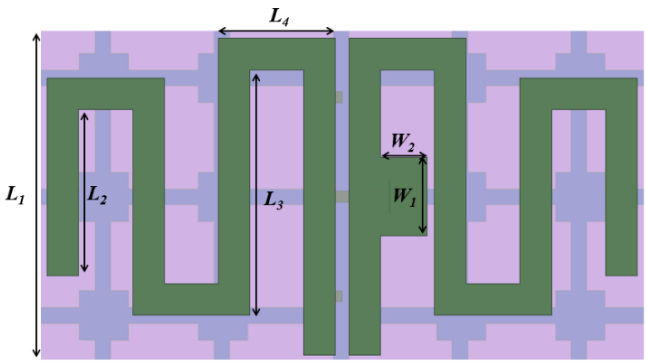

(b)

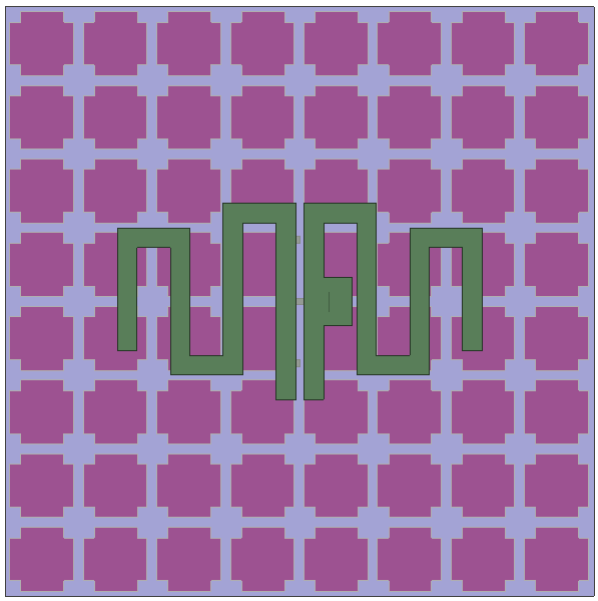

(c)

Fig.1. Structure of the suggested antenna by AMC reflector (a) 3D view (b) printed antenna design (c) Top view.

TABLE 1 SIZES OF SUGGESTED STRUCTURE

Parameters	Values (mm)
L_1	16
L_2	8.8
L_3	12
L_4	4.9
W_1	3.2
W_2	2.6
h_1	0.8
h_2	3
h_3	3
m	3
n	6
k	8.1

Figure 2 draws the schematic of a proposed unit cell for the AMC. This unit cell is constructed using an FR4 substrate with a relative permittivity (ε_r) of 4.4 and a thickness (h) of 3 mm. It is optimized with a ground plane measuring 8.1 mm×8.1 mm. The mushroom-type electromagnetic band gap (EBG) surface is modeled using an LC resonator, the calculation of which can be expressed as outlined in [11]:

$$C = \frac{W_{ebg}\varepsilon_0(1+\varepsilon_r)}{\pi}\cosh^{-1}\left(\frac{2W_{ebg}+g}{g}\right) \quad (1)$$

$$L = \mu_0 h \quad (2)$$

$$BW = \frac{1}{\eta}\sqrt{\frac{L}{C}} \quad (3)$$

The proposed equivalent transmission line model for the printed array with the AMC structure is designed to capture the detailed electrical characteristics and behavior of the antenna system. This model simplifies the complex interactions within the antenna into a combination of lumped elements and transmission line segments, making it easier to analyze and optimize the system's performance. Below is an outline of the key components in the proposed model [20]:

$$C_1 = \frac{\varepsilon_e\varepsilon_0 L_e W}{2h}\cos^{-2}\left(\frac{\pi y_0}{L}\right) \quad (4)$$

$$L_1 = \frac{1}{(2\pi f_r)^2 C_1} \quad (5)$$

$$R_1 = \frac{Q}{\omega C_1} \quad (6)$$

$$Q = \frac{c\sqrt{\varepsilon_e}}{4 f_r h} \quad (7)$$

$$C_c = \frac{-(C_1+C_2)+\sqrt{((C_1+C_2)^2 - 4C_1C_2(1-1/C_p{}^2))}}{2} \quad (8)$$

$$C_p = \frac{1}{\sqrt{Q_1 Q_2}} \quad (9)$$

$$C_2 = C_1\Delta C/(C_1+\Delta C) \quad (10)$$

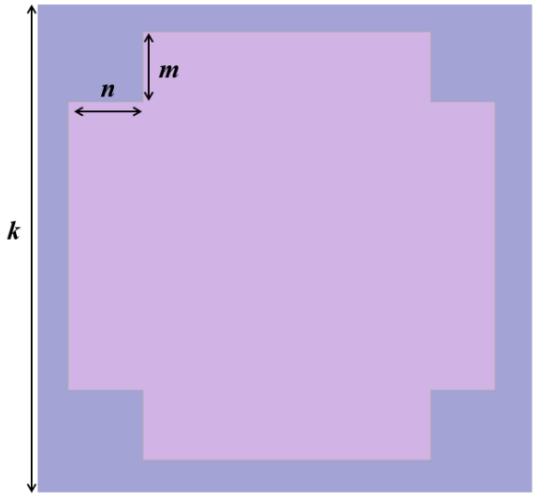

Fig. 2. AMC design.

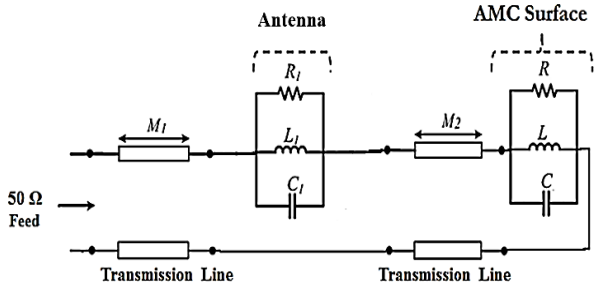

Fig. 3. Introduced equivalent transmission line model

The proposed model in Fig. 3 incorporates various parameters to accurately represent the behavior of the microstrip antenna with the AMC. Here are the key components and their significance. This model for the proposed printed antenna (PDA) involves two RLC resonators because of the symmetric patches. The two symmetric folded strips are represented as L_1C_1 and L_2C_2 elements according to Fig. 3. Additionally, the air ap height between the antenna and the AMC is modeled by the transmission line M_2. Furthermore, an LC resonator is regarded for the periodic surface.

The parameters obtained in equations (4)-(10) are applied to the conventional patch, and the element values of the model are determined using the Agilent Advanced Design System (ADS) simulator, utilizing the method of moments (MOM). The optimized values of the lumped elements which are applied in the model are as follows: R_1=50 Ω, C_1=2.64 pF, L_1=0.241 nH, R=72 Ω, C=0.57 pF, L=0.04 nH, and M_1=3.13 mm.

III. Experimental and Simulation Results

Figure 4 shows the reflection magnitude and phase characteristics of the proposed artificial magnetic conductor (AMC) at an incident angle (θ) of 0˚. The simulated results exhibit a ±90˚ reflection phase within the frequency range of 5.21-7.10 GHz, with a resonance occurring at 6.15 GHz. Compared to previous research [11, 20-22], the suggested AMC demonstrates significantly improved characteristics. The design features a symmetric unit cell, ensuring identical responses for both Transverse Electric (TE) and Transverse Magnetic (TM) waves, which enhances the consistency and reliability of the AMC's performance. Moreover, the proposed AMC offers a notably broader bandwidth of approximately 2 GHz, which is a substantial improvement over earlier designs. This broader bandwidth is achieved while maintaining acceptable stability across the AMC's operational range, making it particularly well-suited for broadband applications within the C-band.

Figure 5 illustrates the S-parameters of the antenna design with and without the AMC. The antenna lacking AMC exhibits a measurement band from 5.32 to 6.73 GHz (22.4%) for S_{11}< -10 dB. Conversely, the antenna equipped with the AMC demonstrates a -10 dB measured bandwidth spanning from 4.51 to 6.83 GHz, representing a bandwidth improvement of more than double.

The dimensions of the antenna without the AMC are as follows: width×length×height; 0.436λL, 0.436λL, and 0.014λL, respectively. In comparison, the dimensions of the antenna with the AMC are 0.362λL, 0.362λL, and 0.101λL, respectively, leading to a size reduction of 35%. Figure 5 (b) illustrates the results of the proposed equivalent model, implemented using ADS software. The simulation results cover 4.64-6.74 GHz, showcasing a well agreement with the measured results. This indicates that the equivalent model accurately captures the electrical behavior of the printed array with the AMC, providing valuable insights for the design and optimization of the antenna system. Simulated S-parameters of the antenna with AMC for various lengths of the parameters m and n are depicted in Figure 6. Figure 7 illustrates the variations in the height of the air gap, h_2, between the antenna and the AMC.

The maximum gain of the proposed antenna with the parasitic AMC across the bandwidth reaches 8 dBi, as observed in Figure 8.

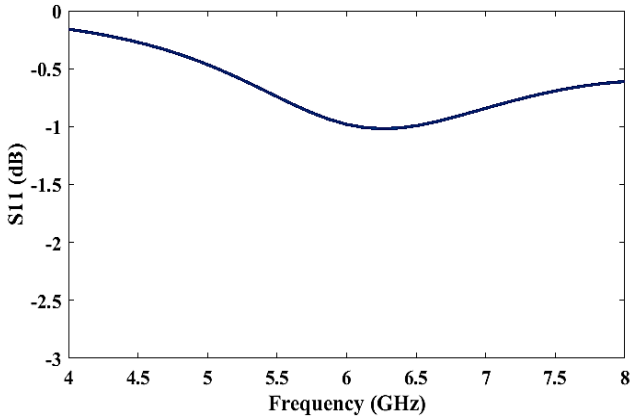

(a)

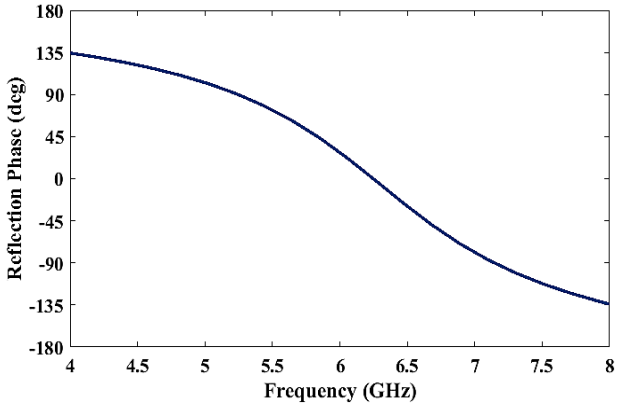

(b)

Fig. 4. Reflection magnitude and phase of AMC for normal incident waves.

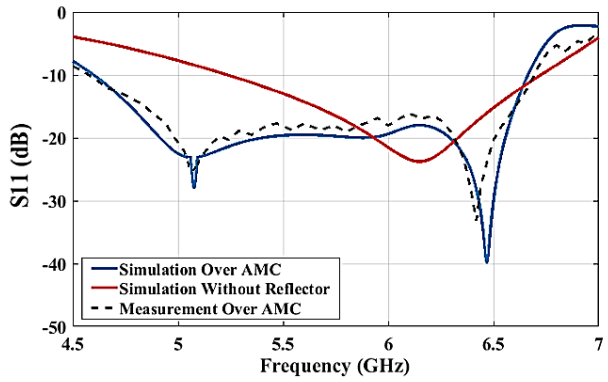

(a)

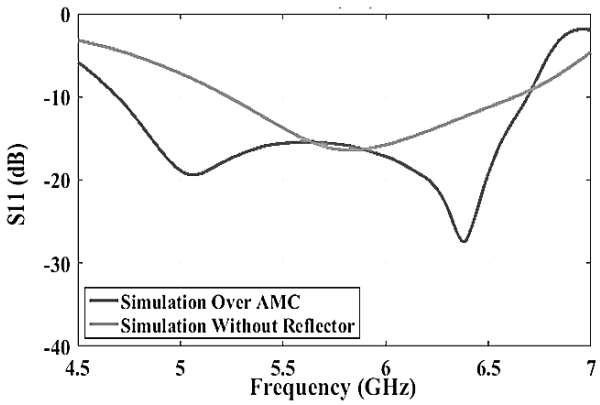

(b)

Fig. 5. Obtained results of S-parameters (a) HFSS (b) proposed model.

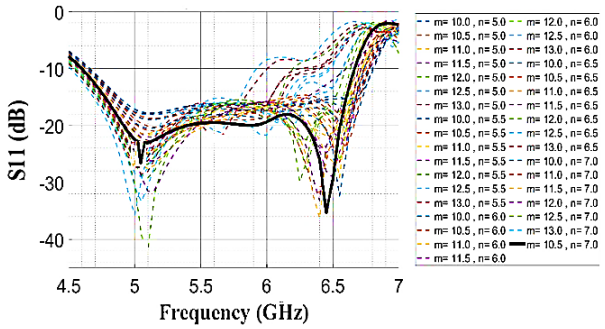

Fig. 6. S-parameters for different lengths of the m and n parameters.

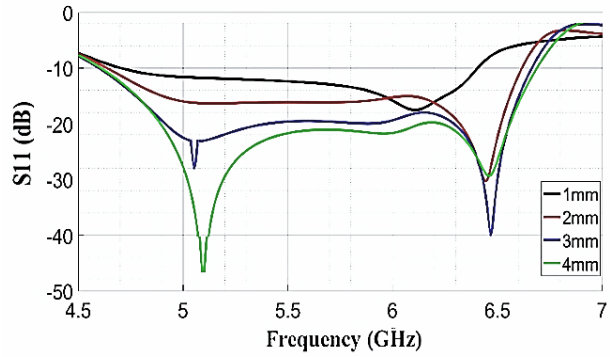

Fig. 7. Simulated S-parameters for different h_2.

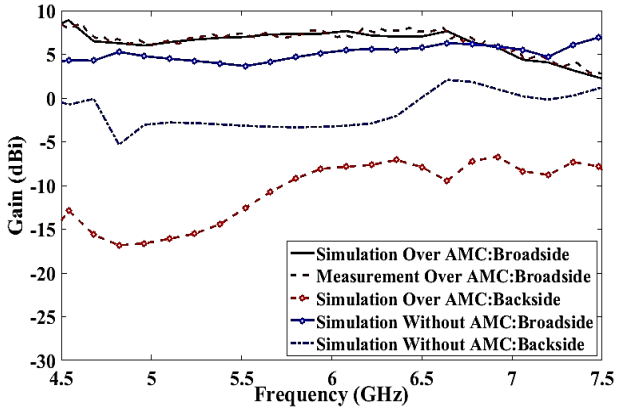

Fig. 8. Gains of the design.

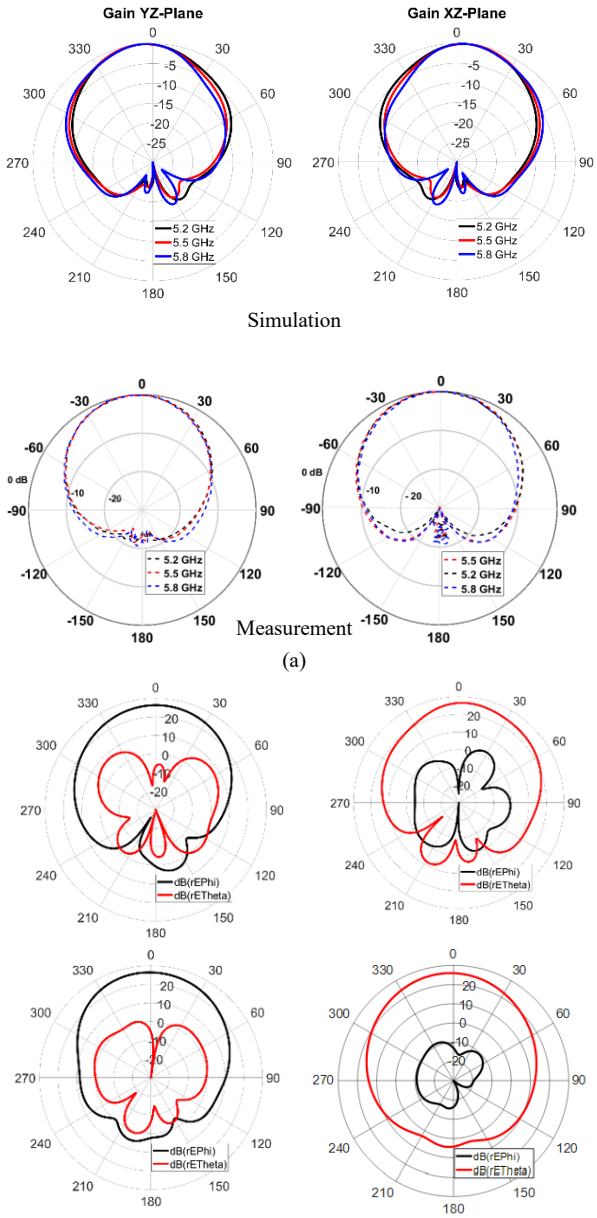

(a)

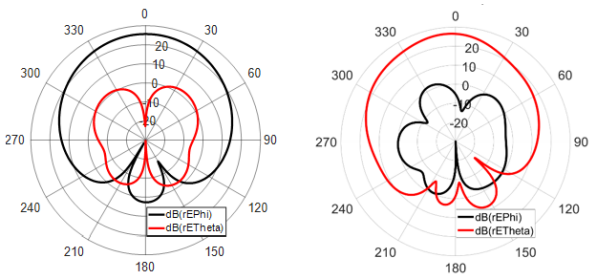

(b)

Fig. 9. Radiation patterns for (a) gain in XZ and YZ-planes (b) co and cross-pol in XZ and YZ-planes at 5.2, 5.5 and 5.8 GHz.

TABLE 2 COMPARISON STUDY

Proposed design	Measrured bandwidth	Width×Length×Height	Measrured Gain and Efficiency
My work	4.51-6.83 GHz (45.1%)	24.6×24.6×6.8 mm^3 0.362λ_L×0.362 λ_L×0.10λ_L	8 dBi 94%
V-shaped patches coupled by a bowtie dipole with 5×5 AMC array [19]	3–4.1 GHz (31%)	75×75×12.7 mm^3 0.75λ_L×0.75λ_L ×0.127λ_L	7.1 dBi 88%
Patch antenna by using triple-band AMC [20]	3.3–3.42 GHz (3.6%) 5.88-6.1 GHz (3.7%)	64×64×1.6 mm^3 0.71λ_L×0.71λ_L ×0.017λ_L	6.29 dBi 86%
Decoupling techniques using two-port feed network MIMO antenna [24]	3.33-3.67 GHz (9.7%)	70×140×0.8 mm^3 0.77λ_L×1.55λ_L ×0.009λ_L	6 dBi 78%
Printed slot antenna with wideband 3×5 AMC array [29]	2.37-2.50 GHz (5.34%)	100×125×7.5 mm^3 1.02λ_L×0.82λ_L ×0.63λ_L	10.3 dBi 88%
Bow-tie printed antenna with 6×9 fractal AMC array [33]	1.64-1.94 GHz (16.8%)	50×70×25 mm^3 0.27λ_L×0.38λ_L ×0.137λ_L	6.5 dBi 85%
Near-Zero-Index Metamaterial Lens Combined with AMC [34]	6.9–7.9 GHz (13.5%)	76×76×7 mm^3 1.75λ_L×1.75λ_L ×0.160λ_L	13 dBi 90%
M-shaped antenna based on 3×3 Jerusalem Cross AMC array [35]	2.2-2.72 GHz (18%)	67.5×67.5×4.5 mm^3 0.5λ_L×0.5λ_L×0.032λ_L	5 dBi 90%

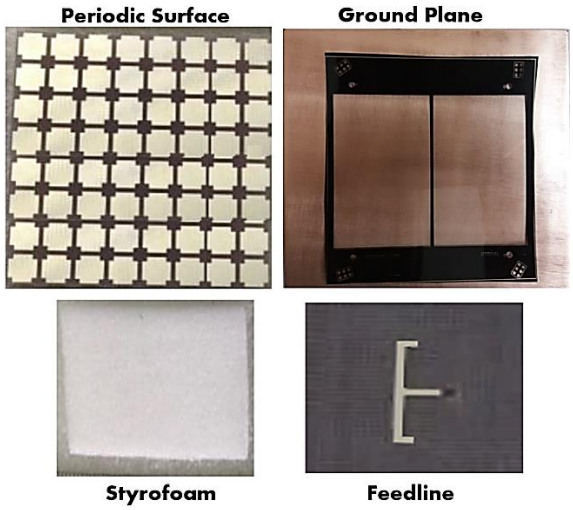

Fig. 10. Images of fabricated cases.

Figure 9 displays the radiation patterns in the XZ-plane and YZ-plane for the antenna design. Table 2 lists the performance of the design with respect to its prominent properties. The proposed design is compared with related works regarding key measurement parameters such as impedance bandwidth, gain, and efficiency. The results demonstrate that the design exhibits superior performance, making it highly suitable for wireless applications Additionally, Figure 10 presents photos of the manufactured antenna.

The proposed antenna is fed using a 50-Ohm probe. For the evaluation of its far-field radiation performance, a measurement setup is employed within an anechoic chamber. In this setup, a well-calibrated standard gain horn antenna acts as the transmitting (TX) antenna, while the prototype antenna serves as the receiving (RX) antenna. The horn antenna is positioned at a far-field distance from the prototype, determined by the formula $2D^2/\lambda$, where D represents the total dimension of the antenna and λ is the wavelength. Amplifiers are utilized to ensure consistent power reception. During the testing process, the prototype antenna is rotated to capture radiation intensity across various orientations. The S-parameters are accurately measured using an Agilent network analyzer.

IV. Conclusions

The introduced AMC design by exhibiting broadband properties within the C-band results in a parasitic patch to cover the range of 5.21-7.10 GHz. The proposed antenna with folded strips using by the AMC structure presents a miniaturized broadband solution for wireless systems. By integrating the 8×8 AMC surface into the antenna, an impressive -10 dB measured bandwidth of 4.51-6.83 GHz (45.1%) is achieved, accompanied by uni-directional radiation patterns and higher gains of up to 8 dBi. Measurement results confirm acceptable efficiency, leading to the conclusion that the design is suitable for wideband

wireless systems. Overall, the proposed equivalent transmission line model aims to provide a simplified yet accurate representation of the antenna with the AMC, allowing for efficient analysis and design optimization of the antenna system.

REFERENCES

[1] H. Malekpoor and S. Jam, "Design, analysis, and modeling of miniaturized multi-band patch arrays using mushroom-type electromagnetic band gap structures," International Journal of RF and Microwave Computer-Aided Engineering., vol. 28, no. 6, pp. 1–13, 2018.

[2] F. Kazemi, "A Compact Antenna with Dual Polarization for Mobile and Wireless Communication," International Journal of Industrial Electronics, Control and Optimization, vol. 6, pp. 73-82, 2023.

[3] S. Jam and H. Malekpoor, "Compact 1×4 patch antenna array by means of EBG structures with enhanced bandwidth", Microw. Opt. Technol. Lett, vol. 58, no. 12, pp. 2983-2989, 2016.

[4] A. A. Althuwayb, "Enhanced radiation gain and efficiency of a metamaterial inspired wideband microstrip antenna using substrate integrated waveguide technology for sub-6 GHz wireless communication systems", Microw Opt Technol Lett, Vol. 63, no. 7, pp 1892-1898, July 2021.

[5] A. Foroozesh, and L. Shafai, "Effects of artificial magnetic conductors in the design of low-profile high-gain planar antennas with high-permittivity dielectric superstrate," IEEE Antennas Wireless Propag. Lett., vol. 8, pp. 10-13, 2009.

[6] Z. F. Dai, Y. Pan, J. J. Huang, L. H. Ye, J. F. Li, H. Jiang, "Low-Profile Broadband Dual-Polarized Dipole Antenna with AMC Reflector," IEEE Antennas Wireless Propag. Lett., vol. 12, pp. 1–5, 2024.

[7] C. Bajaj, D. K. Upadhyay, S. Kumar, B. K. Kanaujia, "GPS-Integrated RFID Antenna With AMC Backing for IoT-Based Sensing and Tracking Applications," IEEE Trans. Antennas Propag., vol. 72, no. 2, pp. 1929 - 1934, 2024.

[8] J. M. Bell, M. F. Iskander, and J. J. Lee, "Ultrawideband hybrid EBG/ferrite ground plane for low-profile array antennas," IEEE Trans. Antennas Propag., vol. 55, no. 1, pp. 4–12, 2007.

[9] D. Nashaat, H. A. Elsadek, E. A. Abdallah, M. F. Iskander, and H. M. E. Hennawy, "Ultrawide bandwidth 2×2 microstrip patch array antenna using electromagnetic band-gap structure (EBG)," IEEE Trans. Antennas Propag., vol. 59, no. 5, pp. 1528–1534, 2011.

[10] S. Barth, and A. K. Iyer, "A Miniaturized Uniplanar Metamaterial-Based EBG for Parallel-Plate Mode Suppression," IEEE Trans. Microw. Theory Tech., vol. 64, no. 4, pp. 1176–1185, 2016.

[11] D. Sievenpiper, L. Zhang, R. F. J. Broas, N. G. Alex´opolous, and E. Yablonovitch, "High-impedance electromagnetic surfaces with a forbidden frequency band," IEEE Trans. Microw. Theory Tech., vol. 47, no. 11, pp. 2059–2074, 1999.

[12] J. Y. Deng, J. Y. Li, L. Zhao, L. X. Guo, "A Dual-Band Inverted-F MIMO Antenna With Enhanced Isolation for WLAN Applications ," IEEE Antennas Wireless Propag. Lett., vol. 6, pp. 2270 - 2273, 2017.

[13] S. Rajagopal, G. Chennakesavan, D. R. P. Subburaj, R. Srinivasan, and A. Varadhan, "A dual polarized antenna on a novel broadband multilayer Artificial Magnetic Conductor backed surface for LTE/CDMA/GSM base station applications," AEU- Int. J. Electron. Commun., vol. 80, pp. 73–79, 2017.

[14] H. Lee, B. Lee, "Compact Broadband Dual-Polarized Antenna for Indoor MIMO Wireless Communication Systems," IEEE Trans. Antennas Propag., vol. 64, pp. 766 - 770, 2016.

[15] E. Ameri, S. H. Esmaeli, and S. H. Sedighy, "Wide band radar cross section reduction by thin AMC structure," AEU- Int. J. Electron. Commun., vol. 93, pp. 150–153, 2018.

[16] S. Ghosh, T. N. Tran, T. L. Ngoc, "Dual-Layer EBG Based Miniaturized Multi-Element Antenna for MIMO Systems," IEEE Trans. Antennas Propag., vol. 62, no. 8, pp. 3985 - 3997, 2014.

[17] X. Y. Liu, Y. H. Di, H. Liu, Z. Wu, and M. M. Tentzeris, "A Planar Windmill-like Broadband Antenna Equipped with Artificial Magnetic Conductor for Off-Body Communications," IEEE Antennas Wireless Propag. Lett., vol. 15, pp. 64 - 67, 2015.

[18] S. Yang, Y. Chen, C. Yu, Y. Gong, and F. Tong, "Design of a Low-Profile, Frequency- Reconfigurable, and High Gain Antenna Using a Varactor-Loaded AMC Ground," IEEE Access, vol. 8, pp. 158635- 158646, 2020.

[19] J. Zhu, S. Li, S. Liao; Q. Xue, "Wideband Low-Profile Highly Isolated MIMO Antenna with Artificial Magnetic Conductor," IEEE Antennas Wireless Propag. Lett., vol. 17 pp. 458 - 462, 2018.

[20] A. Ghosh, V. Kumar, G. Sen, S. Das, "Gain enhancement of triple-band patch antenna by using triple-band artificial magnetic conductor," IET Microw. Antennas Propag., vol. 12, no. 8, pp. 1400-1406, 2018.

[21] N. Othman, N. A. Samsuri, M. Ka. A. Rahim, and K. Kamardin, "Low specific absorption rate and gain-enhanced meandered bowtie antenna utilizing flexible dipole-like artificial magnetic conductor for medical application at 2.4 GHz," Microw Optical. Tech Lett., vol. 62, pp. 3881-3889, 2020.

[22] R. C. Hadarig, M. E. de Cos and F. L. Heras, "Novel miniaturized artificial magnetic conductor," IEEE Antennas Wireless Propag. Lett., vol. 12, pp. 174–177, 2013.

[23] A. S. d. Sena, D. B. d. Costa, Z. Ding, P. H. J. Nardelli, "Massive MIMO–NOMA Networks With Multi-Polarized Antennas," IEEE Trans. Wireless Commun.. vol. 18, pp. 5630 - 5642, 2019.

[24] Z. Xu, and C. Deng, "High-Isolated MIMO Antenna Design Based on Pattern Diversity for 5G Mobile Terminals," IEEE Antennas Wireless Propag. Lett., vol. 19 pp. 467 - 471, 2020.

[25] Z. Wang, G. Zhang, Y. Yin, and J. Wu, "Design of a Dual-Band High-Gain Antenna Array for WLAN and WiMAX Base Station," IEEE Antennas Wireless Propag. Lett., vol. 13, pp. 1721 - 1724, 2014.

[26] S. Jam and H. Malekpoor, "Analysis on wideband patch arrays using unequal arms with equivalent circuit model in X-band", IEEE Antennas Wireless. Propag. Lett., vol. 15, pp. 1861-1864, 2016.

[27] H. Malekpoor, and M. Hamidkhani "Bandwidth and gain improvement for reduced size of stacked microstrip antenna fed by folded triangular patch with half V-shaped slot," International Journal of RF and Microwave Computer-Aided Engineering., vol. 31, no. 6, e22649, 2021.

[28] M. Hamidkhani, H. Malekpoor, and Homayoon Oraizi, "Oscillator Phase-Noise Reduction Using High-

Qsc Active Giuseppe Peano Fractal Resonators", IEEE Microw. and Wireless Components Letters., Vol. 29, pp. 354-356, 2019.
[29] J. Joubert, J. C. Vardaxoglou, W. G. Whittow, and J. W. Odendaal, "CPW-fed cavity-backed slot radiator loaded with an AMC reflector," IEEE Trans. Antennas Propag., vol. 60, no. 2, pp. 735–742, 2012.
[30] D. Feng, H. Zhai, L. Xi, S. Yang, K. Zhang, D. Yang, "A Broadband Low-Profile Circular-Polarized Antenna on an AMC Reflector," IEEE Antennas Wireless Propag. Lett., vol. 16, pp. 2840 - 2843, 2017.
[31] H. Malekpoor and S. Jam, "Improved radiation performance of low profile printed slot antenna using wideband planar AMC surface," IEEE Trans. Antennas Propag., vol. 64, no. 11, pp. 4626–4638, 2016.
[32] G. Andrea Casula, F. Lestini, F. Paolo Chietera, G. Muntoni, C. Occhiuzzi, L. Catarinucci, R. Colella, G. Montisci, G. Marrocco, "Design of On-Body Epidermal Antenna on AMC Substrate for UHF RFID in Healthcare," IEEE Trans. Antennas Propag., vol. 72, no. 5, pp. 4023 - 4035, 2024.
[33] Y. W. Zhong, G. M. Yang and L. R. Zhong, "Gain enhancement of bow-tie antenna using fractal wideband artificial magnetic conductor ground," Electron. Lett., vol. 51, no. 4, pp. 315-317, 2015.
[34] J. P. Turpin, Q. Wu, D. H. Werner, B. Martin, M. Bray, and E. Lier, "Near-zero-index metamaterial lens combined with AMC metasurface for high-directivity low-profile antennas", IEEE Trans. Antennas Propag., vol. 62, no. 4, pp. 1928–1936, 2014.
[35] H. R. Raad, A. I. Abbosh, H. M. Al-Rizzo and D. G. Rucker, "Flexible and compact AMC based antenna for telemedicine applications," IEEE Trans. Antennas Propag., vol. 61, no. 2, pp. 524–531, 2013.
[36] Y. Luo, X. Wang, N. Yan, W. An, K, Ma, "Low-Profile Wide Axial-Ratio Beamwidth Circularly Polarized Antenna Loaded With Artificial Magnetic Conductor," IEEE Antennas Wireless Propag. Lett., vol. 23, no. 3, pp. 935 - 939, 2024.
[37] W. Luo, P. Wang, "A Compact UHF-RFID Tag Antenna With Embedded AMC for Metallic Objects", IEEE Antennas Wireless Propag. Lett., vol. 22, no. 4, pp. 873 - 877, 2023.
[38] H. Cheng, G. Xiao, X. Wang, "A Low-Profile Wideband Patch Antenna With Modified Parasitic Mushroom Structures on Nonperiodic AMC," IEEE Antennas Wireless Propag. Lett., vol. 22, no. 4, pp. 719 - 723, 2023.

Hossein Malekpoor was born in Iran, in 1985. He joined the faculty of the Arak University in 2017, where he is currently an Assistant Professor with the Electrical Engineering Department. His research interests include different antennas design, wideband microstrip antennas for UWB applications and wireless communication, analysis of antenna with equivalent circuit models, phased array antennas, designing the periodic structures such as EBGs, AMCs and FSSs, and antenna design with EBG and AMC surfaces.

Mehdi Hamidkhani was born in Esfahan, Iran, in 1985. He received the B.E. degree in electrical engineering from the Yazd University, Iran, in 2007, and the M.Sc. degree in electrical engineering from the Iran University of Science and Technology (IUST), Tehran, Iran, in 2010, and the Ph.D. degree in electrical engineering from the Shiraz University, Shiraz, Iran, in 2016. He is currently a professor assistant at the Islamic Azad University Dolatabad Branch, Isfahan, Iran. His current research interests are RF microwave circuits, Antenna, wireless networks, IoT.

International Journal Of
Industrial Electronics Control and Optimization
Print ISSN: 3517-2645
Online ISSN: 3568-2645
Homepage: https://ieco.usb.ac.ir/

A Compact, High Efficiency, and Portable Wireless EV Resonant Charger

Jasem Shahsevani | Reza Beiranvand
Tarbiat Modares University, Faculty of Electrical and Computer Engineering, Tehran, Iran
Corresponding Author's Email: beiranvand@modares.ac.ir

Article Info

Article type:
Research Article

Article history:
Received: 23-August-2024
Received in revised form: 03-October-2024
Accepted: 15-November-2024
Published online: 22-June-2025

Keywords:
AC/DC converter,
Charger,
EV charger,
Interleaved converter.

ABSTRACT

Efficient and versatile charging solutions are essential for modern applications requiring portable energy systems. This paper presents a novel portable charger powered by an isolated split-core current clamp, enabling direct charging from power lines. The system utilizes inductive coupling to draw AC current from these lines, which is then regulated to a precise voltage for battery replenishment. The proposed design features an interleaved resonant topology with a semi-active rectifier, achieving high efficiency and adaptability to a wide range of input voltages. This architecture supports a variable DC bus voltage, enabling the resonant converter to operate optimally near its resonant frequency for maximum performance. To ensure a lightweight and efficient design, the converter eliminates traditional transformers, incorporating a capacitive element within the resonant network for galvanic isolation. A cascaded dual-control strategy in the interleaved structure ensures precise voltage regulation. Designed to be compatible with 1-6 cell Li-Ion batteries, the charger offers extensive versatility. Experimental results from a 2.5-200 W prototype, with an output voltage range of 4.2-25.2 V, demonstrate a peak efficiency of 94%, validating the effectiveness of the proposed charger for grid-connected applications.

I. Introduction

Electric Vehicles (EVs) have become integral to modern technological landscapes, serving critical roles in fields such as logistics, precision agriculture, and emergency services [1, 2]. Despite these advancements, a primary challenge persists: limited operation range due to high power consumption and constrained battery capacity. While increasing battery capacity might appear as a straightforward solution, it invariably results in additional weight, which in turn undermines the overall operational efficiency and maneuverability of EVs. Various strategies have been explored to extend operation duration, including the use of Capacitive Coupling Wireless Power Transfer (CCWPT) for charging [3, 4]. These methods typically rely on static charging stations, positioned along predetermined operational paths, requiring the EV to pause at specific nodes for recharging. This disrupts continuous operation and is impractical in rural or remote regions, limiting the potential reach of such systems. Research on optimizing battery utilization and operational paths to enhance range efficiency has shown some promise [5, 6], but the fundamental issues remain unresolved. In the realm of wireless power transfer, Inductive Coupling Wireless Power Transfer (ICWPT) has been extensively investigated [7-21], with advancements such as dynamic charging stations and repositionable transmitter coils for enhanced alignment and power transfer efficiency [9-20], Despite these improvements, most ICWPT systems necessitate precise alignment between the EV and charging unit, making them suboptimal for real-time and in-operation applications.

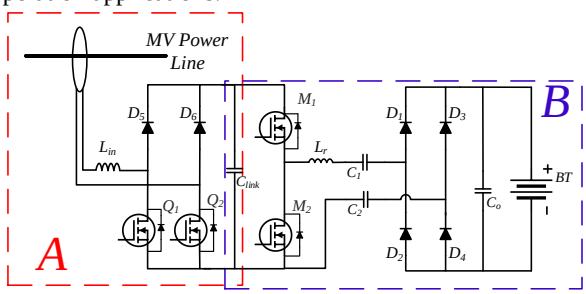

Fig. 1. The proposed portable EV charger.

TABLE1 LI-POL BATTERIES VOLTAGES FOR CHARGING

Number of Cells	Cut off Voltage	Nominal Voltage	Max. Voltage
1	3.0 V	3.7 V	4.2 V
2	6.0 V	7.4 V	8.4 V
3	9.0 V	11.1 V	12.6 V
4	12.0 V	14.8 V	16.8 V
5	15.0 V	18.5 V	21.0 V
6	18.0 V	22.2 V	25.2 V

A major limitation of existing EV charging systems is the low efficiency and power density of the converters employed. Most conventional solutions are heavily dependent on fixed charging infrastructure or constrained by optimization-based routing to maximize the operational radius. Consequently, these methods lack several critical attributes, such as a lightweight form factor, wide input/output voltage adaptability, high efficiency across varying voltage levels, and the capability for in-operation or contactless charging.

To address these limitations, various high-efficiency AC/DC and DC/DC converters have been proposed. While isolated AC/DC converters with transformers offer galvanic isolation, they suffer from increased size and weight, posing a significant drawback for EV applications [22, 23], Non-isolated AC/DC converters provide an alternative but lack the necessary isolation for safety and performance. Similarly, conventional DC/DC converters designed for battery charging are encumbered by bulky transformers, reducing their feasibility for compact EV systems [24, 25]. Non-isolated DC/DC converters have also been explored [26, 27], but they present challenges in terms of safety and electromagnetic interference (EMI) concerns. Furthermore, AC/DC converter designs developed for high-power grid applications [28, 29] are not well-suited for EV charging due to their substantial size, reliance on input inductors, and inability to function effectively with dynamic input voltages encountered during in-operation charging scenarios.

Additionally, existing solutions often lack adequate filtering mechanisms before the transformer stage, leading to increased harmonic distortion, reduced efficiency, and elevated thermal losses. Moreover, the limited input/output voltage range of conventional converters restricts their operational flexibility, failing to meet the diverse voltage requirements of different battery configurations [30-34], Although a few approaches have incorporated capacitive isolation to mitigate transformer-related drawbacks [35] they still fall short in achieving the desired combination of lightweight structure, broad voltage adaptability, and in-operation charging capability.

In this paper, we present a novel transformer-less isolated AC/DC resonant converter specifically designed for EV charging, with a focus on Lithium-Polymer (Li-Pol) batteries. To ensure a compact and portable solution, the proposed converter utilizes a transformer-less topology, employing two series capacitors for galvanic isolation and an interleaved resonant structure for enhanced efficiency. The converter integrates a circular split-core current clamp, enabling it to connect to power lines or perform in-operation charging by harnessing inductive coupling to generate AC voltage. A sophisticated dual-control mechanism is implemented within the interleaved structure, ensuring optimal performance and high efficiency over a wide range of input voltages and operational conditions. The proposed converter successfully addresses the aforementioned limitations, offering a robust solution for uninterrupted EV operation and extended performance range.

The remainder of the paper is structured as follows: Section II presents the proposed converter's architecture and key operating waveforms. Section III provides a detailed analysis of its operational states and control approach, followed by an in-depth analysis of losses in Section IV. Section V discusses the design procedure and validation through experimental results is debated in Section VI. Finally, Section VII concludes the paper by highlighting the significance and potential impact of the proposed converter in advancing EV charging technologies.

II. Proposed Converter and Its Key Waveforms

Lithium-Polymer (Li-Pol) batteries are widely utilized in EVs due to their high capacity and power output, making them suitable for applications that demand lightweight and high-energy density. These batteries typically operate within a voltage range of 4.2-25.2 V, depending on the configuration of one to six cells, with each cell having a maximum voltage of 4.2 V. However, EVs equipped with such batteries face limitations in operation duration, which typically ranges between 15 to 45 minutes, consequently restricting their operational range. To overcome this constraint, an advanced EV charging solution is proposed to enhance operation radius and continuity. The charger addresses critical design considerations such as lightweight structure, broad input/output voltage range, and high efficiency across varying voltage levels, compact form factor for easy installation, and in-operation charging capability. The proposed charging system, illustrated in Fig. 1, is designed to interface with power lines by either direct contact or proximity-based power transfer, allowing the EV to recharge while in motion. It features a split-core current clamp with an adjustable aperture, enabling the EV to connect seamlessly to the power line and induce AC voltage into the converter's input stage, for example as shown in Fig. 2. The converter’s input stage comprises an AC voltage source fed into a semi-active rectifier, which includes a small inductor. This rectifier converts the induced AC voltage into a variable DC voltage to accommodate fluctuations in the input supply and maintain stable output. Following the rectification stage, a series resonant converter is employed. This converter serves two essential functions: first, it stabilizes voltage fluctuations caused by the small input inductor, ensuring a smooth and regulated output voltage. Secondly, it provides input-output isolation through two series

capacitors integrated within the resonant structure, eliminating the need for a traditional transformer and thereby reducing weight and size. By adopting a resonant topology with interleaved operation and semi-active rectification, the proposed converter efficiently charges Li-Pol batteries from one to six cells. The resonant converter operates primarily near its resonant frequency in the ZVS region, enabling soft switching for high efficiency. To further optimize performance, a large link capacitor (C_{link}) is introduced to maintain a stable voltage. However, by allowing up to a 20% voltage variation in Clink, the size of both Clink and the input inductor (L_{in}) can be significantly reduced. This variation is managed by the closed-loop control implemented in Section B of the converter, minimizing the impact on output voltage regulation.

In summary, the variable input voltage governs the overall regulation of the output voltage, while the resonant converter provides galvanic isolation and contributes minimally to output regulation, ensuring high efficiency and lightweight design. Fig. 1 illustrates the architecture of the proposed converter, with Section A responsible for charging the C_{link} capacitor, and Section B regulating the output voltage and powering the load. Fig. 2 demonstrates an application of the converter, and Fig. 3 presents key operational waveforms, showcasing the performance and efficiency of the proposed system.

III. Different Operational States of the Converter and Its Control Algorithm

This section elaborates on the different operational states of the proposed converter and the corresponding control algorithm. The semi-active rectifier is controlled using a Phase-Shift Modulation (PSM) approach at a switching frequency of 300 kHz, while the resonant converter (Section B in Fig. 1) employs a Pulse Frequency Modulation (PFM) strategy within the same frequency range. Due to the significantly higher switching frequency compared to the grid frequency, the grid voltage can be approximated as a DC voltage source for the converter. The overall control scheme is a cascaded configuration, integrating PFM and PSM, wherein the semi-active rectifier primarily manages the output voltage regulation. To minimize the converter's size, a reduced-value input inductor and link capacitor are utilized, which results in a ripple on the link capacitor's voltage. The resonant stage, positioned downstream, mitigates these voltage fluctuations, providing a stable output voltage suitable for battery charging. This is achieved through a dual-loop cascade control approach: an inner PFM loop for the resonant stage and an outer, slower PSM loop for overall output voltage regulation.

The operational states of the isolated converter, which utilizes capacitors C_1 and C_2 for isolation, are depicted in Fig. 3 and are described as follows:

State I: During the interval t_0–t_1 (Fig. 3), switches Q_1 and Q_2 are both turned on, causing L_{in} to charge. As there is no power transfer to C_{link}, its voltage drops. Simultaneously, in Section B, M_1 is conducting, allowing power to flow through C_r, D_1, and D_4 to the load, as shown in Fig. 4(a).

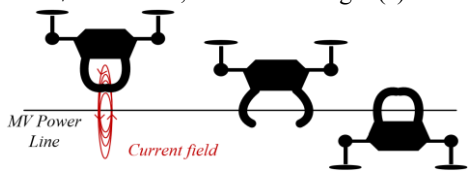

Fig. 2. An Application of the proposed converter for EV charging via in-operation charging through induced current fields or direct connection to power lines.

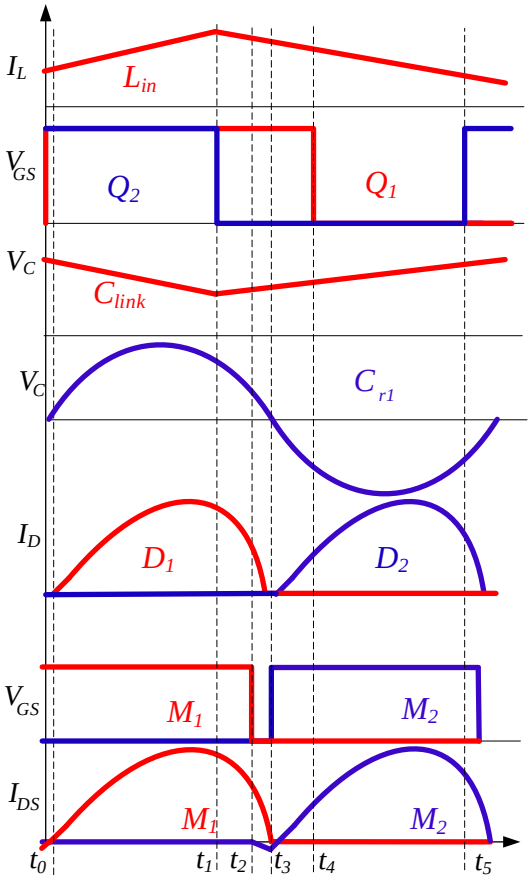

Fig. 3. Some of proposed converter key waveforms in 300 kHz switching frequency operation.

State II: In the interval t_1–t_2 , Q_2 is turned off, halting L_{in}'s charging. L_{in} then discharges into C_{link}, increasing its voltage.

Section B continues its previous operation, as shown in Fig. 4(b).

State III: During t_2–t_3, Section A maintains the previous operation. In Section B, at t_2, M_1 is turned off, and its current passes through M_2's body-diode, achieving Zero Voltage Switching (ZVS) for M_2's turn-on. This action turns off D_1 and D_4, as depicted in Fig. 4(c).

State IV: At t_3, Q_2 is turned off, leaving L_{in} and C_{link} operations unchanged. In Section B, M_2 is turned on under ZVS conditions, energizing D_2 and D_3, as shown in Fig. 4(c).

State V: At t_4, Q_2 is turned on again, and Section B continues its previous operation. Subsequently, the cycle repeats periodically, as illustrated in Fig. 4(d).

It is noteworthy that when Q_1 and Q_2 are turned off, their body-diodes conduct, causing Section A to function as a diode bridge. The converter's output voltage is regulated using a combination of PSM and PFM control. While PFM control tends to be less efficient under low-load conditions, the interleaved structure mitigates efficiency loss. To maintain high efficiency, Section B predominantly operates at the resonant frequency during typical operational conditions. The output voltage is further regulated by the PSM control in Section A, whereas Section B ensures isolation and closed-loop control of the output voltage, significantly influencing the size of the input inductor.

The frequency response characteristics of the proposed converter under various quality factors (Q) and phase shifts are shown in Fig. 5, illustrating its operational dynamics and efficiency performance.

IV. Mathematical Power Loss Analysis

Here, some important power loss components of the proposed converter are calculated. The equations (1-20) are mainly derived from [2, 36, 37].

A. Diode

$$i_{D1}(t)=\begin{cases} n\,I_{Rm}\sin(\omega_o t) & 0\le t<\frac{1}{2}T_o,\\ 0 & \frac{1}{2}T_o\le t<T_s. \end{cases} \quad (1)$$

$$i_{D2}(t)=\begin{cases} 0 & 0\le t<\frac{1}{2}T_s,\\ n\,I_{Rm}\sin(\omega_o t) & \frac{T_s}{2}\le t<\frac{T_s+T_0}{2},\\ 0 & \frac{T_s+T_0}{2}\le t<T_s. \end{cases} \quad (2)$$

Where, ω_o is equal to $2\pi f_o$. In result RMS and average current through each diodes is:

$$I_{D1_{avg}}=\frac{I_o}{2}, I_{Rm}=\frac{\pi I_o}{2n\frac{f_s}{f_o}},\quad I_{D1_{avg}}=\frac{\pi I_o}{4}\sqrt{\frac{f_o}{f_s}}. \quad (3)$$

So power loss due V_f of each diode is:

$$P_{Vf}=V_f I_{D1_{avg}}=V_f\frac{I_o}{2}=\frac{V_f}{V_o}\frac{P_o}{2}. \quad (4)$$

Therefore, we can write:

$$P_{rf}=I_{D1_{rms}}^2 r_f=\frac{\pi^2}{16}\frac{f_o}{f_s}\frac{r_f}{R_L}P_o. \quad (5)$$

$$P_D=P_{D1}+P_{D2}=\left(\frac{V_f}{V_o}+\frac{\pi^{16}}{8}\frac{f_o}{f_s}\frac{r_F}{R_L}\right)P_o. \quad (6)$$

A. Output Capacitor

Output capacitor current is:

$$I_{Co}(t)=\begin{cases} n\,I_{Rm}\sin(2\omega_o t)-I_o & 0\le t<\frac{T_0}{2},\\ -I_o & \frac{T_0}{2}\le t<T_s. \end{cases} \quad (7)$$

$$I_{Co_{rms}}=I_o\sqrt{\frac{\pi^2}{8}\frac{f_o}{f_s}-1}. \quad (8)$$

So its power loss is as follows:

$$P_{r_{Co}}=I_{Co_{rms}}^2 r_{Co}=\left(\frac{\pi^2}{8}\frac{f_o}{f_s}-1\right)I_o^2 r_{Co}$$

$$=\left(\frac{\pi^2}{8}\frac{f_o}{f_s}-1\right)\frac{r_{Co}}{R_L}P_o. \quad (9)$$

In addition, to calculate the power MOSFET switches losses, following parameters are given:

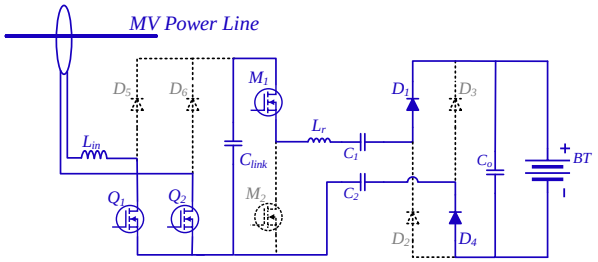

(a)

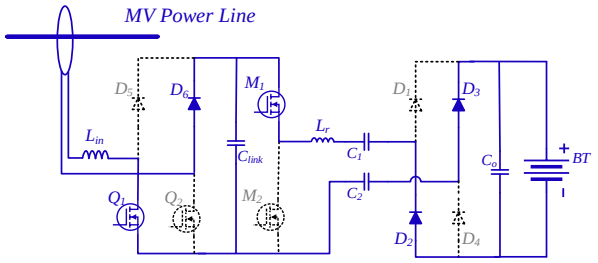

(b)

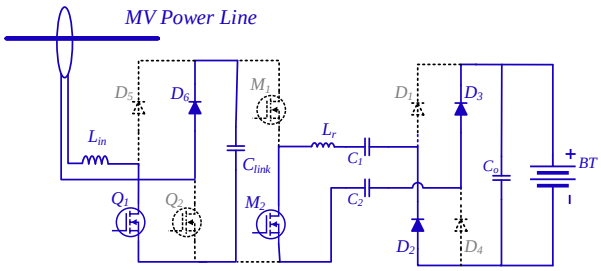

(c)

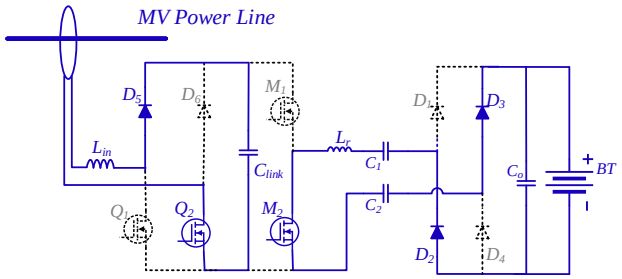

(d)

Fig. 4. The operation of proposed converter.

Discharge Time (t_{dis}): The time it takes for the DC capacitor to discharge from the input voltage to 0 V after the MOSFET is switched off.

Dead Time (t_{dead}): The time interval between the gate-source signals of the high-side and low-side MOSFETs in a half-bridge configuration. This prevents shoot-through current, which can damage the MOSFETs.

Turn-on Delay ($t_{delay(on)}$): The time it takes for the drain-source current to start flowing after the gate-source voltage reaches the threshold voltage.

Body Diode Conduction Time ($t_{body(on)}$): The time the internal body diode of the MOSFET conducts during the turn-on transition.

Gate-Source Voltage (V_{gs}): The voltage applied between the gate and source terminals of the MOSFET.

Body Diode Forward Voltage (V_{bF}): The voltage drop across the body diode when it conducts current.

MOSFET Conduction Time ($t_{ds(on)}$): The time the MOSFET conducts current during the switching cycle.

B. Power MOSFET Drive Circuit Power Loss

This kind of loss is due to gate-source power MOSFET capacitor charge and discharge, which is as follows:

$$P_{drive} = 2\left(\frac{1}{2}C_{gs}V_{gs}^2\right)f_s. \tag{10}$$

C. Diode and MOSFET Body Diode Power Losses

$$t_{dis} = \frac{8}{M_g}L_m(C_{ds1} + C_{ds2})f_s. \tag{11}$$

$$t_{body(on)} = t_{dead} - t_{dis} + t_{delay(on)}. \tag{12}$$

$$P_{body} = 2V_{bF}\left[\left(\frac{nV_o}{L_m}\left(\frac{1}{4}\frac{1}{f_s} - t_{dis}\right)\right)\right]t_{body(on)}f_s. \tag{13}$$

D. MOSFET Turning off Switching Loss

Two assumptions are made in this section. The first one is in the meanwhile of power MOSFET turning off, which its current is near the inductor magnetizing current, and the second one is rising voltage and magnetizing inductor current is linear.

$$V_{ds}(\mathrm{t}) = V_{ds(on)} + \frac{V_{in} - V_{ds(on)}}{t_{dis}}t. \tag{14}$$

$$i_{ds}(t) = \frac{nV_o}{L_m}\frac{1}{4f_s}\left(1 - \frac{t}{t_{dis}}\right). \tag{15}$$

$$p_{tf} = 2f_s\int_0^{t_{dis}} v_{ds}(t)i_{ds}(t)dt$$

$$= \frac{nV_o t_{dis}}{12L_m}\left(V_{in} + 2V_{ds(on)}\right). \tag{16}$$

Some other parameters are given as follows:

$$F = \frac{f_s}{f_r}, \qquad f_r = \frac{1}{2\pi\sqrt{L_r C_{eq}}}, \quad \omega = \frac{1}{2\pi f_r}. \tag{17}$$

$$R_{eq} = \frac{8}{\pi^2}R_L, \quad Q = \frac{1}{R_{eq}}\sqrt{L_r/C_{eq}}. \tag{18}$$

$$i_{Q1,2(AVG)} = \frac{V_i DT}{2L}\frac{V_i D}{V_o - V_i} = \frac{0.02\,V_i^2 D^2}{2L(V_o - V_i)}. \tag{19}$$

$$D = \frac{\theta_2 - \theta_1}{360} = 1 - \frac{V_{in}}{2V_{out}} \tag{20}$$

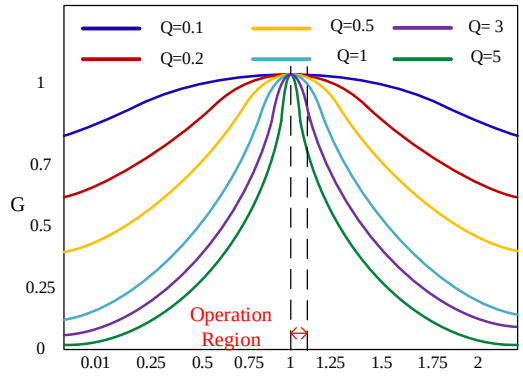

(a) Phase-shift= 180°.

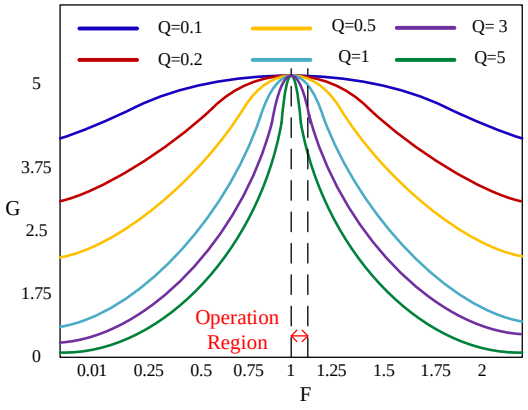

(b) Phase-Shift= 90°.

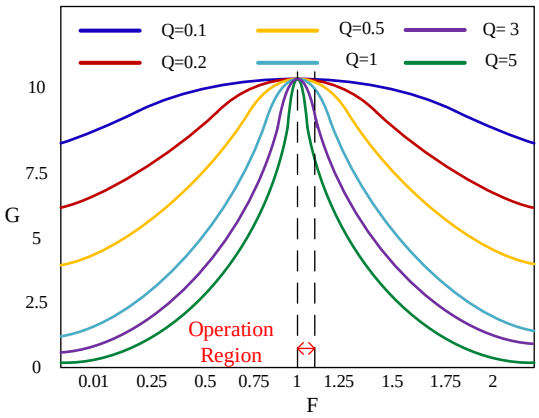

(c) Phase-shift= 0 degree.

Fig. 5. Normalized gain-frequency characteristics of the proposed converter for different quality factors (Q) in (a) Phase-shift=180° (b) Phase-shift=90° (c) Phase-shift=0°.

V. Converter Design Procedure

The design of the proposed converter, specifically tailored for EV charging applications, prioritizes minimizing volume and weight. Typically, the input inductor (L_{in}) in such converters is large and cumbersome. To mitigate this issue, a 20% allowable voltage variation in the output of Section A (as depicted in Fig. 1) is considered. This variation is then corrected by the

- individual capacitor value

must be calculated accordingly.

The design procedure for the converter is visually summarized in Fig. 6.

C. Design of the Circular Current Clamp:

To ensure accurate and efficient power transfer, the design of the circular current clamp must follow these steps:

1. *Define Primary and Secondary Parameters:*
   - The current flowing through the MV power lines is sinusoidal at 50 Hz. Define the power line voltage and its maximum current (I_p). Determine the voltage required at the secondary side (V_s) to meet the charger's specifications.
2. *Selection of Ferrite Core:*
   - Choose a ferrite core suitable for the application. Based on the EV's size and weight limitations, define the core's physical parameters, including the length of the magnetic path (lll) and the cross-sectional area (A) in meters.
3. *Calculation of Number of Turns:*
   - Using Equation (23), calculate the number of turns required for the core, where μ is the permeability of the core material, and $\omega=2\pi f$ is the angular frequency of the grid voltage.

This structured approach ensures the proposed converter meets the stringent requirements for EV charging applications, including compactness, high efficiency, and compatibility with MV power lines.

feedback control loop in Section B. By accepting this voltage fluctuation, the size and volume of L_{in}can be significantly reduced. The design procedure is outlined in the following steps:

A. Design of Section A:

- *Input Inductor (L_{in}) and Link Capacitor (C_{link}):* Calculate the values of L_{in} and C_{link} using Equations (21) and (22). The duty cycle (D) of the semi-active rectifier can be derived using Equation (20). These components are selected to balance efficiency, size, and weight.

B. Design of Section B:

- *Equivalent Load Resistance (R_{eq}):* Determine R_{eq} using Equation (18). Based on the Gain-Frequency-Phase Shift characteristics, select a suitable curve that meets the desired design requirements, including voltage gain and the preferred range of switching frequencies.
- *Quality Factor (Q) and Resonant Frequency:* Identify the quality factor (Q) and the corresponding exact switching frequency from the chosen curve on the Gain-Frequency-Phase Shift characteristics.
- *Resonant Capacitors (C_r) and Inductor (L_r):* Determine C_r and L_r using Equations (17) and (18) as a system of two equations with two unknowns. Note that C_r represents the total capacitance for the two series capacitors, and each

$$L_{in} \leq \frac{D(1-D)V_{out}}{2\, f_s I_{L_r}} \tag{21}$$

$$C_{link} \leq \frac{D\, I_{out\_max}}{0.2\, f_s V_{out}} \tag{22}$$

$$N = \frac{V_s\, l}{\omega\, \mu\, A\, I_p} = \sqrt{\frac{\omega\, \mu\, A\, I_p^2}{P_s\, l}} \tag{23}$$

VI. Experimental Results

To validate the performance of the proposed charger, an experimental prototype was developed to charge 1 to 6 cell Li-Polymer (Li-Pol) batteries, with a power range of 2.5–220 W. For the prototype system, a current clamp, similar to the design depicted in Fig. 7(b), was used to feed the converter. In an industrialized version, the current clamp will be redesigned for a more compact structure and integrated into the converter's control system. The specifications of the prototype converter are listed in Table 2, and the prototype is shown in Fig. 7(a), with its input sourced from the AC current clamp.

The performance of the charger was evaluated under two worst-case scenarios: (i) lowest output power at the highest input voltage and (ii) highest output power at the lowest input voltage. The experimental results for Section B under these conditions are presented in Fig. 8, while Figs. 9 and 10 show the results for Section A. The efficiency curve of the charger is illustrated in Fig. 11.

In both test cases, Section B of the converter operates close to its resonant frequency, ensuring high efficiency. Section A, operating in a broader voltage range, provides the suitable output voltage, though with a notable ripple on C_{link}. Section B then smooths this ripple, providing a stable, regulated output voltage and electrical isolation for the batteries. The proximity to the resonant frequency minimizes noise and enhances efficiency, resulting in similar operational waveforms for both worst-case conditions.

The experimental results demonstrate that the proposed charger meets the stringent requirements of Li-Pol battery charging for EV applications. The charger exhibits robust performance in terms of voltage regulation, power transfer efficiency, and other key metrics, confirming its suitability for EV charging applications. To further emphasize the advantages of the proposed design, a comparison with conventional converters is provided in Table 3, highlighting the superior features and efficiency of the proposed charger.

The charger supports both connected and wireless charging modes, offering flexibility in various operational scenarios.

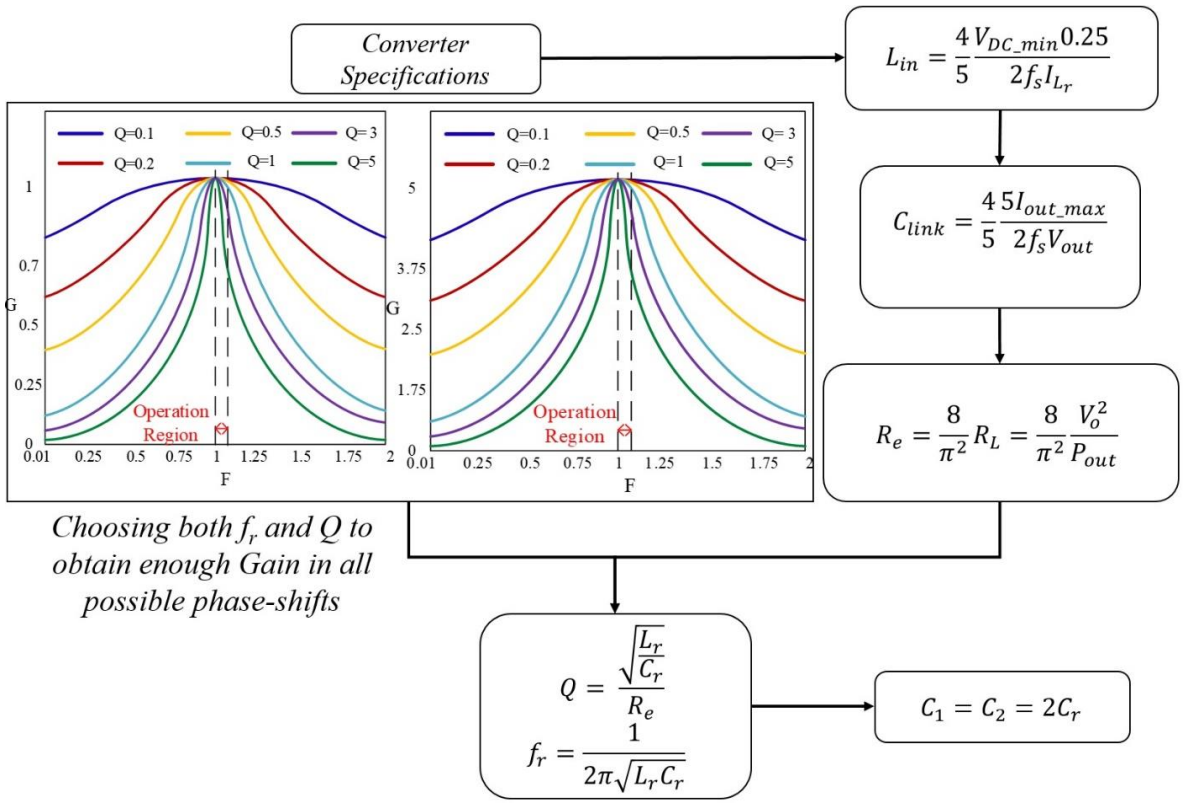

Fig. 6. Design procedure of the proposed converter.

A. *Connected Charging Mode:* In this mode, the process begins by opening the current clamp. Upon engagement with the power line, the clamp induces power that is subsequently transferred to the EV's batteries via the integrated DC-DC converter system this ensures efficient power transfer, effectively charging the batteries and optimizing their performance and lifespan.

B. *Wireless Charging Mode:* In this mode, the current clamp remains closed as the EV flies over the power lines. The innovative design of the clamp allows the current field generated by the power lines to pass through, inducing power within the clamp. The sophisticated converter system then adjusts the output voltage as necessary, ensuring optimal charging conditions tailored to the EV's battery specifications.

The seamless transition between connected and wireless charging modes enhances the charger's adaptability to diverse charging scenarios, maximizing its efficiency and utility. By incorporating dual-mode functionality, the proposed charger offers unparalleled flexibility, whether in connected mode (where power is harnessed directly from the grid) or in wireless mode (where power is induced as the EV flies over power lines). This innovative approach streamlines the charging process and significantly enhances overall operational efficiency and productivity.

VII. Conclusion

This paper presents a novel high-efficiency charger designed specifically to address the limitations of conventional EV charging systems. The proposed charger stands out due to several critical features tailored to the unique requirements of EV applications. EVs, which are characterized by limited payload capacities, require lightweight charging systems to avoid compromising their operational performance. To achieve a compact design, the traditional transformer-based structure has been eliminated, significantly reducing the size

and weight of the converter. Despite the exclusion of the transformer, which typically provides isolation and voltage ratio control, the proposed converter effectively overcomes these challenges through a strategic combination of design elements.

First, isolation is ensured by incorporating two capacitors within the converter's resonant structure, providing the necessary electrical separation between the input and output. Second, the adoption of a semi-active rectifier at the input stage allows for precise AC voltage regulation and enables the desired voltage ratio control, compensating for the lack of a traditional transformer. Moreover, the converter is designed with a minimized input inductor and link capacitor to achieve a lightweight and compact configuration. Although this introduces voltage ripple at the output, a cascade control approach—comprising an outer Phase-Shift Modulation (PSM) loop for the semi-active rectifier and an inner, faster Pulse-Frequency Modulation (PFM) loop for the resonant converter—ensures a well-regulated output voltage suitable for battery charging.

Another key advantage of the proposed converter is its ability to operate with high efficiency over a wide range of input and output voltages. By using the semi-active rectifier as the primary voltage provider, the resonant section of the converter can function near its resonant frequency, resulting in several benefits. This design approach not only maximizes efficiency—critical for portable chargers where energy loss can significantly impact performance—but also minimizes thermal losses that could otherwise lead to overheating and adversely affect the EV's operation. Moreover, operating near the resonant frequency reduces electromagnetic interference, ensuring stable and reliable performance under varying load conditions.

In summary, the proposed charger offers a unique combination of features, including a lightweight and compact structure, a broad input and output voltage range, high efficiency, and low noise operation, making it a versatile and robust solution for portable EV charging applications.

The current clamp used in conjunction with the converter allows the charger to connect directly to power lines, facilitating in-operation charging of Li-Pol batteries. The charger's innovative design also supports wireless charging by flying over MV power lines, where the current clamp induces power to charge the batteries during operation, thereby extending the EV's operational range. The charging process utilizes a circular split-core current clamp to extract power from the lines, with the induced AC voltage directed to the transformer-less semi-active resonant converter for efficient power transfer. The converter is capable of charging 1-6 cell Li-Pol batteries, demonstrating its versatility and adaptability for various EV battery configurations.

Experimental results validate the performance of the proposed converter, with the prototype system achieving a peak efficiency of 94% while charging batteries ranging from 2.5 W to 220 W. These results confirm the charger's high efficiency and suitability for both connected and wireless charging modes, underscoring its potential for broad application in EV missions requiring extended operation durations. With its compact design, high efficiency, and flexible charging capabilities, the proposed charger represents a significant advancement in EV power systems, addressing the limitations of existing solutions and setting a new benchmark for portable EV charging technology.

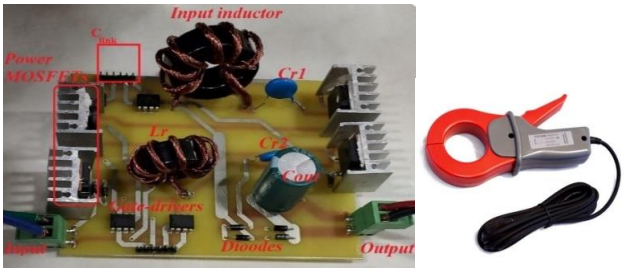

(a) (b)

Fig. 7. (a) Prototype converter, (b) current clamp, to be connected to power lines, the output of the current clamp is connected to the converter.

TABLE 2 THE PROTOTYPE CONVERTER SPECIFICATIONS

Parameter	Value
L_{in}	80 µH
L_r	10 µH
C_{r1}, C_{r2}	60 nF
C_{link}	1 mF
C_o	100 µF
Switching Frequency	290-310 kHz
CT Model	Current Clamp Adapter AC, 52 mm, 1000 A
Phase Shift	0-179 degree
Semi-Active Rectifier Switching Frequency	300 kHz
Output Voltage	Each cell maximum voltage according to Table I
Input Voltage	MV power line
Diode	MUR840
Switch	23N60E
Gate-Drive	TC4427

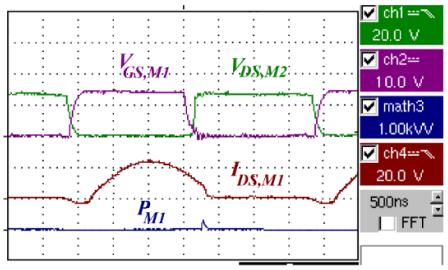

Fig. 8. M_1 and M_2 gate-source voltages, M_1 drain-source current, and M_1 power-loss experimental waveforms, respectively.

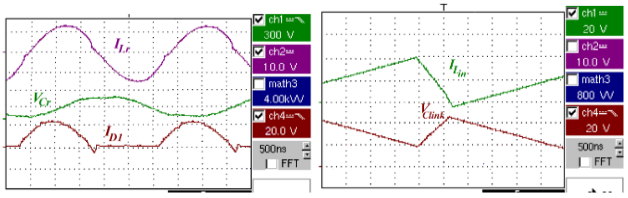

(a) (b)

Fig. 9. (a) Resonant inductor current, resonant capacitor voltage, and D_1 current waveforms and (b) input inductor current and C_{link} voltage in highest input voltage and lowest output power.

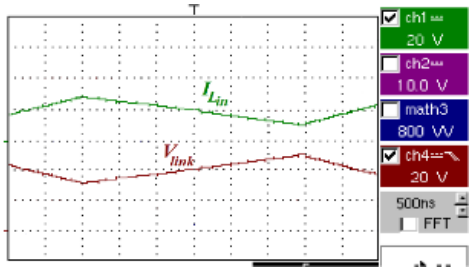

Fig. 10. Input inductor current and C_{link} voltage in lowest input voltage and highest output power.

TABLE 3 COMPARISON OF THE PROPOSED CONVERTER WITH SOME CONVENTIONAL CONVERTERS

	Reference	Input Voltage (V)	Output Voltage (V)	Output Power (W)	Peak-Efficiency (%)	Switching Frequency (kHz)	C_{bus} (µF)	L_{in} (µH)	L_r (µH)	C_r (nF)	Input/output Isolation Method	L_m (µH)	Converter and its control complexity	Number of Components
AC / DC	[34]	230 ac	400	2650	92.7	NM⸸	NO†	100 ×1000	206× 1000	NO	NO	NO	Medium	Medium
	[33]	160-220 ac	48	450	94.5	20	C_f= 0.47	L_f = 2300	NO	NO	NO	L_2= 40	Low	Medium
	[32]	160-260 ac	24 - 72	650	94	20	C_1= 0.47	L_i= 3500	NO	NO	TR*	NM	Low	Medium
	[31]	40-80 RMS	15-48	400	92	100	Cbus	NM	0.44	4.7	TR	NM	Low	Medium
PFC	[38]	85-265 ac	48	300	93	NM	120	NM	177	13	TR	NM	Low	Medium
	[39]	100-130 ac	48	350	92	140	400	2×110	70	16.4	TR	120	Low	Medium
	[40]	277-380 RMS ac	50	100	91	NM	440	NM	58	47	TR	275	High	High
	[29]	370-410	48	650	96	150-450	NM	NM	2×8	35	TR	105	Medium	Medium
WPT	[41]	200	200	1	90	~250	NO	NO	16.2	25	CWPT	81× 1000	Low	Low
	[42]	360-400	12	750	97	NM	NO	NO	19	64	IWPT	64	Medium	Low
	[43]	25-100	210	250	98	80-140	NO	NO	48	15 &5	IWPT	15.8 &5.4 9	Medium	Low
	[44]	390	60-450	NM	97	140	NO	NO	12.8	354	IWPT	354	Medium	Low
	[13]	24	15	30<	74	1000	NO	100	NO	100	IWPT	37	Low	Low
Proposed Converter		20 kV	4.2-25.2	220	94	290-310 kHz	1000	80	10	2×60	IWPT	NO	Medium	Medium

*** TR = Transformer**

† NO = There is no component in the structure

⸸NM = Not Mentioned

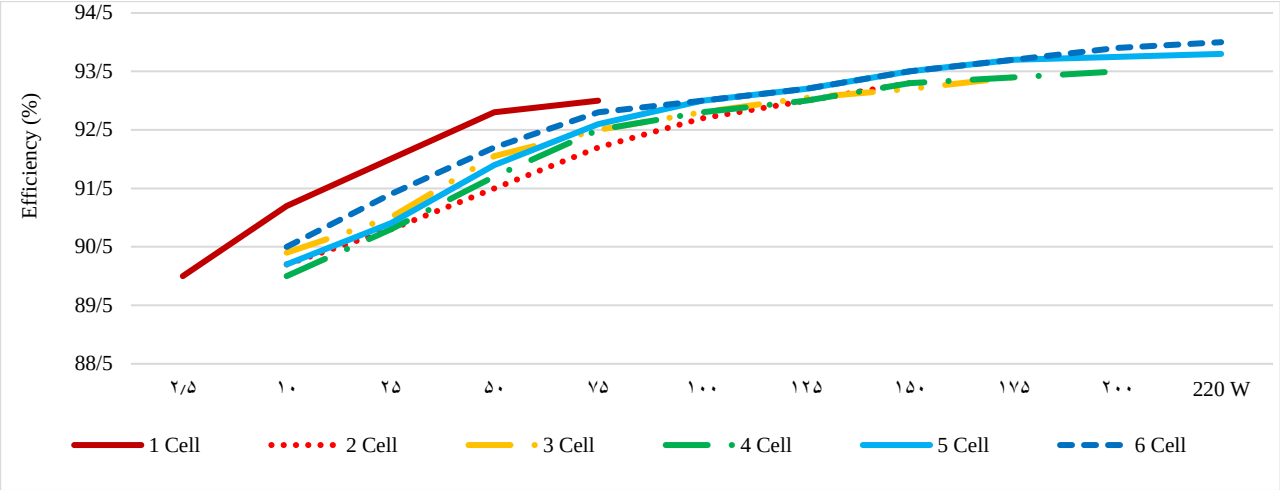

Fig. 11. Efficiency curves of the proposed converter for different types of batteries.

References

[1] J. Shahmoradi, E. Talebi, P. Roghanchi, and M. Hassanalian, "A comprehensive review of applications of EV technology in the mining industry," *EVs*, vol. 4, no. 3, p. 34, 2020.

[2] J. Shahsevani and R. Beiranvand, "An Application-Oriented Review of the LLC-Based Resonant Converters," *IEEE Access*, 2024.

[3] A. Muharam, T. M. Mostafa, and R. Hattori, "Design of power receiving side in wireless charging system for UAV application," in *2017 International Conference on Sustainable Energy Engineering and Application (ICSEEA)*, 2017: IEEE, pp. 133-139.

[4] D. Vincent, P. S. Huynh, L. Patnaik, and S. S. Williamson, "Prospects of capacitive wireless power transfer (C-WPT) for unmanned aerial vehicles," in *2018 IEEE PELS Workshop on Emerging Technologies: Wireless Power Transfer (Wow)*, 2018: IEEE, pp. 1-5.

[5] K. I. Kilic and L. Mostarda, "Heuristic EV pathfinding over optimized charging station grid," *IEEE Access*, vol. 9, pp. 164070-164089, 2021.

[6] H. Huang and A. V. Savkin, "Deployment of charging stations for EV delivery assisted by public transportation vehicles," *IEEE Transactions on Intelligent Transportation Systems*, 2021.

[7] C. H. Choi, H. J. Jang, S. G. Lim, H. C. Lim, S. H. Cho, and I. Gaponov, "Automatic wireless EV charging station creating essential environment for continuous EV operation," in *2016 International Conference on Control, Automation and Information Sciences (ICCAIS)*, 2016: IEEE, pp. 132-136.

[8] T. Campi, S. Cruciani, M. Feliziani, and F. Maradei, "High efficiency and lightweight wireless charging system for EV batteries," in *2017 AEIT International Annual Conference*, 2017: IEEE, pp. 1-6.

[9] J. Chen, C. W. Yu, and W. Ouyang, "Efficient wireless charging pad deployment in wireless rechargeable sensor networks," *IEEE Access*, vol. 8, pp. 39056-39077, 2020.

[10] A. M. Jawad, H. M. Jawad, R. Nordin, S. K. Gharghan, N. F. Abdullah, and M. J. Abu-Alshaeer, "Wireless power transfer with magnetic resonator coupling and sleep/active strategy for a EV charging station in smart agriculture," *IEEE Access*, vol. 7, pp. 139839-139851, 2019.

[11] T. Campi, S. Cruciani, F. Maradei, and M. Feliziani, "Innovative design of EV landing gear used as a receiving coil in wireless charging application," *Energies*, vol. 12, no. 18, p. 3483, 2019.

[12] A. Rohan, M. Rabah, M. Talha, and S.-H. Kim, "Development of intelligent EV battery charging system based on wireless power transmission using hill climbing algorithm," *Applied System Innovation*, vol. 1, no. 4, p. 44, 2018.

[13] A. M. Jawad *et al.*, "Wireless EV charging station using class-E power amplifier in vertical alignment and lateral misalignment conditions," *Energies*, vol. 15, no. 4, p. 1298, 2022.

[14] A. Carloni, F. Baronti, R. Di Rienzo, R. Roncella, and R. Saletti, "On the Sizing of the DC-Link Capacitor to Increase the Power Transfer in a Series-Series Inductive Resonant Wireless Charging Station," *Energies*, vol. 14, no. 3, p. 743, 2021.

[15] A. Rohan, M. Rabah, F. Asghar, M. Talha, and S.-H. Kim, "Advanced EV battery charging system," *Journal of Electrical Engineering & Technology*, vol. 14, no. 3, pp. 1395-1405, 2019.

[16] J. Zhou, B. Zhang, W. Xiao, D. Qiu, and Y. Chen, "Nonlinear parity-time-symmetric model for constant efficiency wireless power transfer: Application to a EV-in-operation wireless charging platform," *Ieee transactions on industrial electronics*, vol. 66, no. 5, pp. 4097-4107, 2018.

[17] D. Raveendhra, M. Mahdi, R. Hakim, R. Dhaouadi, S. Mukhopadhyay, and N. Qaddoumi, "Wireless charging of an autonomous EV," in *2020 6th International Conference on Electric Power and Energy Conversion Systems (EPECS)*, 2020: IEEE, pp. 7-12.

[18] K. Sang-Won, C. In-Kui, and H. Sung-Yong, "Comparison of charging region differences according to receiver structure in EV wireless charging system," in *2017 International Conference on Information and Communication Technology Convergence (ICTC)*, 2017: IEEE, pp. 1058-1060.

[19] S. W. Kim, I. K. Cho, and S. Y. Hong, "Design of transmitting coil for wireless charging system to expand charging area for EV applications," *Microwave and Optical*

Technology Letters, vol. 60, no. 5, pp. 1179-1183, 2018.

[20] C. Cai, J. Wang, H. Nie, P. Zhang, Z. Lin, and Y.-G. Zhou, "Effective-configuration WPT systems for EVs charging area extension featuring quasi-uniform magnetic coupling," *IEEE Transactions on Transportation Electrification*, vol. 6, no. 3, pp. 920-934, 2020.

[21] A. Raciti, S. A. Rizzo, and G. Susinni, "EV charging stations over the buildings based on a wireless power transfer system," in *2018 IEEE/IAS 54th Industrial and Commercial Power Systems Technical Conference (I&CPS)*, 2018: IEEE, pp. 1-6.

[22] R. Wu, S. B. Dewan, and G. R. Slemon, "A PWM AC-to-DC converter with fixed switching frequency," *IEEE Transactions on Industry Applications*, vol. 26, no. 5, pp. 880-885, 1990.

[23] P. N. Enjeti and S. A. Choudhury, "A new control strategy to improve the performance of a PWM AC to DC converter under unbalanced operating conditions," *IEEE Transactions on Power Electronics*, vol. 8, no. 4, pp. 493-500, 1993.

[24] S. Cuk, "A new zero-ripple switching DC-to-DC converter and integrated magnetics," *IEEE Transactions on Magnetics*, vol. 19, no. 2, pp. 57-75, 1983.

[25] B. Arnet and L. P. Haines, "High power DC-to-DC converter for supercapacitors," in *IEMDC 2001. IEEE International Electric Machines and Drives Conference (Cat. No. 01EX485)*, 2001: IEEE, pp. 985-990.

[26] S. Kim and F.-S. Kang, "Multifunctional onboard battery charger for plug-in electric vehicles," *IEEE Transactions on Industrial Electronics*, vol. 62, no. 6, pp. 3460-3472, 2014.

[27] F. Musavi, M. Craciun, D. S. Gautam, W. Eberle, and W. G. Dunford, "An LLC resonant DC–DC converter for wide output voltage range battery charging applications," *IEEE Transactions on Power Electronics*, vol. 28, no. 12, pp. 5437-5445, 2013.

[28] N. Bagheri, H. Alipour, L. Mohammadian, J. Beiza, and M. Ebadpour, "A Multiport isolated resonant LLC converter for grid-tied renewable energy powered bidirectional EV charger," *International Journal of Industrial Electronics Control and Optimization*, vol. 6, no. 1, pp. 37-48, 2023.

[29] E. L. Carvalho, A. Blinov, P. Emiliani, A. Chub, and D. Vinnikov, "Three-phase bidirectional isolated AC–DC matrix-converter with full soft-switching range," *IEEE Access*, vol. 11, pp. 119270-119283, 2023.

[30] I. Burgardt, C. B. Nascimento, A. A. Badin, and R. Gules, "An Integrated AC-DC Isolated Converter Electrolytic-Free with Intrinsic Active Low-Frequency Ripple Reduction," *IEEE Access*, 2024.

[31] Y. Y. Zandabad and S. S. Fazel, "A single-stage variable output AC-DC converter with PFC and soft-switching for renewable energy integration," *Energy Reports*, vol. 11, pp. 4873-4885, 2024.

[32] A. Singh, J. Gupta, and B. Singh, "Design and control of two stage battery charger for low voltage electric vehicles using high gain buck-boost PFC AC-DC converter," *IEEE Transactions on Industry Applications*, vol. 59, no. 5, pp. 6125-6135, 2023.

[33] A. D. Kumar, J. Gupta, and B. Singh, "A single-stage charger for lev based on quadratic buck-boost AC-DC converter topology," *IEEE Transactions on Industry Applications*, vol. 59, no. 4, pp. 4252-4263, 2023.

[34] V. Ramya and R. Marimuthu, "Integration of AC/DC With Multi Input Mode Selection Converter for Fast Charging of Battery in Electric Vehicles," *IEEE Access*, 2024.

[35] J. Shahsevani and R. Beiranvand, "A Bidirectional Resonant Converter for Capacitive Power Transmission in Electric Vehicle and PowerWall Applications," in *2023 31st International Conference on Electrical Engineering (ICEE)*, 2023: IEEE, pp. 264-270.

[36] V. Suel and S. Kizir, "A Comprehensive Loss Analysis of Half-Bridge LLC Resonant Converter used in LED Street Lights," in *2019 1st Global Power, Energy and Communication Conference (GPECOM)*, 2019: IEEE, pp. 146-151.

[37] C.-H. Yang, T.-J. Liang, K.-H. Chen, J.-S. Li, and J.-S. Lee, "Loss analysis of half-bridge LLC resonant converter," in *2013 1st International Future Energy Electronics Conference (IFEEC)*, 2013: IEEE, pp. 155-160.

[38] J. Yi, H. Ma, X. Li, S. Lu, and J. Xu, "A Novel Hybrid PFM/IAPWM Control Strategy and Optimal Design for Single-Stage Interleaved Boost-LLC AC–DC Converter With Quasi-Constant Bus Voltage," *IEEE Transactions on Industrial Electronics*, vol. 68, no. 9, pp. 8116-8127, 2020.

[39] R. Saasaa, W. Eberle, and M. Agamy, "A single-stage interleaved LLC PFC converter," in *2016 IEEE Energy Conversion Congress and Exposition (ECCE)*, 2016: IEEE, pp. 1-6.

[40] Z. Lu and L. Wei-Ming, "A Single-Stage LED Driver Using Step-Down Cuk/LLC with APWM-PFM Hybird Control," in *2018 15th China International Forum on Solid State Lighting: International Forum on Wide Bandgap Semiconductors China (SSLChina: IFWS)*, 2018: IEEE, pp. 1-4.

[41] D. Rozario, N. A. Azeez, and S. S. Williamson, "A modified resonant converter for wireless capacitive power transfer systems used in battery charging applications," 2016, Art no. 7520272, doi: 10.1109/ITEC.2016.7520272.

[42] E. Rong, S. Li, R. Zhang, X. Du, Q. Min, and S. Lu, "A magnetic integration half-turn planar transformer for LLC resonant DC-DC converters," in *2018 IEEE Applied Power Electronics Conference and Exposition (APEC)*, 2018: IEEE, pp. 484-488.

[43] H. Hu, X. Fang, F. Chen, Z. J. Shen, and I. Batarseh, "A modified high-efficiency LLC converter with two transformers for wide input-voltage range applications," *IEEE Transactions on Power Electronics*, vol. 28, no. 4, pp. 1946-1960, 2013, doi: 10.1109/TPEL.2012.2201959.

[44] D. Shu and H. Wang, "An Ultrawide Output Range ${LLC} $ Resonant Converter Based on Adjustable Turns Ratio Transformer and Reconfigurable Bridge," *IEEE Transactions on Industrial Electronics*, vol. 68, no. 8, pp. 7115-7124, 2020.

Jasem Shahsevani received his M.Sc. degree in power electronics engineering from Tarbiat Modares University, Tehran, Iran, in 2021. His current research interests include DC/DC converter, LLC-based resonant converter, wireless power transfer, electric vehicle charging, soft-switching techniques, and PV-based renewable energy systems.

Reza Beiranvand (Senior Member, IEEE) received the MSc and PhD degrees in electrical engineering from Sharif University of Technology, Tehran, Iran, in 1999 and 2010, respectively. From 2010 to 2012, he was a Postdoctoral research fellow with the Electrical Engineering College, Sharif University of Technology. From 1999 to 2007, he was an engineer at the R&D centers of PARS-Electric and RADIO SHAHAB MFGs, Tehran, Iran, where he was engaged in designing the LCD, and LED TVs based on the ST, LT, NXP, and Fairchild devices.

He is currently Head of the Power Electrical Engineering Department and Associate Professor with the Faculty of Electrical and Computer Engineering, Tarbiat Modares University, Tehran, Iran. His research interests include power electronics converters, soft switching techniques, SCCs, SMPS, Capacitive-Coupling Power Transfer and Inductive Power Transfer techniques, and PV-based renewable energy systems. Dr. Beiranvand was the IEEE Consultant (2017-2019) and Head of the Power Electrical Engineering Department (2018-2020) with the Tarbiat Modares University. He is between the top 2 % scientists of the world, based on the Stanford University; Stanford, CA, USA released lists, 2020-2024

International Journal Of
Industrial Electronics Control and Optimization
Print ISSN: 3517-2645
Online ISSN: 3568-2645
Homepage: https://ieco.usb.ac.ir/

Frequency Response Analysis: An Overview of the Measurement Process and Interpretation of Results for Fault Diagnosis and Location in Power Transformers

Hamed Shadfar[1] , Hamid Reza Izadfar[1]

[1] Department of Electrical and Computer Engineering, Semnan university, Semnan, Iran
Corresponding author's email: hrizadfar@semnan.ac.ir

Article Info

Article type:
Research Article
Article history:
Received: 05-August-2024
Received in revised form: 19-October-2024
Accepted: 15- November-2024
Published online: 22-June-2025

Keywords:
Frequency response analysis,
Insulation faults,
Non-destructive method,
Power transformer.

ABSTRACT

One of the main components of a power transformer is the transformer insulation system, namely, transformer insulation oil and transformer insulation paper. Any failure can cause the transformer to fail temporarily or permanently. As a result, regular and non-destructive monitoring of transformers is of particular importance for early detection and prediction of any faults. Frequency response analysis (FRA) is known as a high-accuracy, fast, economical, and non-destructive method for diagnosing the condition of a transformer, which can be used independently or as a complementary method to ensure the results of other diagnostic tests and based on the operational conditions of the transformer, it can be implemented in two methods, online and offline. This paper provides an in-depth discussion of measuring and interpreting FRA results and the ability of this method to detect and locate power transformer faults, especially insulation faults, which have been given less attention in the past .The information confirmed in this survey is expected to provide an important roadmap for future research in monitoring the condition of transformer insulation systems.

I. Introduction

A. Research Motivation

The transformer is a vital and key equipment in the power grid. Its proper operation affects the safe operation of the whole electrical network. This equipment is often exposed to different weather conditions, as well as different electrical and mechanical conditions, and it faces different electrical, electromagnetic, dielectric, mechanical, thermal, or chemical stresses during operation [1-3]. The most common failures that happen to transformers are as short circuits (SC), Axial displacement (AD), radial deformation (RD), coil displacement, disc-space variation (DSV), open circuit (OC), core defect, lightning, etc. Regular and non-destructive monitoring of transformers to detect any changes or faults in the early stages is particularly important for detecting such failures [4-10]. For this purpose, various modern and practical methods including partial discharge (PD), polarization index (PI), polarization and depolarization current (PDC), dissolved gas analysis (DGA), insulation resistance (IR), recovery voltage measurement (RVM), leakage reactance, along with FRA for evaluating the condition of transformers have been presented [11-12]. In the FRA, the amplitude of the applied signal is small. This method is suitable for detecting or locating mechanical faults such as displacement or deformation of windings. On the other hand, it is not able to detect insulation faults between discs or oil and paper faults. Usually, along with this test, other analysis methods such as partial discharge and switching are used. These tests as a supplement to FRA can complete the evaluation results

B. Literature Review

A transfer function (TF) is a tool to explain the behavior of a system. This method is widely used to identify the mechanical integrity of transformers [13-16]. The TF method can be used in the time domain (TD) or the frequency domain (FD). In the FD, it is called FRA. The FRA was first introduced by Dick and Erven in 1978 [17]. All over the world, among other diagnostic methods, FRA is known as a high-precision, fast, economical, and non-destructive method in transformer condition detection [18-28]. FRA can be used as an independent method or as a complementary method to ensure the results of other diagnostic tests [29-33]. The FRA is based on measuring the frequency response (FR) of the transformer in exchange for a wide frequency bandwidth [29]. Because of the winding resistance (R), the inductance of the winding coils (L), and the capacitance (C) of the insulation layers between the coils, windings, winding and core, core and tank, tank and winding, etc., a transformer is modeled a complex network of RLC components. Any change in the condition of the transformer will cause a change in the parameters of this RLC network. The failures, such as SC or OC in the winding, affect the resistance and inductance. AD and RD,

lead to changes in the capacitance or inductance of the RLC network. Therefore, comparing the actual FR with the reference FR when the transformer has no problem can show the changes in the characteristics of transformers and lead to fault diagnosis. The reference FR is called the "signature" or "fingerprint". Therefore, the FRA method is used to identify these small changes in the parameters of the RLC network by examining the FR of the transformer. Based on the operating conditions of the transformer, FRA can be divided into two methods: 1. Offline FRA 2. Online FRA [34-36].

In a steady state, transformers are modeled with a simple model of primary, secondary, and magnetization impedances. But in a transient state, we need a model that provides an accurate response in different conditions. Among the different methods of transformer modeling, the black box model (BBM), a physical model including a multiphase transmission line, detailed and hybrid have been more attention of researchers. The BBM is obtained using the measured results at the transformer terminals. For such modeling, the zero and pole dependence of the system and the structure of the transformer must be known. Physical models are obtained based on the structure and size of the transformer, The physical model is already constrained and valid for a certain frequency range. To increase their frequency range, the details of the model should be increased [28]. Since the frequency analysis method is based on changes in the physical structure and insulation of the transformer, the detailed model is the most suitable model for FRA. In the detailed model, an RLC circuit model is considered for each section of the transformer, so that all the physical and electrical characteristics of that section are included in the model [37-38]. It should be noted that each section can include a turn or a disc of windings. Fig.1 shows the physical structure of the transformer disc winding and how to model each section. As shown in Fig. 1, R and L are respectively the resistance and inductance of each section of the winding, and Rs and Cs model the insulation effect of each section, where Rs is a large value. Rg and Cg are the insulation resistance of each section to ground and the stray capacitance between each section to ground, respectively [39]. In addition, the transformer bushing is modeled using the model shown in Fig. 2.

The equivalent circuit shown in Fig. 3 can be used to model the high-frequency transformer. The elements shown in the equivalent circuit are as follows:

L: inductance of each winding section
M_{ik}: mutual inductance between two windings i and k
RS: ohmic resistance of each winding section
RP: insulation resistance of each section to ground or adjacent windings
Ce: Capacitance of each section to ground (core or tank)
Ki: Equivalent capacitance of each section
CW: Capacitance between two windings

C. Necessity of the research and Novelty

This paper is an in-depth discussion of measuring and interpreting FRA results and the ability of this method to detect and locate power transformer faults, especially insulation faults, which have been given less attention in the past. The information confirmed in this survey is expected to provide an important roadmap for future research in monitoring the condition of transformer insulation systems

D. organization of the paper

This paper aims to peruse the FRA method as an accurate and complementary method for diagnosing and locating transformer insulation faults. For this purpose, the rest of the paper is as follows: Section 2 introduces offline FRA, section 3, the types of FRA configuration, and Section 4, deals with the evaluation of FRA results. Also, in section 5, the FRA frequency range, in section 6, the online FRA, and section 7 deals with FRA results interpretation methods, section 8 deals with fault location based on FRA and finally, in section 9, the conclusions are drawn.

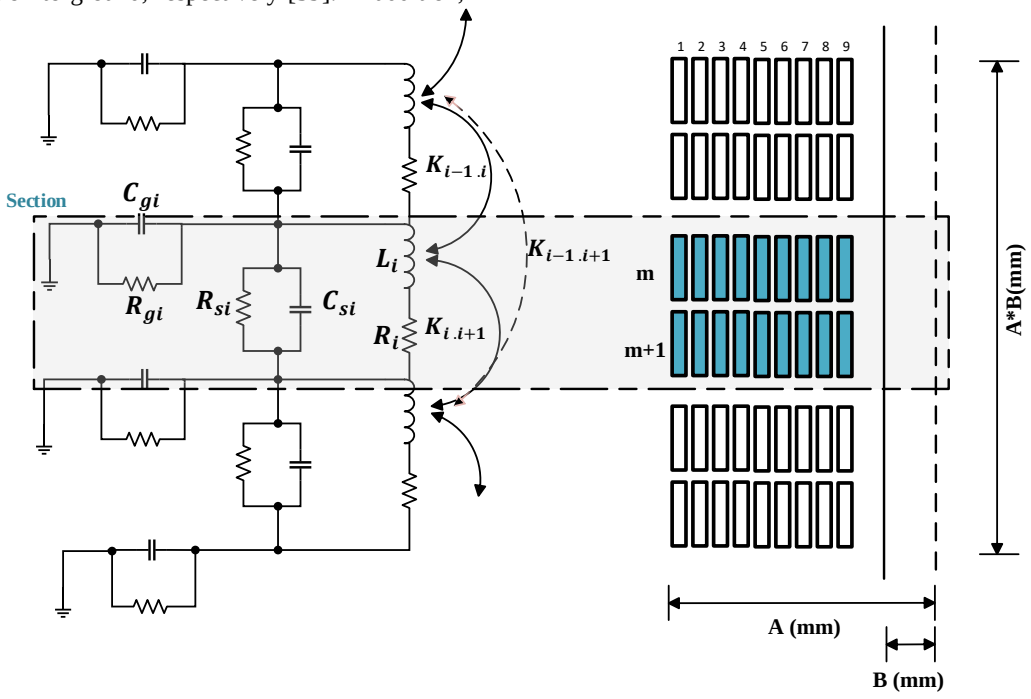

Fig. 1. Detailed model of transformer disc winding [37]

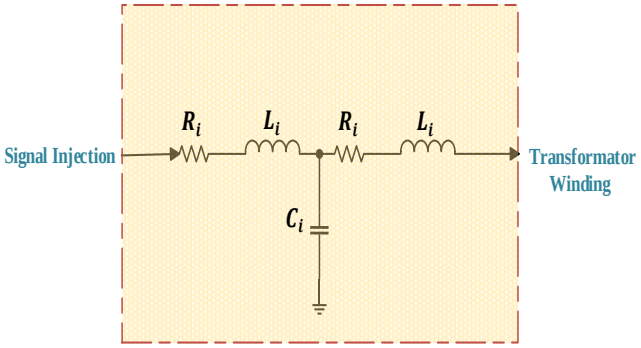

Fig. 2. Bushing model [38]

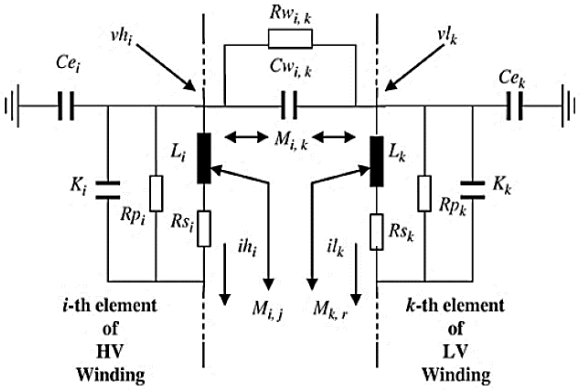

Fig. 3. Detailed equivalent circuit of a winding layer and the connection between them [39]

I. Offline FRA

In the offline FRA method, the transformer must be isolated from the power system source and the tank must be grounded. In this method, an input signal is injected into one of the transformer terminals. It can be sweep frequency, impulse, or step voltage signals to ground. The reference signal is measured through the reference impedance (R_{ref}). According to the type of measurement, the response signal is received through the measurement impedance (R_{me}) which is connected to another terminal. This signal is usually a voltage signal, but can also be a current signal, measured at the output terminal or any other grounded terminal. Fig. 4 shows the schematic of connections in an offline FRA. Two available methods to obtain offline FRA data are frequency domain (FD) and time domain (TD) measurements [36].

A. Measurement in the FD

Measurement in the FD is obtained by applying a sinusoidal voltage signal to the winding. The frequency of this signal varies from Hz to MHz. The response signal is measured and the ratio between the injected signal and the response signal is calculated and displayed. The equipment required to perform offline FRA measurement is shown in Fig. 5. The transformer should be directly connected to the impedance analyzer by some meters of wire [40-43].

B. Measurement in the TD

This method consists of injecting a voltage signal in a short time on the winding structure. The response signal is recorded by digital oscilloscopes or transient recorders. The fast Fourier transform (FFT) analysis is applied to the recorded data. The FFT of signals is divided by the FFT of voltage to obtain the FRA plot [43].

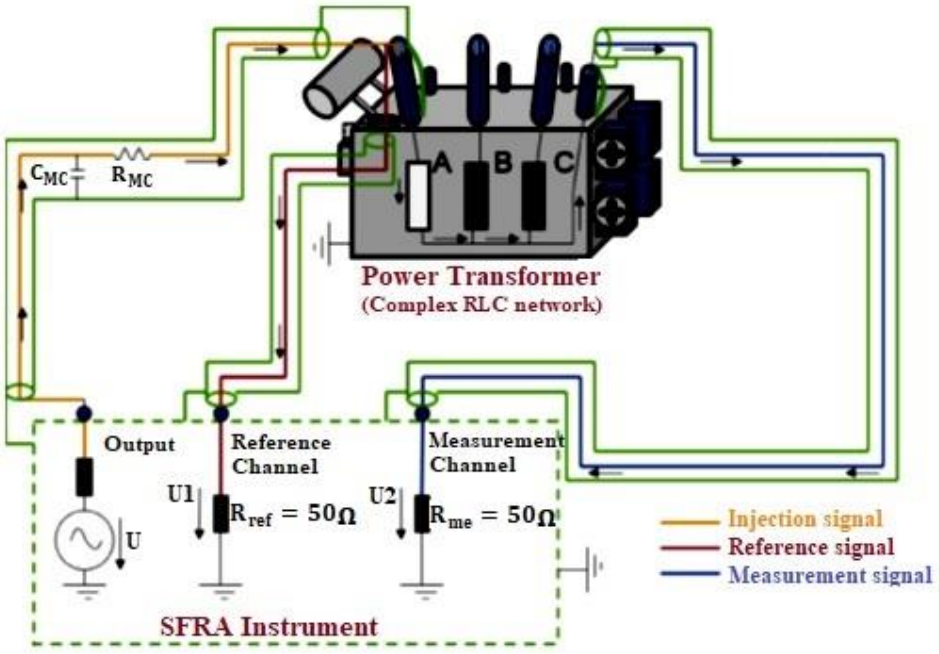

Fig. 4. Connections of offline FRA [36]

Fig. 5. Measuring equipment in the FD [40]

The injection voltage signal can be as follows:

- Impulse voltages: This mode includes low voltage impulse waveforms in microsecond duration.
- Switching overvoltage: these waveforms are similar to the voltages that are produced when the line is turned on or off.
- Lightning overvoltage: these waveforms are similar to those that occur during lightning.
- Wide Bandwidth Noise Signal: the signal frequency does not change and before applying the FFT, the FRA is performed. For this reason, the frequency content of the input signal must be wide enough.

The measurement system in the TD should consist of a signal generator to produce the desired injection signal and recording equipment to record data [43].

C. input signal

There are two methods for injecting the wide range of frequencies required. Based on the injected or reference signal, the FRA can be divided into two groups:

- Sweep Frequency Response Analysis (SFRA)
- Impulse Frequency Response Analysis (IFRA)

SFRA advantages:

- The signal-to-noise ratio is high. Network analysts typically use a narrowband filter to remove noise.
- Given that input and output waveforms are available for a wide frequency range, amplitude and phase angle curves are extracted without any additional conversion.
- The number of desired frequency points can control image resolution. If more precise resolution is required, the range can be divided into multiple frequency bands and then measured. The distribution of points can usually be linear or logarithmic [36].
  - the detection of mechanical faults since these faults cause the high-frequency equivalent circuit parameters to change which, could be detected easily using this test [44].

SFRA disadvantages:

- Using the standard network analyser, it is not possible to determine several TFs at the same time.
- The measurement process takes a long time: depending on the number of points and the amount of filtering, it may take several minutes.
- The signal amplitude is low.
- Averaging techniques are very time-consuming.

IFRA advantages:

- several TFs can be measured simultaneously, reducing outages during revision.
- It is very fast compared to SFRA. The measurement process is usually done in one minute (several impulse signals are applied to create an average time series) [44-45].

IFRA disadvantages:

- Frequency resolution is constant. This leads to poor resolution at low frequencies. This may make it difficult to diagnose electrical faults. In addition, the signals are usually filtered with high-pass filters to reduce the problems associated with the FFT function.
- Noise cannot be filtered.
- The power spectrum of the injected signal is frequency-dependent.
- Signals that are slowly damped are not recorded.
- Noise and faults related to digitizers.
- The reference and response signals are converted to the FD using FFT. Therefore, to some extent, accuracy depends on mathematical calculations [45-46].

SFRA and IFRA should have similar results under the same conditions. Recent research shows these methods can also be used in online FRA [47-48].

II. Types of FRA configuration

The FR can be determined as a voltage ratio (VR) between two terminals of a phase or as the input impedance or admittance of a winding. In practice, using the VR is the most common. Of course, some studies have used input impedance or admittance for FRA and the results show that these TFs can detect faults. As shown in Fig. 6, common circuit connections are [36]:

- open-circuit (OC) connection
- short-circuit (SC) connection
- capacitive inter-winding connection
- inductive inter-winding connection

In Fig. 6, V_r is the reference voltage and V_m is the response voltage [36].

A. Open-circuit

In this connection, the reference signal is injected into one of the winding terminals while all the other terminals are OC, the FR is measured at the other winding terminal (Fig.6(a)). This method is used for windings with Y and D connections as well as for single-phase units. It can be used to evaluate the core [36].

B. Short-circuit

The SC connection is also done in a similar as the OC connection, but on the secondary side, the winding in the identical phase is SC (Fig. 6(b)). Short circuit connection is only suitable for evaluating windings [36].

C. Capacitive inter-winding

In this connection, the reference signal is injected into one of the winding terminals and the response signal is obtained from the same phase winding on the secondary side, while the other terminals are OC (Fig. 6(c)).

D. Inductive inter-winding

This connection is done in the same as the capacitive inter-winding, except that the second terminals of the windings under test are grounded (Fig. 6(d)). The response signal in the low and medium frequency range practically represents the transformer ratio and at higher frequencies does not have beneficial data [35, 42, 45].

According to what has been said, the accuracy of FRA depends on the type of configuration and its components. Some studies have investigated the accuracy and ability to detect FRA in different connections and termination resistors [49-55]. The results show that in many cases, the TFs based on the VR have the highest accuracy and the input admittance has the lowest accuracy in FRA measurement [51]. Also, in the diagnosis of mechanical defects, the capacitive inter-winding connection is

the most precise among the four connections mentioned. Furthermore, adjusting the measuring impedance and terminating resistors significantly reduces the noise in the FRA results [52].

III. Evaluation of FRA results

Response data can be evaluated with reference data, directly (visual inspection) or indirectly (after data processing) [39]. As shown in Fig. 7, three common methods for obtaining reference data are as follows:

A. Time-based

In this method, the fingerprint data is obtained from previous FRA test results on a healthy transformer. This data is obtained when we make sure that the transformer does not have any defects or problems (for example, right after the installation of the transformer) [36].

B. Type-based

Another method to collect reference data is to use the FRA test results of similar transformers. These transformers are named twins or sisters and they mainly include distribution transformers [36].

C. Construction-based

Another recommended alternative method is to use the results of the other phases of the power transformers, due to the symmetry in the construction. This method is mainly used for transformers at the transmission level. [35-36, 42, 57].

IV. Frequency range

The FRA response can be classified into three ranges: low frequency, medium frequency and high frequency. The FRA frequency range should be chosen according to the expected fault. It should be noted that for this purpose, factors such as measuring equipment, noise, natural frequencies of the winding, core magnetization, etc., which can affect the test results, must be taken into account [58-60]. The frequency range is divided into bands which are shown in Table 1. In Table 2, the parameters of the transformer model and the mechanical faults affecting them are given. The effects of ±10% changes in various electrical parameters on the amplitude and resonance frequency of the FRA (compared to the FRA signature) are summarized in Table 3. In Table 4, the effect of changing different parameters of the transformer model on FRA is shown [34].

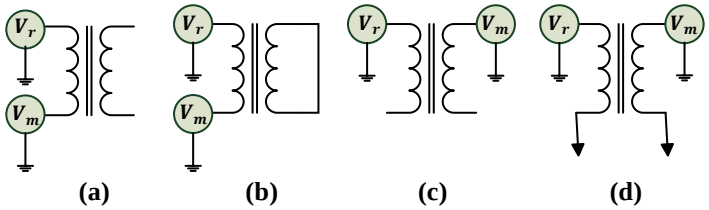

Fig. 6. FRA circuit configurations: a) open-circuit, b) short-circuit, c) capacitive inter-winding, d) inductive inter-winding [36].

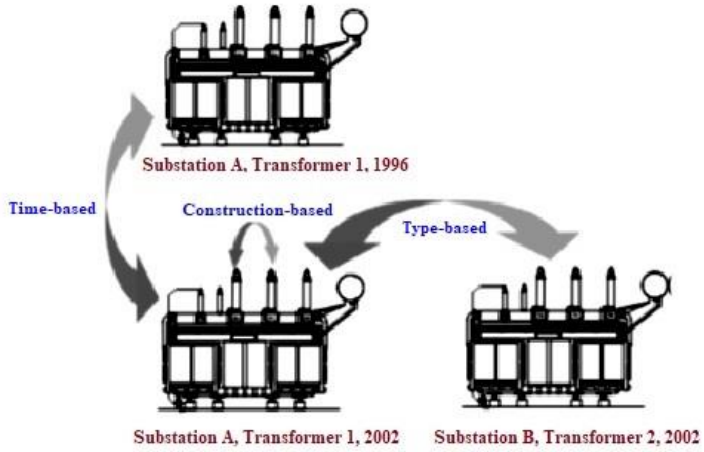

Fig. 7. Types of evaluation in the FRA test

TABLE 1 FREQUENCY BANDS AND THEIR SENSIVITY TO DIFFERENT FAULTS [34]

Fault Sensitivity	**Frequency Band**		
	<20 kHz	20-400 kHz	**>400kHz**
Core deformation, Open circuits, Short turns residual magnetism	Yes	No	**No**
Bulk winding movement, Clamping structure loosing	Yes	No	**No**
Deformation within the main or tap winding	No	Yes	**Yes**
Ground impedance variations	No	No	**Yes**

TABLE 2 CORRELATION BETWEEN MECHANICAL FAULTS AND TRANSFORMER MODEL PARAMETERS [34]

Model Parameter	**Type of Fault**	**Symbol**
Inductance	Disc deformation, Local breakdown, Core deformation and winding short circuit	**L_s**
Shunt capacitance	Disc movement, Buckling due to large mechanical forces, Moisture ingress and loss of clamping pressure	**C_{sh}**
Resistance	Shorted or broken disc, Failure of caulking contacts and tap changer contact wear	**R_s**
Series capacitance	Aging of insulation, Moisture ingress and disc movement	**C_{HL}**

TABLE 3 EFFECT OF CHANGING ELECTRICAL PARAMETERS ON AMPLITUDE AND RESONANCE FREQUENCY [34]

Parameters Variations		Frequency Range		
		<20 kHz	20-400 kHz	**>400kHz**
L_s	10% increase	Magnitude and resonance frequencies decreased	Magnitude and resonance frequencies decreased	**Magnitude and resonance frequencies decreased**
	10% decrease	Magnitude and resonance frequencies increased	Magnitude and resonance frequencies increased	**Magnitude and resonance frequencies increased**
C_{sh}	10% increase	No Impact	No Impact	**Magnitude and resonance frequencies decreased**
	10% decrease	No Impact	No Impact	**Magnitude and resonance frequencies increased**
C_g	10% increase	No Impact	No Impact	**Magnitude and resonance frequencies decreased**
	10% decrease	No Impact	No Impact	**Magnitude and resonance frequencies increased**
M_g	10% increase	Resonance frequencies increased	Resonance frequencies increased	**Resonance frequencies increased**
	10% decrease	Resonance frequencies decreased	Resonance frequencies decreased	**Resonance frequencies decreased**
G	10% increase	No Impact	No Impact	**Magnitude decreased**

TABLE 4 EFFECT OF DIFFERENT PARAMETERS ON FRA SIGNATURE [34]

Parameters Variations		Frequency Range		
		Low	**Medium**	**High**
L_s	10% decrease	Amplitude change	Resonance peaks shift right amplitude change	**Amplitude change**
	10% increase	Amplitude change	Resonance peaks shift right amplitude change	**Amplitude change**
C_{sh}	10% decrease	No Impact	No Impact	**Resonance peaks shift right amplitude change**
	10% increase	No Impact	No Impact	**Resonance peaks shift right amplitude change**
C_g	10% decrease	Amplitude change	Resonance peaks shift right amplitude change	**Resonance peaks shift right amplitude change**
	10% increase	Amplitude change	Resonance peaks shift left amplitude change	**Resonance peaks shift left amplitude change**
R_s	10% decrease	No Impact	No Impact	**Amplitude change**
	10% increase	No Impact	Amplitude change	**Resonance peaks shift right amplitude change**
G	10% decrease	No Impact	No Impact	**No Impact**
	10% increase	Amplitude change	Amplitude change	**Resonance peaks shift right amplitude change**

V. Online FRA

As mentioned, offline FRA has many advantages compared to other methods of assessing the condition of the transformer, but for this, it is necessary to take the transformer out of service. Due to its high importance in the power system, out of service of the transformer imposes a high cost on the network and will reduce the reliability of the grid. For this reason, research is being developed to conduct the online FRA [36].

The problem arises when the transformer is energized during the measurement process. In this condition, high voltage is available and also oil is circulating inside the transformer tank. Among the major problems in measuring online TF, the following can be mentioned [25]:

- Lack of proper signal for injection.
- Isolating the response of the transformer from the external system.
- Problems related to natural variations within the transformer, such as winding temperature and steady-state magnetization.
- transformer state caused by loading conditions;
- Instrumentation system protection against power signal.
- Effect of LV load on the TF results.
- Oil circulation inside the transformer tank.
- Oil bushing on the LV side of the transformer because it does not have a test tap.

Regarding signal injection, it is important to note that making a direct connection to the high-voltage bus or overhead line between the transformer and the surge arrester is complicated and expensive due to the need for insulation. Therefore, the best way is to use the tap bushing of the transformer as an input/output for testing the transformer. It is also suitable for injecting a low-voltage signal as an input when measuring the online TF. The impulse or sweep frequency can be applied through a coaxial cable or optical fiber through an external connection circuit and create a low voltage on the test tap as a reference signal. Then, on the other side of the winding under test that has passed through the neutral bushing, the response signal can be measured. Accordingly, the neutral test tap will be the output probe. If the neutral bushing is connected to the ground, the protective circuit for the neutral bushing is not necessary. In the case of three-phase transformers, if the connection is delta, a protective circuit is required for the input as well as the output test taps. In addition, the measurement can be done between two phases, in this case, the validity of the measured signal is debatable [25, 60-61].

If the signal is controlled, both SFRA and IFRA tests can be performed, but if the signal is uncontrolled, only the IFRA test is applicable. Due to the connection of the transformer to the network and the mentioned limitations, the response signal needs

filtering and a series of mathematical processes. This process is shown in Fig. 8. It should be noted that due to the connection of the transformer to the network, the FR in the online FRA test is affected by the conditions of the network and the transformer in service, and this problem makes the measurement conditions more complicated. [36, 62].

To detect the deformation of transformer windings, the online methods used are the vibration method [63-65], the communication method [66-68], the current deformation coefficient method [69], the ultrasonic method [70], short-circuit impedance and winding stray reactance method [71] and TF method [72-73]. Fig. 9 provides an overview of the development of the online FRA method based on the type of excitation signal [74-80].

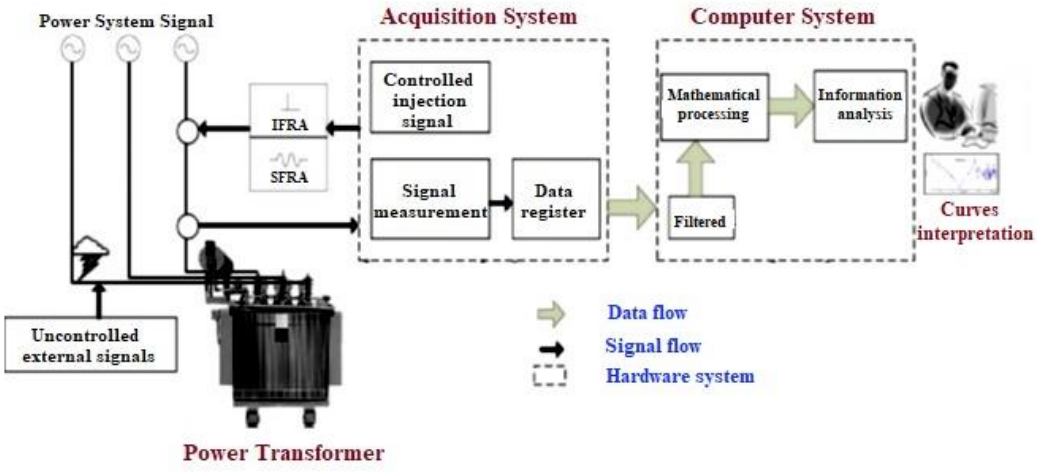

Fig. 8. Online FRA schematic [62]

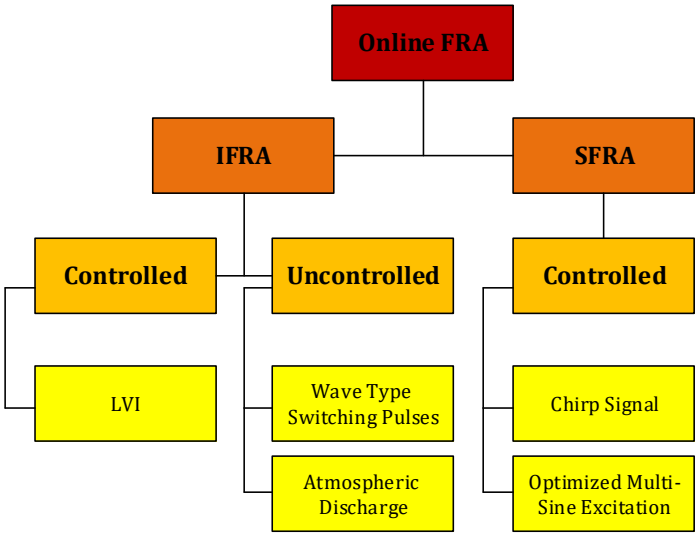

Fig. 9. Online FRA based on the type of stimulation signal

VI. FRA results in interpretation methods

A. Interpretation of FRA results based on numerical indicators

Numerical indices are the most common and intuitive methods to evaluate the amount of change between two FR measurements. Statistical indicators operate based on the degree of compatibility or lack of compatibility between two sets of measurements related to the fault and normal conditions of the transformer [34]. It is easier to use statistical measures and there is no need to calculate the parameters of the models which leads to faults and problems. These indices convert the difference between traces into a unique value that can be easily evaluated [81-88]. The measured indicators can be classified into two main groups:

- Indicators derived directly from FR measurement data (amplitude and phase vectors).
- Indicators based on resonance points (amplitude and frequency)

All indices shown in Table 5, except complex distance (CD) index, are calculated based on amplitude vector. In the CD index, amplitude and phase responses are used to calculate the index. Indicators show different sensitivity to amplitude and FR changes, for example, correlation coefficient (CC) index is not affected by constant amplitude deviation between two traces, so

researchers have developed approaches that combine several indicators [89].

TABLE 5 NUMERICAL INDICES BASED ON FRA VECTORS

Abbreviation	Definition	Equation	References
ASLE	Absolute Sum of Logarithmic Error	$ASLE = \frac{\sum_{i=1}^{N}\lvert 20\log_{10} Y_{1i} - 20\log_{10} Y_{0i}\rvert}{N}$	**[98,119]**
MSE	Mean Square Error	$MSE = \frac{\sum_{i=1}^{N}(Y_{0i} - Y_{1i})^2}{N}$	**[102,108]**
CSD	Comparative Standard Deviation	$CSD = \sqrt{\frac{\sum_{i=1}^{N}[(Y_{0i} - \bar{Y}_0) - (Y_{1i} - \bar{Y}_1)]^2}{N-1}}$	**[103]**
ED	Euclidean Distance	$ED = \sqrt{\sum_{i=1}^{N}(Y_{0i} - Y_{1i})^2}$	**[96]**
SD	Standard Deviation	$SD = \sqrt{\frac{\sum_{i=1}^{N}(Y_{0i} - Y_{1i})^2}{N}}$	**[130]**
RMSE	Root Mean Square Error	$RMSE = \sqrt{\frac{1}{N}\sum_{i=1}^{N}[\frac{\lvert Y_{0i}\rvert - \lvert Y_{1i}\rvert}{\frac{1}{N}\sum_{i=1}^{N}\lvert Y_{1i}\rvert}]^2}$	**[92]**
σ	Spectrum Deviation	$\sigma = \frac{1}{N}\sum_{i=1}^{N}\sqrt{[\frac{Y_{0i} - (\frac{Y_{0i}+Y_{1i}}{2})}{\frac{Y_{0i}+Y_{1i}}{2}}]^2 + [\frac{Y_{1i} - (\frac{Y_{1i}+Y_{0i}}{2})}{\frac{Y_{1i}+Y_{0i}}{2}}]^2}$	**[107,109]**
σ_s	Stochastic Spectrum Deviation	$\sigma_s = \frac{100}{N}\sum_{i=1}^{N}\left\lvert\frac{Y_{0i} + Y_{1i}}{Y_{1i}}\right\rvert$	**[121]**
SSRE	Sum Squared Ratio Error	$SSRE = \frac{\sum_{i=1}^{N}(\frac{Y_{1i}}{Y_{0i}} - 1)^2}{N}$	**[31]**
SSMMRE	Sum Squared Max-Min Ratio Error	$SSMMRE = \frac{\sum_{i=1}^{N}(\frac{\max(Y_{0i},Y_{1i})}{\min(Y_{0i},Y_{1i})} - 1)^2}{N}$	**[119]**
MM	Max-Min Ratio	$MM = \frac{\sum_{i=1}^{N}\min(Y_{0i},Y_{1i})}{\sum_{i=1}^{N}\max(Y_{0i},Y_{1i})}$	**[105,106]**
CCF	Cross Correlation Factor	$CCF = \frac{\sum_{i=1}^{N}(Y_{1i} - \bar{Y}_1) - (Y_{0i} - \bar{Y}_0)}{\sqrt{\sum_{i=1}^{N}(Y_{1i} - \bar{Y}_1)^2}\cdot\sqrt{\sum_{i=1}^{N}(Y_{0i} - \bar{Y}_0)^2}}$	
ρ	Normalized Correlation Coefficient	$\rho = \frac{\sum_{i=1}^{N}\left[\lvert Y_{1i}\rvert - \frac{1}{N}\sum_{i=1}^{N}Y_{1i}\right]\left[\lvert Y_{0i}\rvert - \frac{1}{N}\sum_{i=1}^{N}Y_{oi}\right]}{\sqrt{\sum_{i=1}^{N}\left[\lvert Y_{1i}\rvert - \frac{1}{N}\sum_{i=1}^{N}Y_{1i}\right]^2\sum_{i=1}^{N}\left[\lvert Y_{0i}\rvert - \frac{1}{N}\sum_{i=1}^{N}Y_{0i}\right]^2}}$	**[95]**
CC	Correlation Coefficient	$\mathrm{CC} = \frac{\sum_{i=1}^{N}Y_{0i}Y_{1i}}{\sqrt{\sum_{i=1}^{N}[Y_{0i}]^2\sum_{i=1}^{N}[Y_{1i}]^2}}$	**[97]**
CD	Complex Distance	$CD = \sqrt{\sum_{i=1}^{N}\left(\begin{matrix}\lvert Y_{1i}cos\varphi_{Y_{1i}} - Y_{0i}cos\varphi_{Y_{0i}}\rvert^2 \\ +\lvert Y_{1i}sin\varphi_{Y_{1i}} - Y_{0i}sin\varphi_{Y_{0i}}\rvert^2\end{matrix}\right)}$	**[104]**
DABS	Absolute Difference	$\mathrm{DABS} = \frac{\sum_{i=1}^{N}\lvert Y_{0i} - Y_{1i}\rvert}{N}$	**[103]**

The development of indices based on resonance points involves an additional challenge regarding the position of the resonance points (maximum and minimum), which may seem simple, but especially in the case of noise or small resonances, the detection of the actual resonance frequency is very sensitive and may create faults in these indicators [90]. The vector fitting approach can be used to fit a rational function to the measured FR and thus estimate the maximum and minimum (pole and zero) [91]. The accuracy of the fitting result should be within the reproducible range of the measurement, i.e., the main resonances should be recorded with a frequency deviation less than the recorded frequency resolution [92]. [93] uses the derivative of TF equations by processing FRA data to evaluate the condition of transformer windings. These functions are used for the mathematical description of FRA curves, and by observing the FRA curves produced by these functions, they can check the transformer winding condition.

In Table 5, the most common numerical indices extracted from FRA vectors and also in Table 6, numerical indices extracted from resonance frequency points are presented. In Table 5, Y0 is the reference set of data, Y1 is a set of compared data, $\overline{Y0}$ and $\overline{Y1}$ are the arithmetic mean values of all the accumulated values of a data set and N is the total number of points. In Table 6, the subscripts X and Y refer to new traces and FRA fingerprints, respectively. A(i) and f(i) refer to the amplitude and frequency of the i-th resonance or anti-resonance point, respectively, and AF represents the level below the FRA trace between two anti-resonance points. Pi represents the i-th pole of the rational function, a and b are the numerator and denominator coefficients of the rational function, and m and n are the order of estimation of the numerator and denominator polynomials, respectively. W_{ai} and W_{fi} are the weighting factors of the i-th resonance point.

[94] proposes a transformer winding fault detection method based on the polar plot. The excitation-response ratio is provided

to calculate the relative coefficient for partial fault detection. The fault states are detected by the polar plot distribution, which combines the amplitude-frequency and phase-frequency characteristics.

TABLE 6 NUMERICAL INDICES BASED ON RESONANCE AND ANTI-RESONANCE POINTS

Abbreviation	Definition	Equation	References
MDA	Mean Deviation of Areas	$\mathrm{MDA} = \frac{1}{K}\sum_{i=1}^{K}\lvert AF_Y(i) - AF_X(i)\rvert$	**[90]**
MAD	Mean Amplitude Deviation	$\mathrm{MAD} = \frac{1}{K}\sum_{i=1}^{K}\lvert A_Y(i) - A_X(i)\rvert$	**[90]**
MFD	Mean Frequency Deviation	$\mathrm{MAD} = \frac{1}{K}\sum_{i=1}^{K}\lvert f_Y(i) - f_X(i)\rvert$	**[90]**
IAD	Index of Amplitude Deviation	$\mathrm{IAD} = \sum_{i=1}^{K}\left\lvert\frac{A_Y(i) - A_X(i)}{A_X(i)}\right\rvert$	**[99]**
IFD	Index of Frequency Deviation	$\mathrm{IFD} = \sum_{i=1}^{K}\left\lvert\frac{f_Y(i) - f_X(i)}{f_X(i)}\right\rvert$	**[130]**
F_a	Amplitude Function	$F_a = \sum_{i=1}^{K}\frac{A_Y(i)}{A_X(i)}$	**[132]**
F_f	Frequency Function	$F_f = \sum_{i=1}^{K}\frac{f_Y(i)}{f_X(i)}$	**[132]**
W_a	Weighted Amplitude function	$W_a = \sum_{i=1}^{K}\frac{A_Y(i)}{A_X(i)} \times W_{ai}$	**[103]**
W_f	Weighted Frequency function	$W_f = \sum_{i=1}^{K}\frac{f_Y(i)}{f_X(i)} \times W_{fi}$	**[99]**
FI	Faulted-Intact relation	$\mathrm{FI} = \left(\frac{\sum_{i=1}^{m}\lvert a_Y(i)\rvert}{\sum_{i=1}^{m}\lvert a_x(i)\rvert}\right)\left(\frac{\sum_{i=1}^{n}\lvert b_Y(i)\rvert}{\sum_{i=1}^{n}\lvert b_x(i)\rvert}\right)$	**[100]**
SDP	Sum of absolute Displacement of Poles	$\mathrm{SDP} = \sum_{i=1}^{K}\left\lvert\frac{P_Y(i) - P_X(i)}{P_X(i)}\right\rvert$	**[101]**

B. Interpretation of FRA results based on machine learning

Machine learning and artificial neural networks (ANN) are intelligent algorithms often used for pattern classification by learning from examples. In unsupervised learning, monitoring the network and providing target outputs to match the inputs is unnecessary. In supervised learning, a target output is provided for each input vector injected into the network. Based on the calculated output fault (the difference between the target output and the estimated output), the network adjusts its synaptic weight using heuristic algorithms in each iteration [111-112]. [113] presents a new approach using a multi-layered perceptron model for modeling and direct analysis of FRA data, simulating types and degrees of the transformer winding faults. [114] compares several well-known and widely used classifications of machine learning, including radial basis function (RBF), support vector machine (SVM), and statistical k-nearest neighbour (k-NN). In recent years, due to the ability of these models to solve classification problems, regression, and other applications, they have become very popular in various fields. RBF, SVM, and k-NN networks performed well classification of faults using the CSD index and desired frequency ranges as input.

[115-118] estimates the parameters of a three-phase low-frequency model of the transformer by using the data obtained from the FR. [119-120] estimates the FRA data by a rational function consisting of two polynomials describing the zeros and poles of the transformer model. ANN and fuzzy logic have also been used to compare and interpret the results of the TF of transformers [121-124].

[125] presents an algorithm for interpreting FRA results based on numerical indicators and a supervised machine-learning technique. For this purpose, random forest (RF) classifiers were developed for the first time to identify the

condition of transformer windings and classify various faults in transformer windings. The results show that the

much human intervention. [126] by presenting the enhanced vector fitting algorithm, tries to create an algorithm with appropriate accuracy for the automatic interpretation of the results measured by FRA. However, to detect any spectral deviation as detection of any mechanical damage inside the transformer, the impedance measurement must be free from other influences such as the change in the state of the insulating materials (paper, pressboard and oil) that may cause spectral deviations in the FR of the winding impedance [127].

Furthermore, the laminated steel core can only support magnetic flux up to about 100 kHz. Therefore, any change in a material property (permeability) or clamping structure can

lead to deviation in the FRA spectrum in this frequency range [128]. [129] uses ensemble machine learning techniques to detect and diagnose transformer mechanical faults based on the extraction of winding frequency responses using outlier detection and ensemble algorithms, which together form an efficient hybrid method.

VII. Fault location based on FRA

In many studies, various methods have been presented to detect the type, location, and extent of faults in power transformers. [130] Classification of the type, location and intensity of different faults is done using a support vector machine with cubic polynomial kernel. The accuracy of different indices and amplitude, phase, real and imaginary components of TF have been checked. [131-132] presented a new calculation method of TF comparison indices called windowed calculated index (W-index). The ability and accuracy of the proposed W-index were studied and Fisher discriminant analysis was used to classify the fault as well as to determine the location and intensity of the fault. [133] proposed an algorithm to determine the location and amount of winding buckling. The fault location is determined by comparing the direction of change of the measured and simulated results at resonant frequencies, and the SD index is proposed to determine the amount of deformation of the winding. [134] investigated the mechanical faults of DSV, RD, and AD on three different test samples of similar size using their TF.

To determine the type of fault using the CC index in different frequency ranges, a certain coefficient (α) has been used so that the weight functions of amplitude and frequency can specify the location along with the amount of fault. The disc-disc, RD, and AD faults in the winding are modeled based on the detailed model presented in [135]. Some correlation-based features and other mathematical models of TF measurement were used to train the ANN classifier. The results show an overall accuracy of 98.8% for detecting the type of fault and 95.4% for detecting the location of the fault, and there is no discussion about the amount of fault. [136] proposes a new location method for transformer failure. This method is based on a combination of FRA and evidential reasoning (ER) process.

The wavelet transform (WT) has proven to be very efficient for the study of transient signals, as it can analyze and change the resolution of signals in both the TD and FD. This change occurs because the WT allows good resolution for the analysis of both slowly varying (60 Hz) and rapidly varying components typically associated with high-frequency events [137]. The rationale behind decomposing FRA responses using WT is to create smooth TF versions with different levels of information to improve the signal difference detection process for different frequency regions. This method adds more robustness to the FRA and reduces the possible impact of disturbances during the measurement on the detection result [138]. Also [139] a method based on wavelet transform is proposed as a powerful technique to analyze even slight changes in transformer FR characteristics for fault detection. [140] introduces a new theoretical method to obtain the FR curve with the transformer in service (online) from the transient signals analysis by applying the continuous WT. [141] presents a new method for fault detection and location in power transformers. In this method, the neutral current, whose change is very minor in the event of a minor fault, is analyzed using the WT, and its performance is investigated by considering a fault in different locations. The WT benefits from the TF in three aspects:

1. The neutral current that changes when the fault occurs is seen as a non-constant signal and used directly in the analysis, without any reference to the voltage, as in the TF.
2. The time of fault occurrence can be recognized. This time provides a means to accurately detect the location of the fault in a particular transformer winding, based on the wave propagation speed.
3. It is possible to find very minor faults while it is not possible with TF.

In Table 7, some papers are categorized according to the type of fault identified, and the method of identification and index used.

[142-143] presents a new method for detecting and locating turn-turn faults in power transformers using both the TF method and the ANN technique. Some faults in turn in the winding have been simulated and the corresponding TF has been measured. Then, using ANN and a back-propagation learning algorithm, a method to identify the fault location is presented. The results show that if the ANN network is trained using the provided patterns, it can well detect the location of the fault.

TABLE 7 CLASSIFYING SOME REFERENCES FOR FAULT LOCATION METHOD

Type of Fault	Proposed Method	Ref.
winding fault (SC, OC)	ANN technique	[134],[141], [142]
	Wavelet Transform	[136-140]
	Polar Plot	[92]
Winding deformation (AD, RD, DSV)	Support Vector Machine	[114],[118]
mechanical displacements (AD, RD)	Vector Fitting	[101],[116]

VIII. Conclusion

The power transformer insulation system is one of the vital parts of the power transformer. Thus, the quality of the insulation system must be constantly monitored. One of the most powerful and accurate tools for diagnosing and locating various faults in power transformers is FRA. But interpreting FRA curves still requires a higher level of expertise to identify and quantify faults. Because the FRA interpretive code is not yet widely accepted. Most of the conducted studies have dealt with the detection and location of faults related to the winding. This paper, after an in-depth study of the application of FRA as a fault detection method in transformers, examines the ability of this method to detect and locate insulation faults in transformers. Studies show that based on the detailed model of the transformer, any change in the insulation condition leads to a change in the parameters of this model, and it is possible to detect and locate these types of faults by FRA.

Conflicts of Interest: The authors declare that there is no conflict of interest regarding the publication of this paper.

References

[1] Bagheri, Mehdi, Mohammad Salay Naderi, Trevor Blackburn, et al. "FRA vs. short circuit impedance measurement in detection of mechanical defects within large power transformer." In 2012 IEEE International Symposium on Electrical Insulation, pp.301-305, 2012.

[2] De Klerk, Patrick John, and J. P. Reynders "Winding slackness monitoring as a diagnostic for insulation ageing in oil-paper insulated power transformers." In 1999 Eleventh International Symposium on High Voltage Engineering, pp.185-188, 1999.

[3] Bolduc, L., P. Picher, G. Pare, et al. "transformer Winding Displacement by the Frequency Response of Stray Losses (FRSL)." CIGRE, 2000.

[4] J. Aubin and L. Bolduc, "Determination of transformer Winding Displacement by FRSL Diagnostic Method." Final Report on CEA Project, pp.77-47, 1981.

[5] Trinh, N. Giao, J. Aubin, and L. Bolduc. "Dielectric and short-circuit tests of used transformers." 1982.

[6] Ji, T. Y., W. H. Tang, et al. "Frequency response analysis of power transformer winding deformation based on a hybrid model." In 2011 IEEE Power Engineering and Automation Conference. pp.144-147, 2011.

[7] Sofian, D. M., Z. D. Wang, et al. "Frequency response analysis in diagnosing transformer winding movements-fundamental understandings." In 39th International Universities Power Engineering Conference. pp.138-142, 2004.

[8] Ryder, Simon A. "Methods for comparing frequency response analysis measurements. In Conference Record of the 2002 IEEE International Symposium on Electrical Insulation, pp.187-190, 2002.

[9] Vaessen, P. T. M., and E. Hanique. "A new frequency esponse analysis method for power transformers." IEEE Transactions on Power Delivery, Vol.7, No.1, pp.384-391, 1992.

[10] Zhou, Lijun, Junfei Jiang, Wei Li, et al. "FRA modelling for diagnosing axial displacement of windings in traction transformers." IET Electric Power Applications, Vol.13, No.12, pp. 2121-2127, 2019.

[11] Fofana, Issouf, and Yazid Hadjadj. Electrical-based diagnostic techniques for assessing insulation condition in aged transformers. Energies, Vol. 9, No.9, p.679, 2016.

[12] Wang, M. V. A. J., A. John Vandermaar, et al. "Review of condition assessment of power transformers in service." IEEE Electrical Insulation magazine, Vol.18, No.6, pp. 12-25, 2002.

[13] Florkowski, Marek. "Exploitation stresses and challenges in diagnostics of electrical industrial equipment." In 2011 IEEE International Symposium on Industrial Electronics, pp.15-25, 2011.

[14] Florkowski, M., and J. Furgal. "Identification of winding faults in electric machines using a high-frequency method."In 2007 IEEE International Electric Machines & Drives Conference, pp.590-595, 2007.

[15] García, Belén, Juan Carlos Burgos, and Ángel Alonso. "Winding deformations detection in power transformers by tank vibrations monitoring." Electric power systems research, Vol.74, No.1, pp.129-138, 2005.

[16] García, Belén, Juan Carlos Burgos, and Ángel Matías Alonso. "transformer tank vibration modeling as a method of detecting winding deformations-part I: theoretical foundation." IEEE Transactions on Power Delivery, Vol.21, No.1, pp.157-163, 2005.

[17] Dick, E. P., and C. C. Erven. "transformer diagnostic testing by frequuency response analysis." IEEE Transactions on Power Apparatus and Systems, Vol. 6, No.1, pp. 2144-2153, 1978.

[18] Bagheri, Mehdi, Mohammad Salay Naderi, and Trevor Blackburn. "Advanced transformer winding deformation diagnosis: moving from off-line to on-line." IEEE Transactions on Dielectrics and Electrical Insulation, Vol.19, No.6, pp.1860-1870, 2012.

[19] Sano, Takahiro, and Katsunori Miyagi. "Experimental investigation on FRA diagnosis of transformer faults." IEEJ Transactions on Power and Energy, Vol.127, No.7, pp.791-796, 2007.

[20] Bagheri, Mehdi, Mohammad Salay Naderi, Trevor Blackburn, et al. "Frequency response analysis to recognize inductance variation in transformer due to internal short circuit." In 2012 10th International Power & Energy Conference (IPEC), pp.677-681, 2012.

[21] Ryder, Simon A. "Diagnosing transformer faults using frequency response analysis." IEEE electrical insulation magazine, Vol.19, No.2, pp.16-22, 2003.

[22] Miyazaki, Satoru, Yoshinobu Mizutani, Hiroshi Suzuki, et al. "Detection of deformation and displacement of transformer winding by frequency response analysis." In 2008 International Conference on Condition Monitoring and Diagnosis, pp.964-967, 2008.

[23] Christian, Jochen, and Kurt Feser. "Procedures for detecting winding displacements in power transformers by the transfer function method." IEEE Transactions on Power Delivery, Vol. 19, No.1, pp.214-220, 2004.

[24] Shintemirov, A., W. H. Tang, and Q. H. Wu. "transformer core parameter identification using frequency response analysis." IEEE Transactions on Magnetics, Vol. 46, No.1, pp.141-149, 2009.

[25] Bagheri, Mehdi, Mohammad Salay Naderi, Trevor Blackburn, and Toan Phung. "Practical challenges in online transformer winding deformation diagnostics." In 2011 2nd International Conference on Electric Power and Energy Conversion Systems (EPECS), pp.1-6, 2011.

[26] McNutt, W. J., W. M. Johnson, et al. "Power Transformer Short-Circuit Strength-Requirements, Design, and Demonstration." IEEE Transactions on Power Apparatus and Systems, Vol.8, No.1, pp.1955-1969, 1970.

[27] Kulkarni, Shrikrishna V., and S. A. Khaparde. "transformer engineering." New York: Marcel Dekker, 2004.

[28] Del Vecchio, Robert M., Bertrand Poulin, et al. "transformer design principles." CRC press, 2017.

[29] Wang, M., A. J. Vandermaar, and K. D. Srivastava. "Condition monitoring of transformers in service by the low voltage impulse test method." In 1999 Eleventh International Symposium on High Voltage Engineering, pp.45-48, 1999.

[30] Florkowski, Marek, and Jakub Furgał. "Detection of winding faults in electrical machines using the frequency response analysis method." Measurement Science and Technology, Vol.15, No.10, pp.2067, 2004.

[31] Gómez-Luna, Eduardo, Guillermo Aponte, and Jorge Pleite. "Non-invasive monitoring of transformers using the frequency response from controlled transient signals." Ingenieríay competitividad, Vol.15, No.2, pp.23-33, 2013.

[32] Pandya, Akshay A., and D. B. R. Parekh. "Sweep frequency response analysis (SFRA) an approach to detect hidden transformer faults." International Journal of Advanced Research in Electrical, Electronics and Instrumentation Engineering, Vol. 2, pp.1893-1896, 2013.

[33] Gomez-Luna, Eduardo, Guillermo Aponte Mayor, et al. "Current status and future trends in frequency-response analysis with a transformer in service." IEEE Transactions on power delivery, Vol.28, No.2, pp.1024-1031, 2013.

[34] Alsuhaibani, Saleh, Yasin Khan, Abderrahmane Beroual, and Nazar Hussain Malik. "A review of frequency response analysis methods for power transformer diagnostics." Energies Vol.9, No.11, p. 879, 2016.

[35] IEEE Guide for the Application and Interpretation of Frequency Response Analysis for Oil-Immersed transformers, IEEE C57. Vol.149, 2012.

[36] Senobari, Reza Khalili, Javad Sadeh, and Hossein Borsi. "Frequency response analysis (FRA) of transformers as a tool for fault detection and location: A review." Electric power systems research, Vol. 155, pp. 172-183, 2018.

[37] Chaouche, Moustafa Sahnoune, Hamza Houassine, Samir Moulahoum, et al. "BA to construction of equivalent circuit of a transformer winding from frequency response analysis measurement." IET Electric Power Applications Vol.12, No.5, pp.728-736.

[38] Nosratian Ahour, Jafar, Saeed Seyedtabaie, and Gevork B. Gharehpetian. Modified transformer winding ladder network model to assess nondominant frequencies. IET Electric Power Applications, Vol. 11, No.4, pp.578-585, 2017.

[39] Nasirpour, F., Heidary, A., Niasar, M.G., Lekić, A. and Popov, M. "High-frequency transformer winding model with adequate protection." Electric Power Systems Research, Vol. 223, p.109637, 2023.

[40] Ragavan, K., and L. Satish. "An efficient method to compute the transfer function of a transformer from its equivalent circuit." IEEE Transactions on Power Delivery, Vol. 20, No.2, pp.780-788, 2005.

[41] Hashemnia, Naser, Ahmed Abu-Siada, Mohammad AS Masoum, et al. "Characterization of transformer FRA signature under various winding faults." In 2012 IEEE International Conference on Condition Monitoring and Diagnosis, pp.446-449, 2012.

[42] CIGRE Technical Brochure "Mechanical-Condition Assessment of Transformer Windings using Frequency Response Analysis (FRA)", p. 342, 2008.

[43] Gonzalez, C., J. Pleite, V. Valdivia, et al. "An overview of the online application of frequency response analysis (FRA)." In 2007 IEEE International Symposium on Industrial Electronics, pp.1294-1299, 2007.

[44] Ibrahim, K. H., Korany, N. R., & Saleh, S. M. "Effects of power transformer high-frequency equivalent circuit parameters non-uniformity on fault diagnosis using SFRA test." Ain Shams Engineering Journal, Vol.13, No.4, p.101674, 2022.

[45] Kre, K., and D. König. "Comparison of measured resonance frequencies of coils at sinusoidal and impulse voltage excitation." In Proc. of the 7th Int. Symp. on High Voltage Engineering (ISH 1991), pp.26-30, 1991.

[46] F. Predl "Interpretation of Sweep Frequency Response Analysis (SFRA) Measurement Results", OMICRON Australia, Sydney, 2016.

[47] Gómez-Luna, Eduardo, Guillermo Aponte, et al. "Experimentally obtaining on-line FRA in transformers by injecting controlled pulses" Ingenieria e investigación, Vol. 33, No.1, pp.41-45, 2013.

[48] Kraetge, A., M. Velasquez, J. L. Kruger, H. Viljoen et al. "Aspects of the Practical Application of Sweep Frequency Response Analysis", 6th Southern Africa Regional Conference. Paris: CIGRE, pp. 2-10, 2009.

[49] Behjat, Vahid, Abolfazl Vahedi, Alireza Setayeshmehr, et al. "Sweep frequency response analysis for diagnosis of low-level short circuit faults on the windings of power transformers: An experimental study." International Journal of Electrical Power & Energy Systems, Vol.42, No.1, pp.78-90, 2012.

[50] Samimi, Mohammad Hamed, Stefan Tenbohlen, Amir Abbas Shayegani Akmal, et al. "Dismissing uncertainties in the FRA interpretation." IEEE Transactions on Power Delivery, Vol.33, No.4, pp.2041-2043, 2016.

[51] Jayasinghe, J. A. S. B., Z. D. Wang, et al. "Winding movement in power transformers: a comparison of FRA measurement connection methods." IEEE Transactions on Dielectrics and Electrical Insulation, Vol.13, No.6, pp.1342-1349, 2006.

[52] Samimi, Mohammad Hamed, Stefan Tenbohlen, Amir Abbas Shayegani Akmal, et al. "Effect of different connection schemes, terminating resistors and measurement impedances on the sensitivity of the FRA method." IEEE Transactions on Power Delivery, Vol. 32, No.4, pp.1713-1720, 2016.

[53] Wang, M., A. John Vandermaar, and K. D. Srivastava. "Improved detection of power transformer winding movement by extending the FRA high-frequency range." IEEE Transactions on power delivery, Vol. 20, No.3, pp.1930-1938, 2005.

[54] Samimi, M. H., S. Tenbohlen, AA Shayegani Akmal, et al. "Effect of different terminating resistors on the FRA method sensitivity." In 2015 30th International Power System Conference (PSC), pp.177-183, 2015.

[55] Sano, Takahiro, and Katsunori Miyagi. "Influence factors on FRA waveforms." In 2012 IEEE International Conference on Condition Monitoring and Diagnosis, pp. 601-604, 2012.

[56] Li, Yanming, Gang Liu, Linhai Zhang, et al. "transformer winding deformation diagnosis using middle band frequency response analysis." In 2007 IEEE International Conference on Solid Dielectrics, pp. 677-680, 2007.

[57] Abu-Siada, Ahmed, Naser Hashemnia, Syed Islam, et al. "Understanding power transformer frequency response analysis signatures." IEEE Electrical Insulation Magazine, Vol.29, No.3, pp.48-56, 2013.

[58] De Rybel, Tom, Arvind Singh, et al. "Apparatus for online power transformer winding monitoring using bushing tap injection. IEEE Transactions on Power Delivery, Vol.24, No.3, pp.996-1003, 2009.

[59] Abu-Siada, A.; Hashemnia, N.; Islam, S.; et al. "Impact of transformer Model Parameters Variation on FRA Signature." In Proceedings of the 22nd Australasian Universities Power Engineering Conference (AUPEC), Bali, Indonesia, pp. 26–29, 2012.

[60] Kakolaki, S.E.H., Hakimian, V., Sadeh, J. and Rakhshani, E. "Comprehensive study on transformer fault detection via frequency response analysis." IEEE Access, 2023.

[61] Abeywickrama, Nilanga, Yuriy V. Serdyuk, et al. "Effect of core magnetization on frequency response analysis (FRA) of power transformers." IEEE Transactions on Power delivery, Vol.23, No.3, pp. 1432-1438, 2008.

[62] Florkowski, Marek, and Jakub Furgał. "transformer winding defects identification based on a high frequency method." Measurement Science and Technology, Vol.18, No.9, p.2827, 2007.

[63] Bagheri, M., and B. T. Phung. "Frequency response and vibration analysis in transformer winding turn-to-turn fault recognition." In 2016 International Conference on Smart Green Technology in Electrical and Information Systems (ICSGTEIS), pp.10-15, 2016.

[64] Akhavanhejazi, M., Gevorg B. Gharehpetian, Reza Faraji-Dana, et al. "A new on-line monitoring method of transformer winding axial displacement based on measurement of scattering parameters and decision tree." Expert Systems with Applications, Vol. 38, No.7, pp.8886-8893, 2011.

[65] Hejazi, M. A., G. B. Gharehpetian, G. Moradi, H. A, et al. "Online monitoring of transformer winding axial displacement and its extent using scattering parameters and k-nearest neighbour method." IET generation, transmission & distribution, vol. 5(8), pp.824-832, 2011.

[66] P. M. Joshi and S. V. Kulkarni "A novel approach for online deformation diagnostics of transformer windings", IEEE Power and Energy Society, General Meeting, pp.1-6, 2010.

[67] N. Shu, C. Zhou, F. Hu, et al. "Study on ultrasonic measurement device for transformer winding deformation", IEEE Int'l. Conf. Power Syst.(POWERCON), pp.1401-1404, 2002.

[68] Alpatov, Michael. "On-line detection of winding deformation." In Conference Record of the 2004 IEEE International Symposium on Electrical Insulation, pp. 113-116, 2004.

[69] S.-b. Gao and G. Wang, "Study on on-line monitoring of windings deformation of power transformer." IEEE 8th Int'l. Conf. Developments in Power System Protection, pp. 335-338, 2004.

[70] G. Hu, L. Zhang, X. Wu, et al "Detecting the Capacity of Distribution Transformer Based on an On-Line Method", Asia-Pacific Power and Energy Eng. Conf. (APPEEC), pp.1-4, 2011.

[71] Palani, A., S. Santhi, S. Gopalakrishna, et al. "Real-time techniques to measure winding displacement in transformers during short-circuit tests." IEEE transactions on power delivery, vol. 23(2), pp.726-732, 2008.

[72] M. Bagheri, M.S. Naderi, T. Blackburn, et al. "Bushing characteristic impacts on online frequency response analysis of transformer winding." In IEEE International Conference on Power and Energy, pp. 956-961, 2012.

[73] S. Gopalakrishna, V. Jayashankar, K.V. Jagadeesh, et al. "Online assessment of winding deformation based on optimized excitation." In International Workshop on Applied Measurements for Power Systems, pp. 84-89, 2010.

[74] S. Jiangtao, J. Benedikt, and P.J. Tasker, "A new method for the design of multi-sine excitations for the assessment of non-linear devices." In IEEE Microwave Symposium Digest, pp. 265- 268, 2008.

[75] Annus, Paul, Raul Land, et al. "Simple signals for system identification. Fourier Transform-Signal Processing." InTech, Rijeka, pp. 257-276, 2012.

[76] Y.R. Sood, R. Jarial, and K. Gandhi, "Condition monitoring of power transformer using sweep frequency response analysis." MIT International Journal of Electrical and Instrumentation Engineering, pp. 80-86, 2011.

[77] S. Tenbohlen and S.A. Ryder, "Making frequency response analysis measurements: a comparison of the swept frequency and low voltage impulse methods." In International Symposium on High Voltage Engineering, 2003.

[78] Z. Shen, M. Jaksic, P. Mattavelli, et al. "Three-phase AC system impedance measurement unit (IMU) using chirp signal injection." In IEEE Applied Power Electronics Conference and Exposition, pp. 2666-2673, 2013.

[79] Herrera, Wilder, Guillermo Aponte, et al. "A novel methodology for transformer low-frequency model parameters identification." International Journal of Electrical Power & Energy Systems, Vol. 53, pp.643-648, 2013.

[80] Wang, Zhongdong, Jie Li, et al. "Interpretation of transformer FRA responses—Part I: Influence of winding structure." IEEE Transactions on power delivery, Vol. 24, No.2, pp.703-710, 2009.

[81] Sofian, Dahlina M., Zhongdong Wang, et al. "Interpretation of transformer FRA responses—Part II: Influence of transformer structure." IEEE Transactions on Power Delivery, Vol. 25, No.4, pp.2582-2589, 2010.

[82] G. Kennedy, A. McGrail, and J. Lapworth, "Transformer sweep frequency response analysis (SFRA)", Energize, eepublishers, pp. 1-12, 2007.

[83] A. Islam "Detection of mechanical deformation in old aged power transformer using cross-correlation co-efficient analysis method." Energy Power Eng.Vol.3, pp.585-591, 2011.

[84] Srikanta Murthy, Avinash, Norhafiz Azis, Salem Al-Ameri, et al. "Investigation of the effect of winding clamping structure on frequency response signature of 11 kV distribution transformer." Energies, Vol.11, No.9, p.2307, 2018.

[85] Behjat, Vahid, and Mojtaba Mahvi. "Statistical approach for interpretation of power transformers frequency response analysis results." IET Science, Measurement & Technology, Vol.9, No.3, pp. 367-375, 2015.

[86] Sardar, Suman, Amrendra Kumar, et al. "Application of statistical interpretation technique for frequency response analysis and detection of axial displacement in transformer winding." In 2017 IEEE Calcutta Conference (CALCON), pp. 461-464, 2017.

[87] Abeywickrama, K. G. N. B., Alexander D. Podoltsev, et al. "Computation of parameters of power transformer windings for use in frequency response analysis." IEEE Transactions on Magnetics, Vol.43, No.5, pp.1983-1990, 2007.

[88] Jadhav, Mrs Pradnya R., and P. M. Joshi. "Study of transformer winding parameters as deformation diagnostics techniques using FRA measurement" 2011.

[89] Bigdeli, Mehdi, Davood Azizian, and Gevork B. Gharehpetian. "Detection of probability of occurrence, type and severity of faults in transformer using frequency response analysis-based numerical indices." Measurement, Vol.168, p. 108322, 2021.

[90] Picher, Patrick, Stefan Tenbohlen, et al. "Current state of transformer FRA interpretation" On behalf of CIGRE WG A2. 53. Procedia engineering, pp. 3-12, 2017.

[91] R. Wimmer, S. Tenbohlen, M. Heindl, et al. "Development of algorithms to assess the FRA." In 15th Int. Symp. High Voltage Engineering, Ljubljana, 2007.

[92] Gustavsen, Bjorn, and Adam Semlyen. "Rational approximation of frequencu domain responses by vector fitting. IEEE Transactions on power delivery, Vol.14, No.3, pp.1052-1061, 1999.

[93] M. Heindl, S. Tenbohlen, A. Kraetge, et al. "Algorithmic determination of pole-zero representations of power transformers transfer functions for interpretation of FRA data." In 16th Int. Symp. on High Voltage Engineering, Johannesburg, 2009.

[94] Zhang, Z.," Characterizing transformer HV–LV winding FRA curves through derivation of transfer functions from

FRA data." Electric Power Systems Research, Vol.228, p.110055, 2024.
[95] Li, Z., He, Y., Xing, Z. and Chen, M., "Minor fault diagnosis of transformer winding using polar plot based on frequency response analysis." International Journal of Electrical Power & Energy Systems, Vol.152, p.109173, 2023.
[96] IEEE guide for the application and interpretation of frequency response analysis for oil-immersed transformers. IEEE Std C57. Vol.149, p. 1–72, 2013.
[97] Ghanizadeh, Ahmad Javid, and G. B. Gharehpetian. "ANN and cross-correlation based features for discrimination between electrical and mechanical defects and their localization in transformer winding." IEEE Transactions on Dielectrics and Electrical Insulation, Vol.21, No.5, pp.2374-2382, 2014.
[98] Arispe, Jimmy Cesar Gonzales, and Enrique Esteban Mombello. "Detection of failures within transformers by FRA using multiresolution decomposition. IEEE transactions on power delivery, Vol.29, No.3, pp.1127-1137, 2014.
[99] Nirgude, Pradeep M., D. Ashokraju, et al. "Application of numerical evaluation techniques for interpreting frequency response measurements in power transformers." IET Science, Measurement & Technology, Vol.2, No.5, pp.275-285, 2008.
[100] Rahimpour, Ebrahim, and Danial Gorzin. "A new method for comparing the transfer function of transformers in order to detect the location and amount of winding faults." Electrical Engineering, Vol.88, pp.411-416, 2006.
[101] Bigdeli, Mehdi, Mehdi Vakilian, and Ebrahim Rahimpour. "A new method for detection and evaluation of winding mechanical faults in transformer through transfer function measurements." Advances in Electrical and Computer Engineering, Vol.11, No.2, pp.23-30, 2012.
[102] Karimifard, P., G. B. Gharehpetian, and S. Tenbohlen. "Determination of axial displacement extent based on transformer winding transfer function estimation using vector fitting method." European Transactions on Electrical Power, Vol.18, No.4, pp.423-436, 2008.
[103] Pourhossein, K., G. B. Gharehpetian, E. Rahimpour, and B. N. Araabi. "A probabilistic feature to determine type and extent of winding mechanical defects in power transformers." Electric Power Systems Research, Vol.82, No.1, pp.1-10, 2012.
[104] Sant'Ana, Wilson Cesar, Camila Paes Salomon, et al. "A survey on statistical indexes applied on frequency response analysis of electric machinery and a trend based approach for more reliable results." Electric Power Systems Research, Vol.137, pp.26-33, 2016.
[105] Samimi, Mohammad Hamed, Stefan Tenbohlen, Amir Abbas Shayegani Akmal, et al. "Improving the numerical indices proposed for the FRA interpretation by including the phase response." International Journal of Electrical Power & Energy Systems, Vol.83, pp.585-593, 2016.
[106] Secue, J. R., and E. Mombello. "Sweep frequency response analysis (SFRA) for the assessment of winding displacements and deformation in power transformers." Electric Power Systems Research, Vol.78, No.6, pp.1119-1128, 2008.
[107] Ryder, Simon A. "Transformer diagnosis using frequency response analysis: results from fault simulations." In IEEE Power Engineering Society Summer Meeting, pp. 399-404, 2002.
[108] Tang, W. H., A. Shintemirov, and Q. H. Wu. "Detection of minor winding deformation fault in high-frequency range for power transformer." In IEEE PES general meeting, pp. 1-6, 2010.
[109] Ji, T. Y., W. H. Tang, et al. "Detection of power transformer winding deformation and variation of measurement connections using a hybrid winding model. Electric power systems research, Vol.87, pp.39-46, 2012.
[110] Badgujar, K. P., M. Maoyafikuddin, and S. V. Kulkarni. "Alternative statistical techniques for aiding SFRA diagnostics in transformers." IET Generation, Transmission & Distribution, Vol.6, No.3, pp.189-198, 2012.
[111] Szoka, Wojciech, and Szymon Banaszak. "Evaluation methods of frequency response analysis." In 2018 International Interdisciplinary PhD Workshop (IIPhDW), pp.36-38, 2018.
[112] Samimi, Mohammad Hamed, and Stefan Tenbohlen. "FRA interpretation using numerical indices: State-of-the-art." International Journal of Electrical Power & Energy Systems, Vol.89, pp.115-125, 2017.
[113] Bigdeli, Mehdi, Pierluigi Siano, and Hassan Haes Alhelou. "Intelligent classifiers in distinguishing transformer faults using frequency response analysis." IEEE Access, Vol.9, pp.13981-13991, 2021.
[114] Wang, G.," FRA-DiagSys: A Transformer Winding Fault Diagnosis System for Identifying Fault Types and Degrees Using Frequency Response Analysis." arXiv preprint arXiv: Vol.2406, p.19623, 2024.
[115] Liu, Jiangnan, Zhongyong Zhao, et al. "Classifying transformer winding deformation fault types and degrees using FRA based on support vector machine." IEEE Access, Vol.7, pp.112494-112504, 2019.
[116] Ferreira, Regelii Suassuna De Andrade, Patrick Picher, et al. "Frequency response analysis interpretation using numerical indices and machine learning: A case study based on a laboratory model." IEEE Access, Vol.9, pp.67051-67063, 2021.
[117] Karimifard, P., G. B. Gharehpetian, and S. Tenbohlen. "Localization of winding radial deformation and determination of deformation extent using vector fitting based estimated transfer function." European Transactions on Electrical Power, Vol.19, No.5, pp.749-762, 2009.
[118] Zambrano, G. M. V., A. C. Ferreira, et al. "Power transformer equivalent circuit identification by artificial neural network using frequency response analysis." In 2006 IEEE Power Engineering Society General Meeting, p. 6, 2006.
[119] Fei, Sheng-wei, and Xiao-bin Zhang. "Fault diagnosis of power transformer based on support vector machine with genetic algorithm." Expert Systems with Applications, Vol.36, No.8, pp.11352-11357, 2009.
[120] Flores, Wilfredo C., Enrique Mombello, et al. "Fuzzy risk index for power transformer failures due to external short-circuits." Electric Power Systems Research, Vol.79, No.4, pp.539-549, 2009.
[121] Kim, Jong-Wook, ByungKoo Park, Seung Cheol Jeong, Sang Woo Kim, and PooGyeon Park. "Fault diagnosis of a power transformer using an improved frequency-response analysis. "IEEE transactions on power delivery, Vol.20, No.1, pp.169-178, 2005.
[122] L. Coffeen, J. Britton, and J. Rickmann, "A new technique to detect winding displacements in power transformers using frequency response analysis." In IEEE Bologna Power Tech Conf., 2003.

[123] Moradzadeh, Arash, and Kazem Pourhossein. "Short circuit location in transformer winding using deep learning of its frequency responses." In 2019 International Aegean Conference on Electrical Machines and Power Electronics (ACEMP) & 2019 International Conference on Optimization of Electrical and Electronic Equipment (OPTIM), pp. 268-273, 2019.

[124] Tahir, M. and Tenbohlen, S. "Transformer winding fault classification and condition assessment based on random forest using FRA." Energies, Vol.16, No.9, p.3714, 2023.

[125] J. Back-Jensen, B. Back-Jensen, and S. D. Mikkelsen, "Detection of faults and aging phenomina in transformers by transfer functions." IEEE Trans. Power Del. Vol.10, No.1, pp.308–314, 1995.

[126] Behjat, Vahid, Abolfazl Vahedi, Alireza Setayeshmehr, et al. "Diagnosing shorted turns on the windings of power transformers based upon online FRA using capacitive and inductive couplings." IEEE transactions on power delivery, Vol.26, No.4, pp.2123-2133, 2011.

[127] Premalatha, V., S. S. Sruthi, M. Vikash, et al. "Instrument transformer winding fault analysis using frequency response analysis." In 2012 IEEE International Conference on Advanced Communication Control and Computing Technologies (ICACCCT), pp. 370-374, 2012.

[128] Moravej, Z., Mortazavi, S. M., & Mohseni, M. "Discrimination among Winding Mechanical Defects in Transformer Using Noise Detection and Data Mining Boosting Method." International Journal of Industrial Electronics Control and Optimization, Vol.4, No.3, pp.277-284, 2021.

[129] Pleite, Jorge, Carlos Gonzalez, Juan Vazquez, et al. "Power transformer core fault diagnosis using frequency response analysis." In MELECON 2006-2006 IEEE Mediterranean Electrotechnical Conference, pp. 1126-1129, 2006.

[130] Tarimoradi, Hadi, Hossein Karami, Gevork B. Gharehpetian, and Stefan Tenbohlen. "Sensitivity analysis of different components of transfer function for detection and classification of type, location and extent of transformer faults. Measurement, Vol.187, p.110292, 2022.

[131] Tarimoradi, Hadi, and Gevork B. Gharehpetian. "Novel calculation method of indices to improve classification of transformer winding fault type, location, and extent." IEEE Transactions on Industrial Informatics, Vol.13, No.4, pp.1531-1540, 2017.

[132] Vosoughi, Ahmad, and Mohammad Hamed Samimi. "Transformer fault type discrimination based on window calculation method and frequency response analysis." Measurement, Vol.202, p.111889, 2022.

[133] Karimifard, P., and G. B. Gharehpetian. "A new algorithm for localization of radial deformation and determination of deformation extent in transformer windings." Electric Power Systems Research, Vol.78, No.10, pp.1701-1711, 2008.

[134] Rahimpour, Ebrahim, Mehdi Jabbari, and Stefan Tenbohlen. "Mathematical comparison methods to assess transfer functions of transformers to detect different types of mechanical faults." IEEE transactions on power delivery, Vol.25, No.4, pp.2544-2555, 2010.

[135] Bigdeli, M., M. Vakilian, and E. Rahimpour. "transformer winding faults classification based on transfer function analysis by support vector machine." IET electric power applications, Vol.6, No.5, pp.268-276, 2012.

[136] Duan, Jiajun, Yigang He, and Wenjie Wu. "Fault localization on transformer winding by frequency response analysis and evidential reasoning." The Journal of Engineering, Vol.23, pp.9079-9082, 2019.

[137] Gómez-Luna, E., Cuadros-Orta, D. E., Candelo-Becerra, J. E., & Vasquez, J. C. "The Development of a Novel Transient Signal Analysis: A Wavelet Transform Approach." Computation, Vol.12, No.9, p.178, 2024.

[138] Arispe, J.C.G. and Mombello, E.E. "Detection of failures within transformers by FRA using multiresolution decomposition." IEEE Transactions on power delivery, Vol.29, No.3, pp.1127-1137, 2014.

[139] Pant, S., Nema, R.K. and Gupta, S, "Detecting faults in power transformers using wavelet transform." In 2021 IEEE 2nd International Conference On Electrical Power and Energy Systems (ICEPES), pp. 1-5, 2021.

[140] E. Gómez-Luna, G. Aponte Mayor, J. Pleite Guerra, D. F. Silva Salcedo and D. Hinestroza Gutiérrez, "Application of Wavelet Transform to Obtain the Frequency Response of a Transformer from Transient Signals—Part 1: Theoretical Analysis," in IEEE Transactions on Power Delivery, Vol. 28, No.3, pp.1709-1714, 2013.

[141] Rao, M. R., and B. P. Singh. "Detection and localization of inter-turn fault in the HV winding of a power transformer using wavelets." IEEE Transactions on Dielectrics and Electrical Insulation, Vol.8, No.4, pp.652-657, 2001.

[142] Firoozi, Hormatollah, Mohammad Kharezi, and Hasan Bakhshi. "Turn-to-turn fault localization of power transformers using neural network techniques." In 2009 IEEE 9th International Conference on the Properties and Applications of Dielectric Materials, pp. 249-252, 2009.

[143] Faridi, Mohsen, Ebrahim Rahimpour, Mohammad Kharezi, et al. "Localization of turn-to-turn fault in transformer using artificial neural networks and winding transfer function." In 2010 10th IEEE International Conference on Solid Dielectrics, pp. 1-4, 2010.

Hamed Shadfar received his M.Sc. degree from Semnan University, Semnan, Iran, in 2018 with First class distinction. He is working toward a Ph.D. in the Faculty of Electrical and Computer Engineering, Semnan University, Semnan, Iran. His major research interests include design, modeling, condition monitoring, and fault diagnosis of electric machines.

Hamid Reza Izadfar is currently an Associate Professor in the Electrical and Computer Engineering Department of Semnan University. His main research interests are the design and analysis of electric machines and drives.

IECO

This page intentionally left blank.

International Journal Of
Industrial Electronics Control and Optimization
Print ISSN: 3517-2645
Online ISSN: 3568-2645
Homepage: https://ieco.usb.ac.ir/

Formation Control of Quadcopters with Unknown Target Tracking and Obstacle avoidance Using PID and MPC Controller

Seyedeh Mahsa Zakipour Bahambari | Saeed Khankalantary

Department of Electrical Engineering, K.N. Toosi University of Technology, Tehran, Iran..[1,2]
Corresponding author's email: s.kalantary@kntu.ac.ir

Article Info

Article type:
Research Article

Article history:
Received: 07-June-2024
Received in revised form: 07-November-2024
Accepted: 27-November-2024
Published online: 22-June-2025

Keywords:
Quadcopter,
Position Control,
PID Controller,
Tube-MPC,
Multi-Agent Systèmes Control

ABSTRACT

This article focuses on the design of a controller for quadcopter position control, which is then used to organize a group of quadcopters into a specific formation. Initially, PID controllers are developed to manage all output variables of the quadcopter systems efficiently. Subsequently, a constrained tube-model predictive control (Tube-MPC) approach is implemented to regulate the system's position, comparing its performance to that of the tube-MPC controller. The article also explores the coordination of a group of six quadcopters, focusing on achieving a predefined formation that maintains the desired shape. Three different scenarios are examined to control the formation, assessing how each approach influences the arrangement and coordination of the quadcopters. The dynamics of the system's control are crucial for effective operation in multi-agent systems. Moreover, the configuration of the quadcopters is influenced by each quadcopter's internal controller, ensuring accurate formation and tracking. This study underscores the significance of sophisticated control strategies in improving the performance and coordination of multiple quadcopter systems.

NOMENCLATURE

m	Quadcopter total mass	r_a	Obstacle radios
l	Length of quadcopter arm	K_r	Constant coefficient
I_x	Rotational inertial along the x-axis	K_a	Constant coefficient
I_y	Rotational inertial along y-axis	k	Constant coefficient
I_z	Rotational inertial along z-axis	q_o	Circle position
j_r	Rotor's inertial	λ_i	Constant coefficient
g	Acceleration due to gravity	t_s	Formation transition time
		τ	Exponential rate
		d_i^1	Desired distanc

I. Introduction

In recent years, the field of quadcopters, also known as quadrotor helicopters, has experienced a surge in interest. These UAVs and other unmanned aerial vehicles are no longer limited to military applications but have expanded into civilian, research, and commercial domains. Examples of application scenarios range from military and law enforcement surveillance and reconnaissance to fire monitoring, agricultural services, and nuclear reactor inspection.

The unmanned aerial vehicle (UAV) system is rapidly advancing and proving highly practical in unmanned systems. Its affordability, ease of use, and versatility make it a standout. Among UAV types, the quadrotor stands out for its ability to

hover, take off, land vertically, and fly indoors. As applications and mission requirements grow more diverse, single UAV capabilities are becoming constrained, highlighting the importance of coordinating multiple UAVs for formation flights in various scenarios [1-3]. A fleet of cost-effective UAVs has the potential to substitute costly multi-functional drones in extensive, high-precision missions, thereby boosting mission success rates[4]. The quadrotor's dynamics present a challenge due to having six degrees of freedom but only four inputs. This results in nonlinear, coupled, and under-actuated dynamics, making control difficult. Furthermore, during formation flight, quadrotors are susceptible to aerodynamic effects and random disturbances, necessitating advanced control strategies for stable, autonomous flight. Various strategies have emerged to address these control challenges in formation flight. For instance, Fu et al. delved into algorithms that maintained and reconstructed formations by employing artificial potential fields [5]. While the initial dynamic model of quadcopters is the starting point for all studies, subsequent research has introduced more complex aerodynamic features [6, 7]. Certainty-equivalent model predictive control (MPC) is a contemporary optimization-driven control method widely employed across diverse industrial processes[8, 9]. Wolfe et al. demonstrated the effectiveness of distributed multi-model Model Predictive Control (MPC) for tracking ground targets using quadrotors. The control algorithm was executed on the UAV's onboard computer[10]. Kuriki et al. developed a formation controller with obstacle avoidance capabilities by leveraging distributed Model Predictive Control (MPC) and a linearized model[11]. Additionally, from a geometric perspective, an NMPC design was introduced in [12] to address obstacle avoidance and enable aggressive trajectory tracking. Zhou et al. devised a controller for inward collision avoidance utilizing nonlinear Model Predictive Control (NMPC). Their approach involved a first-order model in two-dimensional space[13]. Unlike certainty-equivalent MPC, robust Model Predictive Control (MPC) offers a feasibility guarantee for the controlled system, typically within a specified uncertainty range[14]. In implementing MPC controllers, the computational time required to derive the feedback law is a major concern. Significant efforts have been dedicated to addressing certainty-equivalent MPC[15]. While the MPC framework has been introduced in previous studies[16, 17], there remains a necessity for additional reduction in computational burden within the control algorithms to facilitate the practical implementation of formation flight. The computational resources conserved could then be allocated to expanding the prediction horizon by employing a more precise UAV dynamics model. Model Predictive Control (MPC) has been utilized in quadcopter systems to track reference trajectories while accommodating disturbances. Additionally, nonlinear H-infinity techniques have enhanced the system's robustness[18]. Different control methods have been investigated for quadcopter control, including PID controllers[19, 20]. Moreover, in most articles related to quadcopters, the primary focus is on the impact of disturbances, addressing simulation results, and, to a large extent, not concentrating on experimental studies[21, 22]. In [23], the fundamental aspects of modeling and controlling quadcopters are discussed as a basis for further research and developments in this field. In the article mentioned above, the differential dynamic equations of a quadcopter are presented and simulated; then, stability is addressed by implementing a PD controller. Additionally, in [24], the motor model of a quadrotor is investigated using body equations and nonlinear simulation. Furthermore, algorithms and tracking models are being utilized to enable a quadcopter to track objects and perform optimal movements accurately[25]. In this study, after examining the mathematical model of a quadcopter and its motion equations, algorithms and controls related to object tracking are adjusted to track objects and perform optimal movements intelligently. In another study[26], a PID controller was designed to control a quadcopter's height, attitude, direction, and position. Subsequently, a PID controller is proposed for the nonlinear model, and the results are analyzed, concluding with a simple interfering PID controller for path tracking. Additionally, extensive research has been conducted on the group arrangement of quadcopters. For example, in[27], a distributed predictive model-based controller is suggested based on consensus theory for the group control of quadcopters. This controller addresses issues such as collision avoidance, obstacle avoidance, and maintaining communication topology during the movement of agents to achieve the desired formation. On a broader scale, a collision avoidance system based on herd decentralization by defining an anti-Laplacian matrix is provided[28]. Moreover, methods and regulations for arranging quadcopters are detailed and simulated in[29]. A robust model predictive control (MPC) approach has been proposed for quadcopter trajectory tracking, addressing the challenges of nonlinearity and disturbances by utilizing differential flatness for variable reformulation. This method transforms the trajectory tracking problem into the stabilization of a constrained linear time-invariant system, enabling effective control under disturbances. The approach is validated through simulations and experiments, demonstrating its capability to maintain robust tracking despite external disturbances in [30]. in [31] presents a tube-based nonlinear model predictive control (NMPC) strategy tailored for non-holonomic systems. The approach addresses the challenge of handling system constraints and disturbances by creating a robust control tube around the desired trajectory, ensuring stability and constraint satisfaction in real-time applications. In [32], formation control of quadcopters with mixed constraints is discussed, and other studies have investigated formation tracking control for a group of quadcopters with desired predefined trajectories in[33]. These challenges arise from

several factors, including the methodology used for control design, the need for effective communication among all agents, the potential for collisions, and the intrinsic complexity of quadcopter dynamics.[34, 35]. In [36], the author uses a leader-follower approach to form and control unmanned surface vehicle (USV) networks. The authors address the challenges posed by system uncertainties and stochastic disturbances in maintaining the formation. They propose a robust control method designed to handle these uncertainties and random disturbances, ensuring the stability of the formation. In [37] considered the DOCC of MASs with input saturation and collision avoidance constraints. On the other hand, [38] explore a method for localizing a radio frequency (RF) source by leveraging the presence of obstacles and their reflective properties. The authors propose a technique that uses a map of obstacles in the environment to enhance the accuracy of RF source localization. By accounting for reflections off surfaces, the method improves localization precision in complex environments where direct line-of-sight might be obstructed. The study demonstrates that incorporating information about obstacles and reflections significantly enhances the ability to pinpoint the RF source's location accurately.

The simulation results presented in the paper demonstrate the effectiveness of the proposed method under various environmental conditions and disturbances. The main contributions of this paper are as follows:

- Design a constrained Tube-MPC controller and compare it with a PID controller with a Disturbance
- Apply single-integrator formation to the nonlinear model with PID controller with three scenarios

This study begins by presenting the nonlinear and linear models of the quadcopter. Subsequently, a PID controller is crafted for the nonlinear model. The design process extends to developing PID and Tube-MPC controllers for the linear system. Furthermore, a continuous endeavor involves formulating a single integrator formation control for a fleet of six quadcopters, explicitly defining control inputs for tracking an unknown target. Lastly, the concluding section showcases simulations and outputs for each phase, facilitating a comprehensive comparative analysis.

The structure of this paper is outlined as follows: Section II describes the mathematical model of the quadcopter, while Section III presents the controllers. Section IV provides the formation control of a multi-agent quadcopter. Section V offers a simulation of controllers and formation of quadcopters. Lastly, the concluding remarks are shown in the final section.

II. Quadcopter Model

A typical quadcopter features four rotors arranged in a cross configuration. Adjusting the throttle involves simultaneously increasing or decreasing the speeds of all four rotors equally, generating a vertical force (U_1) in the body-fixed frame, which enables the quadcopter to ascend or descend. As shown in Fig. 1, controlling the roll movement involves increasing the speed of the left rotor while decreasing the speed of the right rotor. Similarly, pitch movement is controlled by applying the same process to the other two rotors. For yaw motion control, the quadcopter adjusts the front and rear rotors to rotate counterclockwise while the other two rotors rotate clockwise. This allows the quadcopter to perform a yawing maneuver by increasing the speed of the counterclockwise rotating motors and reducing the speed of the clockwise rotating motors.

Two reference frames are established to describe the dynamics of the quadcopter, as depicted in Fig. 1. The quadcopter's orientation is defined by three Euler angles: roll angle (θ), pitch angle (φ), and yaw angle (ψ). The vector $\Omega^T = (\varphi, \theta, \psi)$ represents these Euler angles, specifying the object's orientation. The vehicle's position in the inertial frame is given by the vector $r^T = (x, y, z)$The rotation matrix R is used to transform vectors from the body-fixed to the inertial frame. In this context, terms like $c\theta$ denote the cosine of θ, and $s\theta$ denote the sine of θ, facilitating the transformation between these frames.

$$R = \begin{bmatrix} c\psi.c\theta & c\psi.s\theta.s\varphi - s\psi.c\varphi & c\psi.s\theta.c\varphi + s\psi.s\varphi \\ s\Psi.c\theta & s\psi.s\theta.s\varphi + c\psi.c\varphi & s\psi.s\theta.c\varphi - c\psi.s\varphi \\ -s\theta & c\theta.s\varphi & c\theta.c\varphi \end{bmatrix} \quad (1)$$

Each rotor generates a thrust force perpendicular to its plane of rotation and produces an induction moment that opposes the rotor's direction of rotation. The thrust force for each rotor is specified as follows:

$$T = \sum_{i=1}^{4} |F_i| = b.\sum_{i=1}^{4} \omega_i^2 \quad i = 1,2,3,4 \quad (2)$$

where b represents the constant thrust coefficient, and w_i denotes the angular speed of each rotor [7]. The aerodynamic moment produced by the rotors is defined as follows:

$$\tau_i = d.\Omega_i{}^2 \quad i = 1,2,3,4 \quad (3)$$

where d is the constant drag coefficient of the propeller [7]. The external forces and torques acting on the quadcopter are determined according to criteria (3).

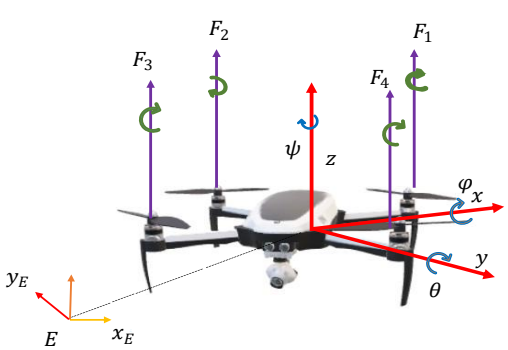

Fig. 1. Configuration inertia and body fixed frame

$$F_B = \begin{pmatrix} 0 \\ 0 \\ b(\omega_1^2 + \omega_2^2 + \omega_3^2 + \omega_4^2) \end{pmatrix} \quad (4)$$

The speeds produced are used to generate a relative speed, F_B, Which is required for quadcopter dynamics, as shown in Equation(4).

$$M = \begin{pmatrix} Lb(\omega_3^2 - \omega_4^2) \\ Lb(\omega_1^2 - \omega_2^2) \\ d(\omega_1^2 + \omega_2^2 - \omega_3^2 - \omega_4^2) \end{pmatrix} \quad (5)$$

the torque M consists of $\tau_\varphi, \tau_\theta, \tau_\psi$ which is the moment's input provided to the actuators to create the angular positional changes. L being the distance between the rotor and the center of mass of the quadcopter, d They can be explained in equation (5).

Overall dynamic model in the following form[38]:

$$\begin{aligned}
\ddot{x} &= -(\cos\varphi \cdot sin\,\theta \cdot \cos\psi + sin\varphi . sin\psi).\frac{U_1}{m} \\
\ddot{y} &= (\cos\varphi \cdot sin\,\theta \cdot cos\,\psi - sin\varphi . sin\,\psi).\frac{U_1}{m} \\
\ddot{z} &= -g + (\cos\varphi \cdot \cos\theta).\frac{U_1}{m} \\
\ddot{\varphi} &= \dot{\theta}\dot{\psi}\left(\frac{I_{yy} - I_{zz}}{I_{xx}}\right) - \frac{J_r}{I_{xx}}\dot{\theta}\Omega_r + \frac{\mathcal{L}}{I_{xx}}U_2 \\
\ddot{\theta} &= \dot{\phi}\dot{\psi}\left(\frac{I_{zz} - I_{xx}}{I_{yy}}\right) + \frac{J_r}{I_{yy}}\dot{\varphi}\Omega_r + \frac{\mathcal{L}}{I_{yy}}U_3 \\
\ddot{\psi} &= \dot{\theta}\dot{\varphi}\left(\frac{I_{xx} - I_{yy}}{I_{zz}}\right) + \frac{1}{I_{zz}}U_4 \\
\Omega_r &= (\omega_1 + \ \omega_2 + \ \omega_3 + \omega_4)
\end{aligned} \quad (6)$$

where g is the gravity coefficient, m is the mass of the quadcopter, φ, θ, ψ represent roll , pitch , and aw . I_{xx}, I_{yy}, I_{zz} is the total moment of inertia , J_r is the rotor moment of inertia, Ω_r is the total of gular speed , U_1, U_2, U_3, U_4 are th control inputs .

$$\begin{aligned}
\omega_1^2 &= \frac{T}{4K} - \frac{\tau_\theta}{2Kl} - \frac{\tau_\psi}{4b} \\
\omega_2^2 &= \frac{T}{4K} - \frac{\tau_\phi}{2Kl} + \frac{\tau_\psi}{4b} \\
\omega_3^2 &= \frac{T}{4K} - \frac{\tau_\theta}{2Kl} - \frac{\tau_\psi}{4b} \\
\omega_4^2 &= \frac{T}{4K} - \frac{\tau_\phi}{2Kl} + \frac{\tau_\psi}{4b}
\end{aligned} \quad (7)$$

$$U_1 = b(\omega_1^2 + \omega_2^2 + \omega_3^2 + \omega_4^2) \quad (8)$$

$$\begin{aligned}
U_2 &= b(\omega_3^2 - \omega_4^2) \\
U_3 &= b(\omega_1^2 - \omega_4^2) \\
U_4 &= d(\omega_1^2 + \omega_2^2 - \omega_3^2 - \omega_4^2)
\end{aligned}$$

Equation 7 is implemented to receive torques and generate the angular velocity of motors. Subsequently, the input control of the model dynamics is presented in Equation 6 .

$$\frac{d}{dt}\begin{bmatrix}\dot{\theta} \\ i_a\end{bmatrix} = \begin{bmatrix} -\frac{B_m}{J} & -\frac{K_t}{J} \\ -\frac{K_t}{J} & -\frac{R_t}{J}\end{bmatrix}\begin{bmatrix}\dot{\theta} \\ i_a\end{bmatrix} + \begin{bmatrix}0 \\ \frac{1}{L_a}\end{bmatrix}v \quad (9)$$

$$y = \begin{bmatrix}1 & 0\end{bmatrix}\begin{bmatrix}\dot{\theta} \\ i_a\end{bmatrix} \quad (10)$$

Equations 9 and 10 present the state-space model of the DC motor introduced in[39]The transfer function is derived and should be positioned within Block 3 before the equations by utilizing these equations. To linearize the above equations, ϕ ,and θ are considered small and ψ is considered to be zero. So that after linearization, they can be effectively neglected.

$$\begin{aligned}
\dot{X} &= AX + BU \\
Y &= CX + DU
\end{aligned} \quad (11)$$

$$A = \begin{bmatrix}
0 & 1 & 0 & 0 & 0 & 0 & 0 & 0 & 0 & 0 & 0 & 0 \\
0 & 0 & 0 & 0 & 0 & 0 & 0 & 0 & 0 & 0 & 0 & 0 \\
0 & 0 & 0 & 1 & 0 & 0 & 0 & 0 & 0 & 0 & 0 & 0 \\
0 & 0 & 0 & 0 & 0 & 0 & 0 & 0 & 0 & 0 & 0 & 0 \\
0 & 0 & 0 & 0 & 0 & 1 & 0 & 0 & 0 & 0 & 0 & 0 \\
0 & 0 & 0 & 0 & 0 & 0 & 0 & 0 & 0 & 0 & 0 & 0 \\
0 & 0 & 0 & 0 & 0 & 0 & 0 & 1 & 0 & 0 & 0 & 0 \\
0 & 0 & g & 0 & 0 & 0 & 0 & 0 & 0 & 0 & 0 & 0 \\
0 & 0 & 0 & 0 & 0 & 0 & 0 & 0 & 0 & 1 & 0 & 0 \\
-g & 0 & 0 & 0 & 0 & 0 & 0 & 0 & 0 & 0 & 0 & 0 \\
0 & 0 & 0 & 0 & 0 & 0 & 0 & 0 & 0 & 0 & 0 & 1 \\
0 & 0 & 0 & 0 & 0 & 0 & 0 & 0 & 0 & 0 & 0 & 0
\end{bmatrix} \quad (12)$$

$$B = \begin{bmatrix}
0 & 0 & 0 & 0 \\
0 & \frac{1}{I_x} & 0 & 0 \\
0 & 0 & 0 & 0 \\
0 & 0 & \frac{1}{I_y} & 0 \\
0 & 0 & 0 & 0 \\
0 & 0 & 0 & \frac{1}{I_z} \\
0 & 0 & 0 & 0 \\
0 & 0 & 0 & 0 \\
0 & 0 & 0 & 0 \\
0 & 0 & 0 & 0 \\
\frac{1}{m} & 0 & 0 & 0
\end{bmatrix} \quad (13)$$

$$C = I_{12\times12} \quad (14)$$

$$D = 0_{12\times4} \quad (15)$$

III. Control Scheme

In this section, the attitude control of the quadcopter is first investigated. Then, the position and attitude of the quadcopter are controlled. The PID, Tube-MPC algorithm is used for attitude and position control of the quadcopter.

A. PID Controller

At the beginning of this section, we design a PID controller for a non-linear system. In this context, we consider the reference values for both x and y to be 10 cm, and the reference value for z to be 20 cm. Moreover, the objective is to bring all angles to zero. The implementation diagram of the PID controller on the quadcopter is illustrated in Fig. 2 .

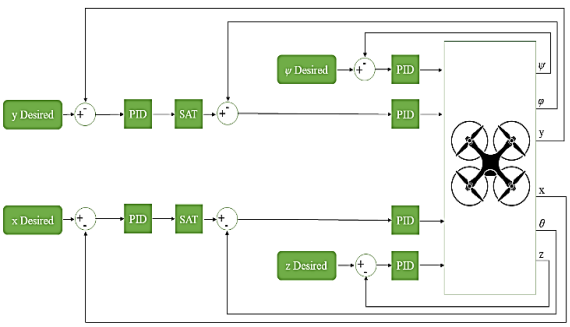

Fig 2. Control diagram for quadcopter system

In the design of the controller for the nonlinear system, the saturation value has been considered in the range of $-\frac{\pi}{36}$ to $\frac{\pi}{36}$. In this case, the PID controller coefficients are obtained through a trial-and-error method to achieve admissible settling time. The PID controller control equation is as follows:

$$u(t) = K_p e(t) + K_i \int e(t)dt + K_d \frac{de(t)}{dt} \qquad (16)$$

$$i = 1,2,3,4,5,6$$

In (16), K_p represents the proportional gain, K_i represents the integral gain and K_d represents the derivative gain. Furthermore, $e(t)$ represents the error between the desired value and the output.

In the Quadcopter system, there are six positional states (x, y, z) and three angular orientations (φ, θ, ψ). However, only four control inputs are available, represented by the angular velocities of the four rotors, denoted as ω_i. The relationship between these states and the total thrust (T) and torque (τ) generated by the rotors is described in the Quadcopter's dynamics, as shown in Equation (1) The total thrust (T) primarily affects the acceleration along the Z-axis, which is g the Z-axis, crucial for maintaining the Quadcopter airborne. Meanwhile, torque τ_φ influences the angular acceleration around the φ angle, torque τ_θ impacts the angular acceleration around the θ angle, and torque τ_ψ contributes to the angular acceleration around the ψ angle. As shown in Fig. 3.

$$\begin{aligned} T &= \big(g + u_1(t)\big) \times \frac{m}{cos\varphi . cos\theta} \\ \tau_\varphi &= \big(u_2(t)\big) \times I_{xx} \\ \tau_\theta &= \big(u_3(t)\big) \times I_{yy} \\ \tau_\psi &= \big(u_4(t)\big) \times I_{zz} \end{aligned} \qquad (17)$$

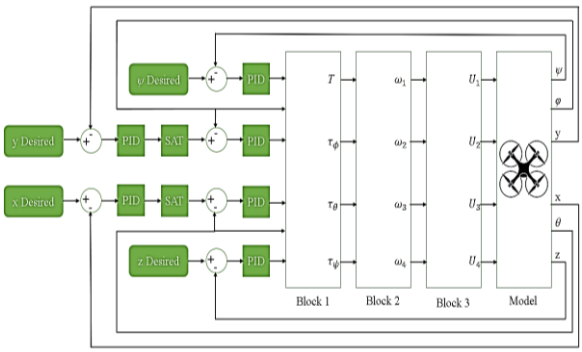

Fig. 3. Control nonlinear dynamic with motor dynamic schematic

B. Tube-MPC Control

This section addresses the design of a Tube-Model Predictive Control (Tube-MPC) for the position control of a quadcopter. Generally, the key advantages of this controller over a PID controller lie in its online nature and adaptability. However, it is worth noting that the Tube-MPC controller tends to be slower than PID, and its implementation on the system is consistently more challenging. The Tube-MPC Controller solves a finite-horizon optimal control problem with constraints on the system at each sampling instant. After solving the problem at each sampling time, it optimizes the system state and then computes the optimal solution for the new state in the next sampling time. To address Tube-MPC problems, the cost function is formulated as follows:

$$J_0(X(0), U_0) = p(X) + \sum_{k=0}^{N-1} q\big(X(K), U(K)\big) \qquad (18)$$

In which $p(x_N)$ represents a Lyapunov function in the form of $p(x_N) = X^T P X$, and $q(X(K), U(K))$ is a quadratic function expressed as $q(X(K), U(K)) = X^T Q X + U^T R U$. Additionally, U_0 denotes the input set over the time interval from 0 to $N-1$.

In general, the solution framework for Tube-MPC problems is as follows:

$$\begin{aligned} &J_0^*\big(X(0)\big) = \min_{U0} J_0(X(0), U_0) \\ &s.t.\ \ X_{k+1} = AX_k + BU_k \qquad k = 0, \dots., N-1 \\ &X_k \in \chi \ \ U_k \in \mathcal{U} \qquad k = 0, \dots., N-1 \\ &\left|\frac{dU}{dt}\right| \le constant \\ &X_N \in \chi_f \\ &X_0 = X(0) \end{aligned} \qquad (19)$$

N is the time horizon and χ, $\mathcal{U}$, χ_f are polyhedral regions.

The introduction of constraints results in a reduction of the adequate size of polyhedral regions. This reduction raises the possibility of encountering situations where a solution for the equation may not be feasible. In response, Tube-MPC controllers can be designed to offer maximum saturation, minimum saturation, or zero, aligning with the specific requirements of the target quadcopter.

The Tube-Model Predictive Control (Tube-MPC), functioning as an online controller, necessitates careful considerations when selecting a control or prediction horizon. Opting for a more extensive horizon may solve the system in a longer time step. Two strategies can be employed for those seeking solutions within a more minor time step. Firstly, one may reduce the control or prediction horizon, understanding that such an adjustment may impact system performance. Alternatively, the use of Explicit Tube-MPC offers a second solution. In this approach, the minimizing answer is computed and provided to the system as a function. However, this solution comes with the drawback of requiring substantial memory, rendering it both costly and resource-intensive. Consequently, quadcopters equipped with larger motors must effectively manage this added load.

Furthermore, in this article, all computations are done by Tube-MPC block in MATLAB-Simulink. Therefore, we designed a Tube-MPC controller by adding four PD controllers to the Tube-MPC block, for this Fig. 4 ., Present a block diagram in Simulink of MATLAB.

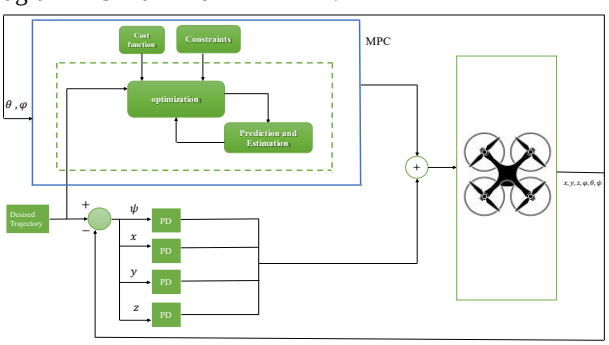

Fig. *4* . Tube MPC schematic

IV. Formation Controller

The proposed framework assumes that each quadrotor within the system senses the positions of other swarm members relative to a reference coordinate system. The control structure incorporates both inner and outer control loops. The inner loop is responsible for stabilizing the platform within a quadrotor, while the outer loop is dedicated to tracking a reference path. Due to the considerable difference in time constants between these two loops, they can be effectively decoupled into low- and high-level dynamics[40], Specifically, high-level dynamics are employed for swarm control, as shown in Fig. 5, which depicts a schematic representation of the controlled nonlinear dynamics in formation.

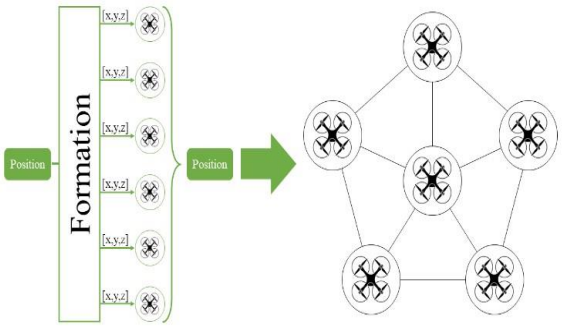

Fig. 5. Schematic Formalization of Nonlinear Controlled Systems

A. Formation Helix

This section aims to leverage the dynamics of a nonlinear quadcopter model to guide a subset of quadcopters toward a specific formation. To accomplish, this, we consider a group comprising six quadcopters .Ultimately, the goal is for all quadcopters to converge into a specific shape. The chosen formation strategy is based on a single-integrator integral-bilayer formation model. The noteworthy aspect involves integrating the dynamics of the nonlinear system controlled in Section Three into the formation strategy.

A nondirectional graph, denoted as G, can be defined as a tuple (V, E), where V represents the set of vertices (1, 2, …, n), and E is a subset of $V \times V$,Constituting the undirected edges. Notably, the inclusion of the vertex pair (i,j) in E implies the inclusion of its counterpart (j,i).

Given an arbitrary ordering of the edges in E, the edge function ϕ: $\mathbb{R}^{nm} \rightarrow \mathbb{R}^{l}$ for a framework F = (G, q), where G = (V, E), is defined as follows [24]:

$$\phi(q) = \left[\dots, \left\|q_i - q_j\right\|^2, \dots\right], \quad (i,j) \in E \tag{20}$$

where q_i represents *i*'th agent position, and the kth component of (19), described as $\left\|q_i - q_j\right\|^2$Corresponds to the kth edge in E connecting vertices i and j. When delving into the infinitesimal rigidity analysis, a framework's rigidity matrix becomes a valuable tool. The rigidity matrix, denoted as R: $\mathbb{R}^{nm} \rightarrow \mathbb{R}^{l\times nm}$, is defined as:

$$R(q) = \frac{1}{2}\frac{\partial \phi(q)}{\partial q} \tag{21}$$

We also represent the relative position of the two agents as follows:

$$\tilde{q}_{ij} = q_i - q_j \tag{22}$$

And consider $\tilde{q} = [\dots, \tilde{q}_{ij}, \dots] \in \mathbb{R}^{ml}$ where $(i,j) \in E^*$, maintaining the same term order as defined in the edge function (19). The distance error is expressed as:

$$e_{ij} = \left\|\tilde{q}_{ij}\right\| - d_{ij} \quad (23)$$

Systems. If we consider $z_{ij} = \left\|\tilde{q}_{ij}\right\|^2 - d_{ij}^2$, According to (19), we can express the equation as follows:

$$z_{ij} = e_{ij}(e_{ij} + 2d_{ij}) \quad (24)$$

Given the above equations, we have the following theories:

Theorem1. Considering the formation $F(t) = (G^*, q(t))$, And assuming that the initial conditions of the error dynamics satisfy $e(0) \in \Omega_1 \cap \Omega_2$, where:

$$\Omega_1 = (e \in \mathbb{R}^l \mid \psi(F, F^*) \leq \delta),$$
$$\Omega_2 = (e \in \mathbb{R}^l \mid dist\big(q, Iso(F^*)\big)\ dist\big(q, Amb(F^*)\big)) \quad (25)$$

where δ represents a suitably small positive constant. The control law is defined as follows:

$$u = u_a := -K_v R^T(\tilde{q}) z \quad (26)$$

And $K_v > 0$ denoting a user-defined control gain. The introduced control law helps the system reach a specific form by considering the distance of agents from their desired values[29].

Theorem2. Considering the formation $F(t) = (G^*, q(t))$ with initial conditions on $e(0)$ as specified in Theorem 1, the control $u = u_a + 1_n \otimes h$, where $u_a = [u_{a1}, \dots, u_{an}]$ defined in (18), and $h = (K_1 + 1)e_T + \hat{v}_T - u_{an}$ Enables the agents to track an unknown object. Where $\hat{v}_T$ Represent target velocity that assumed to be measured by sensors and received by agent 6 and e_T defined.The proof of Theorem 1 and Theorem 2 has been presented in[29]

$$e_T = \begin{bmatrix} x_r \\ y_r \\ z_r \end{bmatrix} - \begin{bmatrix} x_{Agent\ 6} \\ y_{Agent\ 6} \\ z_{Agent\ 6} \end{bmatrix} \quad (27)$$

Formation and Obstacle Avoidance

The following section considers formation and obstacle avoidance in placing quads in a line formation while avoiding the sphere obstacle. The general equations of double integrator with obstacle avoidance can be written as follows:

$$\ddot{q}_i = u_i \quad (28)$$
$$u_1 = \ddot{q}_d + (\dot{q}_d - \dot{q}_1) + (q_d - q_1) + u_{oi} \quad (29)$$
$$r_i = \|q_i - q_0\| - R \quad (30)$$
$$u_i = \sum_j \frac{K_r(q_i - q_j)}{\|q_i - q_0\|} + \sum_j K_a\left((q_j - q_i) + (\dot{q}_j - \dot{q}_i)\right) \quad (31)$$

In the above equations, position is defined as $q = \begin{bmatrix} x \\ y \\ z \end{bmatrix}$. In this formation, even the leader gets control input, as shown in (29). The first part consists of the difference between desired acceleration, velocity, and position and the first agent's acceleration, velocity, and position. The second part of the control input (u_{oi}) Is added to avoid collision as follows:

$$u_{oi} = \begin{pmatrix} K\frac{q_i - q_0}{r_i^2}\left(\frac{1}{r_i} - \frac{1}{r_a}\right) & , r_i \leq r_a \\ 0 & , otherwise \end{pmatrix} \quad (32)$$

In (30), R is the radius of an obstacle, q_i is the position of ith agent and q_o is the position of obstacle (30) is the input control for other agents.

Variation formation

Variation formation in quadcopters, often termed formation control, involves the coordination of multiple quadcopters to maintain a specific spatial configuration during flight. This is achieved through leader-follower models, Model Predictive Control (MPC) The leader-follower approach ensures followers adjust their positions relative to a designated leader, maintaining formation integrity[41] MPC optimizes trajectories for obstacle avoidance and efficient movement, while MPC ensures robust convergence to desired formations despite disturbances. These advanced strategies are pivotal in applications such as surveillance, search and rescue, and environmental monitoring, allowing for precise and reliable multi-agent coordination.

In this section, system is same as the system in (22), even though formation changes after t_s and the relation and distance between agents is determined through the following equation

$$d_i = (d_i^1 - d_i^2)\left(1 - e^{-\tau(t - t_s)}\right)u(t - t_s) \quad (33)$$

According to (33), j and i in d_i^j show the position of the quad in varying formation and the ith agent, respectively. Then, control input is applied to system as follows:

$$u_i = \lambda_1(q_1 - q_i - d_i) + \lambda_2(\dot{q}_1 - \dot{q}_i) \quad (34)$$

V. Simulation and Results

This section explores three scenarios involving various modes of PID and Tube-MPC controllers and their behavior in the presence and absence of disturbances. Subsequent analysis illustrates Tube-MPC controllers' performance under disturbed and undisturbed conditions. Table 1 provides the constant values utilized in the quadcopter simulation.

It is important to note that this discussion is divided into two sections. In the first section, two internal controllers are designed and compared. The second section considers three scenarios for formation control using the selected controller.Table I. Model design parameter.

Table I. Model design parameter

Symbol	Parameter	Value	Unit
m	*Quadcopter total mass*	0.8	kg
l	*Length of Quadcopter arm*	0.3	*m*
I_x	*Rotational inertia along x − axis*	0.01567	kg.m^2
I_y	*Rotational inertia along y-axis*	0.01567	kg.m^2
I_z	*Rotational inertia along z − axis*	0.0283	kg.m^2
J_r	*Rotor's inertia*	6.01e-5	kg.m^2
g	*Acceleration due to gravity*	9.81	$m.s^2$

A. Comparison PID and Tube-MPC Controller

The mathematical model of the quadcopter vehicle and its associated control systems were constructed in MATLAB/Simulink to facilitate simulation. The primary goal of this analysis is to assess the control algorithms' efficacy in preserving the quadcopter's stability. The initial state assumes the quadcopter is in hover mode with specific pitch, roll, and yaw angles. Then, the quadcopter is commanded to transition into a stable state where these angles gradually approach their desired values. Both control strategies are applied in this scenario, and their outcomes are subsequently compared. The gains for the classical PID controller were determined using the Ziegler-Nichols method. We used this approach to determine the PID and Tube-MPC gain parameters presented in Table II. and Table III.

Furthermore, linearized equations are utilized to design the Tube-MPC controller on this system, with a sampling time of 0.001 considered. Moreover, a prediction horizon of 20 and a control horizon of 15 are chosen. On the other hand, the input and output weight values are denoted by $R = diag(0.73891,0.73891,0.73891,0.73891)$ and $Q = diag(10,1,10,0,1,1,100,10,100,10,100,0) \times 7.3891$, Respectively. It should be emphasized that all these values have been determined through trial and error. The coefficients of these four controllers are as follows according to Table III.

Table II. PID controller coefficients for the nonlinear system

	K_p	K_i	K_d
ψ	2	10	2
ϕ	3	10	2
θ	1	0	0.2
x	0.1	0	0.7
y	0.01	0	0.2
z	1	0.5	0.5

Table III. PD controller coefficients for the Tube MPC

controller	K_p	K_d
PD_1	-52.087	-22.98
PD_2	1	0
PD_3	1	0
PD_4	9.94	2.57

The results of applying two controllers to the system are Shown from Fig. 6 . to Fig. 7 . , This clearly shows the system's successful stabilization by the PID and Tube-MPC controller with position and Angles. Moreover, the system outputs have precisely attained the desired reference values. These visuals also illustrate the effective stabilization achieved by the Tube-MPC controller. To investigate the robustness of the design, a disturbance is added from second 5th onwards, which is the sum of a step function and a sinusoidal function with an amplitude of 0.7, to the values of ϕ, θ andψ.

The performance of PID and Tube-MPC controllers was evaluated for both position and angle response characteristics, using key control parameters: Rise Time (RT) and settling Time (ST) These parameters were extracted and analyzed based on the system's position (x,y,z) and angle (ϕ, θ, ψ) responses, specifically focusing on each controller's ability to achieve stability, precision, and rapid response.

The results of the position response for both PID and Tube-MPC controllers reveal a significant difference in their performance. Tube-MPC demonstrated a faster response across all axes, with lower rise times and settling times than PID. Furthermore, the Tube-MPC controller achieved zero overshoot for all position axes, indicating a more stable and precise control behavior. In contrast, the PID controller exhibited a noticeable overshoot, especially in the x and y axes, which could result in oscillations and prolonged settling times. This behavior illustrates the advantage of Tube-MPC in applications where quick and precise positioning is critical.

For the angle responses, the Tube-MPC controller also generally outperformed the PID controller in terms of rise time and settling time, especially in the ϕ and θ axes. The Tube-MPC reached the desired angle with minimal overshoot, ensuring smoother control. In the ψ axis, both controllers experienced high overshoot due to the inherent dynamics of this axis. Still, Tube-MPC achieved a faster settling time, indicating its ability to stabilize even in challenging conditions. This comparison demonstrates Tube-MPC's superiority in achieving quicker and more stable angular responses across multiple axes. All these changes have been calculated in Table IV and Table V, and for IAE and ISE in TableVI and Table VII.

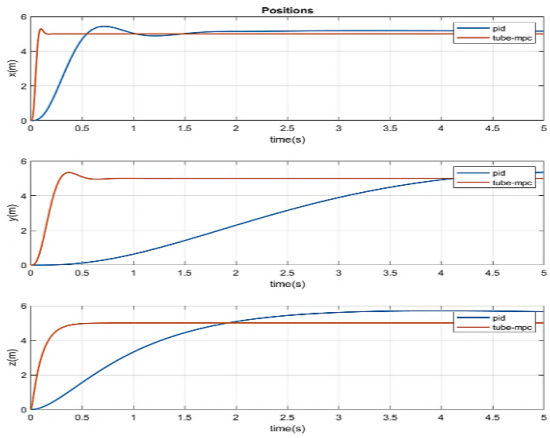

Fig. *6* . Comparison between PID and Tube-MPC position control

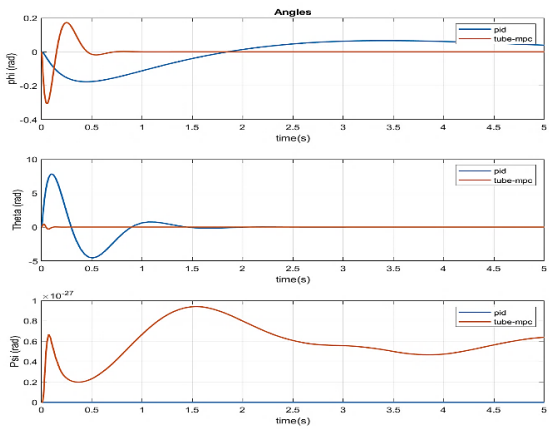

Fig. *7* . Comparison between PID and Tube-MPC attitude control

Table IV. COMPARISON OF CLASSICAL Angles PID AND Tube-MPC Controller

Angle	RT-pid	RT-Tube-mpc	OS-pid	OS-Tube-mpc	ST-pid	ST-Tube-mpc
Roll	0.3	0.15	0.15	0	1	0.5
Pitch	0.3	0.15	0.05	0.002	0.7	0.3
Yaw	0.4	0.3	0.4	0.3	2.5	2

Table V. COMPARISON OF CLASSICAL Position PID AND Tube-MPC Controller

Position	RT-pid	RT-Tube-mpc	OS-pid	OS-Tube-mpc	ST-pid	ST-Tube-mpc
x	0.3	0.15	1.2	0.01	1	0.6
y	1.2	0.3	0.4	0.3	5.1	0.6
z	1.5	0.2	0	0	3.5	0.5

Table VI. COMPARISON OF IAE and ISE for Angles PID AND Tube-MPC Controller

Angle	IAE-pid	IAE-Tube-mpc	ISE-pid	ISE-Tube-mpc
Roll	2.5	0.3	2	0.1
Pitch	1.8	0.2	1.5	0.1
Yaw	3.5	3	2	1.8

Table VII. COMPARISON OF IAE and ISE for Position PID AND Tube-MPC Controller

Position	IAE-pid	IAE-Tube-mpc	ISE-pid	ISE-Tube-mpc
x	3	1	2.5	0.5
y	5	1.2	4	0.6
z	4	0.8	3.5	0.4

B. Formation Control

The results reveal that the Tube-MPC controller effectively rejects disturbances and accurately controls all outputs. Ultimately, we explore a problem involving six agents and conduct comprehensive simulations to implement formation control on a nonlinear model.

At this juncture, it is essential to outline three scenarios to illustrate the controller's performance. The forthcoming discussion will encompass these scenarios, showcasing the robustness and precision of the Tube-MPC controller in various formation control task.

C. Formation Helix

In this scenario, we chose these parameters for the helix formation, adjoint matrix is shown in (35).

$$A = \begin{bmatrix} 0 & 1 & 1 & 1 & 1 & 1 \\ 1 & 0 & 1 & 1 & 1 & 1 \\ 1 & 1 & 0 & 1 & 1 & 1 \\ 1 & 1 & 1 & 0 & 1 & 1 \\ 1 & 1 & 1 & 1 & 0 & 1 \\ 1 & 1 & 1 & 1 & 1 & 0 \end{bmatrix} \tag{35}$$

Additionally, the desired distance matrix has been defined below:

$$d = \begin{bmatrix} 0 & 1.1756 & 1.9021 & 1.9021 & 1.1756 & 1 \\ 1.1756 & 0 & 1.1756 & 1.9021 & 1.9021 & 1 \\ 1.9021 & 1.1756 & 0 & 1.1756 & 1.9021 & 1 \\ 1.9021 & 1.9021 & 1.1756 & 0 & 1.1756 & 1 \\ 1.1756 & 1.9021 & 1.9021 & 1.1756 & 0 & 1 \\ 1 & 1 & 1 & 1 & 1 & 0 \end{bmatrix} \tag{36}$$

Furthermore, to achieve the formation among agents, The value of K_v has been set to 50, and K_1 has been set to 1 Q top from the helix formation for the three dimensions x, y, and z is established in Equation (37)

$$\begin{aligned} x_r &= 5\,sin\frac{\pi}{20}t \\ y_r &= 5\,cos\frac{\pi}{20}t \\ z_r &= 0.1t \end{aligned} \tag{37}$$

The value of the target velocity, assumed to be estimated, is represented below:

$$\hat{v}_T = \begin{bmatrix} \frac{\pi}{4}cos\frac{\pi}{20}t \\ -\frac{\pi}{4}sin\frac{\pi}{20}t \\ 0.1 \end{bmatrix} \tag{38}$$

Therefore, the chart of the formation factors is illustrated in Fig. 8 . Based on Fig. 8 . , it can be concluded that all six

controlled nonlinear dynamic factors have successfully reached the desired formation and can follow the helix formation. Therefore, the results indicate that controlled system dynamics can be employed instead of conventional formation methods to format agents . This involves initially controlling the agents using an internal controller and then applying the specified formulas to the system dynamics, determining the path for helix formation so that they reach a defined form and can be accurately tracked.

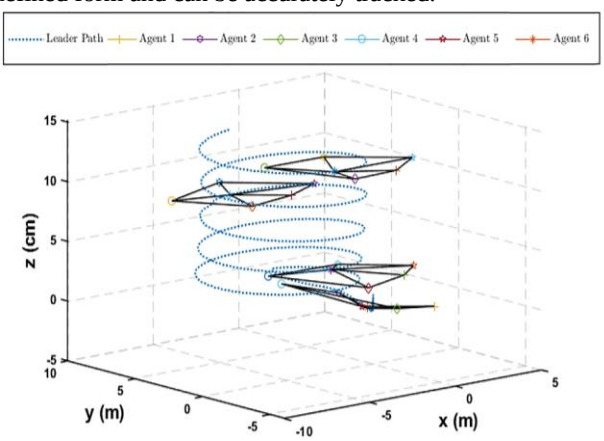

Fig. *8* . Agents' formation in desired path

a) Formation and Obstacle Avoidance

Now, 6 agents choose a line formation and track a particular path. An obstacle is positioned in the path's middle, and agents must bypass it within a determined distance. Parameters of obstacle-avoiding formation are depicted in Table VIII. And it's present in Fig. 9 .

Table VIII. obstacle avoiding formation parameters

symbol	*parameter*	*value*
r_a	*Obstacle radios*	5
k_r	*Constant coefficient*	0.05
k_a	*Constant coefficient*	10
K	*Constant coefficient*	10
q_0	*Circle position*	(10,10,2.5)

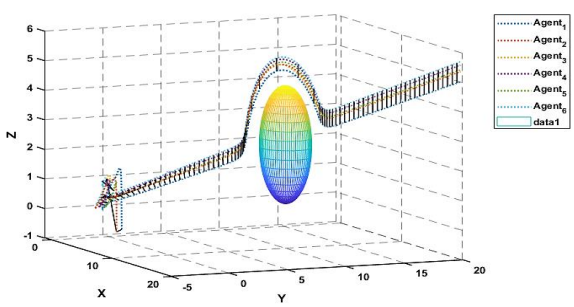

Fig. *9* . Obstacle avoiding formation

D. Variation formation

In this section, time-varying formation is considered. Before the 50s, formation was as a line, and afterward, it was changed to a pentagon shape, as illustrated in Fig. 10 . The Z trajectory is considered zero in the plotting. It is evident from Fig. 10 that agents have to keep their line formation while avoiding the collision through the trajectory. Parameters and gains regarding this formation are shown in Table IX. For better illustration, time-varying formation in 2D can be seen in Fig. 11 .

TABLE IX. VARIATION FORMATION PARAMETERS

symbol	*parameter*	*value*
λ_1	*Constant coefficient*	5
λ_2	*Constant coefficient*	5
t_s	*Formation transition time*	50
τ	*Exponential rate*	10
d_1^1	*Desired distance*	$[0 \quad 6]^T$
d_1^2	*Desired distance*	$[0 \quad 2]^T$
d_2^1	*Desired distance*	$[0 \quad 4]^T$
d_2^2	*Desired distance*	$[2\cos(18) \quad 2\,sin(18)]^T$
d_3^1	*Desired distance*	$[0 \quad 2]^T$
d_3^2	*Desired distance*	$[-2\cos(18) \quad 2\,sin(18)]^T$
d_4^1	*Desired distance*	$[0 \quad -2]^T$
d_4^2	*Desired distance*	$[2\cos(54) \quad -2sin(54)]^T$
d_5^1	*Desired distance*	$[0 \quad -4]^T$
d_5^2	*Desired distance*	$[-2\cos(54) \quad -2sin(54)]^T$

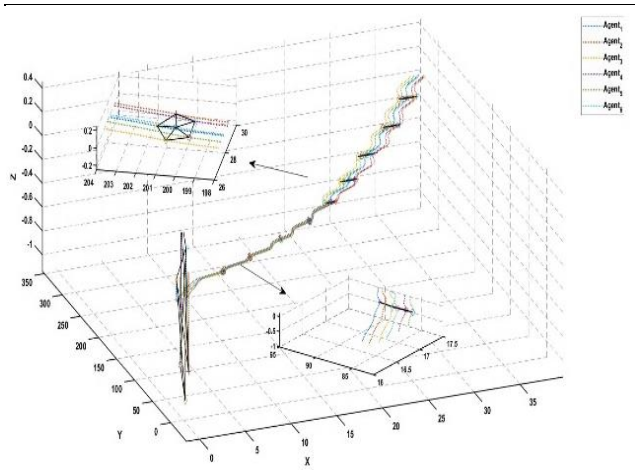

Fig. *10* . pentagonal formation in variation formation

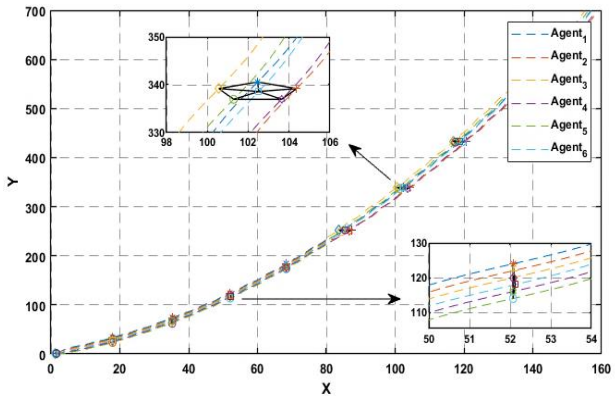

Fig. *11* . variation formation

VI. Conclusion

In this paper, after investigating the nonlinear model of a quadcopter as a case study and examining its parameters, the analysis of the linearized quadcopter system was undertaken and introduced its state space model. In the first section, the control objective is to pursue position control in the nonlinear quadcopter system using a PID controller. For this purpose, six PID controllers were utilized and coefficients were determined to control all system outputs effectively. By examining the system output plots, it is observed that the assigned coefficients appropriately regulate the outputs. A constrained Tube-MPC controller was designed for the nonlinear system in the following section. By examining the plots of the Tube-MPC controller and comparing it with the PID controller, it was concluded that Tube-MPC controlled the outputs better than the PID controller when constraints were considered. Also, according to the physical limitations of the quadcopter, the Tube-MPC controller can apply better control inputs to the system than the PID controller. In the following section, the article's objective was to design a formation for a group of six quadcopters considering nonlinear dynamics, such that, in addition to achieving a specific formation. We first reviewed the formation theories to accomplish this goal and then attempted to implement them on the controlled nonlinear dynamics using a nonlinear PID controller. Simulating this problem and examining the plots, the implemented method successfully utilizes the controlled nonlinear system dynamics to reach an appropriate form.

References

[1] D. Yan, W. Zhang, and H. Chen, "Design of a multi-constraint formation controller based on improved MPC and consensus for quadrotors," *Aerospace*, vol. 9, no. 2, p. 94, 2022.

[2] S. Y. Ku, G. Nejat, and B. Benhabib, "Wilderness search for lost persons using a multimodal aerial-terrestrial robot team," Robotics, vol. 11, no. 3, p. 64, 2022.

[3] M. Sharma, A. Gupta, S. K. Gupta, S. H. Alsamhi, and A. V. Shvetsov, "Survey on unmanned aerial vehicle for Mars exploration: Deployment use case," Drones, vol. 6, no. 1, p. 4, 2022.

[4] Q. Zong, D. Wang, S. Shao, B. Zhang, and Y. Han, "Research status and development of multi UAV coordinated formation flight control," Journal of Harbin Institute of Technology, vol. 49, no. 3, pp. 1-14, 2017.

[5] X. Fu, J. Pan, H. Wang, and X. Gao, "A formation maintenance and reconstruction method of UAV swarm based on distributed control," Aerospace Science and Technology, vol. 104, p. 105981, 2020.

[6] G. Hoffmann, H. Huang, S. Waslander, and C. Tomlin, "Quadrotor helicopter flight dynamics and control: Theory and experiment," in AIAA guidance, navigation and control conference and exhibit, 2007, p. 6461.

[7] H. Huang, G. M. Hoffmann, S. L. Waslander, and C. J. Tomlin, "Aerodynamics and control of autonomous quadrotor helicopters in aggressive maneuvering," in 2009 IEEE international conference on robotics and automation, 2009: IEEE, pp. 3277-3282.

[8] C. E. Garcia, D. M. Prett, and M. Morari, "Model predictive control: Theory and practice—A survey," Automatica, vol. 25, no. 3, pp. 335-348, 1989.

[9] F. Allgöwer and A. Zheng, Nonlinear model predictive control. Birkhäuser, 2012.

[10] S. Wolfe, S. Givigi, and C.-A. Rabbath, "Distributed multiple model mpc for target tracking uavs," in 2020 International Conference on Unmanned Aircraft Systems (ICUAS), 2020: IEEE, pp. 123-130.

[11] Y. Kuriki and T. Namerikawa, "Formation control with collision avoidance for a multi-UAV system using decentralized MPC and consensus-based control," SICE Journal of Control, Measurement, and System Integration, vol. 8, no. 4, pp. 285-294, 2015.

[12] H.-T. Do and I. Prodan, "Experimental validation of an explicit flatness-based MPC design for quadcopter position tracking," arXiv preprint arXiv:2308.15946, 2023.

[13] Z. Chao, S.-L. Zhou, L. Ming, and W.-G. Zhang, "UAV formation flight based on nonlinear model predictive control," Mathematical Problems in Engineering, vol. 2012, no. 1, p. 261367, 2012.

[14] A. Bemporad and M. Morari, "Robust model predictive control: A survey," in Robustness in identification and control: Springer, 2007, pp. 207-226.

[15] Y. Wang and S. Boyd, "Fast model predictive control using online optimization," IEEE Transactions on control systems technology, vol. 18, no. 2, pp. 267-278, 2009.

[16] A. Richards and J. How, "Implementation of robust decentralized model predictive control," in AIAA Guidance, Navigation, and Control Conference and Exhibit, 2005, p. 6366.

[17] T. Schouwenaars, J. How, and E. Feron, "Decentralized cooperative trajectory planning of multiple aircraft with hard safety guarantees," in AIAA Guidance, Navigation, and Control Conference and Exhibit, 2004, p. 5141.

[18] G. V. Raffo, M. G. Ortega, and F. R. Rubio, "An integral predictive/nonlinear H∞ control structure for a quadrotor helicopter," Automatica, vol. 46, no. 1, pp. 29-39, 2010.

[19] Z. Zuo, "Trajectory tracking control design with command-filtered compensation for a quadrotor," IET control theory & applications, vol. 4, no. 11, pp. 2343-2355, 2010.

[20] S. Bouabdallah, A. Noth, and R. Siegwart, "PID vs LQ control techniques applied to an indoor micro quadrotor," in 2004 IEEE/RSJ International Conference on Intelligent Robots and Systems (IROS)(IEEE Cat. No. 04CH37566), 2004, vol. 3: IEEE, pp. 2451-2456.

[21] K. Alexis, G. Nikolakopoulos, and A. Tzes, "Experimental

constrained optimal attitude control of a quadrotor subject to wind disturbances," International Journal of Control, Automation and Systems, vol. 12, pp. 1289-1302, 2014.
[22] X. Yang, H. Pota, and M. Garratt, "Design of a gust-attenuation controller for landing operations of unmanned autonomous helicopters," in 2009 IEEE Control Applications,(CCA) & Intelligent Control,(ISIC), 2009: IEEE, pp. 1300-1305.
[23] T. Luukkonen, "Modelling and control of quadcopter," Independent research project in applied mathematics, Espoo, vol. 22, no. 22, 2011.
[24] S. Norouzi Ghazbi, A. A. Akbari, and M. Gharib, "Quadrotor Full dynamic Modeling, Nonlinear Simulation and Control of Attitudes," Indian Journal of Scientific Research, vol. 1, 2014.
[25] S. Ariram, J. Röning, and Z. Kowalczuk, "Implementation of control system and tracking objects in a quadcopter system," in Interactive Collaborative Robotics: 4th International Conference, ICR 2019, Istanbul, Turkey, August 20–25, 2019, Proceedings 4, 2019: Springer, pp. 19-29.
[26] S. Abdelhay and A. Zakriti, "Modeling of a quadcopter trajectory tracking system using PID controller," Procedia Manufacturing, vol. 32, pp. 564-571, 2019.
[27] S. Vargas, H. M. Becerra, and J.-B. Hayet, "MPC-based distributed formation control of multiple quadcopters with obstacle avoidance and connectivity maintenance," Control Engineering Practice, vol. 121, p. 105054, 2022.
[28] D. F. S. De Sá and J. V. D. F. Neto, "Multi-Agent Collision Avoidance System Based on Centralization and Decentralization Control for UAV Applications," IEEE Access, vol. 11, pp. 7031-7042, 2023.
[29] M. De Queiroz, X. Cai, and M. Feemster, Formation control of multi-agent systems: a graph rigidity approach. John Wiley & Sons, 2019.
[30] H.-T. Do and I. Prodan, "Tube MPC via flatness for multicopter trajectory tracking," in 2024 European Control Conference (ECC), 2024: IEEE, pp. 1449-1454.
[31] H. A. Hassan, "Tube-based NMPC for Non-Holonomic," rn (xk, uk), vol. 2, p. 47, 2024.
[32] S.-S. Liu, T.-F. Ding, M.-F. Ge, X.-G. Dong, and Z.-W. Liu, "Multiquadrotor Formation Tracking with Mixed Constraints: A Hierarchical Rolling Optimization Approach," IEEE Transactions on Aerospace and Electronic Systems, vol. 59, no. 5, pp. 7269-7280, 2023.
[33] F. Borrelli, A. Bemporad, and M. Morari, Predictive control for linear and hybrid systems. Cambridge University Press, 2017.
[34] L. F. C. Ccari and P. R. Yanyachi, "A Novel Neural Network-Based Robust Adaptive Formation Control for Cooperative Transport of a Payload Using Two Underactuated Quadcopters," IEEE Access, vol. 11, pp. 36015-36028, 2023.
[35] D. Shen and Q. Lu, "Hierarchical formation control with applications to multi-quadrotor systems," IEEE Access, vol. 7, pp. 130599-130609, 2019.
[36] A. Azarbahram, N. Pariz, M. B. Naghibi-Sistani, and R. Kardehi Moghaddam, "Leader-Follower Formation Control of Uncertain USV Networks Under Stochastic Disturbances," International Journal of Industrial Electronics Control and Optimization, vol. 5, no. 2, pp. 133-142, 2022.
[37] S. Khankalantary, I. Izadi, and F. Sheikholeslam, "Robust ADP-based solution of a class of nonlinear multi-agent systems with input saturation and collision avoidance constraints," ISA transactions, vol. 107, pp. 52-62, 2020.
[38] N. H. Sahrir and M. A. Mohd Basri, "Modelling and manual tuning PID control of quadcopter," in Control, instrumentation and mechatronics: Theory and practice: Springer, 2022, pp. 346-357.
[39] S. D. Sahputro, F. Fadilah, N. A. Wicaksono, and F. Yusivar, "Design and implementation of adaptive PID controller for speed control of DC motor," in 2017 15th International Conference on Quality in Research (QiR): International Symposium on Electrical and Computer Engineering, 2017: IEEE, pp. 179-183.
[40] J.-W. Lee, N. Xuan-Mung, N. P. Nguyen, and S. K. Hong, "Adaptive altitude flight control of quadcopter under ground effect and time-varying load: Theory and experiments," Journal of Vibration and Control, vol. 29, no. 3-4, pp. 571-581, 2023.
[41] N. Xuan Mung, N. P. Nguyen, D. B. Pham, N. N. Dao, and S. K. Hong, "Synthesized landing strategy for quadcopter to land precisely on a vertically moving apron," Mathematics, vol. 10, no. 8, p. 1328, 2022.

Seyedeh Mahsa Zakipour Bahambari was born in 1999. She received her B.S. degree in Electrical Engineering in 2022. She is currently an M.Sc. student in Mechatronics Engineering at K. N. Toosi University of Technology under supervision of Assistant Professor Saeed Khankalantary. She has found her field of interest in multi-agent systems, specifically in the formation of Quadcopters. She has an extensive experience in programming languages, including MATLAB, C++, Phyton, and Simulink.

Saeed Khankalantary was born in 1991. He received his B.S. degree in Electrical Engineering in 2012 from Yazd University, Yazd, Iran, and M.S. degree in Control Engineering in 2014 from K. N. Toosi University of Technology, Tehran, Iran. He wrote his dissertation under the supervision of Prof. Mohammad Teshnelab. He received his PhD degree at the Isfahan University of Technology, Isfahan, Iran, in 2020. He is currently an Assistant Professor at the Department of Mechatronics, Faculty of Electrical Engineering, K. N. Toosi University of Technology. His research interests are Multi-agent Control Systems, Estimation Theory, Intelligent Control, Sensor Fusion, and Mechatronics.

.

International Journal Of
Industrial Electronics Control and Optimization
Print ISSN: 3517-2645
Online ISSN: 3568-2645
Homepage: https://ieco.usb.ac.ir/

Energy-Efficient Optimal Control of Crude Distillation Columns Using Proportional-Integral-Plus (PIP) Framework: A Simulation-Based Approach

Mir Mohammad Khalilipour | Farhad Shahraki | Jafar Sadeghi | Kiyanoosh Razzaghi

Department of Chemical Engineering, University of Sistan and Baluchestan, Zahedan 98164, Iran
*Corresponding author. E-mail address: a.khalilipour@eng.usb.ac.ir

Article Info

Article type:
Research Article

Article history:
Received: 25-September-2024
Received in revised form: 16-October-2024
Accepted: 06-November-2024
Published online: 22-June-2025

Keywords:
NMSS-PIP;
Energy Optimization;
Process Control;
Energy Efficiency;
Proportional Integral plus

ABSTRACT

The objective of this research is to optimize the crude distillation unit (CDU) in oil refineries by reducing energy consumption and improving operational efficiency through the application of a Proportional-Integral-Plus (PIP) control system within a Non-Minimal State Space (NMSS) framework. Simulations of the CDU were carried out using Aspen Plus for modeling the distillation process and MATLAB for implementing the PIP control structure. The controller was tuned by an economic cost function, optimizing key parameters such as furnace duty, side-draw rates, and condenser heat removal. The PIP control system was compared to traditional control methods, with performance evaluated under various disturbances, including feed rate, temperature, and composition changes. The PIP control strategy significantly improved the CDU's performance, reducing operating costs by up to 100% compared to traditional control methods optimized by the Integral of Time-weighted Absolute Error (ITAE). The PIP system demonstrated superior disturbance handling and energy efficiency while maintaining product quality. The findings indicate that the PIP control system is a highly effective tool for optimizing energy consumption and process stability in modern refineries, especially under fluctuating operational conditions. Its application could lead to substantial cost savings and improved efficiency in CDU operations.

NOMENCLATURE

$\mathbf{A}(z^{-1})$	Denominator matrix polynomial of LMFD	$\mathbf{R}$	Matrix of LQ cost function input weightings
$\mathbf{B}(z^{-1})$	Numerator matrix polynomial of LMFD	$\mathbf{V}$	Matrix of SVF gains
$\mathbf{D}$	MIMO NMSS set-point coefficient matrix	V	Vapor flow rate
$\mathbf{F}$	NMSS system coefficient matrix	$\mathbf{x}_t$	Vector of states in NMSS
F	Feed flow rate	$\mathbf{y}_t$	Vector of outputs (MIMO)
$\mathbf{G}$	NMSS input coefficient matrix	$\mathbf{y}_t^d$	Vector of set-points in MIMO PIP
$\mathbf{H}$	NMSS output coefficient matrix	y	Output variable
$\mathbf{I}$	Identity matrix	z^{-1}	Time shift operator
J	LQ cost function	$\mathbf{z}_t$	Integral-of-error state variable
$\mathbf{K}$	Matrix of integral gains	τ	Time constant
L	Liquid flow rate	S	Side product flow rate
M	Liquid holdup	$\mathbf{u}$	Vector of inputs (MIMO)
$\mathbf{Q}$	Matrix of LQ cost function state weightings	u	Input variable

I. Introduction

The crude distillation column is one of the most energy-intensive and crucial units in oil refineries, responsible for separating crude oil into valuable fractions. Given the significant energy consumption and the critical role it plays in product quality, optimizing control strategies for this process is essential. In modern industrial practice, there is an increasing demand for advanced control systems that ensure operational efficiency, reduce energy consumption, and maintain desired output specifications, especially as energy sustainability becomes a global priority [1].

Historically, various control methodologies have been applied to distillation columns, with conventional proportional-integral-derivative (PID) control being one of the earliest and most widely adopted strategies. Despite its simplicity and ease of implementation, PID control often falls short in dealing with multivariable interactions, nonlinearities, and the dynamic nature of the distillation process. As a result, PID-based control schemes often lead to suboptimal energy usage and reduced control over product quality, particularly when facing disturbances or changes in operating conditions [2].

To overcome these limitations, advanced control techniques, such as Model Predictive Control (MPC), have been introduced and extensively studied in recent decades. MPC excels in handling multivariable systems and has the ability to predict future system behavior using dynamic models. Numerous studies have demonstrated its effectiveness in optimizing the operation of distillation columns, particularly in reducing energy consumption and improving control precision [3-5]. However, MPC requires accurate models and can be computationally expensive, limiting its application in real-time or highly dynamic environments [6]. Furthermore, tuning MPC parameters for complex processes like crude distillation can be challenging and time-consuming [7]. Recent studies have proposed hybrid approaches that integrate multi-objective optimization with nonlinear model predictive control (NMPC) to address some of these challenges in complex processes [8].

Other notable approaches include nonlinear control strategies, adaptive control, and fuzzy logic control, each offering advantages in handling system uncertainties and nonlinearities. For instance, multi-objective MPC methods, as explored by Bemporad et al. [9], integrate multiple production objectives, providing a more robust solution for systems with variable process dynamics and multiple objectives. This approach enables decision-making strategies to balance energy efficiency and control performance in complex industrial systems, such as distillation columns. Adaptive control methods have shown promise in addressing dynamic variations in distillation columns [10], though these methods can be limited by computational complexity and implementation challenges. Recent advances have explored the use of machine learning, particularly reinforcement learning, as part of adaptive control systems to develop more autonomous and efficient process control solutions that learn from operational data [11].

Research has focused on optimizing energy consumption in crude oil distillation units, but practical application of optimal control strategies for these systems remains limited. Optimal control involves determining control actions that meet operational constraints while optimizing objectives like energy efficiency or product quality [12, 13]. Typical steps for implementing optimal control include modeling the system dynamics, identifying constraints, and defining a cost function to guide the control process.

In optimal control, physical constraints must be defined for both states and controllers. This approach aims to select a cost function that, when minimized, enhances system performance and reduces costs. Specifically, we seek an acceptable control strategy that guides the system along a desired trajectory while minimizing the cost function. In the PIP control for the crude oil distillation tower, the weight matrices Q and R were adjusted to simultaneously minimize the system cost and functional error. By fine-tuning these matrices, the control strategy is better equipped to balance energy consumption with product quality, which remains a key challenge in distillation control.

One particularly promising method is the Nonsquare Multivariable Non-Minimal State Space Proportional Integral Plus (NMSS-PIP) control, introduced by Khalilipour et al [14]. Their work demonstrated the effectiveness of NMSS-PIP control in an industrial crude distillation column, where the system exhibited ill-conditioning due to nonsquare configuration. The proposed control was based on a Singular Value Factorization (SVF) control design using the Linear Quadratic (LQ) optimal control method. The weighting matrices of the PIP control (Q and R) were optimized by minimizing the Integral of Time-weighted Absolute Error (ITAE), leading to smooth input manipulation and robust output control under several challenging scenarios. This approach outperformed conventional PI controllers, which struggled with the nonsquare nature of the system and provided suboptimal control [14]. Their findings strongly support the NMSS-PIP structure as a more robust and efficient solution for managing the complex dynamics and interactions in crude distillation columns.

The NMSS-PIP control strategy offers a balance between complexity and performance. Unlike traditional control methods, NMSS-PIP incorporates a more flexible control framework that is well-suited for multivariable systems with strong interactions [15]. Recent studies have demonstrated the potential of NMSS-PIP control in various industrial applications, showing significant improvements in both energy efficiency and process stability [16, 17]. For example, Kharaji et al. [18] applied NMSS-PIP to a tert-amyl methyl ether

(TAME) production unit using reactive distillation, which previously suffered from oscillatory behavior under conventional PI controllers. Their study revealed that NMSS-PIP completely eliminated the oscillations, providing smoother responses and better settling time than PI configurations. Furthermore, the ITAE criterion was significantly reduced by 88% using NMSS-PIP control, highlighting its potential for improving process control in multivariable systems [18].

Additionally, the integration of NMSS-PIP control with data-driven soft sensors further demonstrates its versatility and effectiveness in process monitoring. In a study by Bidar et al. [19], a data-driven soft sensor using the Local Instrumental Variable (LIV) technique was developed to monitor ASTM-D86 of side products in a crude distillation unit. By implementing the NMSS-PIP control structure alongside the soft sensor model, they achieved smoother responses and better alignment with dynamic process changes when compared to conventional methods. The proposed soft sensor model, applied to an Aspen dynamic simulation of the column, showed strong predictive performance and validation against Aspen soft sensors, further establishing the merit of NMSS-PIP control in matching with soft sensors to enhance process optimization [19].

Recent advancements in process control have highlighted the potential of integrating modern techniques such as artificial neural networks (ANN) and Proportional-Integral-Plus (PIP) control into industrial applications. For instance, Shin et al. [20] developed a model predictive control (MPC) system utilizing an ANN model for a depropanizer. This study revealed that replacing traditional linear models with ANN significantly improved the optimization speed and accuracy, resulting in superior performance compared to conventional PID control. The results demonstrated a marked reduction in settling and rise times, showcasing the ANN's efficacy in enhancing operational efficiency in distillation processes.

Similarly, Li et al. [21] implemented PIP control in a high redundancy actuator for a railway track switch system. Their study emphasized the advantages of closed-loop control, which increased the reliability of the actuation system. The development of a model-based PIP controller illustrated its capability to meet actuation requirements effectively, providing valuable insights into the design of redundant control systems. This work underscores the adaptability and robustness of PIP control, further validating its relevance in various industrial contexts.

Despite these advancements, there is still a gap in the literature regarding the integration of NMSS-PIP control with energy optimization objectives in distillation processes. Most studies have focused on either improving the control precision or minimizing energy consumption, without fully addressing the simultaneous optimization of both factors. The use of a cost objective function within the NMSS-PIP framework, as proposed in this paper, aims to fill this gap by providing a method that balances energy efficiency with product quality [22, 23].

The primary contribution of this paper lies in the application of the NMSS-PIP control structure within a non-minimal state space context for the optimization of a crude distillation column. This control strategy enables centralized control pairing and utilizes a cost objective function aimed at minimizing the energy consumption of the column while maintaining high product quality. By addressing these dual objectives, this work aims to improve the operational efficiency of the distillation process, potentially offering a more sustainable and economically viable solution for the industry. The remainder of the paper is organized as follows: Section 2 provides a detailed overview of the NMSS-PIP control theory and its application to distillation processes. Section 3 outlines the non-minimal state space formulation, and Section 4 presents the simulation results and comparative analysis. Finally, Section 5 offers conclusions and recommendations for future work.

I. Methodology

A. NMSS-PIP Control Theory and Its Application to Distillation Processes

The PIP control strategy, grounded in the NMSS framework, provides an effective balance of complexity and control precision for multivariable systems like distillation columns. Originally conceptualized in the 1960s, the NMSS model extends conventional minimal state space formulations by allowing a broader representation of the system dynamics without the need for state reconstruction. This approach enables direct state measurement, facilitating the implementation of a full-state feedback controller that promotes robust and efficient control, even in high-disturbance environments. As a logical successor to conventional PI/PID controllers, the NMSS-PIP model simplifies the process design while enhancing the stability and performance of control systems. In particular, the PIP controller offers practical implementation advantages comparable to traditional PI/PID control strategies but is structured in the optimal state space, akin to General Predictive Control (GPC). As part of the SVF control design, PIP can be integrated into multiple design methods, including closed-loop pole assignment and optimal control frameworks like linear quadratic (LQ) or robust LQG/H∞ control.

The use of the NMSS-PIP approach is especially advantageous in the context of crude distillation units (CDUs), where multivariable interactions, nonlinearities, and large time delays pose challenges for conventional controllers. NMSS-PIP controllers are particularly adept at handling these complexities because they minimize both energy consumption and process deviations, optimizing energy efficiency and product quality. This study leverages these attributes by tuning the NMSS-PIP controller through an economic cost function

that targets key parameters such as furnace duty, side-draw rates, and condenser heat removal, enabling effective control under varied operational disturbances like fluctuations in feed rate, temperature, and composition.

In this work, the PIP control framework is applied to an atmospheric distillation column at Shiraz Refinery. The atmospheric distillation tower separates crude oil into various fractions, such as overhead products, naphtha, kerosene, and gas oil, through a series of complex, nonlinear operations as depicted in figure 1. This column consists of 43 trays, two mid-tower condensers (pumparounds), and three 6-stage strippers, with a maximum operating capacity of 60,000 bbl/day. Superheated stripping steam is injected from the bottom of the column to adjust the temperature profile and remove light hydrocarbons from the stripper's side products. The feed is preheated by heat recovery from the pumparounds, kerosene, and gas oil, and its temperature is increased to 690°F using a fired heater.

TABLE 1 INPUT VARIABLES [14]

Variable	Description	u_0	Unit
u_1	Side-draw of naphtha	29,748.8	lb/h
u_2	Side-draw of kerosene	12,8254.6	lb/h
u_3	Side-draw of gas oil	122,868.1	lb/h
u_4	Furnace duty	110,173,828	Btu/h
u_5	Reflux split fraction	0.61676	—
u_6	Heat removed in pumparound1	−22,428,847	Btu/h
u_7	Heat removed in pumparound2	−26,172,804	Btu/h

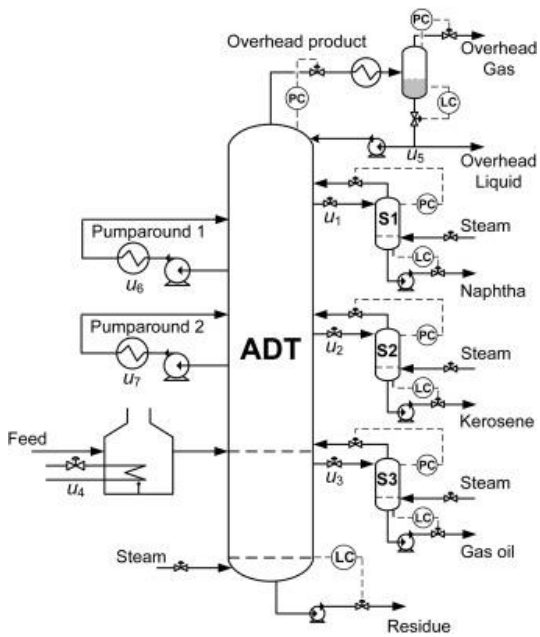

Fig. 1. Process flowsheet of atmospheric distillation column [14]

B. *Non-Minimal State Space Formulation and waiting functions*

Possible manipulated variables that influence product quality include heat removal from the mid-condensers, fired heater duty, reflux split fraction, and side-draw flows of naphtha, kerosene, and gas oil. The system is configured with 7 manipulated variables and 4 controlled variables, after addressing the pressure and level control challenges, as shown in Tables 1 and 2.

TABLE 2 OUTPUT VARIABLES [14]

Variable	Description	Set point (R)	Unit
y_1	Overhead temperature	295.7	K
y_2	95% -ASTMD86 of naphtha	385.69	K
y_3	95% -ASTMD86 of kerosene	502.23	K
y_4	95% -ASTMD86 of gas oil	622.87	K

The NMSS formulation is an essential part of the PIP control design for complex chemical processes like distillation. In this formulation, the system's transfer function is represented using the left matrix fraction description (LMFD). The state vector is a combination of present and past output values, past input values, and the integral of the error between the setpoint and the output, ensuring a robust framework for addressing process disturbances and maintaining product quality.

In NMSS representation, the transfer function is expressed as LMFD [24]:

$$\mathbf{y}_t = \left[\mathbf{A}(z^{-1})\right]^{-1}\mathbf{B}(z^{-1})\mathbf{u}_t \tag{1}$$

where $\mathbf{A}(z^{-1})$ and $\mathbf{B}(z^{-1})$ are defined by:

$$\mathbf{A}(z^{-1}) = \mathbf{I}_p + \mathbf{A}_1 z^{-1} + ... + \mathbf{A}_n z^{-n} \tag{2-a}$$

$$\mathbf{B}(z^{-1}) = \mathbf{B}_1 z^{-1} + ... + \mathbf{B}_m z^{-m} \tag{2–b}$$

Transfer function in the form of NMSS can be written as:

$$\mathbf{x}_t = \mathbf{F}\mathbf{x}_{t-1} + \mathbf{G}\mathbf{u}_{t-1} + \mathbf{D}\mathbf{y}_t^d \tag{3–a}$$

$$\mathbf{y}_t = \mathbf{H}\mathbf{x}_t \tag{3–b}$$

The state vector ($\mathbf{x}_t$) in Eq. (3) is directly related to present and past values of outputs, past values of inputs and integral of error ($\mathbf{z}_t^T$) between referenced value ($\mathbf{y}_t^d$) and output as:

$$\mathbf{x}_t = \left[\mathbf{y}_t^T \ \mathbf{y}_{t-1}^T \ldots \mathbf{y}_{t-n+1}^T \ \mathbf{u}_{t-1}^T \ .... \ \mathbf{u}_{t-1}^T \ \mathbf{u}_{t-m+1}^T \ \mathbf{z}_t^T\right]^T \tag{4–a}$$

$$\mathbf{z}_t = \mathbf{z}_{t-1} + \left[\mathbf{y}_t^d - \mathbf{y}_t\right] \tag{4–b}$$

The state matrices of Eq. (3) are defined as:

$$\mathbf{F} = \begin{bmatrix} -\mathbf{A}_1 & -\mathbf{A}_2 & \cdots & -\mathbf{A}_{n-1} & -\mathbf{A}_n & \mathbf{B}_2 & \mathbf{B}_3 & \cdots & \mathbf{B}_{m-1} & \mathbf{B}_m & \mathbf{0} \\ \mathbf{I}_p & \mathbf{0} & \cdots & \mathbf{0} & \mathbf{0} & \mathbf{0} & \mathbf{0} & \cdots & \mathbf{0} & \mathbf{0} & \mathbf{0} \\ \mathbf{0} & \mathbf{I}_p & \cdots & \mathbf{0} & \mathbf{0} & \mathbf{0} & \mathbf{0} & \cdots & \mathbf{0} & \mathbf{0} & \mathbf{0} \\ \vdots & \vdots & \ddots & \vdots & \vdots & \vdots & \vdots & \ddots & \vdots & \vdots & \vdots \\ \mathbf{0} & \mathbf{0} & \cdots & \mathbf{I}_p & \mathbf{0} & \mathbf{0} & \mathbf{0} & \cdots & \mathbf{0} & \mathbf{0} & \mathbf{0} \\ \mathbf{0} & \mathbf{0} & \cdots & \mathbf{0} & \mathbf{0} & \mathbf{0} & \mathbf{0} & \cdots & \mathbf{0} & \mathbf{0} & \mathbf{0} \\ \mathbf{0} & \mathbf{0} & \cdots & \mathbf{0} & \mathbf{0} & \mathbf{I}_r & \mathbf{0} & \cdots & \mathbf{0} & \mathbf{0} & \mathbf{0} \\ \mathbf{0} & \mathbf{0} & \cdots & \mathbf{0} & \mathbf{0} & \mathbf{0} & \mathbf{I}_r & \cdots & \mathbf{0} & \mathbf{0} & \mathbf{0} \\ \vdots & \vdots & \ddots & \vdots & \vdots & \vdots & \vdots & \ddots & \vdots & \vdots & \vdots \\ \mathbf{0} & \mathbf{0} & \cdots & \mathbf{0} & \mathbf{0} & \mathbf{0} & \mathbf{0} & \cdots & \mathbf{I}_r & \mathbf{0} & \mathbf{0} \\ \mathbf{A}_1 & \mathbf{A}_2 & \cdots & \mathbf{A}_{n-1} & \mathbf{A}_n & -\mathbf{B}_2 & -\mathbf{B}_3 & \cdots & -\mathbf{B}_{m-1} & -\mathbf{B}_m & \mathbf{I}_r \end{bmatrix} \tag{5–a}$$

$$\mathbf{G}=\begin{bmatrix}\mathbf{B}_1 & \mathbf{0} & \mathbf{0} & \cdots & \mathbf{0} & \mathbf{I}_r & \mathbf{0} & \mathbf{0} & \cdots & \mathbf{0} & -\mathbf{B}_1\end{bmatrix}^{\mathrm{T}} \quad (5\text{–b})$$

$$\mathbf{H}=\begin{bmatrix}\mathbf{I}_p & \mathbf{0} & \mathbf{0} & \cdots & \mathbf{0} & \mathbf{0} & \mathbf{0} & \cdots & \mathbf{0} & \mathbf{0}\end{bmatrix} \quad (5\text{–c})$$

$$\mathbf{D}=\begin{bmatrix}\mathbf{0} & \mathbf{0} & \mathbf{0} & \cdots & \mathbf{0} & \mathbf{0} & \mathbf{0} & \cdots & \mathbf{0} & \mathbf{I}_p\end{bmatrix}^{\mathrm{T}} \quad (5\text{–d})$$

where $\mathbf{I}_p$ and $\mathbf{I}_r$ denote $p \times p$ and $r \times r$ identity matrices, respectively and **0** is an appropriately defined matrix of zeros. The controllability of the NMSS model is discussed in Wang et al.[23]. The NMSS transformation of Eq. (3) can be formulated based on optimal LQ design. The SVF control law is written as:

$$\mathbf{u}_t = -\mathbf{V}\mathbf{x}_t \quad (6)$$

where $\mathbf{V}$ is the control gain matrix (CGM). It can be calculated from LQ optimal control by minimizing the quadratic cost function of Eq. (7) for an infinite horizon.

$$J=\sum_{i=0}^{\infty}\mathbf{x}_i^T\mathbf{Q}\mathbf{x}_i+\mathbf{u}_i^T\mathbf{R}\mathbf{u}_i \quad (7)$$

It is worthy of that tuning of Q and R is usually limited to the diagonal weights because translation of weighting matrices are not readily convert into typical closed loop response. Further information can be found in earlier publications [27-28]. The weighting matrices and are defined as symmetric positive semi-definite and symmetric positive definite, respectively. The gain matrix which minimizes Eq. (7) can be obtained by solution of discrete algebraic riccati equation (ARE) [28]. Within the NMSS-PIP framework, the critical step involves defining the weight matrices Q and R, which dictate the performance criteria in the controller's objective function. These matrices can be configured by minimizing the economic cost function or by tuning them based on system-specific performance objectives. By using an Integral of ITAE criterion—particularly suited for systems with extended time delays—the control structure can prioritize minimizing persistent errors, leading to stable and energy-efficient operation. This tuning process was performed in MATLAB, ensuring precise configuration for application in the CDU context.

This work utilizes the NMSS-PIP framework as a pioneering approach to achieve optimal control in distillation processes. The results presented here underscore the NMSS-PIP's promise as an effective control strategy for maintaining process stability and energy efficiency in real-world scenarios, laying a foundation for further exploration and application in other critical process systems.

It's important to define the changes and limitations in optimal control regarding modes and controllers. To achieve this, the cost of modifying each input is treated as a cost function, with the change cost per variable unit established for all inputs. Since the prices of products within a quality range are generally uniform for all outputs from the distillation tower, minimizing performance error is preferred over maximizing profit. For side flows, the operational cost was represented by the pumping cost and the associated electricity usage [29].

$$E=\frac{2F}{3600\eta_{pump}} \quad (8)$$

The pump efficiency η is set at 0.96, and F represents the flow rate. Equation (9) calculates the change cost per variable unit of furnace heat rate.

$$Q_{furnace}=F_{fuel}\times(\eta_{furnace}\times Q_{fuel}) \quad (9)$$

In this regard, $\eta_{furnace}$ the efficiency of the unit furnace (equal to 0.96) and Q_{fuel} is the low heat value of the fuel used in the furnace, whose value is considered equal to Q_{fuel} = 41,816 kJkg^{-1}. The Cooling water consumption in terms of t/h for intermediate condensers is expressed in the form of equation (10):

$$F_{Cw}=\frac{Q_C}{C_{P,Cw}\Delta T_{Cw}} \quad (10)$$

In this equation, $C_{P,Cw}$ and ΔT_{Cw} are the specific heat capacity for the cooling water and the increase in the temperature difference of the cooling water, respectively while passing through the condenser. It is clear that the input cost function is equal to the sum of the mentioned costs, which is expressed in the form of the equation (11):

$$f_{cost}=\Delta C_{fuel}+\Delta C_{Cw}+\Delta C_{elec} \quad (11)$$

which ΔC_{fuel}, ΔC_{Cw} and ΔC_{elec} are increased in fuel consumption, cooling water and electricity respectively while calculated by equations (12-14):

$$\Delta C_{fuel}=P_{fuel}(F_{fuel}-F_{fuel}^0) \quad (12)$$

$$\Delta C_{Cw}=P_{Cw}(F_{Cw}-F_{Cw}^0) \quad (13)$$

$$\Delta C_{elec}=P_{elec}(F_{elec}-F_{elec}^0) \quad (14)$$

In these relationships, P denotes the costs of fuel, cooling water, and electricity, with the superscript 0 indicating their values in the system's steady state (initial values). Table (3) provides the costs for electricity, cooling water, and furnace fuel.

TABLE 3 COSTS FOR ELECTRICITY, COOLING WATER, AND FURNACE FUEL [30]

Variables	Description	Cost (USDs)
P_{fuel}	Furnace fuel (t)	673.17
P_{Cw}	Cooling water (t)	0.17
P_{elec}	Electricity(kWh)	0.19

Next, these costs should be organized by the input variable. Table (4) shows the cost for each input variable per unit change, based on the specified cost functions.

To perform a dynamic simulation of the proposed control structures under realistic conditions of the crude oil distillation tower, a conventional proportional-integral (PI) controller was initially used to benchmark the PIP controller. The PI controllers were tuned using a sequential adjustment approach, systematically refining controller parameters within a closed-loop configuration until minimal oscillations (within 10% of the set range) were achieved.

TABLE 4 THE COST OF INPUT VARIABLES PER UNIT CHANGE

Variable	Unit	Cost of input variables change*	Normalized value
u_1	\$/(lb/h)	9.7857×10^{-7}	1
u_2	\$/(lb/h)	9.7857×10^{-7}	1
u_3	\$/(lb/h)	9.7857×10^{-7}	1
u_4	\$/(Btu/h)	1.769×10^{-5}	18.0773
u_5	\$	0.367	375,530
u_6	\$/(Btu/h)	2.8×10^{-6}	2.861
u_7	\$/(Btu/h)	2.8×10^{-6}	2.861

* Such as electricity of pump and utility cost

Controller parameters were later refined using the Tyros-Leiben method, which applies smaller gains and a larger integrator constant than Ziegler-Nichols, optimizing stability for chemical processes. In the simulations, temperature control loops were assigned realistic delays: one minute at the tower top, three minutes for feed, and three minutes for side products, reflecting the slower response dynamics in furnaces relative to heat exchangers. The resulting matrices for the NMSS-PIP control structure, essential for real-time CDU management, were generated from open-loop gain tests and detailed in [14]. Finally, the distillation tower model was linked with the PIP control algorithm in ASPEN Dynamics through the SIMULINK interface, with a custom PIP controller toolbox designed in MATLAB to ensure seamless integration of control and dynamic models.

To streamline the optimization process, the cost per variable change has been normalized, as shown in the third column of table (4). Profit reduction from specific quality intervals and product storage relates solely to decreased production output. Since the profit reduction costs for all products are nearly identical due to similar pricing, the normalized output values have been set to one. Additionally, the optimization requires adjusting one of the integrators. The optimization scenario mirrored the previous case, featuring a 5% step change in the input feed rate. Based on the normalized values in table (4), the optimal values for weight matrices Q and R, are derived from relations (15).

$$\mathbf{Q} = \mathrm{diag}\left[q_1(1 \quad 1 \quad 1 \quad 1) \quad 1 \quad q_2 \quad q_3 \quad q_4\right] \tag{15–a}$$

$$\mathbf{R} = \mathrm{diag}\left(r_1\left[1 \quad 1 \quad 1 \quad 18.0773 \quad 375{,}530 \quad 2.861 \quad 2.861\right]^2\right) \tag{15–b}$$

In equation (15-a), the first four elements of the matrix represent the four outputs in the weight matrix, while the last four values correspond to the available integrators. Since chemical processes have significant time delays between inputs and outputs. Among the integral of error methods, ITAE places greater emphasis on long-lasting errors. Our optimization goal is to minimize the performance error of the PIP controller, using the weight functions Q and R from equations (15-a) and (15-b) based on ITAE (equation 16). The optimization algorithm employed in MATLAB is the Nelder-Mead simplex method. The optimal values of Q and R are provided in table (5).

$$\mathrm{ITAE} = \int_0^\infty t\left|e(t)\right|dt \tag{16}$$

TABLE 5 OPTIMAL VALUES OF PARAMETERS OF WEIGHT MATRICES

PARAMETERS OF WEIGHT MATRICES	OPTIMAL VALUE
q_1	6.7741
q_2	0.0621
q_3	0.9993
q_4	0.9959
r_1	1.1×10^{-5}

The weight matrices were computed using the proposed algorithm:

$$\mathbf{Q} = \mathrm{diag}\left[(6.7741 \quad 6.7741 \quad 6.7741 \quad 6.7741 \quad 1 \quad 0.0621 \quad 0.9993 \quad 0.9959\right] \tag{17–a}$$

$$\mathbf{R} = \mathrm{diag}\left[1.1\times10^{-5} \quad 1.1\times10^{-5} \quad 1.1\times10^{-5} \quad 0.0036 \quad 1.55\times10^{6} \quad 9.03\times10^{-5} \quad 9.03\times10^{-5}\right] \tag{17–b}$$

Based on the results from equation (17-a), it can be concluded that only one integrator was effective for optimal control performance.

While the NMSS-PIP approach offers substantial advantages over traditional plant-wide control methods, several limitations and challenges exist in practical applications. Unlike conventional control strategies that often require variable pairing, the NMSS-PIP framework facilitates comprehensive dynamic interaction without needing such pairing, allowing for a more streamlined setup. Additionally, as compared to centralized control systems, NMSS-PIP can directly measure state variables without reconstruction algorithms, like observers or predictors, thereby simplifying implementation. This simplicity makes NMSS-PIP particularly accessible for field engineers, allowing them to effectively manage and adjust the system in real-world operations.

However, NMSS-PIP control is most effective in regulatory and continuous processes, where it consistently maintains performance. In batch processes, frequent setpoint changes can necessitate recalculations of the weight matrices Q and *R*, potentially requiring additional estimations to maintain optimal performance. Moreover, tuning these matrices for

dynamic, high-variability environments may demand further adjustments to the control algorithm. Despite these limitations, the NMSS-PIP control structure continues to perform effectively in the TAME process for crude distillation units, demonstrating improved oscillation suppression, faster settling times, and lower ITAE values when compared to conventional PI control structures, even under cost-based function optimization.

II. Test Results

The performance of the NMSS-PIP control strategy in the CDU was evaluated using simulations carried out in Aspen Plus for the distillation process and MATLAB for the control implementation. The primary objectives of this study were to optimize energy consumption while maintaining product quality and to examine the robustness of the control strategy against disturbances, such as changes in feed rate, temperature, and composition.

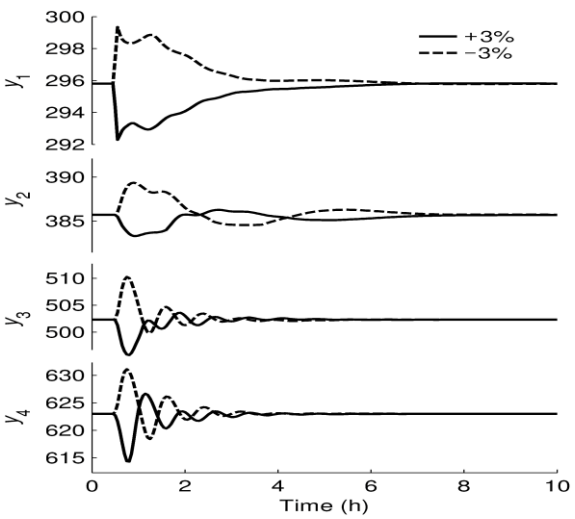

Fig. 2. Output response to ±3% changes in input feed, NMSS-PIP controller for economic weight functions

Figures 2 and 3 illustrate the output response and input changes when a ±3% step change was applied to the feed rate.

The NMSS-PIP controller, with weight matrices derived from the economic cost function, effectively dampens the disturbances. As seen in Figure 2, the system's output response is smooth, and the overshoot remains within an acceptable range, indicating that the controller effectively maintains product quality despite the input variation. Notably, the economic weighting functions allow for efficient control actions without introducing large oscillations, which can be detrimental in industrial operations. The input changes, shown in Figure 3, demonstrate that the control efforts are minimized, keeping the system inputs well-regulated while avoiding abrupt control actions that could lead to inefficiencies.

The results suggest that the NMSS-PIP controller, tuned using economic weight functions, offers superior disturbance rejection. For instance, in the crude oil distillation process, where even small changes in feed rate can significantly impact the separation of crude oil into different fractions, this level of control precision is crucial. By minimizing both energy consumption and deviation from product setpoints, the NMSS-PIP control structure enhances process stability, making it ideal for energy-intensive systems like the CDU.

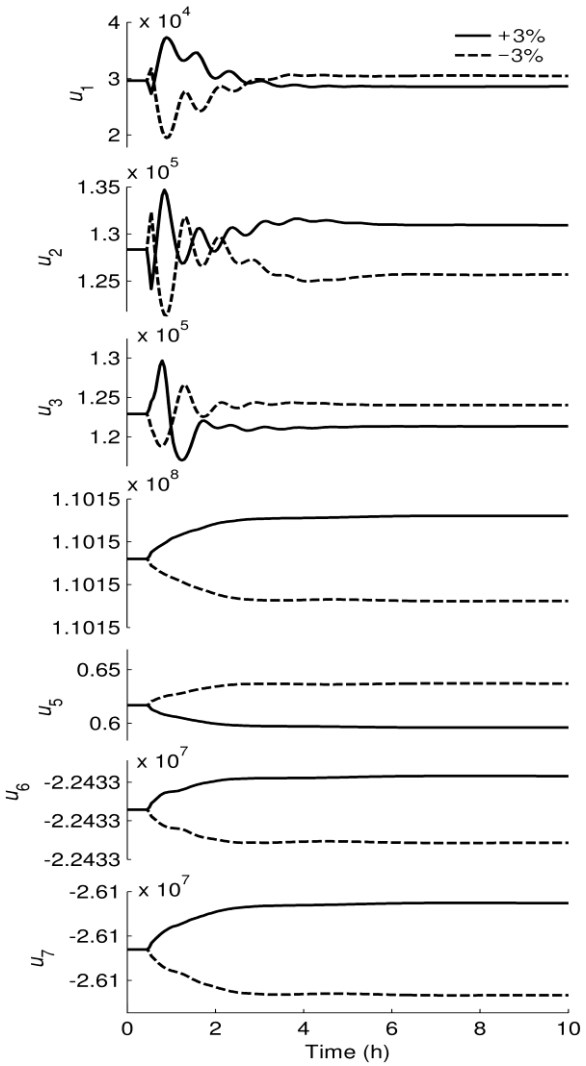

Fig. 3. Input changes to ±3% changes in input feed, NMSS-PIP controller for economic weight functions

The NMSS-PIP controller was further tested against step changes in feed temperature, as shown in Figures 4 and 5, where a ±5°F step change was applied. The results indicate that the controller maintained steady outputs within the desired range, with minimal oscillation. The ability of the NMSS-PIP controller to maintain tight control over the product temperature demonstrates its robustness, even in the presence of feed temperature disturbances. In practical terms, this can help prevent undesirable changes in the output product's quality, especially when the crude oil feedstock's properties fluctuate.

Given the stringent temperature requirements for the fractionation process, particularly for fractions like naphtha and gas oil, the NMSS-PIP controller's performance is significant. Maintaining optimal temperatures directly correlates with energy savings, as excessive heating or cooling is avoided. Furthermore, the controller adapts to changing conditions quickly, ensuring smooth transitions without a loss in product quality.

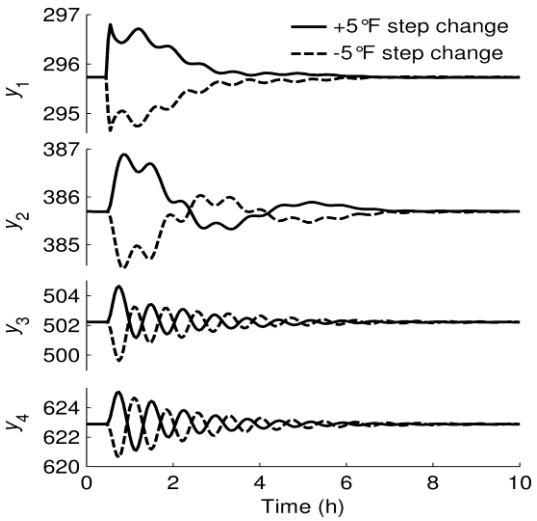

Fig. 4. Output response to ±5°F step change in input feed temperature for economic weighting functions

To assess the effectiveness of the NMSS-PIP control strategy in handling disturbances, a change in the feed composition was introduced. Specifically, after a set time, 95% of the input feed was mixed with 5% of the upstream flow, while keeping the volumetric flow rate constant. This allowed for the evaluation of the controller's performance when faced with composition variations, independent of volumetric disturbances. The true boiling point (TBP) specifications for the primary feed, the overhead product, and the combined feed are provided in Table 6, offering a detailed breakdown of the thermodynamic properties of the feed mixtures.

True Boiling Point (TBP) specifications for various feedstock volumes and the corresponding overhead product, including values for the combined feed in the distillation tower are elucidate in Table 6. This table highlights the TBP differences between crude, overhead, and combined feeds, illustrating the control requirements for maintaining product quality under variable feed compositions.

II. As depicted in Table 6, the TBP specifications vary across different volumetric fractions, highlighting the complexity of the composition change. For instance, the TBP of the combined feed reaches 1,328°F at 100% volume, whereas the overhead product shows a more controlled range, indicating the separation effectiveness. The ability to maintain such distinct separation profiles, despite the composition shift, is essential for achieving high product quality and efficient energy use.

TABLE 6 TRUE BOILING POINT (TBP) SPECIFICATIONS FOR FEEDS AND OVERHEAD PRODUCT

Volume percentage of distillated product %	TBP of crude (°F)	TBP of overhead product (°F)	TBP of combined feed (°F)
0	25	-12	26
10	120	52	110
5	188	88	180
30	399	185	362
50	594	236	573
70	806	282	791
90	1088	321	1075
95	1221	339	1214
100	1330	368	1328

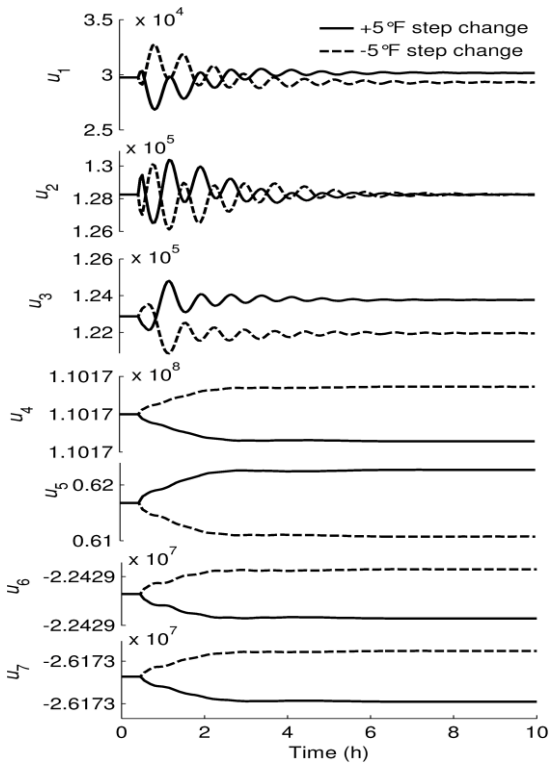

Fig. 5. Input changes for ±5°F Step change in input feed temperature for economic weighting functions

Figures 6 and 7 show the system's response to these disturbances. The NMSS-PIP controller managed the feed composition change smoothly, ensuring only minor deviations in the controlled outputs. These deviations were quickly corrected as the system returned to its setpoints, demonstrating the controller's ability to adapt to varying feedstock compositions. Notably, even with the introduction of an upstream flow and the alteration in the TBP characteristics, the system maintained stable operation, underscoring the robustness of the NMSS-PIP control strategy.

This result is critical in industrial scenarios where crude oil feedstocks often exhibit varying properties due to differences in sourcing. The refinery's ability to process crude from multiple origins without significant process disruptions or the

need for continuous manual intervention is crucial for maintaining consistent product quality. By responding swiftly and efficiently to changes in feed composition, the NMSS-PIP controller ensures that the distillation column operates within desired specifications, reducing the likelihood of costly off-spec products or energy wastage. Furthermore, the smooth control actions prevent overcompensation in input variables, thereby optimizing the energy consumption of critical subsystems, such as the furnace and intermediate condensers.

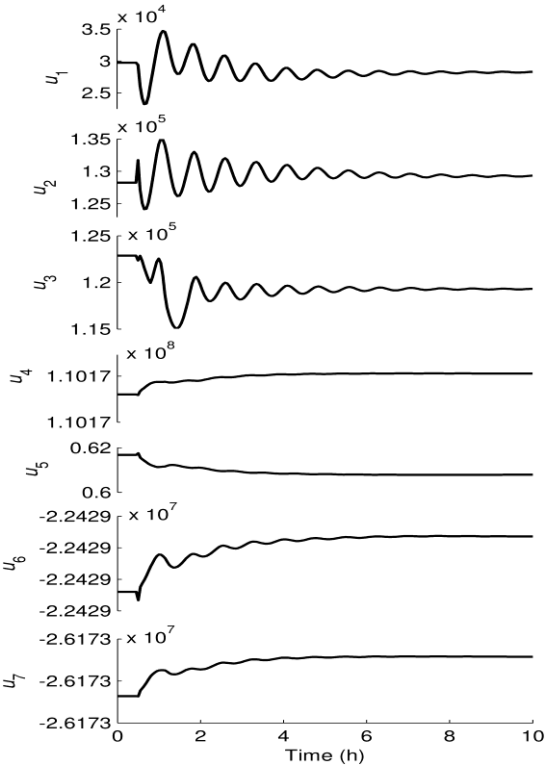

Fig. 6. Input changes affecting the percentage composition of input feed for economic weighting functions

Figure 8 shows the output response of the NMSS-PIP controller to ±1°F setpoint changes, demonstrating that the controller maintained system stability without inducing significant oscillations. The slight overshoot observed during the +1°F step change is well within operational tolerances. The control actions, depicted in Figure 9, show smooth and gradual input adjustments, further confirming the effectiveness of the NMSS-PIP controller.

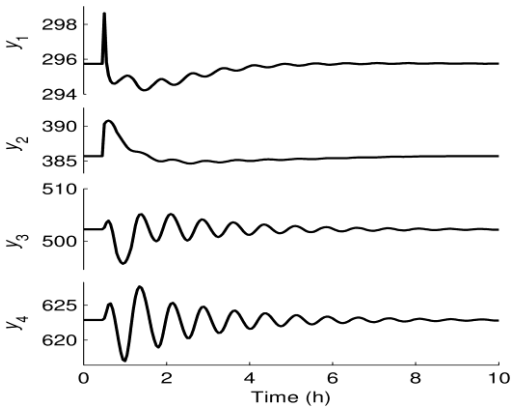

Fig. 7. Output response to change in input feed percentage composition for economic weight functions

The setpoint control performance is particularly relevant for optimizing production in response to market demands. Refineries may need to adjust product specifications to meet customer requirements, and the ability to make such adjustments dynamically, without energy penalties or compromising product quality, is a valuable asset for process optimization.

The comparison of energy consumption between two tuning methods, namely the economic cost function and ITAE minimization, is summarized in Table 7.

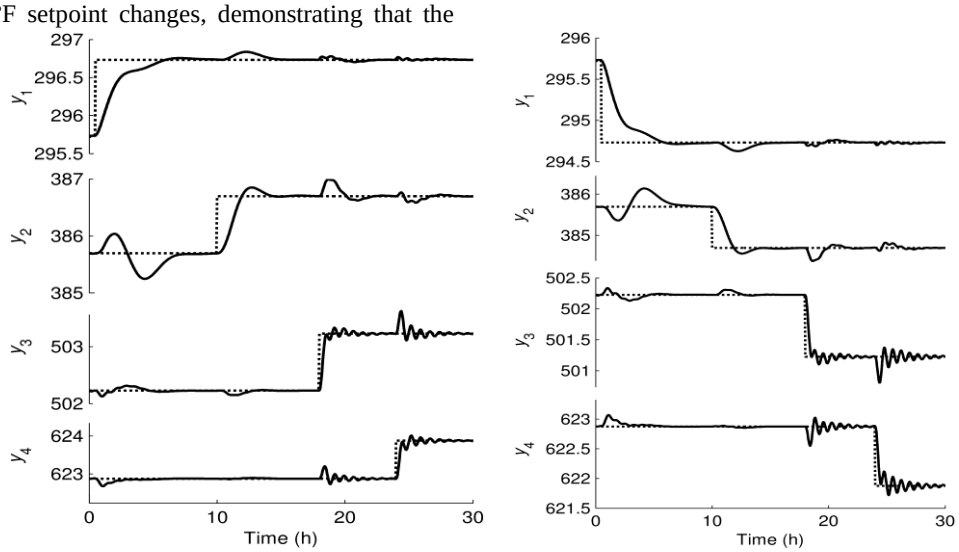

Fig.8. Input changes affecting the percentage composition of input feed for economic weighting functions

TABLE 7 . COMPARISON OF OPERATING COSTS USING ECONOMIC WEIGHTING FUNCTIONS AND ITAE TUNING

Scenario	$C_{furnace}$ ($/h)		$C_{pumparounds}$ ($/h)		C_{pumps} ($/h)		C_{total} ($/h)	
	Case a	Case b	Case a	Case b	Case a	Case b	Case a	Case b
Change in feed rate	117.5	0	0.2	0.005	0.0001	0	118	0.006
Change in feed temperature	34.5	0	0.03	0	0	0.015	34.5	0.015
Change in Feed composition	56.5	0	0.009	0	0.003	0.006	57	0.006
Change in setpoint	18.5	0	0.1	0	0	0.001	19	0.001

Scenario (a): Weighting matrices based on minimizing ITAE; Scenario (b): Weighting matrices based on economic cost functions.

This table presents an operating cost comparison between the NMSS-PIP control strategy with economic weighting functions and the ITAE tuning scenario. It breaks down furnace, pumparounds, and pumping costs under various disturbances (feed rate, temperature, composition, and setpoint changes), highlighting the NMSS-PIP controller's cost-saving advantages in energy management. In Table 7, furnace cost refers to the operating cost per input variation in the furnace by the end of each scenario, pumparounds cost indicates the operating cost for intermediate condensers per input variation, pumping cost represents the cost associated with pump operation per input variation, and total operating cost is the sum of all input variable variations. Additionally, Scenario (a) represents NMSS-PIP control tuned using ITAE minimization weighting functions, while Scenario (b) corresponds to tuning based on economic weighting functions. Across all scenarios, the NMSS-PIP control based on the economic cost function led to significant cost savings, reducing operating costs by nearly 100% relative to the ITAE-based scenario. This improvement is particularly evident in the furnace's operating costs and cooling water usage, both of which saw substantial reductions. In terms of practical implications, these cost reductions can translate into considerable economic benefits for refineries. For example, the study shows that an increase in feed rate by 1800 barrels per day over one month could result in cost savings of approximately $84,700. These findings underscore the importance of using a control method that not only optimizes product quality but also minimizes energy consumption, making the process more sustainable and economically viable.

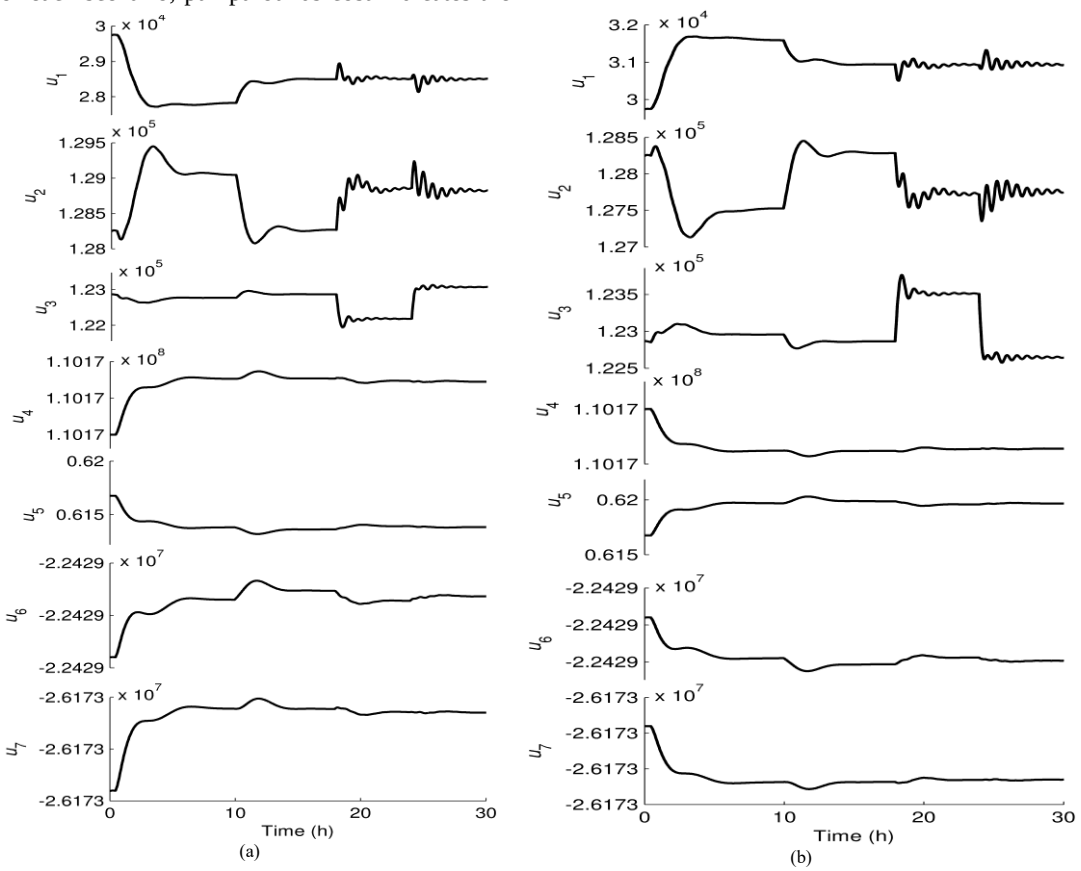

Fig. 9. Input changes in response to setpoint variations for the NMSS-PIP controller under the application of economic weighting functions: (a) +1°F step change; (b) -1°F step change.

The results from this study highlight the effectiveness of the NMSS-PIP control strategy for managing complex, multivariable processes in crude distillation columns. The economic cost function approach used to tune the controller

demonstrates clear advantages in reducing energy consumption and maintaining product quality across different operating conditions. Compared to traditional control methods like PID and even advanced strategies like MPC, the NMSS-PIP controller offers a balanced solution, providing robustness and efficiency with fewer computational demands.

Moreover, the flexibility of the NMSS-PIP controller allows for easy integration with existing refinery infrastructure, making it a practical choice for operators looking to improve their process control without investing in entirely new systems.

In terms of closed-loop stability, the robustness of the NMSS-PIP control structure has been validated in previous research by Taylor et al. [27], who developed and tested robust PIP controllers within the non-minimal state space (NMSS) framework. Their work demonstrated that the PIP control strategy maintains stable closed-loop performance even under challenging conditions, such as model uncertainties and significant disturbance inputs. Specifically, Taylor et al. evaluated this control structure on multivariable systems, including laboratory-scale materials handling and stochastic benchmark simulations, underscoring its capability to handle variability and 'worst-case' disturbance scenarios. Therefore, this study relies on Taylor et al.'s findings as a foundational stability assessment for the NMSS-PIP controller, focusing here on its optimization for energy efficiency and cost functions.

The NMSS-PIP control method demonstrates marked advantages in optimizing energy consumption, maintaining product quality, and managing disturbances within the CDU framework, effectively addressing the limitations encountered with traditional PI control. As illustrated in the results, the NMSS-PIP controller not only minimized operating costs by nearly 100% through economically weighted tuning but also maintained consistent product quality across varied operational conditions. For instance, in scenarios of ±5°F step changes in input feed temperature, the NMSS-PIP controller ensured product output stability with minimal oscillation, a notable improvement over PI, which often struggled to stabilize under similar disturbances. Moreover, with its centralized nature, the NMSS-PIP can be tuned based on cost objective functions, making it particularly suited to address the energy efficiency demands of Industry 4.0 as global energy shortages intensify. The NMSS-PIP's adaptable structure and direct compatibility with industry-standard software position it as a viable next-generation industrial controller, providing a practical alternative to the PI controller for large-scale processes. This combination of robustness, cost optimization, and practical scalability underscores the potential of NMSS-PIP to evolve as an advanced, energy-conscious control solution in modern industrial applications.

III. Conclusions

This study demonstrates the effectiveness of the NMSS-PIP control strategy in optimizing the operation of crude distillation units (CDUs). By implementing the PIP control system within a Non-Minimal State Space (NMSS) framework, the controller achieved substantial energy savings while maintaining product quality under disturbance scenarios, such as changes in feed rate, temperature, and composition. The economic cost function approach used to tune the controller's weight matrices led to significant reductions in operating costs, particularly in furnace duty and cooling water usage, highlighting its energy-saving potential. Results indicate that the NMSS-PIP strategy outperforms traditional PID and ITAE-tuned controllers in both energy efficiency and control precision, offering robust disturbance rejection with smooth control actions.

However, the NMSS-PIP control strategy may be most effective in continuous, steady-state processes, such as regulatory control in CDUs, rather than in highly variable or batch processes, where frequent recalibration of weighting matrices could be required. Additionally, while the NMSS-PIP method shows promise for enhancing operational efficiency in energy-intensive environments like refineries, further research is needed to validate its performance across different refinery units and under varying feed compositions over extended periods.

In conclusion, the NMSS-PIP control framework presents a powerful tool for optimizing crude distillation processes, with significant potential to improve energy savings, operational efficiency, and process stability. Future work could explore real-time implementations and assess the adaptability of NMSS-PIP control in broader refinery applications, contributing to more sustainable process control in the oil and gas industry.

REFERENCES

[1] Zhang, H., Liu, X., and Wang, Y., "Sustainable optimization of crude oil distillation through integrated energy-saving control systems," *Energy Reports*, vol. 9, pp. 435-450, 2023.
[2] S. Skogestad, "Probably the best simple PID tuning rules in the world," J. Process Control, vol. 13, no. 4, pp. 291–309, 2007.
[3] M. L. Darby and M. Nikolaou, "MPC: Current practice and challenges," Control Eng. Pract., vol. 20, no. 4, pp. 328–342, 2012.
[4] S. J. Qin and T. A. Badgwell, "A survey of industrial model predictive control technology," Control Eng. Pract., vol. 11, no. 7, pp. 733–764, 2003.
[5] E. F. Camacho and C. Bordons, Model Predictive Control. New York: Springer, 2004.
[6] A. Bemporad and D. Muñoz de la Peña, "Multiobjective model predictive control," Automatica, vol. 45, no. 12, pp. 2823–2830, 2009.
[7] W. L. Luyben, Process Modeling, Simulation, and Control for Chemical Engineers. New York: McGraw-Hill, 2006.
[8] F. Sun, T. Liu, B. Song, Y. Cui, Z. K. Nagy, and R.Findeisen, "Multi-objective optimization based nonlinear

model predictive control of seeded cooling crystallization process with application to β form L-glutamic acid," Chemical Engineering Science, vol. 299, 2024, 120475. Doi: 10.1016/j.ces.2023.120475.

[9] 9. Alberto Bemporad, David Muñoz de la Peña, "Multiobjective model predictive control," Automatica, vol. 45, no. 12, pp. 2823-2830, 2009. DOI: https://doi.org/10.1016/j.automatica.2009.09.032

[10] Qin, S. J. and Badgwell, T. A., "A survey of industrial model predictive control technology," Control Engineering Practice, vol. 11, no. 7, pp. 733-764, 2003.

[11] G. Dulac-Arnold, R. Evans, P. E. Sountsov, "Challenges of Real-World Reinforcement Learning," NeurIPS 2019. [DOI: 10.48550/arXiv.1904.12901]

[12] T. Skogestad, "Dynamics and control of distillation columns—a tutorial introduction," Chemical Engineering Research and Design, vol. 75, no. 6, pp. 539-562, 1997.

[13] Kunru Yang, Shirun Liu, Chang He, Bingjian Zhang, Qinglin Chen, Ming Pan, "Improving energy saving of crude oil distillation units with optimal operations," Journal of Cleaner Production, vol. 263, p. 121340, 2020.

[14] M. M. Khalilipour, J. Sadeghi, F. Shahraki, and K. Razzaghi, "Nonsquare multivariable non-minimal state space-proportional integral plus (NMSS-PIP) control for atmospheric crude oil distillation column," Chem. Eng. Res. Des., vol. 113, pp. 140–150, 2016, doi: 10.1016/j.cherd.2016.07.018.

[15] C. Taylor, S. Chotai, and P. Young, Proportional-Integral-Plus Control of Multivariable Systems. New York: Springer, 2013.

[16] L. Larsson and S. Skogestad, "Energy efficient control of distillation columns," J. Process Control, vol. 10, no. 1, pp. 69–77, 2000.

[17] B. Kiani Talaei, F. Shahraki, J. Sadeghi, M. Khalilipour," Optimal metaheuristic state-dependent parameter proportional-integral-plus control: Alternative to gain-scheduled controller for control of a nonlinear continuous stirred tank reactor", Systems and Soft Computing, Vol. 5, 20053, 2023.

[18] S. Kharaji, J. Sadeghi, F. Shahraki, and M. M. Khalilipour, "A new control structure for tert-amyl methyl ether production using reactive distillation," ISA Trans., vol. 97, pp. 53–66, 2020, doi: 10.1016/j.isatra.2019.07.021.

[19] B. Bidar, M. M. Khalilipour, F. Shahraki, and J. Sadeghi, "A data-driven soft-sensor for monitoring ASTM-D86 of CDU side products using local instrumental variable (LIV) technique," J. Taiwan Inst. Chem. Eng., vol. 84, pp. 49–59, 2018, doi: 10.1016/j.jtice.2018.01.009.

[20] Y. Shin, R. Smith, and S. Hwang, "Development of model predictive control system using an artificial neural network: A case study with a distillation column," *Journal of Cleaner Production*, vol. 277, p. 124124, 2020, doi: 10.1016/j.jclepro.2020.124124.

[21] L. Li, R. Dixon, E. Stewart, and H. Duan, "Implementation of proportional-integral-plus control to a high redundancy actuator for a track switch system," *IFAC-Papers OnLine*, vol. 56, no. 2, pp. 4406-4411, 2023, doi: 10.1016/j.ifacol.2023.05.095.

[22] J. Hernández and L. Jiménez, "Energy optimization of distillation columns," Ind. Eng. Chem. Res., vol. 38, no. 9, pp. 3446–3453, 1999.

[23] W. L. Luyben and B. Tyreus, Process Control and Design for Chemical Engineers. New York: McGraw-Hill, 1998.

[24] T. Kailath, Linear systems, Prentice-Hall Englewood Cliffs, NJ1980.

[25] C.-L. WANG, P.C. YOUNG, Direct digital control by input-output, state variable feedback: theoretical background, International Journal of Control 47 (1988) 97-109. DOI:10.1080/00207178808905999

[26] C.L. Phillips, H.T. Nagle, Digital control system analysis and design, Prentice Hall Press2007.

[27] C. Taylor, A. Chotai, P. Young, Robust PIP control of multivariable stochastic systems, Robust Control: Theory, Software and Applications (Digest No: 1997/380), IEE Colloquium on, IET, 1997, pp. 2/1-2/3.

[28] J. Sadeghi, Modelling and Control of Non-linear Systems Using State-Dependent Parameter (SDP) Models and Proportional-Integral-Plus (PIP) Control Method., Ph.D Dissertation, Lancaster University, UK, 2006.

[29] Yao H., Chu J., Operational optimization of a simulated atmospheric distillation column using support vector regression models and information analysis, Chemical Engineering Research and Design, Vol. 90, pp. 2247-2261, 2012.

[30] F. Castillo, R. E. Hernández, and L. M. Sánchez, "Cost estimation for utilities in crude distillation units: A review of recent trends," AIChE Proceedings, pp. 1-10, 2023.

Mir Mohammad Khalilipour received his bachelor's degree in Chemical Engineering from Azad University, Iran, in 2004, and his master's and Ph.D. degrees in Chemical Engineering Process Design from the University of Sistan and Baluchestan, Zahedan, Iran, in 2008 and 2016, respectively. Over the course of his career, he has been actively involved in numerous industrial projects focused on process control and safety management within the chemical industry. He is currently an Associate Professor in the Chemical Engineering Department at the University of Sistan and Baluchestan. His research interests include chemical process safety, control, and simulation, with a particular focus on process control, fault detection, carbon capture and the use of soft sensors in chemical processes.

Farhad Shahraki received the B.S. degree in chemical engineering from the University of Sistan and Baluchestan, Zahedan, Iran, in 1989, the M.S. degree in chemical engineering from Tarbiat Modares University, Tehran, Iran, in 1992, and the Ph.D. degree in chemical engineering from The University of Manchester, Manchester, U.K., in 2001. He is currently a Professor of Chemical Engineering with the University of Sistan and Baluchestan. His research interests include process integration, process modeling, and optimization.

Jafar Sadeghi received the B.S. degree in chemical engineering from the Isfahan University of Technology, Isfahan, Iran, in 1991, the M.S. degree in chemical engineering from the Sharif University of Technology, Tehran, Iran, in 1995, and the Ph.D. degree in chemical engineering from the University of Lancaster, Lancaster, U.K., in 2007. He is currently an Associate Professor with the University of Sistan and Baluchestan, Zahedan, Iran. His research interests cover process modeling and simulation, process control, process identification, process intensification, automation, and instrumentation.

Kiyanoosh Razzaghi received the B.S. degree in chemical engineering from the Iran University of Science and Technology, Tehran, Iran, in 2002, the M.S. and Ph.D. degrees in chemical engineering from the University of Sistan and Baluchestan, Zahedan, Iran, in 2005, and 2010. He is currently an Assistant Professor with the University of Sistan and Baluchestan, Zahedan, Iran. His research interests cover process modeling and simulation, process control and optimization, low pressure drop static mixers.

IECO

This page intentionally left blank.

International Journal Of
Industrial Electronics Control and Optimization
Print ISSN: 3517-2645
Online ISSN: 3568-2645
Homepage: https://ieco.usb.ac.ir/

Torque Vector Control and Direct Force Control in a Three-Phase Bearing-Less Induction Motor

Reza Ghanizadeh[1] | Hamed Azadrou[2] |

[1]Department of Electrical Engineering, Urmia Branch, Islamic Azad University, Urmia, Iran.
[2]Department of Electrical Engineering, Salmas Branch, Islamic Azad University, Salmas, Iran.
Corresponding author's email: azadrou.elec@gmail.com

Article Info

Article type:
Research Article

Article history:
Received: 28-May-2024
Received in revised form: 22-September-2024
Accepted: 15-October-2024
Published online: 22-June-2025

Keywords:
Bearing-less motor,
Torque control,
Levitation force control,
Vector control,
Direct force control.

ABSTRACT

Bearing-less induction motors (BLIMs) are suitable candidates for high-speed applications but suffer from low torque density and complex control issues due to the interaction of torque and levitation forces. To address these challenges, this paper presents a new control strategy that combines vector control and direct torque control (DTC) for torque management, alongside a novel force control method based on finite element analysis (FEA). The proposed approach minimizes interference between torque and force magnetic fields by employing a parallel winding structure and distinct control units for torque and force. Simulation results demonstrate that the proposed method significantly reduces torque ripple and improves steady-state performance compared to conventional vector control and DTC. Furthermore, the force control unit outperforms a dual field-oriented control (FOC) method in regulating rotor position, offering better suspension force control and faster stabilization. This work contributes to the development of more efficient control strategies for BLIMs, enhancing their performance in industrial applications.

NOMENCLATURE

W_m	Magnetic energy	L_{2s}	Torque windings self-inductances
i_{ab}	Two-phase current vector	L_{4s}	Force windings self-inductances
L_{ab}	Inductance matrix	F_{av}	Average suspension force
F_x and F_y	Suspension forces in x and y directions	T_{av}	Average electromagnetic torque
ω_{rm}	Mechanical rotor speed	$\psi_{2\alpha r}, \psi_{2\beta r}$	Flux linkages
ω_{2s}	Two pole slip frequency	v_k	Terminal voltage vector
ω_{4s}	Four pole slip frequency	i_k	Winding current vector
$i_{2\alpha s}, i_{2\beta s}$	Two pole stator constant dc currents	ψ_k	Flux linkage vector
$i_{2\alpha r}, i_{2\beta r}$	Two pole rotor constant dc currents	L	Inductance matrix
$i_{4\alpha s}, i_{4\beta s}$	Four-pole stator constant dc currents	γ	Angle between stator and rotor fluxes
$i_{4\alpha r}, i_{4\beta r}$	Four pole rotor constant dc currents	n_{1p}	Number of pole pairs in torque windings
M'_{24}	Mutual inductance between torque and force windings		

I. Introduction

Bearing-less motors are attractive electrical machines that work without any mechanical connection between the stationary and moving parts. This offers advantages such as low thermal problems, low maintenance requirements, high-speed capability, and no spark [1]. The stator in a bearing-less induction motor is same as a conventional induction motor. But, two separate windings are located in each slot which are connected to distinct power supplies. Fist P pole winding called torque or motoring winding which generates the torque electromagnetic field. The second one, is P±2 pole force winding which generates the suspension force field [2-5]. Despite the simplicity of this structure, the torque density is very low, which is due to the occupation of the slot space

by the force winding. The combined winding structure partially solves the problem and enhances the efficiency as much as conventional induction motors. In this method both fields are produced by a single set of windings [6-8]. However, the combined winding strategy requires a complicated power electronics converter constructed. Moreover, there is speed induced voltage in force windings which reduces the quality of performance, especially at high speeds.

The motor proposed in this work, has been designed and manufactured based on a novel winding strategy presented in [9] and [10]. The structure consists of two three phase parallel coils, one of which has a neutral point, while the other is connected to the force power supply. Researches have shown that parallel winding structure can reduce the speed induced voltage in the force windings to zero.

Control of a BLIM is an inherently challenging problem due to the effect of rotor induced currents. In addition to the torque current, force current is also induced in the rotor bars which degrade the torque and force quality. Also, the magnetic suspension force is defined with respect to displacement and current. So, the transfer function is unstable complicating the controller design. Vector control in a bearing-less motor with combined winding structure has been explained in [11]. In [12], a non-linear control system for an especial type bearing-less motor with rotor angle consideration has been presented. Fuzzy logic systems have been used in some articles to control the rotor position [13] and [14]. This method is usually fast and does not require complex mathematical equations. Among the other methods that can be used for estimating the parameters of an induction motor in control methods is the PSO algorithm [15]. Accurate estimation of the induction motor parameters has a significant impact on the performance and quality of the control system. The effects of cross-coupling in a combined winding BM by extracting an appropriate disturbance transfer function has been investigated in [16]. Decouple and separate control of the torque and force windings voltage disturbances is the most important point in a bearing-less motor. [17] investigated a DPNV type bearing-less motor and has shown that the structure is very effective in the field interference reduction. Optimization of the commutation period in a bearing-less motor has been proposed in [18]. In the work, the turn- on angle and conduction region of each phase winding have been chosen as the control targets.

In this work, a new control strategy has been provided for a BLIM. Force control unit is based on finite element analysis without any need to complex mathematical equations. Torque control unit is a modified direct torque control method based on phase currents controllers.

II. Proposed BLIM

A. Structure of the motor

Traditional BLIMs consist of two separate windings located in same slots which create torque field and force field. In combined winding structure, both fields are generated by only one winding set. But the existence of non-zero speed induced voltage in the force windings significantly reduces the system efficiency. To solve the problem, a parallel winding structure has been used which is shown in Fig. 1.

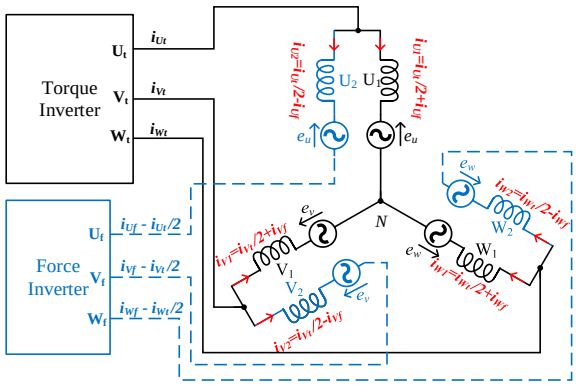

Fig. 1. BLIM with parallel winding structure

This structure has two sets of terminals, one for torque current and the other for suspension force current. Although both terminals belong to the common coil, the torque terminal is connected in such a way that the two similar parts of the coil have opposite directions. The winding of phase k (k=u, v, w) has two parallel parts denoted by k_1 and k_2 in Fig. 1, one is connected to the neural point point and the other one is connected to the force inverter. The current of phase k of the torque winding is divided between two parts k_1 and k_2, so that half of the current enters each of coils and induces the speed voltage (e_k) in them. The force inverter supplies current $(i_{kt}/2 - i_{kf})$ into the winding, where the force current i_{kf} flows through both coils k_1 and k_2. The speed induced voltage in one of the force windings is negative while the other winding has a positive induced voltage, so that eventually the windings will be without voltage. In this way, the force current can be controlled independently of the rotor speed and without the need for isolation with the torque inverter.

B. Dynamic equations

Terminal voltage in the torque and force inverters consists of three components including the resistance drop voltage, the electromotive force, and the speed voltage.

$$v_k = R_k i_k + L\frac{di_k}{dt} + \omega\frac{d\psi_k}{dt} \quad (1)$$

where the bold parameters v_k. i_k. and ψ_k represent the windings voltage vector, windings current vector, and flux linkage vector, respectively.

$$v_k = \begin{bmatrix} v_{U1} \\ v_{U2} \\ v_{V1} \\ v_{V2} \\ v_{W1} \\ v_{W2} \end{bmatrix},\ i_k = \begin{bmatrix} i_{U1} \\ i_{U2} \\ i_{V1} \\ i_{V2} \\ i_{W1} \\ i_{W2} \end{bmatrix}, \text{and } \psi_k = \begin{bmatrix} \psi_{U1} \\ \psi_{U2} \\ \psi_{V1} \\ \psi_{V2} \\ \psi_{W1} \\ \psi_{W2} \end{bmatrix}, \quad (2)$$

And L denotes the self and mutual inductances in a 6×6 matrix as follows.

$$L = \begin{bmatrix} L_u & M_{11} & M_{12} & M_{13} & M_{12} & M_{13} \\ M_{11} & L_u & M_{13} & M_{12} & M_{13} & M_{12} \\ M_{12} & M_{13} & L_v & M_{11} & M_{12} & M_{13} \\ M_{13} & M_{12} & M_{11} & L_v & M_{13} & M_{12} \\ M_{12} & M_{13} & M_{12} & M_{13} & L_w & M_{11} \\ M_{13} & M_{12} & M_{13} & M_{12} & M_{11} & L_w \end{bmatrix} \quad (3)$$

where, M_{11} denotes the mutual inductance between two coils $k_1$and k_2, M_{12} is the mutual inductance between coil k_1 and $k_2{}'$, M_{13} illustrates the mutual inductance between coil k_1 and $k_3{}'$, and L_k denotes the self inductance of winding k, while $L_u = L_v = L_w = L$.

Considering $R_k = R$ and according to the matrixes, the voltage in terminals u_1 and u_2 are written as:

$$v_{u_1} = R\left(\frac{i_{ut}}{2} + i_{uf}\right) + \frac{1}{2}(L + M_{11} - M_{12} - M_{13})\frac{di_{ut}}{dt} + (L - M_{11} - M_{12} + M_{13})\frac{di_{uf}}{dt} + \omega\frac{d\psi_u}{dt} \quad (4)$$

$$v_{u_2} = R\left(\frac{i_{ut}}{2} - i_{uf}\right) + \frac{1}{2}(L + M_{11} - M_{12} - M_{13})\frac{di_{ut}}{dt} - (L - M_{11} - M_{12} + M_{13})\frac{di_{uf}}{dt} + \omega\frac{d\psi_u}{dt} \quad (5)$$

According to Fig. 1, the terminal voltage of the force converter can be calculated as:

$$v_{u_f} = v_{U_1} - v_{U_2} = 2R.i_{uf} + 2(L - M_{11} - M_{12} + M_{13})\frac{di_{uf}}{dt} \quad (6)$$

Same equations can be written for two other phases. The equation indicates that voltage of the force winding is independent of the speed induced component.

III. Control of BLIM

There are different factors that affect a BLIM performance. A delay in force response of a BLIM is one of them, which can be caused by iron losses, saturation, etc. Another factor is the error of the angular position of the rotor, which is caused by the interference of suspension force in axes x and y. Also, the interference between the torque and force fields is very important in suspension system performance in a BLIM. The motor proposed in this work has been constructed with the special structure explained in the previous section which almost eliminates the interference between the electromagnetic fields. Due to the non-linear structure, mathematical model can't guarantee the precise performance of the BLIM, especially at high speeds. In order to compensate the direction error and the delay in suspension force generation system, a new method has been proposed in this work which is based on finite element analysis (FEA) of the motor. In the presented control method, all non-linear working conditions of the motor are taken into account in FEA, and there is no need for complicated and time-consuming mathematical equations in force control unit. Moreover, a new torque control strategy including a switching table and current controller has been proposed that shows a precise and fast responses.

A. Proposed Force Control Strategy

In the proposed system, the data obtained by finite element analysis are used to model the system. Therefore, there is no need to use complex and high-order equations. Fig. 2 shows some rotor displacements from the center and the appropriate compensating force vectors. It can be seen that without any deviation, there is only a constant force F_0 in vertical direction to suspend the rotor.

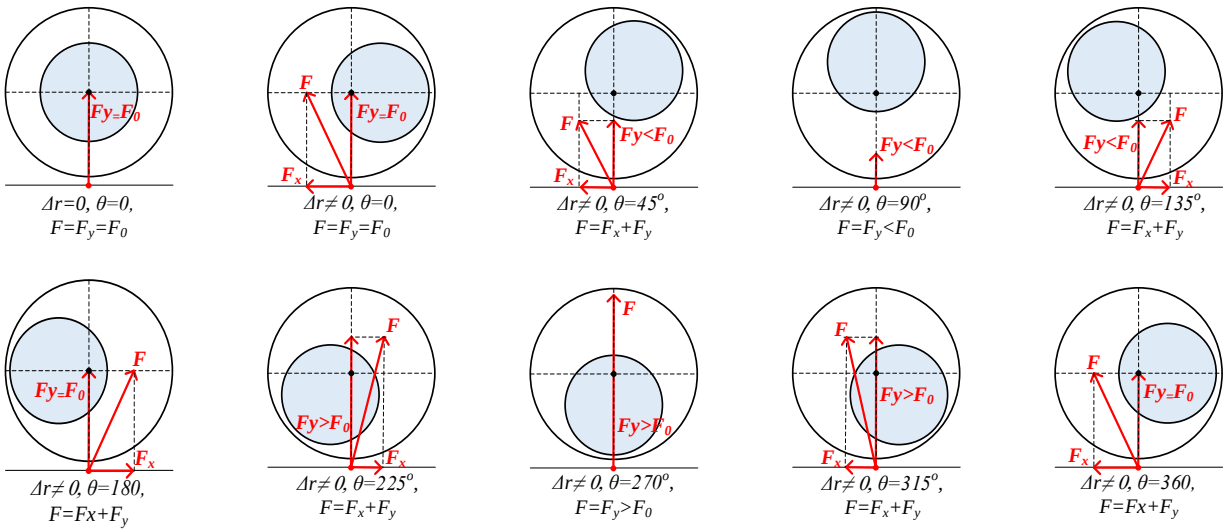

Fig. 2. Rotor deviation in different directions and suspension force vector

By defining Δr as the deviation of the rotor from the center and θ as the counterclockwise deviation angle from the horizontal axis, at the first step the suspension force vector $\vec{F} = F_x + F_y$ is determined for the command position of the rotor $\Delta r = 0$ and $\theta = 0$. In the following, the force factor is obtained for $\theta = 0$, and $\Delta r = 0.2.0.4 \ldots \ldots 2$ mm. The step is repeated exactly for $\theta = 5.10. \ldots .360$ and the corresponding force values are recorded. In this way, a set of data has been obtained that show the relationship between the force and the deviation from the center of the rotor in the entire movement range.

By defining Δr as the deviation of the rotor from the center and θ as the counterclockwise deviation angle from the horizontal axis, at the first step the suspension force vector $\vec{F} = F_x + F_y$ is determined for the command position of the rotor $\Delta r = 0$ and $\theta = 0$. In the following, the force factor is obtained for $\theta = 0$, and $\Delta r = 0.2\ 0.4 \ldots \ldots 2$ mm. The step is repeated exactly for $\theta = 5.10. \ldots .360$ and the corresponding force values are recorded. In this way, a set of data has been obtained that show the relationship between the force and the deviation from the center of the rotor in the entire movement range. By using curve fitting technique, the above relationship is made continuous covering all points of the air gap. The obtained profile for the proposed BLIM is shown in Fig. 3. Further investigations shown that the profiles are independent of the load torque value.

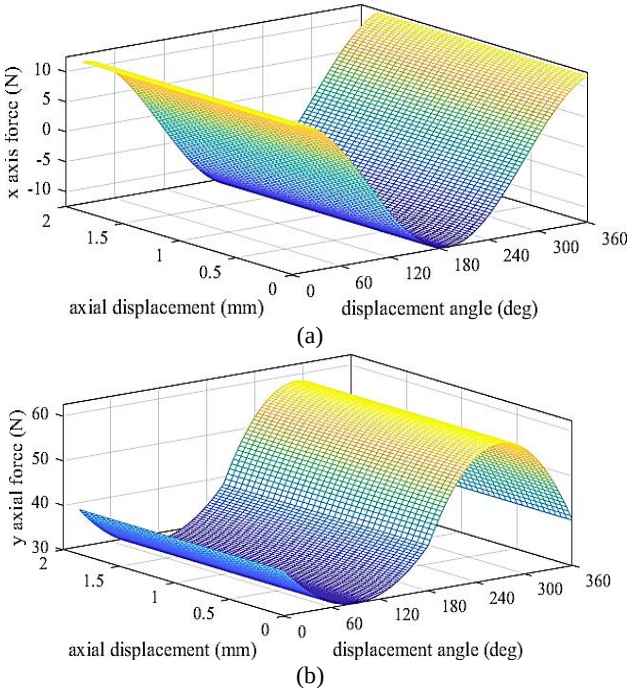

Fig. 3. Data obtained by FEA for the proposed BLIM

The data obtained by FEA are used to extract the suspension force vector for each deviation of rotor from the center. Block diagram of the proposed force control system is shown in Fig. 4.

As deviation of the rotor is determined by the position sensors, parameters Δr and θ are calculated and entered into the FEA block. This block is the continuous form of Fig. 3, which, selects the values F_x^* and F_y^* for a specified load torque. Assuming that the stator and rotor currents are specified by *s* and *r*, the suspension force in a squirrel cage BLIM has been illustrated in [19] as a matrix equation.

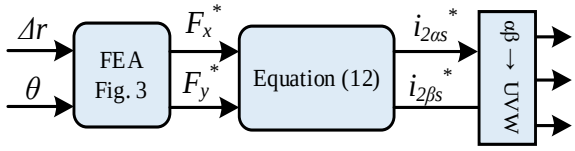

Fig. 4. Force control system

$$\begin{bmatrix} F_x \\ F_y \end{bmatrix} = M' \begin{bmatrix} i_{1\alpha g} & i_{1\beta g} \\ -i_{1\beta g} & i_{1\alpha g} \end{bmatrix} \begin{bmatrix} i_{2\alpha g} \\ i_{2\beta g} \end{bmatrix} \quad (7)$$

$$\begin{cases} i_{2\alpha g} = i_{2\alpha s} + i_{2\alpha r} \\ i_{2\beta g} = i_{2\beta s} + i_{2\beta r} \end{cases} \quad (8)$$

where M' is a parameter related to the motor dimensions and characteristics, calculated as [19]. Numbers 1 and 2 in parameters correspond to the torque and force windings current, respectively. Also, α and β are axes in the two phases system. For example, $i_{1\alpha g}$ and $i_{2\alpha g}$ denote the airgap flux component of current in torque and force windings, respectively. The BLIM proposed in this work has a special rotor structure presented in [4]. This structure has a main advantage that no current is induced by the stator force currents on the rotor. This means $i_{2\alpha r} = i_{2\beta r} = 0$, and so, $i_{2\alpha g} = i_{2\alpha s}$ and $i_{2\beta g} = i_{2\beta s}$. In this way, the suspension force will be proportional to the torque winding current.

$$i_{2\alpha s} = \frac{F_x^*}{M'.I_m} = k_f F_x^* \text{ and } i_{2\beta s} = \frac{F_y^*}{M'.I_m} = k_f F_y^* \quad (9)$$

This is an assumption that greatly simplifies the analysis. But the study on the BLIM and its control system showed that the use of exact motor equations leads to a better response and compensates the delay. Flux linkages in the two-phase system can be expressed as:

$$\begin{cases} \psi_{2\alpha r} = L_u \times i_{2\alpha r} + M_2 \times i_{2\alpha s} \\ \psi_{2\beta r} = L_u \times i_{2\beta r} + M_2 \times i_{2\beta s} \end{cases} \quad (10)$$

where M_2 is the mutual inductance between the stator force winding and the rotor. By combining the equations (8) and (10), it may be written

$$\begin{cases} i_{2\alpha g} = i_{2\alpha s} + \frac{1}{L_u}(\psi_{2\alpha r} - M_2 i_{2\alpha s}) \\ i_{2\beta g} = i_{2\beta s} + \frac{1}{L_u}(\psi_{2\beta r} - M_2 i_{2\beta s}) \end{cases} \quad (11)$$

Also, in an airgap flux-oriented vector control method, the vertical current component is zero ($i_{1\beta g} = 0$). For a constant α axis current ($i_{2\alpha s}$=I_m), combination of (7) and (11) is:

$$\begin{cases} i_{2\alpha s} = \left(\frac{F_x^*}{M'.I_m} - \frac{\psi_{2\alpha r}}{L_u}\right) / \left(1 - \frac{M_2}{L_u}\right) \\ i_{2\beta s} = \left(\frac{F_y^*}{M'.I_m} - \frac{\psi_{2\beta r}}{L_u}\right) / \left(1 - \frac{M_2}{L_u}\right) \end{cases} \quad (12)$$

The complete block diagram of the BLIM control system is shown in Fig. 6.

The obtained two phase force winding currents are compared with the corresponding actual currents measured by sensors and the error is entered to a PI controller. Proportional and integral gains of this controller in this controller have been obtained based on trial-and-error method as 1.28 and 0.025, respectively.

B. Proposed Torque Control Strategy

Various vector control (VC) structures have been presented for induction motors in all of them the stator current is used to control the produced torque. Assuming that indices "1" show the values related to the torque windings, the current is decomposed into two perpendicular torque and flux components denoted by $i_{1\alpha}$ and $i_{1\beta}$, which are used to control the torque and flux, respectively. So, the torque in rotor flux reference frame can be written as

$$T_e = \frac{3}{2} n_{1p} \frac{L_{1m}}{L_r} \left(\psi_{1\alpha r} \times i_{1\beta r} - \psi_{1\beta r} \times i_{1\alpha r}\right) \quad (13)$$

where L_{1m} and L_r denote the magnetizing inductance and rotor inductance, respectively. n_{1p} is the number of pole pairs in the torque windings. Also, $\psi_{1\alpha r}$ and $\psi_{1\beta r}$ indicate two perpendicular axes rotor flux linkages. Ignoring the flux in α axis, it can be written as:

$$T_e = \frac{3}{2} n_{1p} \frac{L_{1m}}{L_r} \left(\psi_{1\alpha r} \times i_{1\beta r}\right) \quad (14)$$

On the other hand, a direct torque control (DTC) system does not require any current controller. The equations of a DTC for the torque windings of a BLIM can be written as:

$$T_e = \frac{3}{2} n_{1p} I_m\{\vec{\psi}_{1s}^{*}\, \vec{i}_{1s}\} \quad (15)$$

$$\vec{i}_{1s} = \frac{1}{\sigma L_{1s}} \vec{\psi}_{1s} - \frac{L_m}{\sigma L_{1s} L_r} \vec{\psi}_{1r}.\ \sigma = 1 - \frac{L_m^2}{L_{1s} L_r} \quad (16)$$

Combining the equations, following equation is obtained.

$$T_e = \frac{3}{2} n_{1p} \frac{L_m}{\sigma L_{1s} L_r} |\vec{\psi}_{1s}||\vec{\psi}_{1r}| sin\gamma \quad (17)$$

Where γ denotes the angle between the stator and rotor flux linkage vectors. The derivative of (17) indicates that, the produced torque depends on angle γ. Therefore, the motor torque can be controlled quickly by adjusting the angle γ. By applying appropriate voltage vectors to the stator torque windings, the phase equation for a torque winding on stator can be written as follows.

$$\frac{d\vec{\psi}_{1s}}{dt} = \vec{V}_{1s} - R_{1s}\vec{i}_{1s} \approx \vec{V}_{1s} \rightarrow \Delta\vec{\psi}_{1s} = \vec{V}_{1s}\Delta t \quad (18)$$

$$\frac{d\vec{\psi}_{1r}}{dt} + \left(\frac{L_m}{\sigma L_{1s} L_r} - \frac{R_r}{L_r} - j\omega_2\right)\vec{\psi}_{1r} = \frac{R_r L_m}{\sigma L_{1s} L_r}\vec{\psi}_{1s} \quad (19)$$

where indices "1" show the values related to the torque windings. In order to obtain a fast response with low ripple and high precision, a new control strategy has been presented in this work which includes a switching table instead of pulse width modulation (PWM) method. Also, hysteresis current controllers have been used to adjust the torque winding currents. Assuming that the flux is constant and Δ denotes small variation, the equations of the conventional vector control method in the torque windings can be written as:

$$\begin{cases} |\vec{\psi}_{1r}| = K_\alpha \times i_{1\alpha} \\ T_e = K_\beta \times i_{1\beta} \end{cases} \rightarrow \begin{cases} |\vec{\psi}_{1r}| \propto i_{1\alpha} \\ T_e \propto i_{1\beta} \end{cases} \rightarrow \begin{cases} \Delta|\vec{\psi}_{1r}| \propto \Delta i_{1\alpha} \\ \Delta T_e \propto \Delta i_{1\beta} \end{cases} \quad (20)$$

Based on direct torque control strategy, by applying a voltage in a short switching interval, the stator flux vector rotates from $\vec{\psi}_{1s}$ to $\vec{\psi}_{1s}^{1}$, as shown in Fig. 5. Due to the large time constant of the rotor, it can be assumed with reasonable accuracy that the rotor flux linkage is constant in this interval.

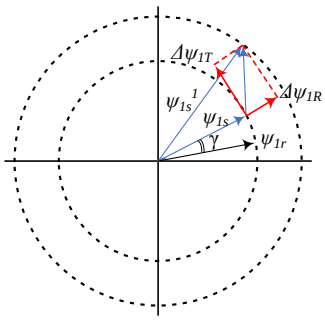

Fig. 5. Flux change in a short switching interval

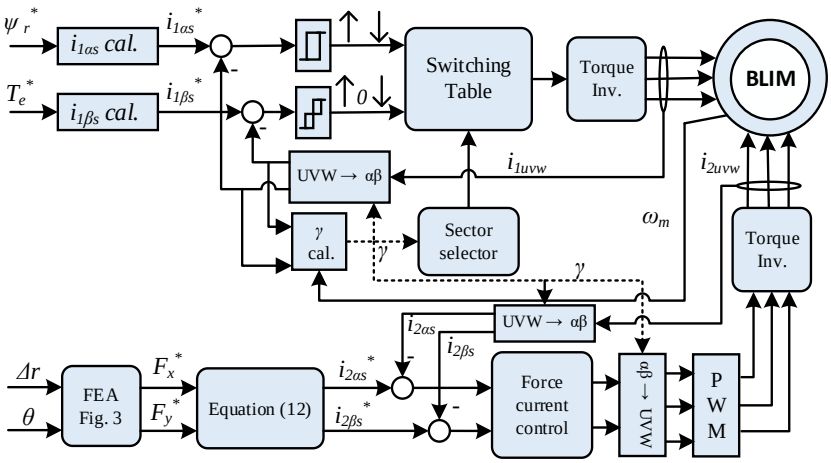

Fig. 6. Block diagram of the proposed control system for the BLIM.

Change of stator flux $\Delta\vec{\psi}_{1s}$ is decomposed into two radial and tangential components denoted by $\Delta\vec{\psi}_{1R}$ and $\Delta\vec{\psi}_{1T}$, respectively. According to Fig. 5, (17) can be rewritten as follows:

$$\Delta T_e = K\left|\vec{\psi}_{1r}\right|\left(\left|\vec{\psi}_{1s}^{1}\right| sin(\gamma+\Delta\gamma) - \left|\vec{\psi}_{1s}\right| sin\gamma\right) \quad (21)$$

With suitable approximations

$$sin(\gamma+\Delta\gamma) = sin\gamma + cos\gamma\ sin\Delta\gamma \quad (22)$$

$$sin\Delta\gamma = \frac{\Delta\vec{\psi}_{1T}}{\left|\vec{\psi}_{1s}\right|} \quad (23)$$

$$\left|\vec{\psi}_{1s}^{1}\right| = \left|\vec{\psi}_{1s}\right| + \Delta\vec{\psi}_{1T} \quad (24)$$

Equation (21) can be written as follows.

$$\Delta T_e = K\left|\vec{\psi}_{1r}\right|\left\{\Delta\psi_{1T} cos\gamma + \Delta\psi_{1R}\ sin\gamma + \frac{\Delta\psi_{1T}\,\Delta\psi_{1R}}{\left|\vec{\psi}_{1s}\right|} cos\gamma\right\} \quad (25)$$

Second and third terms are ignorable. Therefore, (25) can be simplified as:

$$\Delta T_e = K\left|\vec{\psi}_{1r}\right|\Delta\psi_{1T}\ cos\gamma \ \rightarrow\ \ \Delta T_e \propto \Delta\psi_{1T} \quad (26)$$

$$\Delta\left|\vec{\psi}_{1s}\right| = \Delta\psi_{1R} \quad (27)$$

Ignoring the first order delay between stator and rotor linkage fluxes in (19), it can be obtained

$$\Delta\left|\vec{\psi}_{r}\right| = \Delta\psi_{1R} \quad (28)$$

Comparing the equations (18), (26), and (28) gives the following results.

$$\Delta\psi_{1R} \propto \Delta i_{1\alpha} \quad (29)$$

$$\Delta\psi_{1T} \propto \Delta i_{1\beta} \quad (30)$$

According to the analysis, block diagram of the proposed control method is shown in Fig. 6. It can be seen that the proposed torque controller is a direct control method in which, unlike the conventional DTC, the phase currents are controlled. The obtained results show that this has a good effect on the performance quality with respect to the conventional DTC. On the other hand, PI controllers and PWM have been eliminated, which reduces the system response time with respect to the conventional vector control method. The proposed controller includes hysteresis controllers for the current components, like a vector control, and a switching table as a direct torque control strategy.

IV. Simulation Evaluation

In order to examine the performance of the proposed control system, the BLIM along with the control system have been simulated in Matlab/Simulink software. Parameters of the BLIM are shown in TABLE I. For a more complete study, the results obtained by the proposed controller are compared with the dual field oriented method [10]. The suspension force profile with respect to other parameters are shown in Fig. 7.

To evaluate the performance of the four-pole motoring unit, an external load has been applied to the motor at t= 0.8 s. The obtained results using conventional vector control (VC), direct torque control (DTC), and the proposed control system have been shown in Fig. 8. As mentioned in the previous section, the proposed system is a current controller system which works based on switching table. The results indicate that the torque resulted by proposed system has less ripple than the conventional DTC method, while its transit time is better than the VC.

TABLE 1 PARAMETERS OF THE PROTOTYPE BLIM

Parameter	Symbol	Constraints
Power	P	2200 W
Speed	N	15000 rpm
Torque winding poles	P_t	2
Force winding poles	P_f	4
Supply frequency	f	250 Hz
Stator slots	Q_s	30
Rotor slots	Q_r	24
Voltage	V_L	220 V
Torque winding phase current	I_t	10 A
Force winding phase current	I_s	5 A
Stack length	l	38 cm
Rotor slot depth	h_{rp}	2.5 cm
Stator slot fill factor	f_f	0.6

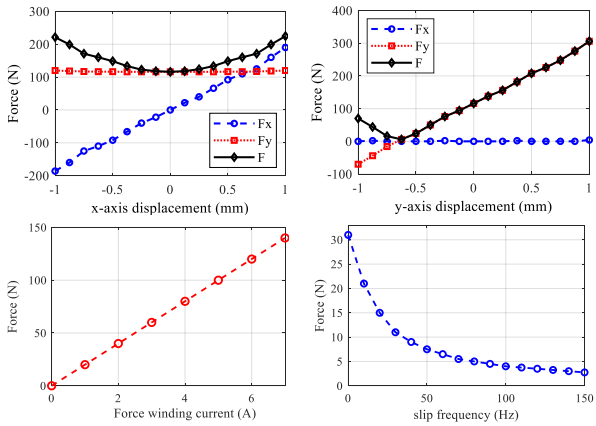

Fig. 7. Electromagnetic force in BLIM.

To show the force controller performance, it is assumed that the rotor is initially located at point $x = -0.2$ mm and $y = -0.1$ mm. As shown in Fig. 9, the electromagnetic forces are generated in two directions to return the rotor to the center of the stator. Fig. 9 (a) indicates the forces in the dual field-oriented control (FOC) presented in [11] while forces obtained by the proposed controller are shown in Fig. 9 (b). In both Fig. 9 (a) and Fig. 9 (b), the horizontal axis force (F_x) is produced for a short time and when the rotor

reaches the center, this force becomes zero. But the vertical force is reduced to a specified value to levitate the rotor in the center in normal performance condition. In this work, the displacement tolerance of the rotor in two directions is defined as 0.01 mm. In this way, after the rotor returns to this range, the force becomes zero. The rotor position variation in the process is shown in Fig. 9 (c) and (d) for the dual FOC and proposed system, respectively. The results indicate that using the proposed control system, the rotor returns to the center almost directly and in a short time.

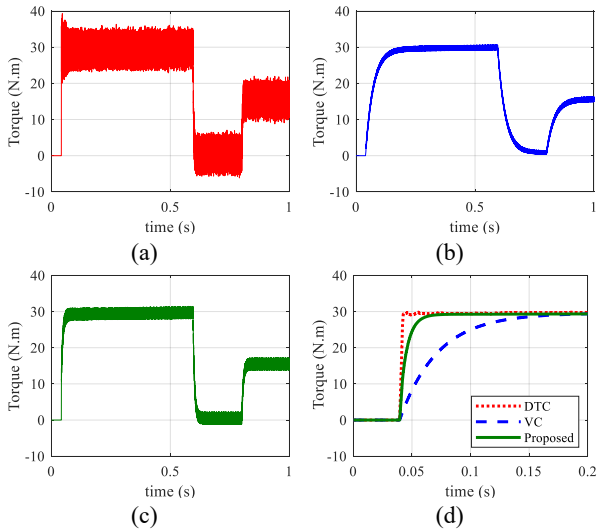

Fig. 8. Torque comparison, (a) direct torque control, (b) vector control, (c) proposed control, (d) transient time comparison.

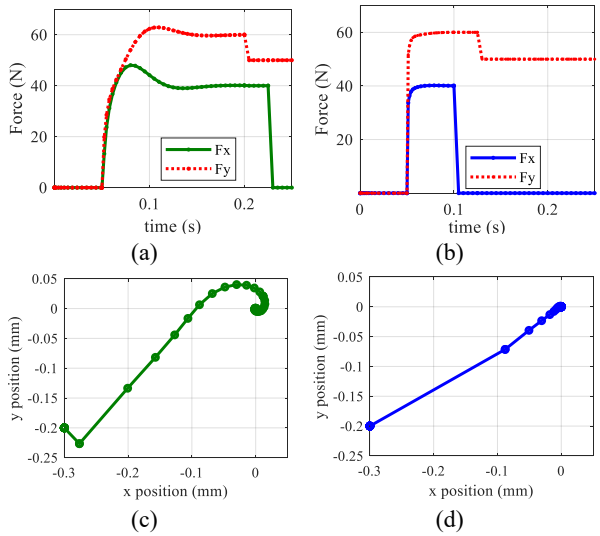

Fig. 9. Force comparison, (a) dual FOC method, (b) proposed method..

In order to investigate the rotor deviation in critical situations, an external load was applied to the motor at t=0.8 s and the results were extracted as Fig. 10. Comparison of position fluctuations using the dual FOC and the proposed controller confirm that the proposed force control method can regulate the suspension force so that the rotor has less fluctuations. To further demonstrate the effectiveness of the proposed control method, its performance on the bearingless induction motor has been compared with the method proposed in reference [20]. This comparison, under load conditions and during the moment of load application at t= 1.2 s, is shown in Fig. 11. This figure shows the currents with rotor deviation from the center. Fig. 11 (a) and (b) compare the force winding currents and Fig. (c) and (d) demonstrate the torque winding current of the motor using two control strategies. It can be observed that the proposed radial position control exhibits a short transient time during both startup and load application.

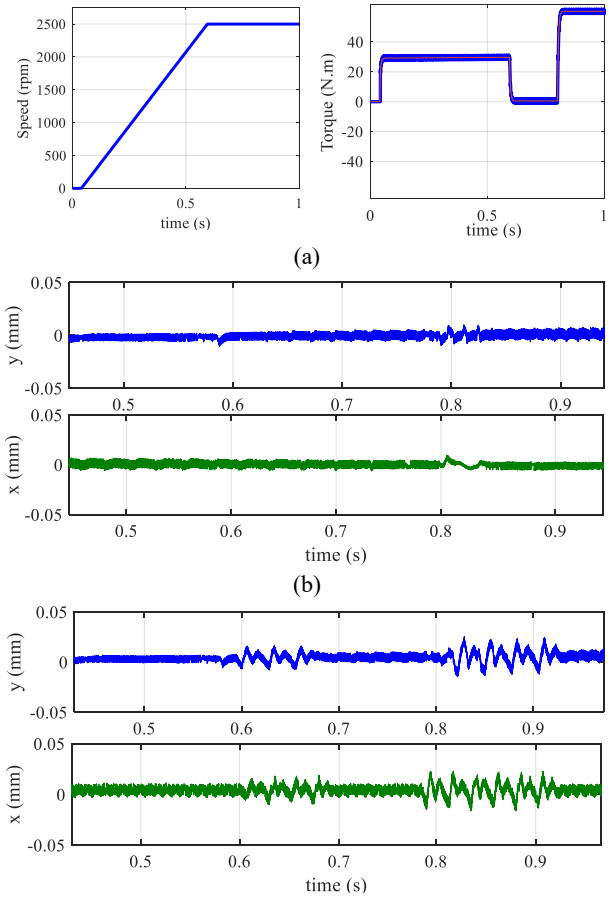

Fig. 10. Rotor position comparison, (a) speed and torque profiles, (b) proposed method, (c) dual FOC method.

V. Conclusions

A new control method for a parallel winding bearing-less induction motor has been presented. The method includes distinct torque and force control units. A direct torque control strategy with a current controller was used to adjust the motor torque and speed. The outputs obtained by the strategy is faster than conventional direct torque controller while includes fewer ripples in compare with conventional vector controller. Also, a new force control strategy was

presented that uses finite element analysis data to determine the appropriate force winding current. Using this method, the suspension force is adjusted without any complicated mathematical equations. The results obtained by simulation showed that the proposed control system shows acceptable capability in distinct control of torque and force in a bearing-less induction motor. The effect of load application on the force current is negligible using the proposed control strategy, and the rotor returns to the center position more quickly during startup.

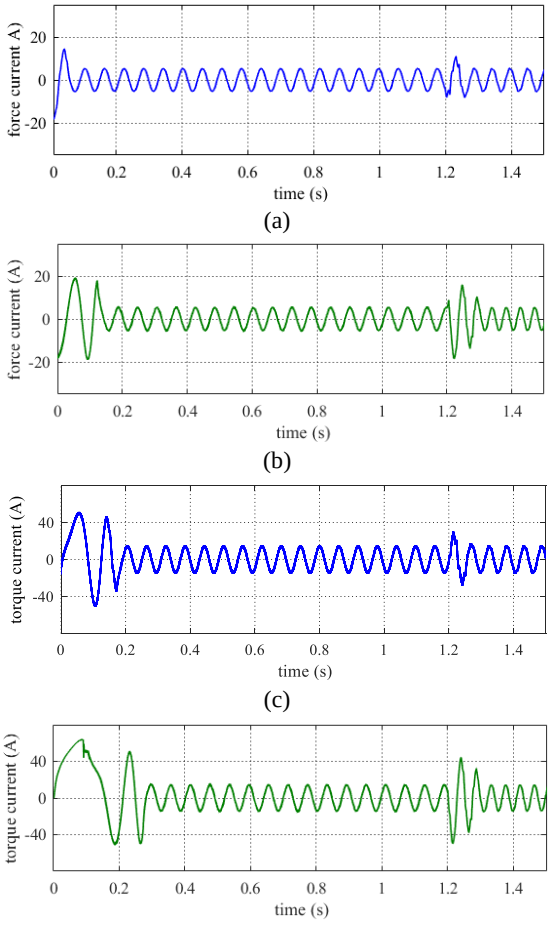

Fig. 11. Current comparison, (a) force current, proposed method, (b) force current, method presented in [20], (c) torque current, proposed method, (d) torque current, method presented in [20].

REFERENCES

[1] H. Azadrou, "Design and Optimization of a Very High Speed Three Phase Bearingless Induction Motor", International Journal of Industrial Electronics Control and Optimization, vol. 6, no. 4, pp. 283-289, 2023.

[2] T. Tera, Y. Yamauchi, A. Chiba, T. Fukao, and M. A. Rahman, "An improved mathematical model for speed sensorless control of fixed pole bearingless induction motor", *IEEE Trans. On Ind. Electronics*, vol. 71, no. 2, pp. 1286-1295, 2024.

[3] C. Lu, Z. Yang, X. Sun, Q. Ding, "Vibration compensation control strategy of composite cage rotor bearingless induction motor based on fuzzy coefficient adaptive-linear-neuron method", *ISA Transactions*, vol. 43, no. 1, pp. 66-77, 2024.

[4] S. Zhang, and F. L. Luo, "Direct control of radial displacement for bearingless permanent-magnet-type synchronous motors", *IEEE Trans. On Ind. Electronics*, vol. 56, no. 2, pp. 852-861, 2008.

[5] A. Chiba, D. Akamatsu, T. Fukao, and A. A. Rahman, "An improved rotor resistance identification method for magnetic field regulation in bearingless induction motor drives", *IEEE Trans. On Ind. Electronics*, vol. 55, no. 2, pp. 542-553, 2009.

[6] J. Huang, B. Li, H. Jiang, and M. Kang, "Analysis and control of multiphase permanent-magnet bearingless motor with a single set of half-coiled winding," *IEEE Trans. Ind. Electronics*, vol. 61, no. 7, pp. 3137–3145, 2014.

[7] H. Mitterhofer, B. Mrak, and W. Gruber, "Comparison of high-speed bearingless drive topologies with combined windings," *IEEE Trans. Ind. Applications*, vol. 51, no. 3, pp. 2116–2122, 2015.

[8] G. Sala, G. Valente, A. Formentini, and et al., "Space vectors and pseudoinverse matrix methods for the radial force control in bearingless multisector permanent magnet machines," *IEEE Trans. Ind. Electron*., vol. 65, no. 9, pp. 6912–6922, 2018.

[9] R. Oishi, S. Horima, H. Sugimoto, and A. Chiba, "A Novel Parallel Motor Winding Structure for Bearingless Motors", *IEEE Transactions on Magnetics*, vol. 49, no. 5, pp. 2287-2290, 2013.

[10] J. Chen, Y. Fujii, M. W. Johnson, A. Farhan, and E. L. Severson, "Optimal Design of the bearingless induction motor", *IEEE Trans. Ind. Applications*, vol. 57, no. 2, pp. 1375–1389, 2021.

[11] W. Gruber, and S. Silber, "Dual field-oriented control of bearingless motors with combined winding system", *2018 International Power Electronics Conference* (*IPEC-Niigata* 2018 *-ECCE Asia*), Oct. 2018.

[12] N. Turk, N. Bulic, W. Gruber, "Nonlinear control of a bearingless flux-switching slice motor with combined winding system", *IEEE/ASME Transactions on Mechatronics*, vol. 25, no. 1, pp. 152-163, 2019.

[13] Q. K. Jasim, M. Moanes, E. Ali, "Design of suspension control system for bearingless induction motor using fuzzy-I controller", *International Journal of Power Electronics and Drive System (IJPEDS)*, vol. 14, no. 2, pp. 771-780, 2023.

[14] Z. Yang, J. Jia, X. Sun, T. Xu, "A fuzzy-ELADRC method for a bearingless induction motor", *IEEE Trans. On Power Electronics*, vo. 37, no. 10, pp. 11803-11813, 2022.

[15] R. Havangi, M. Moredi, "PSO Based EKF Wheel-rail Adhesion Estimation", International Journal of Industrial Electronics Control and Optimization, vol. 6, no. 1, pp. 49-62, 2022.

[16] Y. Jiang, R. A. Torres, and E. L. Severson, "Current regulation in parallel combined winding bearingless motors", *IEEE Trans. On Ind. Applications*, vol. 55, no. 5, pp. 4800-4810, 2019.

[17] N. Petersen, A. Khamitov, T. Slininger, and E. L. Severson, "Machine design and precision current regulation for the parallel DPNV bearingless motor winding", *IEEE Trans. On Ind. Applications*, vol. 57, no. 6, pp. 7000-7011, 2021.

[18] Y. Su, Z. Yang, X. Sun, Z. Shen, "Direct torque control of bearingless induction motor based on super-twisting sliding mode control", *Journal of Control and Decision*, vol. 37, no. 11, pp. 13238-13249, 2024.

[19] D. Akamatu, A. Chiba, and T. Fukao, “A novel rotor resistance indentification in slip frequency controlled bearingless induction motors,” in Proc. 9th ISMB, Lexington, KY, Aug. 2004, CD-ROM.
[20] X. Ye, X. Tang, K. Xing, H. Wang, J. Yao, T. Zhang, “Repetitive control for vibration suppression of bearingless induction motor”, IEEE ACCESS, vol. 12, pp. 60532-60540, 2024.

Reza Ghanizadeh received the B.S. degree in electrical engineering from the Ardabil Branch, Islamic Azad University, Ardabil, Iran, in 2009, and the M.S. and Ph.D. degrees in electrical engineering from the University of Birjand, Birjand, Iran, in 2012 and 2017, respectively. He is currently an Assistant Professor with the Urmia Branch, Islamic Azad University, Urmia, Iran. His research interests include power quality, robust optimization, design of microgrid controllers, FACTS device and machine drives.

Hamed Azadrou was born in Salmas, Iran, in 1983. He received his B.S. degree in electrical engineering from Islamic Azad University, Abhar Branch, Abhar, Iran, and M.S. degree from Dezful Branch, Dezful, Iran, and PhD degree from Islamic Azad University, Urmia Branch, Urmia, Iran. He is a member of science in Islamic Azad University, Salmas Branch, Iran since 2012.

IECO

This page intentionally left blank.

International Journal Of
Industrial Electronics Control and Optimization
Print ISSN: 3517-2645
Online ISSN: 3568-2645
Homepage: https://ieco.usb.ac.ir/

Motion Shape Control of Superstructure in Base-Isolated Tall Buildings using GBMO-Based Uniform Deformation Techniques

Sadegh Etedali[1]

[1]Department of Civil Engineering, Birjand University of Technology, P.O. Box 97175-569, Birjand, Iran
[1]Corresponding author's email: etedali@birjandut.ac.ir

Article Info

Article type:
Research Article

Article history:
Received: 16-September-2024
Received in revised form: 10-November-2024
Accepted: 27-November-2024
Published online: 22-June-2025

Keywords:
Base-isolated structure,
GBMO algorithm,
Motion shape control,
Seismic performance,
Tall building

ABSTRACT

This paper proposes three techniques aimed at enhancing the seismic performance of base-isolated tall buildings through uniform deformation of the superstructure. The first and second methods focus on generating a uniform modal shape and an even distribution of seismic loads across the floors, while the third method seeks to minimize the standard deviation of story drifts. For these purposes, an optimization procedure based on a gas Brownian motion optimization (GBMO) algorithm is defined. Simulation results, compared to those for a 20-story reference base-isolated structure, demonstrate that these techniques effectively reduce maximum floor displacement, particularly in the upper levels of the studied buildings. The proposed methods show clear advantages in lowering maximum floor drift, a critical factor in seismic damage. Specifically, methods 1 and 3 resulted in significant reductions in maximum floor drift, ranging from 30% to 80% in the upper floors. Additionally, these methods led to a reduction of 10% to 15% in maximum acceleration and seismic forces on the upper floors, while a slight increase was observed in the lower floors. Among the methods, method 1 exhibited the best overall performance, yielding average reductions of 6.65%, 32.65%, and 0.88% in maximum floor displacement, drift, and acceleration, respectively, when compared to the reference base-isolated structure. While methods 2 and 3 resulted in only modest reductions in displacement and acceleration, they were effective in significantly lowering maximum floor drift.

I. Introduction

Base isolation is an engineering technique to protect structures from the damaging effects of earthquake excitations. Decoupling the structure from ground motion, significantly reduces the seismic forces transmitted to the structure, thereby enhancing its resilience and safety during an earthquake. This method has been increasingly adopted in the design and retrofit of both new and existing structures, particularly in regions prone to seismic activity [1]. Base isolation systems were initially designed for short-period structures, such as low-rise buildings, which are subjected to short-period ground motions, like those from far-field earthquakes. The use of base isolation techniques shifts the fundamental period of typical low-rise buildings to 2.0–3.0 seconds, thereby significantly reducing seismic force demands during far-field ground motions and the spectral acceleration decreases. However, However, the concerns regarding the application of base isolation systems in high-rise buildings arise primarily from the relatively long fundamental period of the fixed-base superstructure [2-3]. Although the seismic performance of base isolation in tall buildings may not be as pronounced as those observed in short-period structures, they are still significant when compared to the improvements achieved in the response of long-period structures using some well-established seismic protection systems [3]. Over the last decade, the 18-story office Sendai MT building, the 41-story Thousand Tower, and a super high-rise building with a height of 177.4 m are some examples of utilizing the base isolations in tall buildings [2-3]. Furthermore, several studies have been carried out on base-isolated high-rise buildings. Roussis and Constantinou [4] introduced innovative devices designed to address the damage caused by the uplift of isolators during significant earthquakes. Ariga et al. [5] examined the resonant behavior of these buildings under long-period

ground motions, highlighting critical vulnerabilities. Hino et al. [6] employed the Monte Carlo method to evaluate the limitations on the height-to-width ratio for base-isolated buildings, ensuring their stability. Ma et al. [7] Studied the seismic response of base-isolated tall buildings under fully nonstationary excitation. The effects of stiffness of a base-isolation layer and a superstructure for a base-isolated high-rise building were studied in [8]. Darwish and Bhandari [9] investigated the seismic performance of two 12-story and 15-story base-isolated steel–concrete composite buildings equipped with lead rubber bearing isolators. Li et al [10] conducted a comprehensive investigation on the reduced model and the seismic response of the inter-story isolated building.

In recent years, metaheuristic optimization algorithms have garnered significant attention from researchers for the optimal design of seismic isolators in structures subjected to earthquakes. Shourestani et al. [11] applied a particle swarm optimization algorithm for seismic control of a smart base-isolated structure considering soil-structure interaction effects. Pal et al. [12] employed a genetic algorithm to optimize base isolation parameters across various soil conditions, including hard, medium, and soft soils. Etedali et al. [13] addressed the optimal design of pure-friction isolators with restoring devices in seismic-excited structures using a multi-objective cuckoo search-based approach. Ockak et al. [14] conducted a comprehensive study on the optimization of seismic isolators at the base of structures, using an adaptive harmony search algorithm. Öncü-Davas [15] explored various metaheuristic approaches for optimizing non-linear base isolation systems under near-fault earthquakes, considering the flexibility of the superstructure. Etedali and Khosravi Kareshk [16] proposed two optimal isolator distributions in the base story of asymmetric base-isolated structures to reduce torsional responses. Lastly, Lei and Yang [17] proposed an improved method for stochastic optimization of electromagnetic inertial mass dampers in nonlinear hybrid isolation systems subject to seismic excitations.

Base isolators are known to significantly reduce spectral acceleration by increasing the fundamental period of the structure. Optimal seismic isolation performance is achieved when the superstructure behaves as a rigid body, making base isolators particularly effective for low-rise structures with greater rigidity. This results in substantial reductions in inter-story displacements and absolute acceleration of the superstructure floors. Conversely, as the number of floors and the flexibility of the superstructure increase, the response of the base-isolated structure becomes increasingly influenced by the superstructure's lateral movements and interactions. In such scenarios, the effectiveness of seismic isolation in controlling inter-story drift and absolute floor acceleration generally diminishes. However, the motion shape of the superstructure can be controlled through the optimal design of floor stiffness, employing an optimization process to achieve uniform deformation across the superstructure. This technique aims to create an ideal state of isolation for the structure. This study proposes three uniform deformation techniques based on the GBMO algorithm to enhance the seismic performance of base-isolated tall buildings. Numerical analyses were conducted on a 20-story base-isolated building, and the seismic performances of these three proposed techniques were compared.

The structure of the paper is as follows. Section 2 introduces the equation of motion for the nonlinear base-isolated structures. Section 3 presents three methodologies for seismic performance enhancement of base-isolated tall buildings. An overview of the GBMO algorithm is provided in Section 4. Section 5 includes a numerical study on a 20-story base-isolated structure. The simulation results are discussed in Section 6. The paper concludes with a summary of the findings in the end section.

II. Equation of Motion for Nonlinear Base-Isolated Structures

The mathematical representation of the motion for a base-isolated structure under the ground acceleration $\ddot{x_g}(t)$ is expressed as [18]:

$$M\ddot{\mathrm{u}}(t) + \mathrm{C}\dot{\mathrm{u}}(t) + \mathrm{Ku}(t) + \Lambda \mathrm{f}(t) = -\mathrm{M1}\ddot{x_g}(t) \quad (1)$$

Here, M, C, and K denote the mass, damping, and stiffness matrices of the structure, respectively. Also, t is the duration of the ground acceleration. The terms $\mathrm{u}(t)$, $\dot{\mathrm{u}}(t)$, and $\ddot{\mathrm{u}}(t)$ represent the vectors of relative displacement, velocity, and acceleration of the base story and superstructure floors relative to the ground. The vector 1 indicates the location of the earthquake, Λ is the vector corresponding to the location of the isolation system and $\mathrm{f}(t)$ represents the restoring force of the isolation system. The restoring force of a lead rubber bearing (LRB) as a well-known isolation system can be calculated as:

$$\mathrm{f}(t) = Q_{pb} + \mathrm{k}_1 x_1(t) + c_1 \dot{\mathrm{x}}_1(t) \quad (2)$$

In this context, Q_{pb} represents the yield force of the lead plug, while k_1 and c_1 denote the linearized average stiffness of the nonlinear force-displacement loop of LRB and the viscous coefficient of the linearized LRB damping, respectively. The terms $x_1(t)$ and $\dot{x}_1(t)$ correspond to the relative displacement and velocity across the bearing. The yield force of the lead plug can be expressed as follows:

$$Q_{pb} = (1 - k_{yield}/k_{initial})Q_y \quad (3)$$

Here, k_{yield} and $k_{initial}$ are the post-yield and initial shear

stiffness, respectively, and Q_y represents the yield force arising from both the lead plug and rubber stiffness. While the nonlinear behavior of the LRB can be modeled using a bilinear approach, this model tends to overestimate the acceleration responses of the structure. To address this issue, the Bouc-Wen model, which better aligns with experimental results, can be employed. In this model, the hysteretic force component Q_{hyst} is defined as:

$$Q_{hyst} = Q_{pb}\, z(t) \tag{4}$$

The evolutionary variable z can be described by the differential equation:

$$\dot{z}(t) = A\dot{x}_1(t) - \gamma z(t)|\dot{x}_1(t)||z(t)|^{n-1} - \beta\dot{x}_1(t)|z(t)|^n \tag{5}$$

where $n = 1$, and the parameters $A = 2\gamma = 2\beta = k_{intial}/Q_y$ define the shape of the hysteresis loop.

III. Methodology

An optimization problem is formulated to determine the optimal distribution of the superstructure's stiffness along its height, ensuring that the superstructure behaves like a rigid body. This is achieved by seeking a more uniform deformation of the superstructure compared to the original structure, which can be addressed using the following methods:

A. Method 1

The first method involves identifying a stiffness distribution along the height of the superstructure that results in a uniform modal shape. The standard deviation of the first mode shape vector, denoted as σ_φ is given by:

$$\sigma_\varphi = \sqrt{\frac{1}{N+1}\sum_{i=1}^{N+1}(\varphi_{i1} - \bar{\varphi}_1)^2} \tag{6}$$

where N is the number of structural floors, $\varphi_{i1}$is the ith element of the first mode shape vector, and $\bar{\varphi}_1$ is the mean of the first mode shape vector, defined as:

$$\bar{\varphi}_1 = \frac{1}{N+1}\sum_{i=1}^{N+1}\boldsymbol{\varphi}_{i1} \tag{7}$$

By considering the ratio of the standard deviation of the first mode shape vector of the structure relative to that of the original structure as the cost function J_1 , the following optimization problem is formulated to achieve a uniform deformation of the superstructure:

$$\begin{aligned} &\text{Find:} && k_s = \{k_2, k_3, \dots, k_{N+1}\} \\ &\text{Minimize:} && J_1 = \frac{\sigma_\varphi}{\widetilde{\sigma_\varphi}} \\ &\text{Subjected to:} && k_{s-min} \ll k_s \ll k_{s-max} \end{aligned} \tag{8}$$

where k_s represents the design vector of the stiffness coefficients for the superstructure's floors, and k_{s-min} and k_{s-max} are the lower and upper bounds of the design vector.

B. Method 2

The second method seeks to find a stiffness distribution along the height of the superstructure that ensures a uniform distribution of seismic loads across the floors. The optimization problem is defined as follows:

$$\begin{aligned} &\text{Find:} && k_s = \{k_2, k_3, \dots, k_{N+1}\} \\ &\text{Minimize:} && J_2 = \frac{\sigma_f}{\widetilde{\sigma_f}} \\ &\text{Subjected to:} && k_{s-min} \ll k_s \ll k_{s-max} \end{aligned} \tag{9}$$

where σ_f represents the standard deviation of the seismic forces applied to the structure, calculated by:

$$\sigma_f = \sqrt{\frac{1}{N+1}\sum_{i=1}^{N+1}(\max(f_i(t)) - \bar{f}(t))^2} \tag{10}$$

Here, max $(f_i(t))$ is the maximum force on the i–th floor, and $\bar{f}$(t) is the mean of the maximum forces across the floors, given by:

$$\bar{f} = \frac{1}{N+1}\sum_{i=1}^{N+1}\max(f_i(t)) \tag{11}$$

Additionally, $\widetilde{\sigma_f}$ denotes the corresponding standard deviation of the seismic forces applied to the original structure.

C. Method 3

To achieve a rigid body-like behavior in the superstructure, the standard deviation of the story drifts σ_d is minimized through the following optimization problem:

$$\begin{aligned} &\text{Find:} && k_s = \{k_2, k_3, \dots, k_{N+1}\} \\ &\text{Minimize:} && J_3 = \frac{\sigma_d}{\widetilde{\sigma_d}} \\ &\text{Subjected to:} && k_{s-min} \ll k_s \ll k_{s-max} \end{aligned} \tag{12}$$

where

$$\sigma_d = \sqrt{\frac{1}{N+1}\sum_{i=1}^{N+1}(\max(d_i(t)) - \bar{d}(t))^2} \quad (13)$$

$$\bar{d} = \frac{1}{N+1}\sum_{i=1}^{N+1}\max(d(t)_i) \quad (14)$$

In these expressions, $\max(d_i)$ denotes the maximum drift of the i–th, and $\bar{d}$ is the average maximum drift across all floors. The term $\widetilde{\sigma_d}$ represents the corresponding standard deviation of the story drifts in the structure.

IV. Gas Brownian Motion Optimization

The GBMO algorithm is a noteworthy addition to the suite of metaheuristic optimization methods, delivering strong performance in traversing complex search spaces. It is introduced by Abdechiri et al. [19]. The GBMO leverages the physical principles of gas molecule dynamics, specifically their Brownian motion and turbulent rotational movement. This algorithm is designed to tackle complex optimization challenges by thoroughly exploring the search space to locate global optima. The GBMO algorithm has found applications in various domains where intricate optimization problems are common, including engineering design, machine learning, and operations research. Its capability to avoid local optima and effectively search for global solutions makes it particularly useful in situations where conventional optimization techniques may fall short. In this approach, the positions of molecules symbolize potential solutions within the search space. As these molecules move, their collective actions guide the process toward the global optimum. In the GBMO, each molecule is characterized by four primary attributes: position, mass, velocity, and turbulent radius. The algorithm follows these steps [19]:

1. Gas molecules are randomly generated within the search space.
2. Each molecule is assigned a random radius within the range [0, 1].
3. The system temperature is initialized, acting as a convergence criterion. The temperature starts high at the beginning of the optimization process and gradually decreases over time.
4. The positions and velocities of the molecules are updated according to the following equations:

$$v_i^d(t+1) = v_i^d(t) + \sqrt{\frac{3kT}{m}} \quad (15)$$

$$x_i^d(t+1) = x_i^d(t) + v_i^d(t+1) \quad (16)$$

where $x_i^d(t)$ and $v_i^d(t)$ represent the position and velocity of the ith molecule in the d-th dimension at iteration t, respectively. Additionally, T, k, and m are the temperatures, the Boltzmann constant, and the mass value associated with each molecule.

5. The fitness of each molecule's position is evaluated using the objective function.
6. In addition to Brownian motion, each molecule also undergoes turbulent rotational motion, which is generated by a chaotic sequence generator under the setting $a = 0.5$ and $b = 0.2$, described by the following equation:

$$x_i^d(t+1) = x_i^d(t) + b - \left(\frac{a}{2\pi}\right) sin(2\pi x_i^d)\, mod(1), \quad (17)$$

7. The objective function is re-evaluated, and the fitness of the molecules is compared based on their updated positions.
8. The mass and temperature of the molecules are adjusted using the following equations:

$$worst(t) = min\, fit_i(t) i \in \{1,2,..,N\} \quad (18)$$

$$best(t) = max\, fit_i(t) i \in \{1,2,..,N\} \quad (19)$$

$$m_i(t) = \frac{fit_i(t) - worst(t)}{best(t) - worst(t)} \quad (20)$$

$$T = T - \left(\frac{1}{mean(fit_i(t))}\right) \quad (21)$$

In Eq. (19), $worst(t)$ and $best(t)$ are the worst and best fitness values at iteration t, while $fit_i(t)$ represents the fitness of the ith molecule during the same iteration.

9. If the stopping criterion is met, the algorithm concludes. If not, steps 4 through 8 are repeated until the criterion is satisfied.

V. Numerical studies

To evaluate the proposed methodologies for enhancing the seismic performance of base isolation systems in tall buildings, a 20-story shear building is considered for numerical studies. The parameters of the superstructure and LRB as an isolation system are summarized in Table 1. An artificial earthquake for modeling the ground acceleration is produced using a band-limited Gaussian white noise. The well-known Kanai-Tajimi power spectral density function (PSDF) is often applied to model artificial earthquake excitations [20]. However, several attempts have been carried out to overcome the existing drawbacks in the PSDF. A second-order filter was proposed by Nagarajaiah and

Narasimhan [21] with the following PSDF:

TABLE 1 THE PARAMETERS OF THE SUPERSTRUCTURE AND LRB

Number of stories	$\boldsymbol{N = 20}$
Story mass (*i=2,..., N+1*)	$m_i = 1024$ kg
The damping ratio of the structure	$\xi_s = 5\%$
Base story mass	$m_b = 1024$ kg
The damping ratio of the LRB	$\xi_b = 10\%$
The target period of the LRB	T_b=3 sec.
Post-yield to pre-yield stiffness ratio	0.1
Yield force	$Q_y = 0.05W$

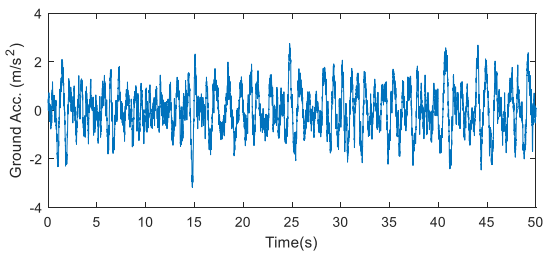

Fig. 1. The artificial earthquake excitation

$$s(\omega) = \frac{4\xi_g \omega_g \omega}{\omega^2 + 2\xi_g \omega_g \omega + \omega_g^2} \qquad (22)$$

where ξ_g and ω_g are the damping ratio and angular frequency of the ground. The above-mentioned artificial earthquake excitation was widely employed for modeling the earthquakes to apply to the base-isolated structures [22-24]. Figure 1 indicates the output of this filter which is applied to simulate the ground acceleration.

The nonlinear time-history analyses of the base-isolated structure are carried out using the MATLAB/Simulink software package [25]. Based on the optimization problem defined in section 3, the optimal floor stiffnesses are obtained using the GBMO algorithm. With an initial temperature of 30 °C and $\varepsilon = 0.001$, the GBMO algorithm with 200 gas molecules is implemented to find the optimal stiffnesses of the superstructure's floors. The convergence graphs of the GBMO algorithm for methods 1, 2, and 3 are illustrated in Figure 2. As can be seen, the convergences of the GBMO algorithm for methods 1, 2, and 3 are achieved in iterations 90, 90, and 150, respectively.

I. Results and discussion

The time responses of the fixed-base (FB) structure, the reference base-isolated (BI) structure, and the base-isolated structures designed using methods 1, 2, and 3 are compared in terms of top-floor displacement in Figure 3. Similarly, the time responses of the structures in terms of top-floor drift and top-floor acceleration are presented in Figures 4 and 5, respectively.

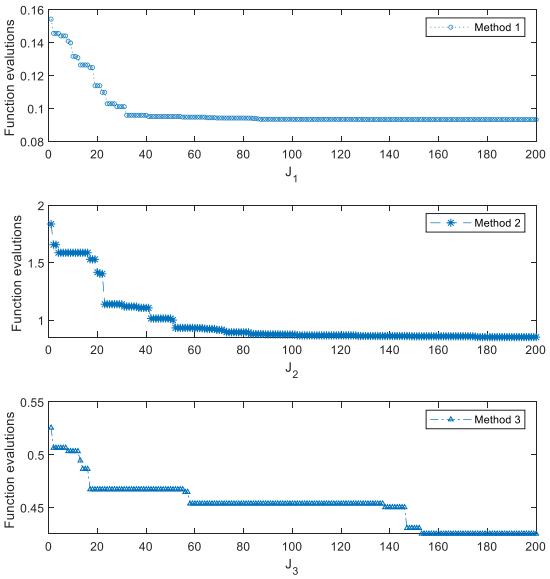

Fig. 2. The convergence graphs of the GBMO algorithm for methods 1, 2, and 3

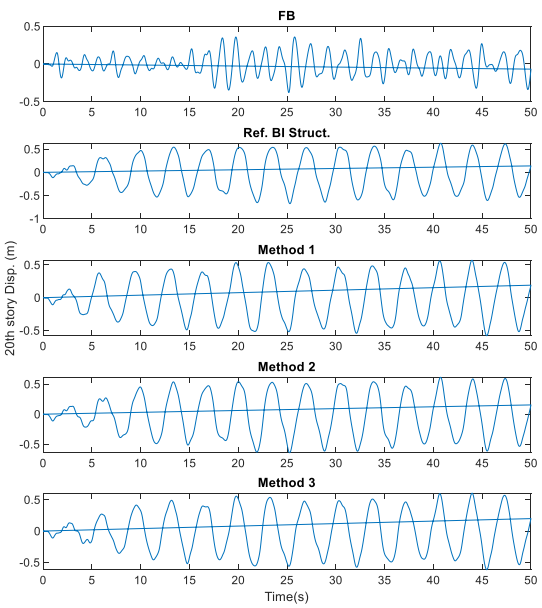

Fig. 3. Time histories of top floor displacement of the FB structure, reference BI structure, and the base-isolated structures designed using the proposed methods

As shown, the maximum top-floor displacement of the reference BI structure increases from 37.89 cm in the FB structure to 67.53 cm. Meanwhile, the maximum top-floor drift decreases from 3.46 cm to 1.65 cm, and the maximum top-floor acceleration reduces from10.58 m/s² to 4.77 m/s².

Therefore, it can be concluded that seismic isolation significantly reduces key seismic responses of the structure

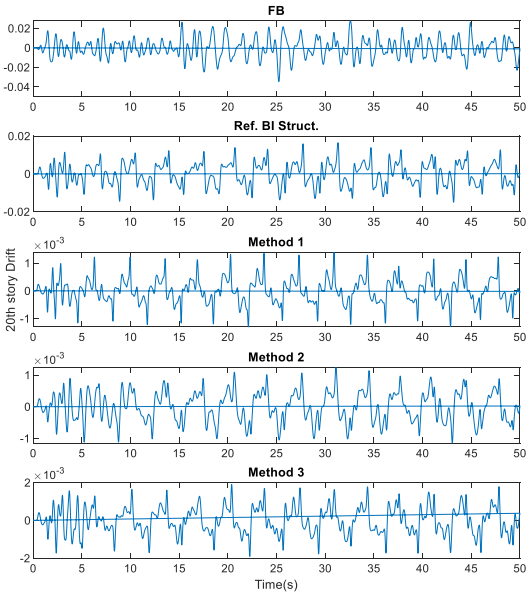

Fig. 4. Time histories of top floor drift of the FB structure, reference BI structure, and the base-isolated structures designed using the proposed methods

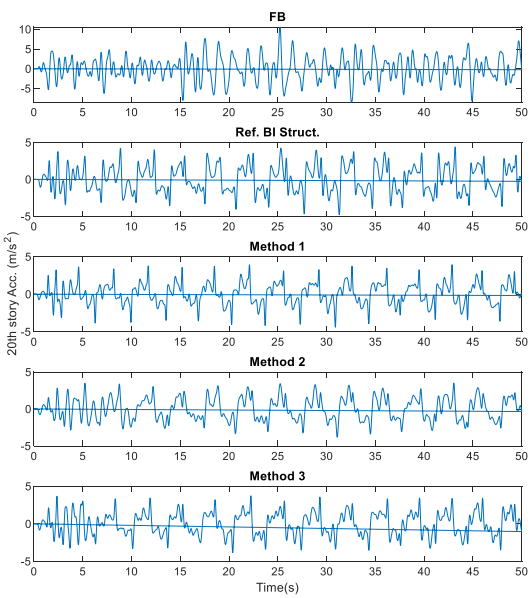

Fig. 5. Time histories of top floor acceleration of the FB structure, reference BI structure, and the base-isolated structures designed using the proposed methods

(i.e., maximum floor drift and acceleration), which often cause structural and non-structural damage. Furthermore, the proposed methods result in a notable decrease in the maximum top-floor drift compared to the reference BI structure. Specifically, the maximum top-floor drift decreases from 1.65 cm to 0.14 cm, 0.12 cm, and 0.19 cm for methods 1, 2, and 3,

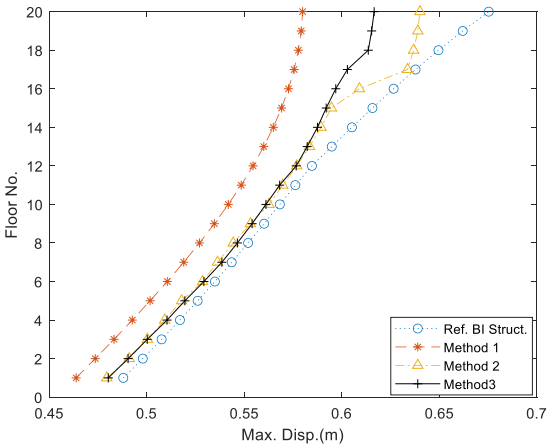

Fig. 6. Maximum floor displacements for the reference BI structure and the base-isolated structures designed using methods 1, 2, and 3.

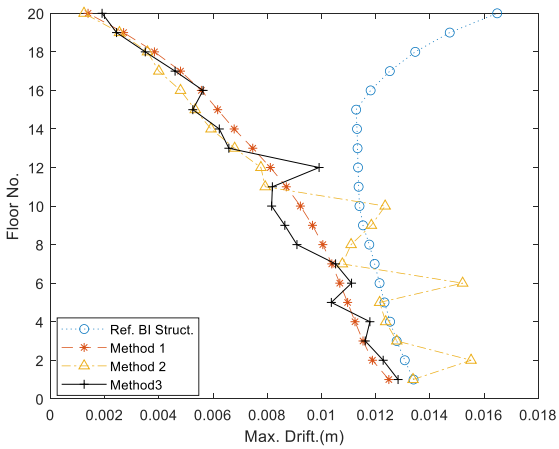

Fig. 7. Maximum floor drifts for the reference BI structure and the base-isolated structures designed using methods 1, 2, and 3

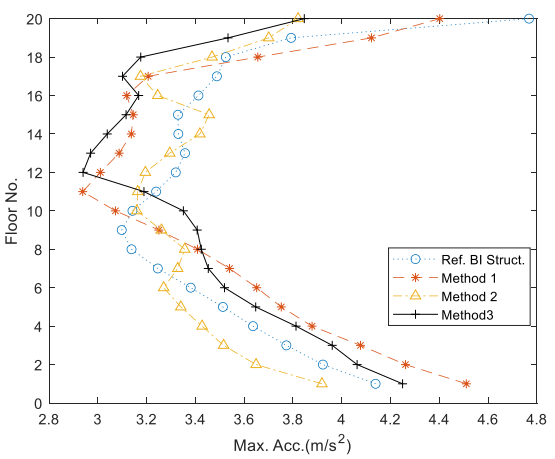

Fig. 8. Maximum floor accelerations for the reference BI structure and the base-isolated structures designed using methods 1, 2, and 3.

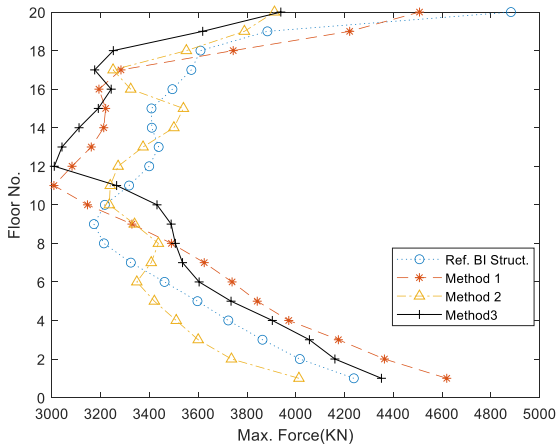

Fig. 9. Maximum floor forces for the reference BI structure and the base-isolated structures designed using methods 1, 2, and 3.

respectively. Similarly, the maximum floor acceleration in the reference BI structure is reduced to 4.40 m/s², 3.82 m/s², and 3.84 m/s² using methods 1, 2, and 3, respectively.

Figure 6 compares the maximum floor displacement values for the reference BI structure and the base-isolated structures designed using methods 1, 2, and 3. As shown, all three methods effectively reduce the maximum floor displacement, with the reduction being more pronounced on the upper floors of the studied structures. Method 1 demonstrates the best performance in reducing the seismic responses. Figure 7 presents the maximum floor drifts for the reference BI structure and the base-isolated structures designed using methods 1, 2, and 3. Methods 1 and 3 significantly reduce the maximum floor drift, particularly on the upper floors. Although method 2 does not perform as well in reducing the maximum drift on some lower floors, it effectively reduces the maximum drift on the upper floors.

Figures 8 and 9 compare the maximum floor accelerations and seismic forces of the reference BI structure and the base-isolated structures designed using methods 1, 2, and 3. The proposed methods reduce the maximum acceleration and seismic force on the upper floors of the studied structures. However, on the lower floors, there is a slight increase in these responses. It is important to note that even with this increase, the acceleration levels remain significantly lower than those in the FB structure and fall within the range of non-destructive floor accelerations. In conclusion, the advantages of the proposed methods in reducing maximum displacement and drift are achieved at the cost of a slight increase in maximum acceleration and seismic force on the lower floors.

The hysteresis loops of the seismic isolators in the reference BI structure and the base-isolated structures designed using methods 1, 2, and 3 are shown in Figure 10. There is no significant difference between the loops, indicating that the amount of dissipated energy by the seismic isolators in all four structures is nearly the same.

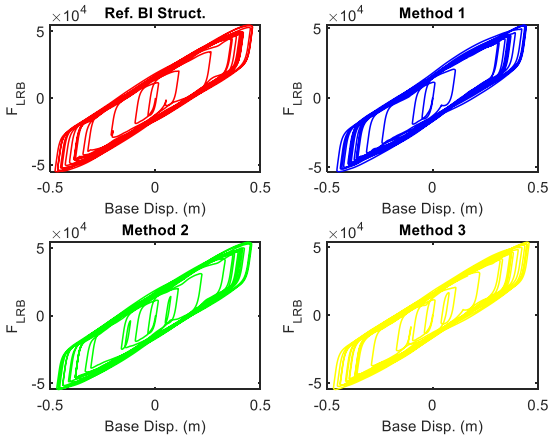

Fig. 10. Hysteresis loops of the seismic isolators for the reference BI structure and the base-isolated structures designed using methods 1, 2, and 3.

For further comparison, the reductions in seismic responses of the base-isolated structures designed using methods 1, 2, and 3, relative to the reference BI structure, are illustrated in figures 11, 12, 13, and 14. These figures respectively show the reduction percentages in maximum floor displacement, maximum floor drift, maximum floor acceleration, and maximum seismic force in comparison with those given for the reference BI structure. Figure 11 shows that method 1 results in a 5% to 14% reduction in maximum floor displacement, providing the best performance among the methods in reducing this response. Although the other methods also reduce maximum floor displacement, method 1 is the most effective. The efficiency of the proposed methods is particularly evident in reducing maximum floor drift, as shown in Figure 12. While the reduction is less pronounced on the lower floors, there is a significant 30% to 80% reduction in maximum drift on the upper 10 floors of the studied structures. This is crucial, as major structural and non-structural damages during earthquakes are often caused by large relative displacements between floors. Figures 13 and 14 demonstrate that the proposed methods result in a bit of reduction in maximum floor acceleration and seismic force on the upper floors of the studied structures, although there is a bit increase in these responses on the lower floors. However, it is important to note that the maximum floor accelerations remain within a range that is considered non-destructive.

To provide a general assessment of the seismic performance of the proposed methods, the average reductions in seismic responses, compared to the reference BI structure, are summarized in Table 2. These reductions are reported in terms of maximum floor displacement, maximum floor drift, maximum floor acceleration, and maximum seismic force. Overall, method 1 delivers the best performance, achieving reductions of 6.65%, 32.65%, and 0.88% in maximum floor displacement, drift, and acceleration, respectively, relative to

the reference BI structure. Although methods 2 and 3 show.

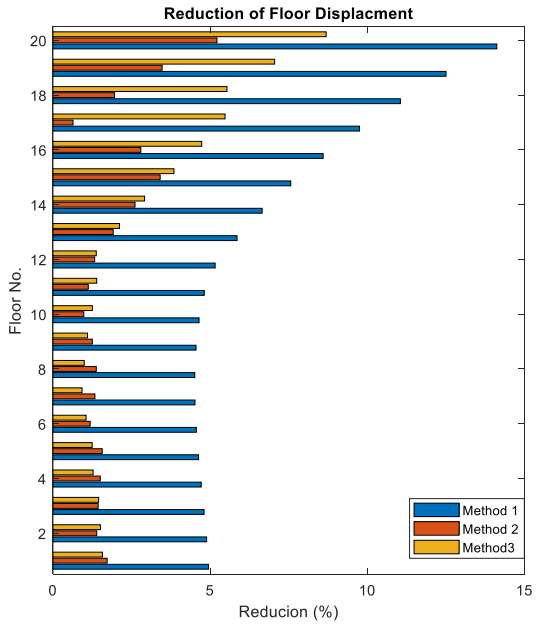

Fig. 11. The reduction percentages in maximum floor displacement for the base-isolated structures designed using methods 1, 2, and 3.

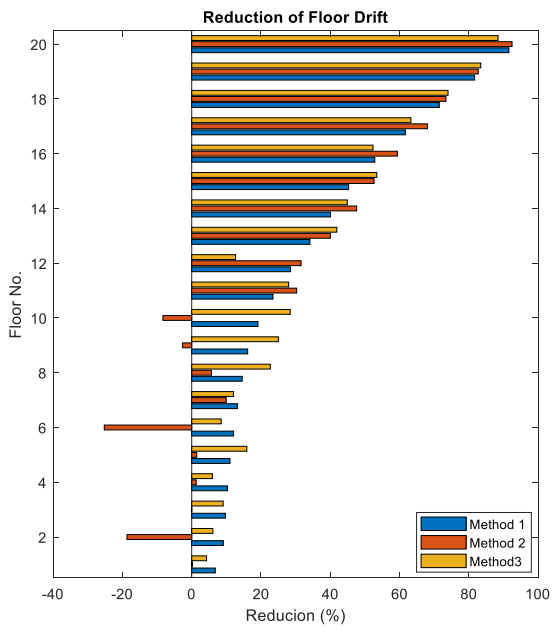

Fig. 12. The reduction percentages in maximum floor drift for the base-isolated structures designed using methods 1, 2, and 3.

only minor reductions in displacement and acceleration, they perform well in reducing the critical seismic response of maximum floor drift.

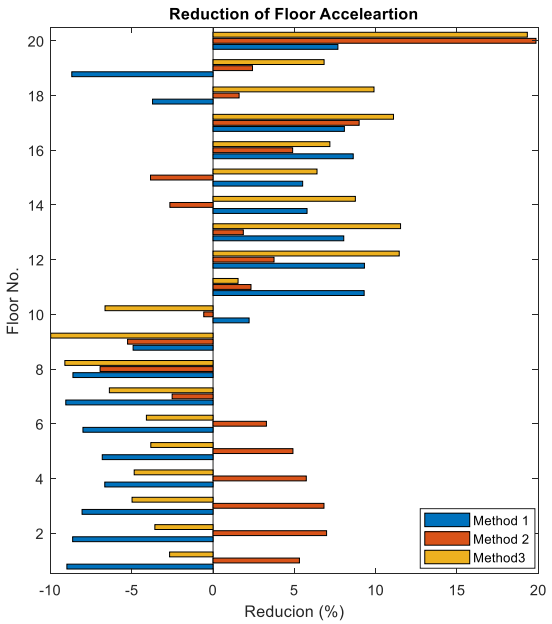

Fig. 13. The reduction percentages in maximum floor acceleration for the base-isolated structures designed using methods 1, 2, and 3.

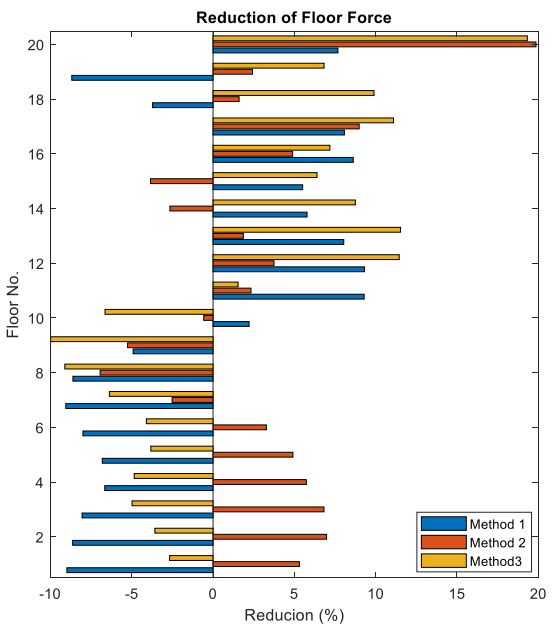

Fig. 14. The reduction percentages in maximum floor force for the base-isolated structures designed using methods 1, 2, and 3.

II. Conclusions

The seismic performance of base-isolated tall structures is often influenced by the superstructure's response and the relative lateral movements between its floors. In such cases

TABLE 2 THE AVERAGE REDUCTIONS IN SEISMIC RESPONSES

Seismic responses	Average reductions (%) in Method 1	Method 2	Method 3
Max. Disp.	6.65	1.91	2.78
Max. Drift	32.65	27.091	34.02
Max. Acc.	0.88	2.85	1.89
Max. Force	0.88	2.85	1.89

the effectiveness of seismic isolation in controlling inter-story drift and absolute acceleration of the floors is typically diminished. However, it is possible to regulate the superstructure's deformations by optimally designing floor stiffness through an optimization process aimed at achieving uniform deformation of the superstructure. This approach can create an optimal isolation condition where the superstructure behaves like a rigid body. In this study, three techniques were proposed to enhance the seismic performance of base-isolated tall buildings by promoting uniform deformation of the superstructure. Numerical analyses were performed on a 20-story base-isolated building, and the seismic performance of these techniques was evaluated and compared. The key findings are as follows:

1. All three methods effectively reduced maximum floor displacement, particularly in the upper floors. Method 1 achieved the best results, with reductions ranging from 5% to 14%.
2. These methods significantly minimized maximum floor drift, a critical seismic response. Methods 1 and 3 were notably successful, with reductions of 30% to 80% in the upper floors. While Method 2 was less effective on some lower floors, it still delivered significant reductions in the upper floors.
3. The proposed methods also achieved a 10% to 15% reduction in maximum acceleration and seismic forces on the upper floors. However, there was a slight increase in these responses on the lower floors, though they remained within non-destructive limits.
4. Method 1 provided the most consistent performance, achieving reductions of 6.65%, 32.65%, and 0.88% in maximum floor displacement, drift, and acceleration, respectively, compared to the reference base-isolated structure. Although Methods 2 and 3 showed only modest reductions in displacement and acceleration, they were highly effective in significantly reducing maximum floor drift, which is the most critical seismic response of the structure.

References

[1] F. Naeim, *Design of Seismic Isolated Structures: from theory to practice*: John Wiley & Sons, 1999.

[2] C. Ma, Y. Zhang, P. Tan, and F. Zhou, "Seismic response of base-isolated high-rise buildings under fully nonstationary excitation," Shock and Vibration, vol. 2014, p. 401469, 2014.

[3] H. Anajafi, K. Poursadr, M. Roohi, and E. Santini-Bell, "Effectiveness of seismic isolation for long-period structures subject to far-field and near-field excitations," Frontiers in Built Environment, vol. 6, p. 24, 2020.

[4] P. C. Roussis and M. C. Constantinou, "Uplift-restraining friction pendulum seismic isolation system," Earthquake engineering & structural dynamics, vol. 35, pp. 577-593, 2006.

[5] T. Ariga, Y. Kanno, and I. Takewaki, "Resonant behaviour of base-isolated high-rise buildings under long-period ground motions," The Structural Design of Tall and Special Buildings, vol. 15, pp. 325-338, 2006.

[6] J. Hino, S. Yoshitomi, M. Tsuji, and I. Takewaki, "Bound of aspect ratio of base-isolated buildings considering nonlinear tensile behavior of rubber bearing," Structural Engineering and Mechanics, vol. 30, pp. 351-368, 2008.

[7] C. Ma, Y. Zhang, P. Tan, and F. Zhou, "Seismic response of base-isolated high-rise buildings under fully nonstationary excitation," Shock and Vibration, vol. 2014, p. 401469, 2014.

[8] A. Nakai, D. Sato, T. Murakami, and K. Kasai, "Evaluation of stiffness of base-isolation layer and superstructure of high-rise baseisolated building based on seismic observation recording," AIJ J. Technol, vol. 24, pp. 571-576, 2018.

[9] A. Q. Darwish and M. Bhandari, "Seismic response reduction of high rise steel-concrete composite buildings equipped with base isolation system," Materials Today: Proceedings, vol. 59, pp. 516-524, 2022.

[10] Z. Li, G. Huang, X. Chen, and X. Zhou, "Seismic response and parametric analysis of inter-story isolated tall buildings based on enhanced simplified dynamic model," International Journal of Structural Stability and Dynamics, vol. 22, p. 2240008, 2022.

[11] S. Shourestani, F. Soltani, M. Ghasemi, and S. Etedali, "SSI effects on seismic behavior of smart base-isolated structures," Geomechanics & engineering, vol. 14, pp. 161-174, 2018.

[12] S. Pal, A. Hassan, and D. Singh, "Optimization of base isolation parameters using genetic algorithm," Journal of Statistics and Management Systems, vol. 22, pp. 1207-1222, 2019.

[13] S. Etedali, K. Hasankhoie, and M. R. Sohrabi, "Optimal design of pure-friction isolators with and without restoring device: A multi-objective cuckoo search-based approach for seismic-excited structures," in Structures, 2020, pp. 708-719.

[14] A. Ocak, S. M. Nigdeli, G. Bekdaş, S. Kim, and Z. W. Geem, "Optimization of seismic base isolation system

using adaptive harmony search algorithm," Sustainability, vol. 14, p. 7456, 2022.

[15] S. Öncü-Davas, R. Temür, and C. Alhan, "Comparison of meta-heuristic approaches for the optimization of non-linear base-isolation systems considering the influence of superstructure flexibility," Engineering Structures, vol. 263, p. 114347, 2022.

[16] S. Etedali and M. K. Kareshk, "Mitigation of torsional responses in asymmetric base-isolated structures using an optimal distribution of isolators in base story," in Structures, 2022, pp. 807-817.

[17] Y. Lei and X. Yang, "Stochastic Optimization of Electromagnetic Inertial Mass Dampers in Nonlinear Hybrid Base Isolation Systems Under Seismic Excitations," International Journal of Structural Stability and Dynamics, p. 2450241, 2023.

[18] S. Etedali and A.-A. Zamani, "Semi-active control of nonlinear smart base-isolated structures using MR damper: sensitivity and reliability analyses," Smart Materials and Structures, vol. 31, p. 065021, 2022.

[19] M. Abdechiri, M. R. Meybodi, and H. Bahrami, "Gases Brownian motion optimization: an algorithm for optimization (GBMO)," Applied Soft Computing, vol. 13, pp. 2932-2946, 2013.

[20] M. Shahi, M.R. Sohrabi, S. Etedali and A.A. Zamani, " Simultaneous optimal design of PID and MATMD considering their proposed elevation placement for seismic control of tall buildings on soft soil," International Journal of Industrial Electronics, Control and Optimization, vol. 6, pp. 241-259, 2023.

[21] S. Nagarajaiah and S. Narasimhan, "Seismic control of smart base isolated buildings with new semiactive variable damper," Earthquake Engineering & Structural Dynamics, vol. 36, pp. 729-749, 2007.

[22] A.A. Zamani, S. Tavakoli, S. Etedali, and J. Sadeghi, "Adaptive fractional order fuzzy proportional–integral–derivative control of smart base-isolated structures equipped with magnetorheological dampers," Journal of Intelligent Material Systems and Structures, vol. 29, pp. 830-844, 2018.

[23] S. Etedali, K. Hasankhoie, and M. R. Sohrabi, "Seismic responses and energy dissipation of pure-friction and resilient-friction base-isolated structures: A parametric study," Journal of Building Engineering, vol. 29, p. 101194, 2020.

[24] S. Etedali, "Sensitivity analysis on optimal PID controller for nonlinear smart base-isolated structures," International Journal of Structural Stability and Dynamics, vol. 19, p. 1950080, 2019.

[25] MATLAB. The Math Works, Inc., Natick, MA, 2000

Sadegh Etedali received his Ph.D. in Structural Engineering from the University of Sistan and Baluchestan, Zahedan, Iran, in 2014. He is currently an Associate Professor in the Department of Civil Engineering at Birjand University of Technology. Dr. Etedali has published over 100 scientific papers in national and international journals and conference proceedings. He has supervised/advised more than 20 M.Sc. and Ph.D. students. In recognition of his contributions to the field, he was listed among the top 2% of most influential scientists by Stanford University in both 2022 and

International Journal Of
Industrial Electronics Control and Optimization
Print ISSN: 3517-2645
Online ISSN: 3568-2645
Homepage: https://ieco.usb.ac.ir/

A New Soft Switching Dual-input High Step-up Converter for Renewable Energy Systems

Hayder Ameer Hasan Al-Ameede[1], Majid Delshad [1], Nadheer A. Shalash[2] , Bahador Fani[1]
Department of Engineering, Isfahan (Khorasgan) Branch, Islamic Azad University, Isfahan, Iran[1]
Electrical Engineering Department, University of Technology, Baghdad, Iraq[2]
Corresponding author's email: delshad@khuisf.ac.ir

Article Info

Article type:
Research Article

Article history:
Received: 22-August-2024
Received in revised form: 30-November-2024
Accepted: 30-November-2024
Published online: 22-June-2025

Keywords:
Dual-input converter,
Soft switching,
High efficiency,
Pulse width modulation (PWM).

ABSTRACT

Objective: This paper presents a new converter featuring an auxiliary circuit configuration, designed to facilitate soft switching conditions while minimizing the number of components used. This auxiliary circuit is innovatively developed to achieve zero voltage switching (ZVS) and effectively recover snubber energy on the input side, thereby enhancing the converter efficiency. Furthermore, the deliberate integration of coupled inductors into the converter's design significantly boosts its gain while reducing voltage stress on the switching components. The modular architecture of the auxiliary circuit allows for adding circuit branches and increasing power capacity without requiring extra components for its auxiliary circuit. To evaluate the performance of the proposed converter, extensive simulations were performed using PSPICE software, along with the construction of a laboratory prototype capable of operating at 170 W. The alignment between the experimental results and simulation data strongly supports the theoretical analysis, illustrating the converter's potential for efficient power conversion in renewable energy systems.

Nomenclature

f	Switching frequency	DIC	Dual Input Converter
n	Turn ratio of coupled-inductor	L_M	Magnetizing inductor
I_{sw}	Final current of the switch before turning it off	I_{LM}	Magnetizing inductor current
V_{sw}	Final voltage across switch before turning on	C_S	Snubber capacitor
t_r	Switch current rise time	L_K	Leakage inductance
t_f	Switch current fall time	D	Duty cycle
V_D	Diode voltage	Po	Output power
T	Switching cycle period	PWM	Pulse width modulation
V_o	Output voltage	ZVS	Zero voltage switching
Vin	Input voltage	ZCS	Zero current switching
Vs	Switch voltage		

I. Introduction

Recently, rising environmental issues and the depletion of fossil fuels have significantly boosted the demand for renewable energy sources like wind turbines, photovoltaic (PV) panels, and fuel cells (FCs). PV sources generate low-amplitude DC voltage, requiring high step-up DC-DC converters in DC-AC systems to boost this voltage to the desired level. The classical DC-DC boost converter is an essential solution for voltage boosting [1]-[4]. However, the

efficiency of PV systems is generally decreased by the use of converters, highlighting the need for high-efficiency converters [5-7]. Such converters are preferred over PV systems due to their high efficiency, low cost, and ability to achieve high voltage gains with fewer circuit elements. Achieving high efficiency and voltage gain in these converters typically requires several passive components, which increases the circuit's volume. To optimize converter size and efficiency and reduce input current ripple, new step-up converters are designed that employ techniques involving coupled inductors, transformers, and multiplier units [3]. Recent proposals include a new high step-up DC-DC converter topology that allows for high voltage conversion ratios with low voltage stress on power switches. This topology, combined with alternative designs that integrate SEPIC and boost converters, aims to address challenges such as high-power losses in passive components and semiconductors, as well as reverse recovery issues that decrease efficiency. Novel approaches include multi-input structures integrating energy from different sources, enhancing reliability and power generation [8]-[10].

Dual Input Converters (DICs) are categorized into isolated, non-isolated, and semi-isolated types based on their design and operational characteristics. Isolated DICs feature magnetic coupling between input and output ports through transformers or coupled inductors, incorporating multiple switches but offering favorable soft-switching conditions. In contrast, non-isolated DICs lack galvanic isolation between the inputs and outputs, often resulting in the loss of soft-switching capabilities and generally lower voltage gains [11]-[13]. These converters, however, offer advantages like a reduced number of semiconductor components and enhanced power density. Semi-isolated DICs uniquely isolate only one port (typically the output) via a transformer, enhancing voltage gain and providing soft switching due to the transformer's leakage inductance. Similar to non-isolated converters in that the input ports are not isolated from each other, semi-isolated DICs manage to use fewer semiconductors while providing satisfactory power sharing.

The converter presented in [14] features two interleaved boost converters combined with a Cockcroft–Walton (CW) multiplier cell. By incorporating additional stages of the CW multiplier, the voltage gain of the converter is increased. However, a substantial rise in the number of stages increases conduction losses, thereby reducing the overall efficiency. To address this, a multi-input converter with a novel voltage multiplier was proposed in [16]. A technique for cascading boost converters was presented in [17] and [18], allowing each input source to independently transfer power to the output. Additionally, an active clamping circuit was employed to achieve soft-switching conditions, though it resulted in significant circulating current.

In [20], the introduction of series diodes and unidirectional current flow in the auxiliary circuit helped to reduce the current stress on the switches. Nevertheless, the primary challenges of this converter include limited voltage gain and high voltage stress on the main switches.

This paper introduces a new dual-input converter, characterized by its high efficiency and the capability to redirect snubber energy back to the input. This innovative design reduces voltage stress on switches and solves the diode reverse recovery issue by implementing ZCS conditions for them.

II. Description of the Proposed Converter

The proposed dual-input converter has an innovative auxiliary circuit with a switch Sa, an auxiliary inductor La, two auxiliary diodes D_{a1} and D_{a2}, and two snubber capacitors C_{s1} and C_{s2}. This converter uses two coupled inductors L_1-L_2 and L_3-L_4 to increase the gain. In addition, two capacitors C_1 and C_2 are connected in series to the coupled inductors. This converter also has diodes D_1 and D_2 and D_{o1} and D_{o2}. Capacitor C_o and two main switches S_1 and S_2 are the main components of the converter. Switches S_1 and S_2 are turned on simultaneously, but due to the difference in their input voltages, they have different duty cycles. The auxiliary switch is turned on shortly before switches S_1 and S_2 and is turned off once they are turned on. Figure 1 demonstrates a schematic view of the proposed converter.

A. Operation of Proposed Dual-input Converter

The proposed dual-input converter has eight operation modes, which are explained. For the simplicity of the analysis of circuit operation, it is assumed that the output voltage and capacitors C_1 and C_2 are constant. Magnetizing inductors' current is also supposed to be constant in one cycle. Fig. 2 demonstrates the switching waveforms theoretically and Fig. 3

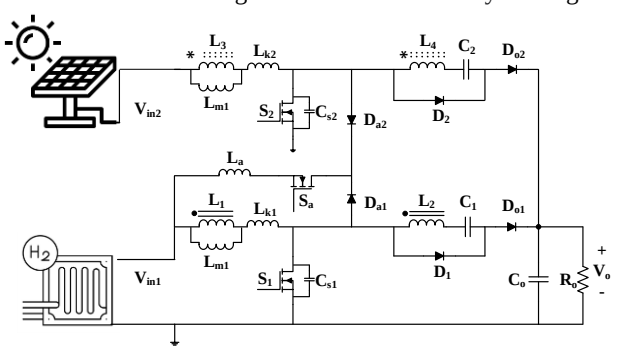

Fig. 1. A schematic view of the proposed converter

illustrates the equivalent circuits of different modes of converter.

Before the first status, it is assumed that both switches S_1 and S_2 are off and diodes D_{o1} and D_{o2} conduct, so the energy of magnetizing inductors L_{m1} and L_{m2} is transmitted to output through these diodes.

The first mode: This condition starts when the auxiliary switch S_a is turned on. Due to the existence of the auxiliary inductor L_a in series with this switch, its current is increased linearly because the constant voltage V_o-V_c-V_{in} across it drops. In this mode, diodes D_{a1} and D_{a2} are on, and as the current L_a is increased, the current of diodes D_{o1} and D_{o2} decreases. When current L_a reaches the value of I_{in1}+I_{in2}, diodes D_{o1} and D_{o2} are turned off under ZC conditions.

The second mode: When D_{o1} and D_{o2} are turned off, inductor L_a resonates with capacitors C_{S1} and C_{S2} and fully discharges the energy of the capacitors. In this mode, capacitors C_1 and C_2 also start to be charged from the path of diodes D_1 and D_2.

The third mode: At the beginning of this mode, capacitors C_{S1} and C_{S2} are fully discharged and body diodes S_1 and S_2 are turned on. Since then, these switches will be turned on under zero voltage switching (ZVS) conditions. Also, the inverse voltage – V_{c1}/n drops across L_a and its current decreases linearly so that it reaches zero at the end of this mode. In the first to third modes, when the auxiliary switch is turned on, both snubber capacitors start to discharge at the input through the auxiliary inductor (L_a), so the energy of the snubber circuit is not dissipated and is transferred to the input.

The fourth mode: This mode starts when D_{a1} and D_{a2} are turned off under ZC conditions. When switch Sa is turned off, the auxiliary circuit is fully disconnected from the converter.

The fourth mode: This mode starts when D_{a1} and D_{a2} are turned off under ZC conditions. When switch Sa is turned off,

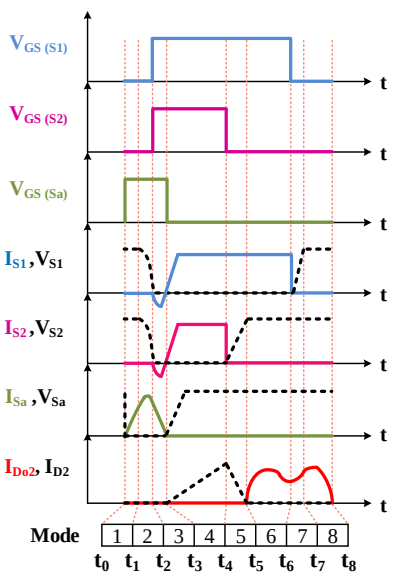

Fig.2 Theoretical main waveforms of the proposed converter

the auxiliary circuit is fully disconnected from the converter. Both switches are active, causing the magnetizing inductances L_{m1} and L_{m2} to charge linearly, while the load current is provided by the output capacitor Co.

The fifth mode: In this mode, switch S_2 is turned off under ZV conditions due to the presence of snubber capacitor C_{S2}, and capacitor C_{S2} is charged by current I_{Lm1} up to voltage $V_o/(n+1)$.

The sixth mode: When C_{S1} voltage reaches Vo/(n+1), diode D_2 is turned off and diode D_{o2} is turned on. This mode continues until S_1 is turned off.

The seventh mode: When S_1 is turned off, capacitor C_{S1} is charged linearly by I_{Lm2} current to reach Vo/(n+1). This mode ends when D_{o1} is turned on and D_1 is turned off.

The eighth mode: When D_1 is turned off, this mode starts and the energy of inductors L_{m1} and L_{m2} starts to be discharged at the output. This mode concludes when the auxiliary switch is turned back on.

III. Analysis of the Proposed Dual-input Converter

This section analyzes the dual-input converter. Firstly, the converter gain and voltage stress on semi-conductor elements are calculated parametrically, and then the passive elements of the design equations of the proposed dual-input converter are explained.

B. The Converter Voltage Gain:

By deriving the volt-second balance equation and applying Kirchhoff's Voltage Law (KVL) in the output loop, we have:

$$-V_{in} + V_{L1} + nV_{L1} - V_C + V_o = 0 \quad (1)$$

$$V_{L1} = \frac{V_{in} + V_{C1} - V_o}{n+1} \quad (2)$$

$$DTV_{in} + (1-D)T(V_{in} - \frac{V_o}{n+1}) = 0 \quad (3)$$

$$V_{C1} = nV_{in} \quad (4)$$

$$\frac{V_o}{V_{in}} = \frac{n+1}{1-D} \quad (5)$$

Fig. 4 demonstrates the gain diagram for different values of the turn ratio.

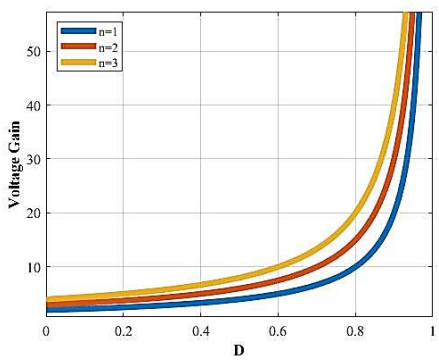

Fig. 4 The gain diagram of the proposed converter for different values of turn ratio.

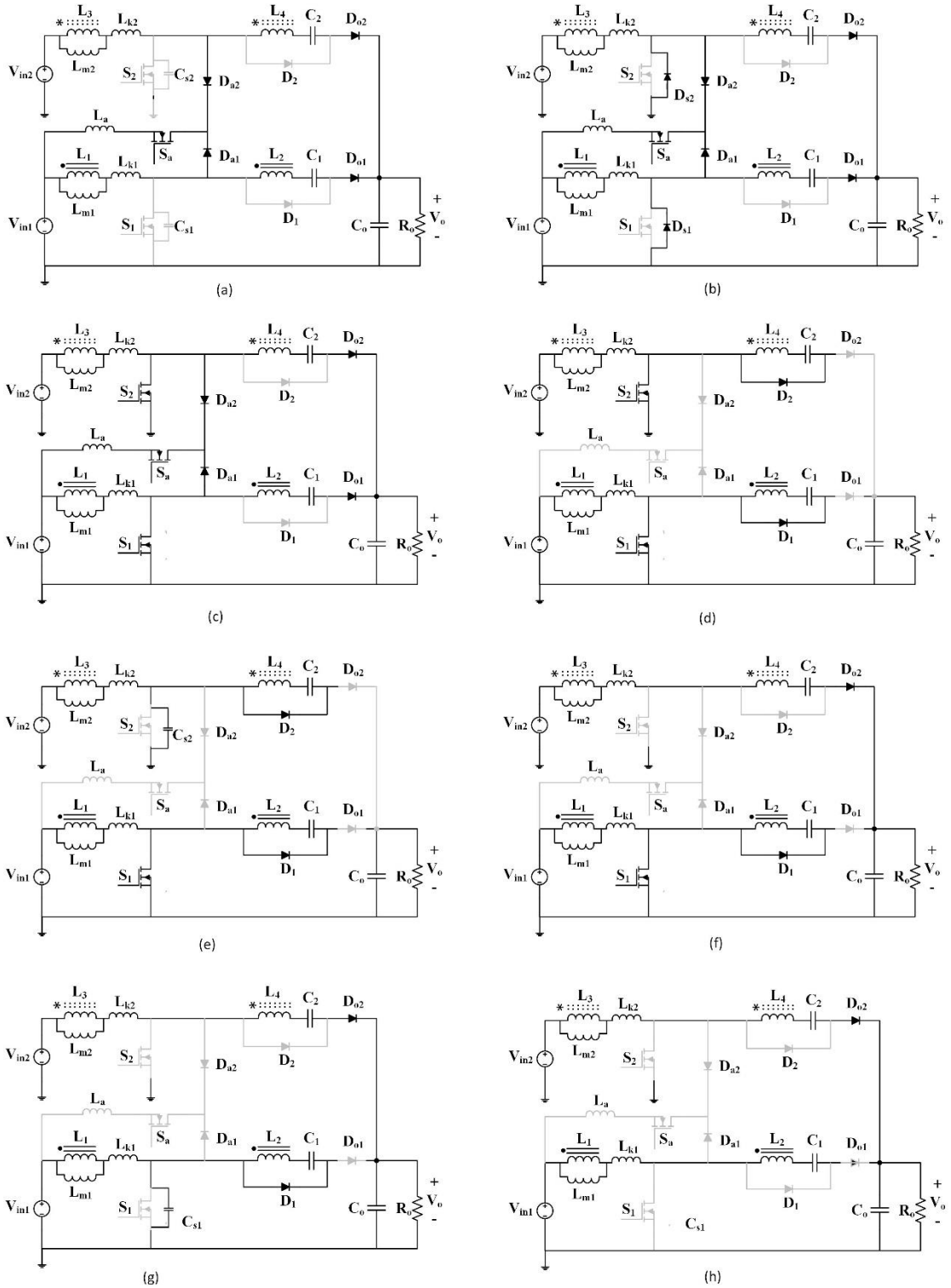

Fig. 3. Equivalent circuit of the proposed converter at the a) first, b) second, c) third, d) fourth, e) fifth, f) sixth, g) seventh, and h) eighth modes

C. Voltage Stress of Semiconductor Elements

By writing KVL in the ring in which switches and diodes are located (in the off mode), the element's voltage stress can be obtained. Fig. 5 illustrates the normalized stress diagram of the components for different values of turn ratio.

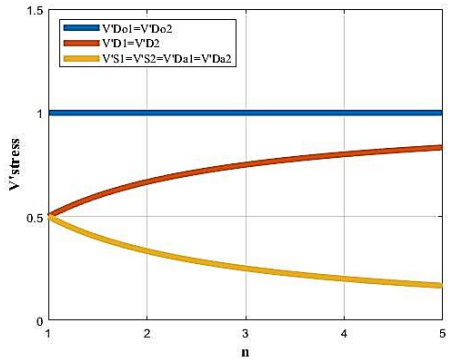

Fig. 5. Diagram of normalized stress across the components for varying turn ratio values.

$$V_{S1} = V_{S2} = \frac{V_o}{n+1} \quad (6)$$

$$V_{D1} = V_{D2} = nV_{L1} - V_{C1} = \frac{nV_o}{n+1} \quad (7)$$

$$V_{Do1} = V_{D02} = V_o \quad (8)$$

TABLE 1. SPECIFICATIONS OF THE PROPOSED CONVERTER AND THE VALUES OF ITS COMPONENTS

Elements/specifications	Value/part name
Switches	IRF740
All diodes	MUR860
C_{s1},C_{s2}	1nF
C_1,C_2	1µF
C_o	47µF
n	2
P_o	170W
First input voltage	30V
Second input voltage	60V
Output voltage (V_o)	410V
Switching frequency	100kHz

D. The Design of Auxiliary Elements

We use the snubber equation to design the auxiliary inductor L_a.

$$L_a > \frac{V_{sw}.t_r}{I_{sw}} > 2.2\mu H \quad (9)$$

in which t_r is the switch current ascending time, voltage V_{sw} is the final voltage across the switch before turning on, and I_{sw} is the final current of the switch before turning off. In addition, snubber capacitors can be obtained from Equation 10.

$$C_s > \frac{T_{res}^2}{2\pi L_a} > 11.5nF \quad (10)$$

E. The design of the Main Elements

The following equations are derived to calculate the values of the main circuit components based on the nominal output power, switching frequency, and voltage ripple across capacitors C_1, C_2, and the output capacitor, as well as the current ripple in the magnetizing inductance. It should be noted that all passive components have been designed with larger values to ensure compliance with the required conditions.

$$C_o > \frac{D_{max}V_O}{\Delta V_o f R_o} > 41\mu F \quad (11)$$

$$C_1, C_2 > \frac{I_o D}{4f\Delta V_C} > 0.64\mu F \quad (12)$$

$$L_m > \frac{D(1-D)^2 R_o}{4(1+n)^2 f} > 160\mu H \quad (13)$$

IV. Simulation Results of the Proposed Dual-input High Step-up Converter

Based on the design steps outlined in the previous section, the converter is simulated for an output power of 170 W and an output voltage of 410 V. Table 1 lists the values and specifications of all components. To verify the accuracy of the conducted analyses, the proposed converter was simulated using PSPICE software.

The layout of the simulated converter is depicted in Fig. 6, with simulation results illustrated in Figs. 7 to 12. Fig. 7 shows the gate-source pulse waveforms for both the main and auxiliary switches. Figs. 8 and 9 present the simulated current and voltage waveforms for the main switches S1 and S2. These figures indicate that when the switches are turned on, the switch current is negative, causing the body diode to conduct and enabling ZVS conditions. Additionally, the voltage across the switches gradually increases at turn-off moments, establishing Zero Voltage (ZV) conditions for the main switches during turn-off.

Fig. 10 demonstrates the auxiliary switch current waveform. According to the current slope, the auxiliary switch is on and is turned off under zero current switching (ZCS) conditions. Figs. 11 and 12 show diodes D_1-D_{o1} and D_2-D_{o2} current waveforms of the proposed converter, respectively. In all the figures, it is evident that the diode current exhibits a sloped increase and decrease, indicating that the diodes turn on and off under ZCS conditions.

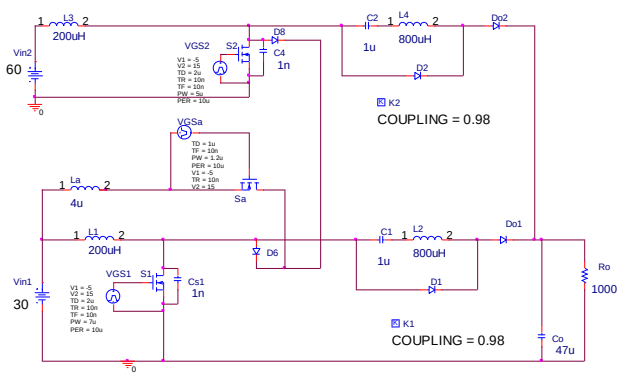

Fig.6 A schematic view of the proposed dual-input high step-up converter simulated in PSPICE software

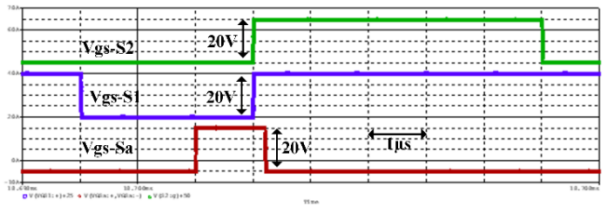

Fig.7. The gate-source pulse waveform of switches S_1 (blue), S_2 (green), and Sa (red) of the simulated converter

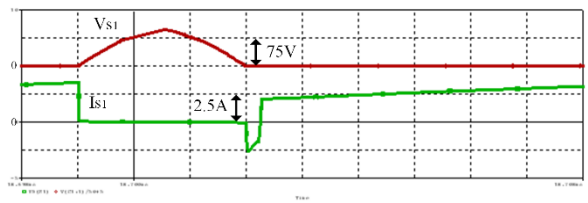

Fig.8. The simulated converter switch S_1 voltage (top) and current (bottom) waveform

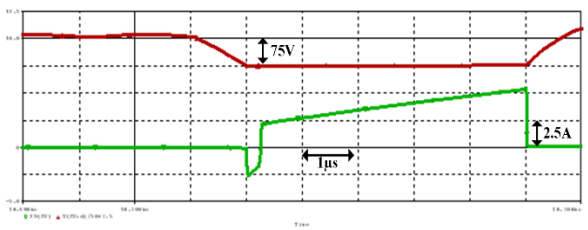

Fig.9 The simulated converter switch S_2 voltage (top) and current (bottom) waveform

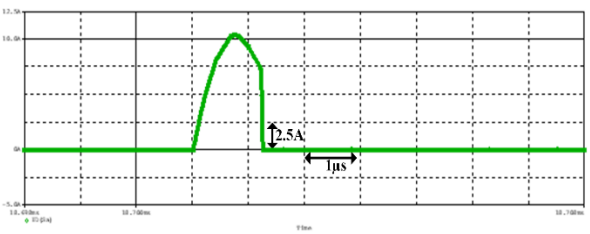

Fig.10. The simulated converter switch S_a current waveform

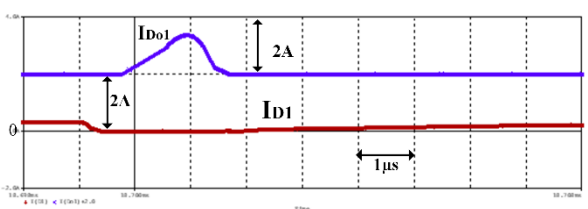

Fig.11. The simulated converter diode D_1 current (bottom) waveform and diode D_{o1} current (top) waveform

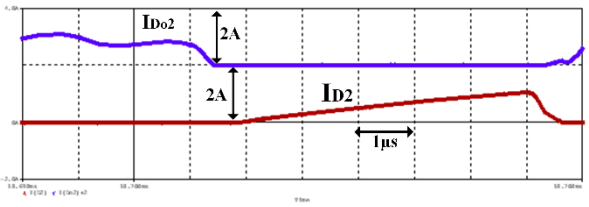

Fig.12. The simulated converter diode D_2 current (bottom) waveform and diode D_{o2} current (top) waveform

V. Practical Results

To verify the accuracy of the theoretical analysis, a 170-W experimental prototype of the proposed converter was implemented and tested according to Table 1. Fig. 13 displays the laboratory setup of the proposed converter. In the experimental setup, a MEGATEK M0-3003 power supply was employed to provide a stable DC voltage. To capture and analyze the waveforms accurately, a GW Instek GDS-2104 oscilloscope was used, allowing precise observation of voltage and current waveforms across various components of the converter. Also, to control and drive the switches, an FPGA Spartan 6 is utilized, along with an HCPL3120 as the driver.

Fig. 14 depicts the practical waveforms for the voltage and current of the switches and diodes in the proposed converter. According to this figure, all switches and diodes of the proposed converter operate under soft-switching conditions. In Figs. 14a and 14b, the switch current is negative when the switches are turned on, causing the body diode to conduct and create ZVS conditions for the switches. At turn-off, the voltage increases gradually, achieving ZV conditions for the main switches. The maximum voltage across the main switches is 160 V, significantly lower than the 410 V output, which helps reduce conduction losses. In Fig. 14c, the steep rise in current through switch S_a establishes ZCS conditions for the auxiliary switch during both turn-on and turn-off. Fig. 14d shows soft switching for diodes D_1 and D_{O1}, where their current rises and falls gradually, ensuring ZCS conditions and eliminating reverse recovery issues.

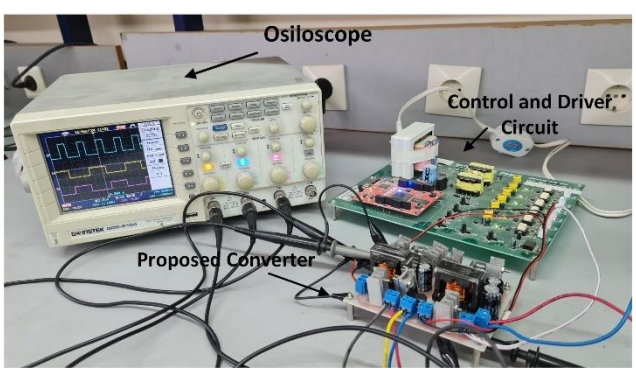

Fig. 13. The experimental setup of the proposed converter

VI. Analysis of the Proposed Converter Efficiency

Fig. 8 compares the efficiency between the proposed dual-input, high step-up converter, and its dual-input. The inclusion of a coupled inductor necessitates the use of a clamp circuit for the switches in the hard-switching version, leading to increased circuit losses due to resistance, thereby reducing efficiency. However, as illustrated in Fig. 8, the efficiency of the converter under soft-switching conditions is markedly improved over that of the hard-switching setup. This improvement is attributed to the auxiliary circuit's brief connection time within the proposed converter, which limits the circulating current and minimizes its impact on losses. Nonetheless, at low output power, the auxiliary circuit may slightly reduce the converter's efficiency. According to Fig. 8, the efficiency of the proposed converter at a rated power of 170 W reaches 95%, achieving a 5% increase over the hard-switching counterpart.

VII. Comparison of the Proposed Converter with Previous Converters

Table 2 provides a comparative analysis of the proposed converter against previously developed similar converters, focusing on criteria such as component count, voltage gain, and voltage stress on the switches. Table 2 reveals that the component count for both the proposed converter and converters [13], [14] is the same and lower than that of [11], [12]. However, converters [14] and [15] operate under hard switching conditions and exhibit significantly lower efficiency. The proposed converter achieves equivalent gain and stress

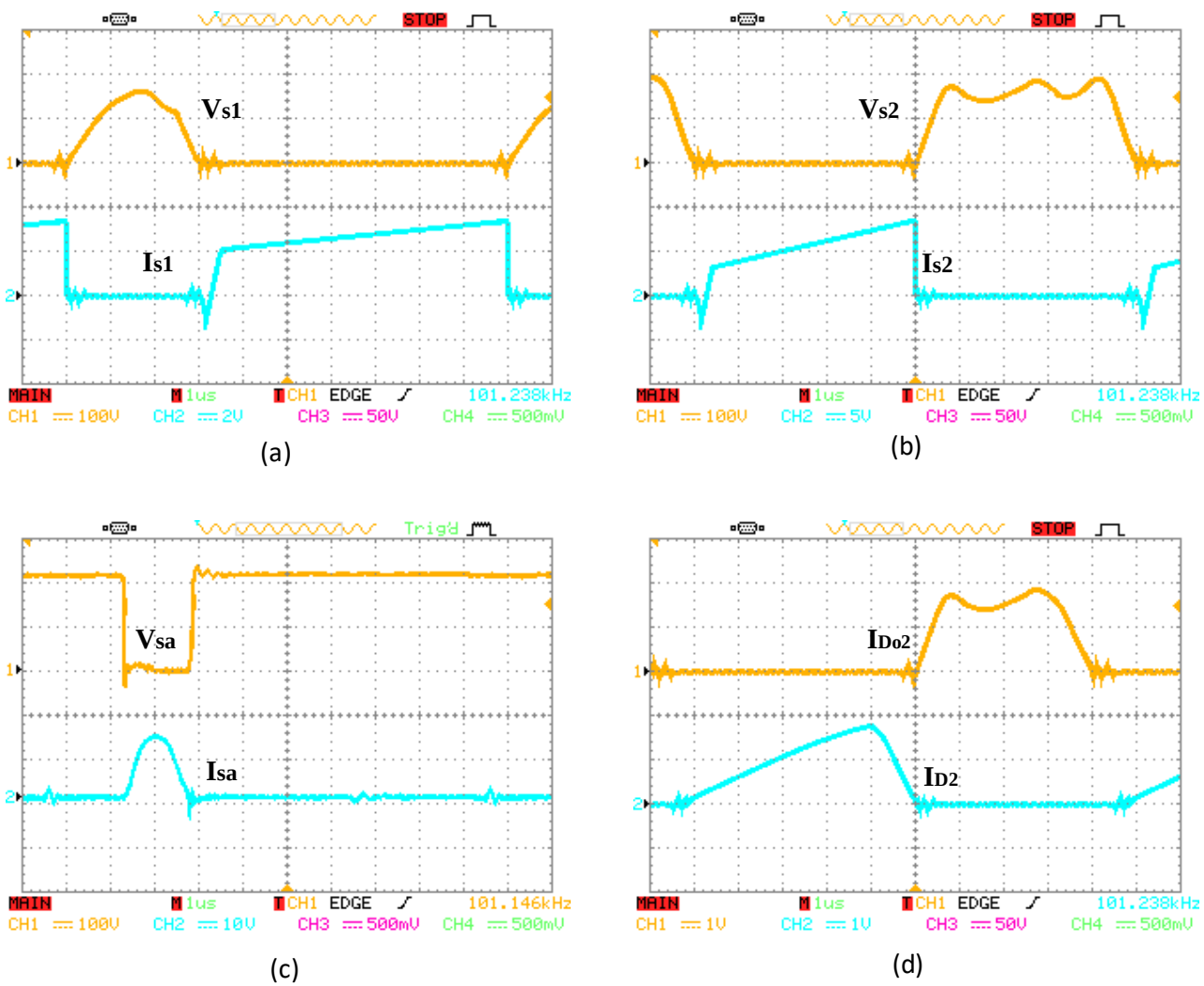

Fig.14. The practical results of (a) the measured voltage (up) and current (bottom) waveform of S_1 (100V/div, 2A/div, 1µs/div) (b) the measured voltage (up) and current (bottom) waveform of S_2 (100V/div, 5A/div, 1µs/div), (c) the measured voltage (up) and current (bottom) waveform of S_a (100V/div, 10A/div, 1µs/div), (d) the measured current waveform of D_2 (bottom) and D_{o2} (up) (1A/div, 1µs/div).

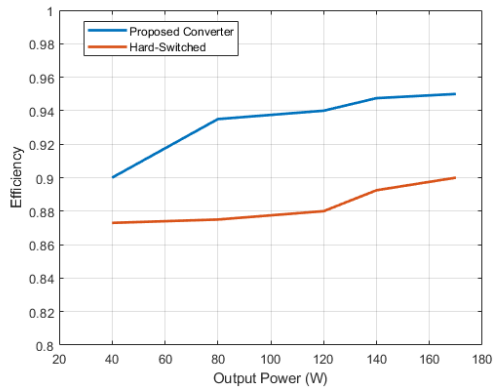

Fig. 15. The efficiency curve of the proposed converter in comparison to its hard-switching counterpart.

levels as observed in converters [12], [13], [15], and [20], yet it utilizes fewer components than [12]. Converters [19]-[21] achieve high voltage gain without using a coupled inductor and require fewer components than the proposed converter. However, converter [19] operates with hard switching and has a floating source on the switch, necessitating driver circuit isolation. Converter [20], while efficient, suffers from switching losses and high voltage stress on the switches, leading to increased costs. Converter [21] has a low component count and continuous input current but also experiences high voltage stress and requires an isolated driver.

VIII. Conclusions

This paper introduced a new dual-input converter with a modular auxiliary circuit designed to reduce conduction and switching losses. The modularity of the auxiliary circuit enables it to remain unchanged while universally adapting to an increasing number of converter inputs. Additionally, the proposed converter achieves soft switching across all semiconductor devices, delivers high voltage gain, and reduces voltage stress on the switches. All diodes turn off under zero current (ZC) conditions, effectively eliminating reverse recovery issues, while the main switch operates under ZV conditions, thereby avoiding capacitive turn-on losses and switching losses. Since the number of auxiliary circuit elements is low and the auxiliary switch is on for a short duration, the auxiliary circuit does not impose significant losses on the converter. Furthermore, the proposed converter efficiently recovers the energy stored in the snubber capacitors by redirecting it to the input, thereby enhancing overall efficiency. As a result, the converter's efficiency improves by 5% at full load compared to its hard-switched counterpart.

TABLE 2. A COMPARISON OF THE PROPOSED DUAL-INPUT CONVERTER PARAMETERS WITH SIMILAR PREVIOUS CONVERTERS

Reference / Parameter	[11]	[12]	[13]	[14]	[15]	[19]	[20]	[21]	Proposed converter
Number of elements	18	17	14	14	12	12	11	10	14
Switching Condition	ZV	ZV	ZC	Hard	Hard	Hard	Hard	Hard	ZV
Voltage Gain	4/(1-D)	(n+1)/(1-D)	(n+1)/(1-D)	(n+1+D)/(1-D)	(n+1)/(1-D)	$(3-D)/(1-D)^2$	(n+1)/(1-D)	(1-D)/(1-2D)	(n+1)/(1-D)
Voltage Stress on Switch	Vo/4	Vo/(n+1)	Vo/(n+1)	Vo/(n+1+D)	Vo/(n+1)	Vo(3-2D)/(6-2D)	Vo	Vo/(1-D)	Vo/(n+1)
Common Ground	No	No	Yes	Yes	Yes	Yes	Yes	No	Yes

References

[1] M. Elmi, M. R. Banaei, and H. Afsharirad, "Study on a Non-Isolated High Step-Up SEPIC-Based DC-DC Converter with Continuous Input Current for Photovoltaic Applications," *Int. J. Ind. Electron. Control Optim.*, 2024. doi: 10.22111/ieco.2024.48587.1558.2.

[2] M. Delshad, A. T. Harchegani, M. Karimi, and M. Mahdavi, "A new ZVT Multi Input Converter for hybrid sources systems," *in 2016 Int. Conf. Appl. Electron.* (AE), Pilsen, Czech Republic, 2016, pp. 61-64. doi:10.1109/AE.2016.7577242

[3] N. Bagheri, H. Alipour, L. Mohammadian, J. Beiza, and M. Ebadpour, "A Multiport Isolated Resonant LLC Converter for Grid-Tied Renewable Energy Powered Bidirectional EV Charger," *Int. J. Ind. Electron. Control Optim.*, vol. 6, no. 1, pp. 37-48, 2023. doi: 10.22111/ieco.2023.43543.1447.

[4] A. Iranpour Mobarakeh, R. Sadeghi, H. Saghafi, and M. Delshad, "Techno-economic energy management of micro-grid in the presence of distributed generation sources based on demand response programs," *Int. J. Electr. Power Energy Syst.*, vol. 141, 2022.doi: https://doi.org/10.1016/j.ijepes.2022.108169

[5] S. S. Dobakhshari, S. H. Fathi, and J. Milimonfared, "High step-up double input converter with soft switching and reduced number of semiconductors," *IET Power Electron.*, vol. 13, pp. 1995-2007, 2020. doi: 10.1049/iet-pel.2019.1394.

[6] C.-L. Shen, L.-Z. Chen, and H.-Y. Chen, "Dual-Input Isolated DC-DC Converter with Ultra-High Step-Up Ability Based on Sheppard Taylor Circuit," *Electronics*, vol. 8, p. 1125, 2019. doi: 10.3390/electronics8101125.

[7] S. Shabani, M. Delshad, R. Sadeghi, and H. H. Alhelou, "A High Step-Up PWM Non-Isolated DC-DC Converter With Soft Switching Operation," *IEEE Access*, vol. 10, pp. 37761-37773, 2022. doi:10.1109/ACCESS.2022.3163146

[8] M. Delshad and E. Shahri, "A new soft switching interleaved boost converter with high voltage gain," *in Proc. 8th Electr. Eng. Electron. Comput. Telecommun. Inf. Technol. (ECTI) Assoc*. Thailand Conf., Khon Kaen, Thailand, 2011, pp. 744-747. doi: 10.1109/ECTICON.2011.5947947

[9] A. Samadian et al., "A new dual-input high step-up DC–DC converter with reduced switches stress and low input current ripple," *IET Power Electron*., vol. 14, pp. 1669-1683, 2021. doi: 10.1049/pel2.12143.

[10] M. R. Banaei et al., "Non-isolated multi-input–single-output DC/DC converter for photovoltaic power generation systems," *IET Pow*er Electron., vol. 7, no. 11, pp. 2806-2816, 2014. doi: https://doi.org/10.1049/iet-pel.2013.0977

[11] B. Zhu, Q. Zeng, Y. Chen, Y. Zhao, and S. Liu, "A dual-input high step-up DC/DC converter with ZVT auxiliary circuit," *IEEE Trans. Energy Convers*., vol. 34, no. 1, pp. 161-169, Mar. 2019.doi: 10.1109/TEC.2018.2876303

[12] B. Zhu, Q. Zeng, D. M. Vilathgamuwa, Y. Li, and X. She, "Non-isolated high-voltage gain dual-input DC/DC converter with a ZVT auxiliary circuit," *IET Power Electron.*, vol. 12, no. 4, pp. 861-868, Apr. 2019. doi:https://doi.org/10.1049/iet-pel.2018.5465

[13] R. Wai and L. Hong, "High-efficiency dual-input converter with high voltage gain and internal charge function," IET Power Electron., vol. 7, no. 2, pp. 299-315, Feb. 2014. https://doi.org/10.1049/iet-pel.2013.0152

[14] S. Pourjafar, H. Shayeghi, F. Sedaghat, and S. SeyedShenava, "A dual-input DC-DC structure with high voltage gain suggested for hybrid energy systems," *IET Power Electron.*, vol. 14, no. 10, pp. 1792-1805, Aug. 2021. doi: 10.1049/pel2.12149

[15] S. M. Taheri, A. Baghramian, and S. A. Pourseyedi, "A novel high step-up SEPIC-based non-isolated three-port DC-DC converter proper for renewable energy applications," *IEEE Trans. Ind. Electron*., vol. 70, no. 10, pp. 10114-10122, Oct. 2023. doi:10.1109/TIE.2022.3220909

[16] L. Müller and J. W. Kimball, "High gain DC–DC converter based on the Cockcroft–Walton multiplier," IEEE Trans. Power Electron., vol. 31, no. 9, pp. 6405-6415, Sep. 2016. doi:10.1109/TPEL.2015.2505678

[17] T. Jalilzadeh, N. Rostami, E. Babaei, and S. Hosseini, "Multi-port DC-DC converter with Step-up capability and reduced voltage stress on switches/diodes," *IEEE Trans. Power Electron.* vol. 35, no. 11, pp. 11902-11915, Nov. 2020.

[18] R. Faraji and H. Farzanehfard, "Fully soft switched multi-port DC-DC converter with high integration," *IEEE Trans. Power Electron.*, vol. 36, no. 2, pp. 1901-1908, Feb. 2021.

[19] F. Mohammadi and A. Khorsandi, "Dual-input single-output high step-up DC–DC converter for renewable energy applications," *IET Power Electron*., vol. 17, pp. 337–349, 2024. doi: 10.1049/pel2.12646. doi:10.1049/pel2.12646.

[20] S. Harini, N. Chellammal, B. Chokkalingam and L. Mihet-Popa, "A Novel High Gain Dual Input Single Output Z-Quasi Resonant (ZQR) DC/DC Converter for Off-Board EV Charging," in *IEEE Access*, vol. 10, pp. 83350-83367, 2022, doi: 10.1109/ACCESS.2022.3195936.

[21] N. V. Sivaram, A. Lavanya, and J. D. Navamani, "Dual Input Single Output Quadratic Boost Converter for DC Microgrid," *e-Prime - Advances in Electrical Engineering*, Electronics and Energy, vol. 9, 2024, Art. no. 100683. doi: 10.1016/j.prime.2024.100683.

Hayder Ameer Hasan Al-Ameedee was born in Babylon, Iraq on April 10, 1982. He graduated from the Islamic Azad University of Mashhad with a master's degree in electrical engineering. He also has a bachelor's degree in electrical engineering from the Furat AL Awsat Technical University in Babylon, Iraq. He currently is a PhD candidate in electrical engineering at the Islamic Azad University of Isfahan (Khorasgan) Branch.

Majid Delshad was born in Isfahan, Iran, in 1979. He received the B.Sc. and M.Sc. degrees in electrical engineering from Kashan University and Isfahan University of Technology, Iran, in 2001 and 2004, respectively, and the Ph.D. degree in electrical engineering from the Isfahan University of Technology in 2010. He is an associate professor of Electrical Engineering with the Department of Isfahan (Khorasgan) Branch, IAU. His research interest includes soft switching techniques in DC-DC converters and current-fed converters.

Nadheer A. Shalash received his B.Sc. (2003) and M.Sc. degrees (2008) from the University of Technology (UOT) and his Ph.D. degree in Electrical Power Engineering from UMP, Malaysia in 2015. He was a Lecturer at AL-Ma'moon University College from 2008 to 2023. Currently, he is an Assistant Professor in the Department of Electrical Engineering, at the University of Technology

Bahador Fani received his B.Sc., M.Sc., and Ph.D. degrees in electrical engineering from the Isfahan University of Technology, Isfahan, Iran, in 2003, 2005, and 2010, respectively. He is presently working as an associate professor in the Department of Electrical Engineering, Islamic Azad University, Isfahan (Khorasgan) Branch, Isfahan, Iran. His current research interests include power system analysis, power system dynamics, power quality, and the protection of power systems.